UNIVERSITY OF SOUTHAMPTON

Dielectrics for High Temperature Superconducting Applications

by

Linh H. Truong

A thesis submitted in partial fulfillment for the
degree of Doctor of Philosophy

in the
Faculty of Engineering and Applied Science
Department of Electronics and Computer Science

July 2013

UNIVERSITY OF SOUTHAMPTON

ABSTRACT

FACULTY OF ENGINEERING AND APPLIED SCIENCE
DEPARTMENT OF ELECTRONICS AND COMPUTER SCIENCE

Doctor of Philosophy

by Linh H. Truong

This thesis is concerned with the development of condition monitoring for future design of high temperature superconducting (HTS) power apparatus. In particular, the use of UHF sensing for detecting PD activity within HTS has been investigated. Obtained results indicate that fast current pulses during PD in LN_2 radiate electromagnetic waves which can be captured by the UHF sensor. PD during a negative streamer in LN_2 appears in the form of a series of pulses less than 1 μs apart. This sequence cannot be observed using conventional detection method due to its bandwidth limitation. Instead, a slowly damped pulse is recorded which shows the total amount of charge transferred during this period.

A study into PD streamer development within LN_2 has been undertaken that reveals the characteristics of pre-breakdown phenomena in LN_2. For negative streamers, when the electric field exceeds a threshold value, field emission from the electrode becomes effective which leads to the formation of initial cavities. Breakdown occurs within these gaseous bubbles and results in the development of negative streamers. For positive streamers, the process is much less well-understood due to the lack of initial electrons. However, from the recorded current pulses and shadow graphs, the physical mechanism behind positive streamer development is likely to be a more direct process, such as field ionisation, compared with the step-wise expansion in the case of negative streamers.

The mechanisms that cause damage to solid dielectrics immersed in LN_2 have been investigated. Obtained results indicate that pre-breakdown streamers can cause significant damage to the solid insulation barrier. Damage is the result of charge bombardment and mechanical forces rather than thermal effects. Inhomogeneous materials, such as glass fibre reinforced plastic (GRP), tend to introduce surface defects which can create local trapping sites. The trapped charges when combined with those from streamers can create much larger PD events. Consequently, damage observed on GRP barriers is much more severe than that on PTFE barriers under similar experimental conditions. Thus, design of future HTS power apparatus must consider this degradation phenomenon in order to improve the reliability of the insulation system.

Contents

List of Figures

List of Tables

Nomenclature

Symbol	Meaning	Units
ρ	Liquid density	$\mathrm{kgm^{-3}}$
λ	Mean free path	m
ϵ_0	Vacuum permittivity	$\mathrm{Fm^{-1}}$
ϵ_r	Dielectric permittivity	
μ_+	Positive ion mobility	$\mathrm{cm^2V^{-1}s^{-1}}$
μ_-	Negative ion mobility	$\mathrm{cm^2V^{-1}s^{-1}}$
μ_e	Electron mobility	$\mathrm{m^2V^{-1}s^{-1}}$
μ_b	Electron mobility in bounded state	$\mathrm{cm^2V^{-1}s^{-1}}$
μ_f	Electron mobility in free state	$\mathrm{cm^2V^{-1}s^{-1}}$
σ	Conductivity	$\mathrm{Sm^{-1}}$
c	Concentration of neutral ion pairs	$\mathrm{m^{-3}}$
d	Gap distance	m
E	Electric field	$\mathrm{Vm^{-1}}$
e	Charge of a electron	C
E_{val}	The broadening of the valence levels	eV
I	Current	A
I_{gas}	Ionisation energy in the gas phase	eV
I_{liq}	Ionisation energy in the liquid phase	eV
I_p	Peak current	A
K_D	Dissociation rate	
K_D^0	Dissociation rate at zero field	
K_R	Recombination rate	
m^*	Mass of a liquid molecule	kg
n_0	Number of primary electrons at cathode	$\mathrm{m^{-3}}$
$n_{\pm0}$	Ions at zero electric field	$\mathrm{m^{-3}}$
N	Density number	
N_b	Number of electrons in bounded state	
N_f	Number of electrons in free state	
P_+	Polarisation energy	eV
P	Pressure	Pa
q	Charge	C

R	Molecular radius	m
r_p	Needle tip radius	m
R_{max}	Maximum bubble radius	m
V	Voltage	V
v	Streamer velocity	ms^{-1}
V_0	Electron affinity	eV
V_p	Peak voltage	V
W	Work function of metal	eV
W_{eff}	Effective work function	eV
W_{fi}	Field ionisation work function	eV
W_i	Energy dissipation	eV
W_{vac}	Work function in vacuum	eV

Declaration of authorship

I, Linh Hoang Truong, declare that the thesis entitled

Dielectrics for High Temperature Superconducting Applications

and the work presented in the thesis are both my own, and have been generated by me as the result of my own original research. I confirm that:

- this work was done wholly or mainly while in candidature for a research degree at this University;
- where any part of this thesis has previously been submitted for a degree or any other qualification at this University or any other institution, this has been clearly stated;
- where I have consulted the published work of others, this is always clearly attributed;
- where I have quoted from the work of others, the source is always given. With the exception of such quotations, this thesis is entirely my own work;
- I have acknowledged all main sources of help;
- where the thesis is based on work done by myself jointly with others, I have made clear exactly what was done by others and what I have contributed myself;
- parts of this work have been published as: see Appendix C

Signed: ....

Date: ....

Acknowledgements

I wish to thank my thesis supervisors, Prof. Paul Lewin and Dr. David Swaffield, for their guidance and support. The constructed criticism and encouragement received from them have kept me concentrated and motivated throughout my studies.

I wish to thank to all my colleagues in the Tony Davies High Voltage Laboratory for their support and valuable discussion. In particular, Mr.Neil Palmer, Mr.Mike Smith, Mr Brian Rogers and Mr Richard Howell for their assistance with the experimental preparation.

The financial support of University of Southampton and Vietnamese Ministry of Education and Training is also gratefully acknowledged.

To my dearest family and friends

Chapter 1

Introduction

1.1 Superconductivity

In recent decades, the demand for electricity has increased continuously while natural energy sources are reducing. As a response to this problem, research into the application of superconductivity have been undertaken with expectations of improving efficiency and performance of power systems. Traditional conductors such as copper and aluminium have good conductivity. However, their resistivity even though very small ($\sim 1.72 \cdot 10^{-8}$ Ωm) is responsible for major losses. Therefore, elimination of the conductor resistance would have a dramatic impact on the power device performance; and it is achievable by using superconductors.

The idea of superconducting power equipment originated in the early twentieth century with the discovery of Low Temperature Superconductors(LTS). Superconductivity is given to the phenomena that the resistance of certain conductors disappear as temperatures approach absolute zero. In other words, current can be transmitted with no measurable resistive losses around liquid helium temperature (4 K). Therefore, superconducting equipment can have better electrical efficiency than conventional room-temperature devices. In addition, superconductors also allow an increase in power density which can result in more compact apparatus. Moreover, the possibility of lowering operational voltage levels in transmission and distribution networks promises smaller and cheaper substation equipment such as sealing ends and transformers. Unfortunately, many demonstration projects had shown that the cost and technical complication of cooling helium put LTS beyond commercial use.

In 1986, Muller and Bednorz discovered that the compound of lanthanum, barium, copper and oxygen could superconduct at 35 K. Several years later, Chu and his colleagues substituted yttrium for lanthanum and formulated YBCO which performed superconductivity at 92 K [1]. The discovery was crucial because the operating temperature of YBCO is above liquid range of nitrogen, 61.3-77 K, at atmosphere pressure. The term

High Temperature Superconductor (HTS) was then applied for materials which have the ability to superconduct above the normal boiling point of LN_2.

The birth of HTS renewed the interest in superconducting applications. Major cooling complications of LTS before can be solved by substituting liquid helium by liquid nitrogen. LN_2 can be supplied in large quantities at reasonable cost from condensing gas which is readily available from the atmosphere. The gases can be disposed of without any effects on the environment. In addition, the cooling power required to maintain operations at 77 K is much less than that at 4K. Lastly, LN_2 has a larger heat capacity than LHe which means better cooling ability. Since many HTS can perform superconductivity well above 77 K, a more reliable system than LTS can be achieved. For instance, common HTS such as BSCCO-2223 has a critical temperature of 110 K. The ability of superconducting 33 K above LN_2 normal boiling point implies that a small transient temperature fluctuation caused by heat leakage or AC losses can be tolerated while still maintaining overall high efficiency. It is worth mentioning that the AC losses are the result of alternating current and alternating magnetic fields. This parameter is positive despite the zero DC resistance of the superconductors. Several recent successful HTS applications using LN_2 are shown in Table 1.1. In some projects, HTS devices have been used in a live power grid [2].

Year	**Institution**	**Location**	**Application**	**References**
1998	WES,ORNL	USA	Transformer	[3]
1999	University of Southampton	UK	Transformer	[4]
2000	Pirelli-EPRI	USA, Italy	Cable	[2]
2002	AMSC	USA	Rotary Machine	[2]
2004	Yunna	China	Cable	[5]
2008	Nexans	Germany	Fault Current Limiter	[6]

Table 1.1: Recent HTS applications.

1.2 Study motivation

Beside the role of coolant, LN_2 is also acting as an electrical insulating medium in a HTS device. Liquefied nitrogen is a non-polar liquid dielectric. Its leakage conductivity is neglected and intrinsic dielectric strength is from 0.02 up to 0.38 MVmm^{-1} at normal boiling point [7] [8]. However, in practice, breakdown of LN_2 is subject to various defects such as impurities, high stress point and more importantly bubbles. Since breakdown of gaseous nitrogen occurs at much lower electric field than the liquid phase, the existence of gaseous bubbles will compromise the dielectric performance of liquid nitrogen. Therefore, dielectric failure of LN_2 is often observed well below its intrinsic breakdown strength.

Pre-breakdown phenomena in LN_2, often referred as streamers, is the precursor to electric breakdown of the liquid. Due to its narrow liquid range, LN_2 is very susceptible to vaporisation. Heat dissipation by electric discharges can create an increase in transient temperature which leads to the formation of gaseous bubbles. Partial discharges (PD) can initiate inside the bubbles which have a breakdown strength much lower than that of the surrounding liquid. The result is the initiation and development of pre-breakdown streamers. Since the streamer channels are conductive, fully developed streamers can lead to complete breakdown of the liquid. Therefore, understanding streamer behaviour under AC voltages is of paramount importance.

The ability of detecting PD is essential to provide early protection for a power apparatus from more catastrophic events such as complete breakdown. The IEC 60720 is an international standard which includes a set of specifications for PD measurements using coupling capacitors. Although this technique has been well-developed over many years with a large amount of in-field experience, the use of a capacitor limits the bandwidth of the measurement system. In dielectric liquids, such as transformer oils, PD occur in the form of pulse burst events which can only be observed by wideband measurement techniques [9]. A UHF sensor which has a bandwidth up 3 GHz is amongst these wideband, non-convention PD detection methods. It can provide a cost-effective, easy to use solution for PD measurement. The application of a UHF sensor in a LN_2 insulation system is much less well-developed than in gas or oil-filled mediums. Therefore, the study of the applicability of UHF sensors to measure PD during pre-breakdown phenomena in LN_2 can provide fundamental background for the application of such methods for PD monitoring systems of future HTS devices.

1.3 Aims and objectives

The first part of this project investigates the streamer behaviour in LN_2 under controlled conditions. Experiments utilise a point-to-plane configuration with a solid barrier placed over the planar electrode in order to prevent complete breakdown. PD are measured using conventional and non-conventional methods simultaneously. In addition, a specific imaging system allows capture of images of density change streamers as well as correlating those with the recorded PD data. Pre-breakdown streamers are characterised by applied voltage and liquid gap distance. The results from this study also provide a comparison between narrow and wideband PD measurements in a LN_2-filled insulation system.

The use of a solid barrier over the planar electrode simulates a liquid/solid insulation system. Similar systems can be found in many HTS power apparatus. In order to prevent breakdown, the solid barrier must be able to withstand the high electric field produced by streamer attachment. Providing that a single streamer even cannot breakdown the solid dielectric, accumulation of multiple PD events can degrade the material over time and lead to premature failure. The degradation of solid dielectrics in a LN_2-filled system has been observed [10], however comprehensive research has yet to be undertaken. Therefore, in order to improve the reliability of a cryogenic insulation system, another objective of this work is to study the degradation phenomenon of solid dielectrics in a LN_2-filled environment.

1.4 Thesis layout

Chapter 1 discusses the superconductivity phenomenon and its prospect for power applications. Motivation of the research as well as aims and objectives have been included. In Chapter 2, an overview of pre-breakdown phenomena in dielectric liquids is given with the emphasis on LN_2. The chapter begins with the discussion of basic physical properties of liquid dielectrics such as molecular structure and charge transport. Charge generation and multiplication processes are also explained. Then, initiation and propagation of pre-breakdown streamers are reviewed from the experimental data and the mechanisms governing these processes are also discussed.

Chapter 3 describes the experimental apparatus used in the study of PD streamers in LN_2. All experiments were taken inside a cryostat which allows good control of temperature and pressure. The experimental configuration includes: a PD source which is a sharp tungsten needle pointing towards a flat electrode, PD measurement system which consists of conventional and non-convention methods and an imaging technique using a high speed camera and a laser light source. A triggering sequence that allows correlation between the captured images and the recorded discharge data is also explained. Also, a testing procedure is included such that the experimental variables can be well-controlled.

Chapter 4 focuses on the feasibility of using UHF sensors to measure PD during pre-breakdown phenomena in LN_2. The chapter starts with the discussion on the influence of the cryostat structure on the propagation of radiated electromagnetic wave. Then, simultaneous PD measurement data during the streamer process in LN_2 are presented. Direct and indirect calibration methods of UHF signals to apparent charge are also investigated. From the obtained experimental results, advantages and disadvantages of different PD measurement techniques in a LN_2-filled environment are discussed.

In Chapter 5, PD streamers in LN_2 under AC voltages are investigated. PD data from wideband and narrowband measurements together with correlated images are given for various experimental conditions. From the experimental data, the initiation and propagation of streamers are discussed together with the mechanisms governing these processes. In addition, phase resolved analysis of a LN_2/solid dielectric insulation system is studied by the use of ϕ-q-n plots. Gap distance and material of solid barrier are the two experimental parameters considered in this investigation.

Chapter 6 investigates the degradation behaviour of cryogenic dielectrics due to PD streamers in LN_2. Two materials of interest are polytetrafluoroethylene (PTFE) and glass fibre reinforced epoxy (GRP). Damage is characterised by microscopic images and Raman spectroscopy. PD data during the testing period are also given. Laser ablation is used to simulate thermal effects on these two materials. Comparison between laser ablation and erosion data together with the analysis of the damage profile on the tested samples has provided an insight into the mechanisms causing the degradation of solid dielectrics under cryogenic conditions.

Finally, a summary of the conclusions drawn from the obtained experimental results in this research is given in Chapter 7. The Chapter concludes with recommendations for future experimental and theoretical work in order to improve the knowledge on the subject as well as further validate several hypotheses that have been proposed in this thesis.

1.5 Summary

This chapter provides the information on superconductivity and its applications in the power system. The role of LN_2 in a HTS device has also been discussed. Motivation of the research as well as its aims and objectives have also been defined. Organisation of this thesis is also given with a brief description of the content of each Chapter.

Chapter 2

Literature Review

2.1 Introduction

Liquid nitrogen is categorised as a dielectric liquid which is defined as having extremely low conductivity (Table 2.1). As a part of an insulating system, it is expected to hold off the voltage and prevent any undesirable current flowing between conductors. When the applied field increases, it is more and more difficult to maintain insulation due to various mechanisms such as field emission/ionisation and electron multiplication. At a certain stress, the liquid can no longer sustain its resistance and becomes electrically conductive. Such failure can cause catastrophic damage to power equipment and the surrounding environment. Moreover, insulation failure in major power equipment such as a transformer can lead to operational interruption and may have a high replacement cost.

Reliable dielectrics are of paramount importance to safe operation of any power equipment. Insulation systems must be able to exhibit low losses at certain high withstand voltages for a long period of time as well as withstand overvoltages caused by switching surges or lightning strikes. Liquids such as LN_2 are able to self-heal after discharges and chemical degradation is not important because nitrogen molecules are considered as chemically inactive. However, the damage which is caused by excessive current to the solid parts of the system such as adjacent electrodes and solid insulation is irreversible. Therefore, such phenomenon needs to be better understood so that future HTS power apparatus can improve resilience to electrical faults.

Liquid Dielectric	**Conductivity ($\mathbf{Sm^{-1}}$)**	**References**
Liquid Helium	$> 10^{-16}$	[11]
Liquid Nitrogen	$> 10^{-16}$	[12]
Mineral Oil	$10^{-10} - 10^{-12}$	[13]

Table 2.1: Electrical conductivity of several liquid dielectrics

The breakdown strength of liquids never solely depends on pure material properties. Intrinsic breakdown strength is unrealistic since every liquid consists of a certain amount of impurities. Under laboratory conditions, many purification processes can be applied but the result from purified materials can only be considered as a rough reference when considering performance in the field. Commercial liquid is expected to fail at much lower stress due to many different reasons for example; impurities, size effects, stressing time, pressure, non-uniform fields, electrically or thermally induced bubbles [11]. These factors usually lead to local discharges which can result in the formation of conductive channels propagating through the liquid; which are referred as streamers. Streamers are conductive low density structures which are formed in the region of high electrically stressed LN_2. These pre-breakdown phenomena play an important role in the breakdown of liquefied nitrogen. Intensive electric fields can allow injection and multiplication of charge carriers into liquids [14]. The movement of these carriers can result in heat dissipation [15] which is thought to cause density change in LN_2. Figure 2.1 shows an example of cathode filamentary streamers in LN_2 close to boiling point. The streamer initiates at the tip of the needle and propagates towards the ground electrode. The different refractive index between the streamer body and surrounding LN_2 is important evidence of the change in density. This phenomenon is also observed in other room-temperature liquids [16] [17].

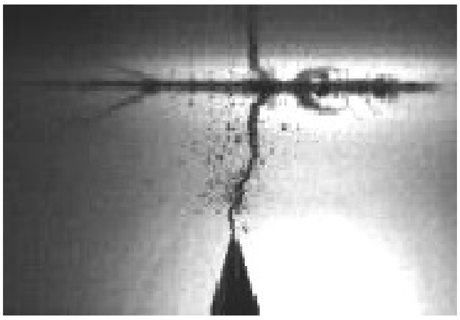

Figure 2.1: Cathode filamentary streamer in LN_2 at 77.5 K, atmospheric pressure, 26.4 kV AC (reproduced from [10]).

After the initial development of HTS, there has been a significant increase in research to understand and characterise behaviour of pre-breakdown phenomena of LN_2. Much of the work has been focused on experiments and characterisation of streamers. Meanwhile, very little effort has been devoted to understanding the physics or underlying mechanisms of these events. This is because of the difficulty of the liquid structure and limitations of understanding of behaviour of charge carriers in liquid. The published experimental results show significant variations between authors; which makes it even more difficult to analyse any mechanism behind breakdown. As a result, a model for breakdown in liquid nitrogen has not been proposed or universally accepted.

2.2 The physical properties of liquid dielectrics

The last few decades have seen a vast amount of studies on the dielectric properties of insulating liquids due to their importance in high voltage applications. From the experimental data, many theories and models have been suggested, however, there are still gaps in the present knowledge on the pre-breakdown phenomena in dielectric liquids especially for LN_2. Therefore, rather than just focusing on LN_2 in particular, this section reviews the state of the art of the related subjects on insulating liquids in general together with the discussion on the applicability of a given model for liquid nitrogen.

Before reviewing the ionization and conduction process, it is important to discuss the molecular structure of the liquid state. The interaction between molecules in the liquid form has some similarities with the other states of matter. Therefore, some of the models for gaseous and solid dielectrics have been applied to insulating liquids. Basically, the hypothesis is that a liquid can be considered as either a solid or a condensed gas. Such theories can only be used successfully to explain some of the observed phenomena and for particular liquids. The main problem is that although the liquid form is in between the other states, its molecules interact with each other in a much different way. Understanding the liquid structure and differences with respect to solid and gaseous dielectrics is essential to validate the existing models for electrical breakdown of insulating fluids.

2.2.1 The liquid state

At absolute zero, material exists in a perfect crystalline state. When heat is added, the substance melts into a liquid, at its melting point, and eventually vaporises into a gas at its boiling point. The atoms in a solid are strictly bound together in a well ordered structure. Meanwhile, gas molecules can move independently in space. The liquid state is in between the two: there is some structure as well as disorder. Instead of the long-range order of atoms in a crystalline solid, particles of a liquid are held together by intermolecular forces. The forces are able to maintain short-range order about several atomic diameters. At the same time, thermal displacement can also occur. Once a molecule has moved to a new location, a local short-range equilibrium is formed. The change of position due to thermal vibrations is the starting point for the discussion of hole theory of the liquid state.

Due to weak cohesive forces in liquids, there is a finite probability that an atom can acquire enough kinetic energy to separate itself and move up to several molecular diameters to another equilibrium position. Spontaneously, it leaves behind a vacant site, or cavity, or “void”, surrounded by previous neighbour atoms. The term “void” needs to be carefully understood. It can be explained as a wider gap between the atoms. These gaps might not have a definite shape or size, and can immediately move to another position by closing down spaces and opening at adjacent ones. One must bear in mind that without external forces, these vacant sites cannot develop into a macroscopic scale due to the intermolecular forces mentioned above. When a void collapses at a certain place, another one arises in the neighbourhood; therefore, at any given instance, a system of microscopic cavities exists in the structure of the liquid [18]. As the liquid temperature increases, additional thermal displacement of the fluid molecules is observed which results in volume expansion and eventual vaporisation into gas phase.

The distribution of voids in a liquid is not expected to be uniform. From the discussion above, this point of view seems obvious since movement of atoms caused by kinetic energy is a random event. In conventional thermodynamic theory in which average quantities over long time intervals are concerned, the fluctuation in density at a certain point is ignored and so is the random void distribution. This assumption remains correct as long as long intervals of time and average values are considered. However for transient analysis, notions such as equally distributed atoms or molecules are to be reconsidered. Pre-breakdown phenomenon in liquid, which is a sub-microsecond event, falls into the latter category. The question then is whether or not electric fields affect the void generation or distribution within a liquid. A theory developed by Lewis [19] would suggest so. At a high field region, liquid dielectrics experience higher void generation rate than without the influence of applied voltages. In order words, a lower density region is formed close to a needle tip in a point-plane configuration, e.g. where the electric field is the highest. However, due to the lack of experimental proof, the effects of such phenomenon on streamer behaviour are still unclear and are discussed later on in this Chapter.

The concept of voids had been applied to explain many phenomena in liquids such as viscosity and diffusion. The analysis which is involved with thermodynamics and fluid mechanics is outside the scope of this thesis and therefore, will not be discussed. Further details can be found in [18].

2.2.2 The electronic band model

The band model of energy level was originally developed for solid substances. It was widely accepted to explain many properties of solids such as the differences of conductors, insulators and semiconductors. In the absence of a crystalline structure, a material in liquid form does possess a short-range order. In addition, for many semiconductors and in their liquid forms, experimental data have shown similar relationship between temperature and conductivity to that obtained in the solid state. Other justifications for the use of band model for non-polar liquids can be found in [20].

Assuming that there is a valance band and conduction band in the electronic model for a liquid dielectric, the band gap is defined as the ionisation energy of molecules I_{liq}, e.g. the energy required to promote an electron from a localised to a delocalised state. As for most non-polar liquids, the values range between 6.8 to 10 eV [20]. Due to the high energy band gap, the model will consist of a fully-filled valance band and empty conduction band since thermal excitation of electrons can be neglected. The liquids considered here are, therefore, insulators. An example of electron energy levels in a liquid is illustrated in Figure 2.2. I_{gas} is the ionisation energy in gas phase. V_0 denotes the electron affinity, the energy of electron at the bottom of conduction band. A positive value means that a certain amount of energy, V_0, is required to move a delocalised electron from a gas phase into a liquid phase, a negative value implies otherwise. E_{val} is related to the broadening of the valence band due to the intermolecular forces that keep the short-range order in the liquid phase. P_+ is the polarisation energy of a spherical charge.

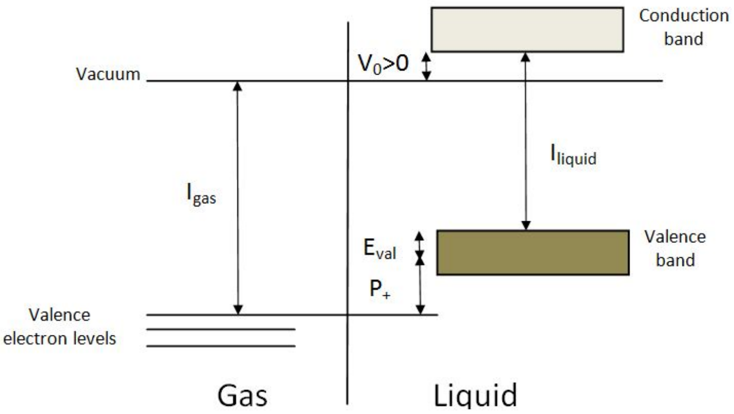

FIGURE 2.2: Energy band model in liquid.

The band gap of a liquid can be expressed as:

$$I_{liq} = I_{gas} + P_+ + V_0 - E_{val} \tag{2.1}$$

In which, P_+ is given as [21]:

$$P_+ = -\frac{e_0^2}{8\pi\epsilon_0 R}[1 - \frac{1}{\epsilon_r}] \tag{2.2}$$

The value of I_{gas} for nitrogen is 15.58 eV [22]. Electron affinity, V_0, was estimated at 0.05 eV for LN_2 [23]. From equation (2.1), the energy gap of LN_2 can be calculated as 14.5 eV. In this case, the ionisation energy is lower in the liquid phase than in the gas phase. However, this behaviour is not always the case for all non-polar liquids. For example, liquid helium and neon hold an opposite relationship, e.g. higher energy is required to ionise molecules in the liquid than the gas phase, due to lower dielectric constants and higher values of electron affinity [21].

There are a couple of important points that need to be mentioned on the adoption of an electronic band model for liquids. First of all, the actual existence of a broadening band has not been fully proved. Secondly, E_{val} if it exists has to be strongly dependent on the applied pressure. As mentioned above, this parameter is the consequence of atomic interactions. Increasing molecule density certainly will result in more interactions, thus, further broadening the electronic band is expected. If this is correct, there is a probability that at a certain pressure, the band gap will be reduced small enough for thermal activation of charge carriers. As a matter of fact, it is has been found that when LN$_2$ was compressed to 20-50 GPa by a shock wave, a transient increase in conductivity was recorded which was the result of a charge concentration of $2 \cdot 10^{17}$ cm^{-3}. This phenomenon was also observed in LH2 and LD2 at 140 GPa [24]. Lastly, if an electron is promoted into conduction band, it is debatable whether the term "hole" as in positive vacancy can be applied here. This is because a crystalline order does not exist in the liquid state of matter. The movement of this positive quantum which is defined as movement of electrons in an opposite direction, as in the case of solids, is no longer applicable. The produced positive ions, $N^{+}{}_2$ for example, can be dislocated to a new position due to thermal vibrations or the influence of external electric field. The one thing that is certain about the band model is that an amount of energy is required to remove an electron out of a liquid molecule, defined as I_{liq}. This value is expected to be less than that in gaseous nitrogen due to the low magnitude of electron affinity compared with the polarisation energy.

2.3 Charge transportation in liquid dielectrics

The properties of charge dynamics are different from one insulating liquid to another. Electron mobilities in dielectric liquids can vary by up to six order of magnitudes. In liquid xenon, μ_e was measured at 2000 cm^{2}V^{-1}s^{-1}, while for liquid neon this is $1.8 \cdot 10^{-7}$ cm^{2}V^{-1}s^{-1} [25]. As suggested in [26], three categories can be distinguished here:

1. $\mu_e > 10$ cm^{2}V^{-1}s^{-1}. Electrons are considered as quasi-free. A completely free electron only exists in vacuum. Interaction between electrons and liquid molecules can be considered as single scattering system. This is the case for heavy rare gases such as Ar, Kr and Xe [26].
2. $\mu_e < 0.1$ cm^{2}V^{-1}s^{-1}. Electrons are trapped within voids due to the fluctuation of liquid density as discussed previously. The low mobility is due to the fact that an electron spends most of its time localised.
3. 0.1 cm^{2}V^{-1}s^{-1} $< \mu_e <$ 10 cm^{2}V^{-1}s^{-1}. This scenario is between the two cases listed above. Electrons are regarded as quasi-localised.

Liquid nitrogen of which electron mobility was measured at $2 \cdot 10^{-3}$ cm^{2}V^{-1}s^{-1} falls into the second category. The reason for the low mobility of electrons in LN$_2$ is suggested to be the result of localisation of the electron which is discussed in the following section.

2.3.1 Electron mobility in liquid nitrogen

The process of electron trapping inside LN_2 is illustrated in Figure 2.3. Consider an electron that has been injected into the liquid, it will possess a certain amount of energy depending on the injection method. As moving through the fluid, the electron will encounter collisions with molecules. Once the electron enters a vacant site, or void, it can be temporarily trapped due to the positive value of V_0. Density fluctuation will occur due to the repulsive force between the electron and liquid molecules. The result is the formation of a cavity as shown in Figure 2.3 (c). It is worth mentioning that in this case, the "cavity" mainly consists of a void or holes without any LN_2 molecules. The change in energy of an electron between delocalised and localised states has been discussed in detail in [27]. Localised electrons can still move but with much lower velocity.

At a certain time, some of the electrons being injected into the liquid are bounded, N_b, while the others are quasi-free, N_f. The mobility of electrons is a combination of the mobility in localised, μ_b, and delocalised states, μ_f:

$$\mu_e = \frac{N_f \mu_f + N_b \mu_b}{N_f + N_b} \tag{2.3}$$

At lower temperatures, e.g. close to the triple point, electrons in LN_2 are in full localisation mode within microscopic cavities having radius below 1 nm. As the temperature increases, electrons can be removed from the bound state to delocalised state. In LN_2 this phenomenon becomes effective close to the critical point at 126 K [28]. Experimental results [29] have shown an increase of mobility above 115 K which is in agreement with the theory discussed above.

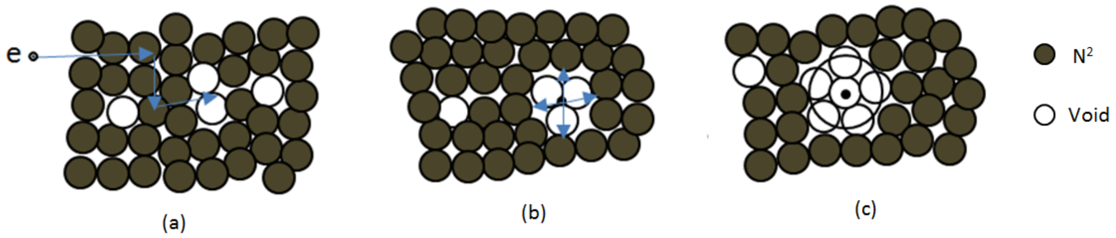

FIGURE 2.3: Formation of electron bubble in liquid nitrogen. (a) injection of electron, (b) temporarily trapped electron, (c) formation of electron bubble. Redrawn from similar model for liquid neon [20]

The low mobility of electrons in LN_2 can also be explained by electron attachment and detachment. In a solution, electrons can be attached to liquid molecules in order to form negative ions [29]. Attachment can happen between one electron and one or multiple molecules in order to form a more stable cluster of negative charge:

$$N_2 + e^- \rightleftharpoons N_2^- \tag{2.4}$$

$$N_2^- + N_2 \rightleftharpoons N_2N_2^- \tag{2.5}$$

$$e^- + nN_2 \rightleftharpoons nN_2^- \tag{2.6}$$

The effective lifetime of negative ions in gas has been estimated as in the order of 0.7 ps and increases with density [30].

Due to the lack of experimental results, it is difficult to comment on which hypothesis is more accurate to explain the electron dynamics in LN_2. However, the similarity of the two models is that electron transport through LN_2 will experience localisation either in the form of a cavity or a cluster of negative ions. This results in much lower electron mobility compared with other cryogenic liquids such as argon, helium and xenon. It is worth mentioning that negative charge mobility in liquid nitrogen increases significantly under high field conditions. Such a change was observed during mobility measurement above $0.6 \cdot 10^7$ Vm^{-1} [31]. Pre-breakdown currents in LN_2 also suggest a mobility in the order of 10^{-1} $cm^2V^{-1}s^{-1}$ at 10^7 Vm^{-1} [32]. The influence of electric field on electron mobility can be explained by either a lower attachment rate at high field or the existence of more delocalised electrons due to the Coulomb force from the external field.

2.3.2 Mobility of positive charge carriers in liquid nitrogen

In the case of semiconductors, when an electron is promoted to the conduction band, a positive hole is created. The movement of this electronic entity is in the form of electron jumping between neighbour molecules. A similar phenomenon can be considered for dielectric liquids under the assumption that some form of order between the liquid atoms or molecules exist. In this case, if an electron was removed, it will leave behind a positive ion. Then under the influence of the external field and the positive charge, an electron from a neighbouring molecule is transferred to the positive charge and neutralises it. The migration of electrons in the opposite direction with applied field can be considered as movement of a positive charge along the field lines. The movement of liquid molecules is not involved in this process, therefore, the mobility of positive holes is expected to be greater than that of positive ions. A hole transport mechanism has been suggested for liquid Xenon [33] and some other extremely purified hydrocarbon samples [34].

The hole transport mechanism in liquid dielectrics is debatable since the order of molecules in the liquid state only exists over a short range in contrast to the crystalline structure of solids. Disorder of a liquid structure can occur by thermal displacement of the liquid molecules. Therefore, migration of a positive hole will be stopped if a vacant site is created between the neighbouring molecules of the positive charge. In this case, the transfer of an electron from a neutral atom or molecule into the adjacent positive hole is disrupted due to the increased distance between them. Positive hole transport can also be terminated if there is an impurity of which ionisation energy is lower than the liquid itself. In this case, electron transfer occurs from the impurity to the positive hole to from a neutralised liquid molecule and a positive impurity ion.

In the case of LN_2, positive mobility has been measured between $1-2\cdot10^{-3}$ $cm^2V^{-1}s^{-1}$ at 77 K [35]. This value is comparable with that of negative ions at the same temperature, $2.5 \cdot 10^{-3}$ $cm^2V^{-1}s^{-1}$ [30]. Therefore, positive hole transport does not seem to be the dominant mechanism. Instead, it is the movement of positive nitrogen molecules. Prediction of positive ion mobility in LN_2 using the formula for gases has yielded a lower value than measurement results. The difference is suggested to be the result of the formation of a cluster of molecules around the centre ion. Mobility of positive ions in LN_2 was found to decrease in a stepwise manner as the external electric fields increased. It is hypothesised that the given phenomenon is the consequence of the change in cluster size due to the influence of the applied voltage [35].

In general, mobilities of positive and negative charge carriers in LN_2 are lower than other cryogenic liquids and gaseous nitrogen at the same density. This is because of the formation of cluster of molecules and bubbles which trap the charges inside. Positive and negative charge carrier mobilities behave differently under high field conditions. The actual values of mobilities above 10^7 Vm^{-1} have not been found for either polarities. However, from the suggested hypothesises, electrons would be more quasi-free [31] while positive ions would move slower [35] as the applied fields increase. Whether or not these relationships are still applicable under a pre-breakdown field condition in LN_2 remains unclear at this point.

2.3.3 Electron transfer at the liquid/vapour interface

The interface of interest is liquid/vapour, the situation between liquid and solid (metal) will be explained in Section 2.4. When an electron approaches the interface between two materials with different permittivity, it will experience a force caused by its image charge in the opposite medium. Consider the liquid/vapour interface, two scenarios will happen as shown in Figure 2.4. In the first case, an electron in the vapour phase is approaching the solution. Since the molecules in the liquid phase have higher polarisability, the polarity of charge at the interface will be positive. Therefore, the electron will experience an attractive force toward the interface by the positive image charge. In the other scenario, an electron in the liquid is moving toward the liquid/vapour interface. Because it is more difficult to polarise the solution than the vapour, negative image charge occurs at the interface. Thus, the force in this case is repulsive.

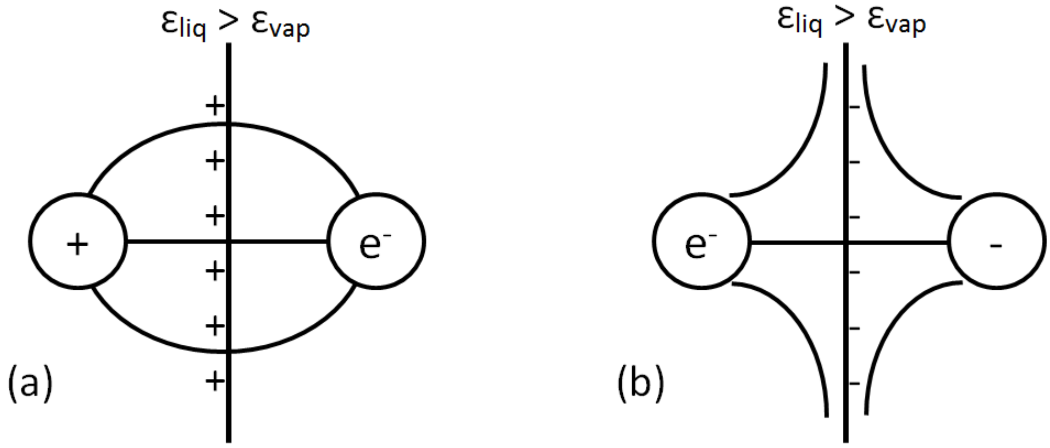

FIGURE 2.4: Electron at liquid/gas interface. (a) electron is in the liquid and approaching the vapour, the force is attractive (b) electron is in the vapour and approaching the solution, the force is repulsive. Redrawn from [20]

At the same time, when an electron is moving from a gas to liquid phase, a potential barrier of V_0 is presented at the interface. This value can either be positive or negative depending on the liquid. In the case of LN_2, the value is positive. The potential V_0 superimposes on the potential energy caused by the image charge. Four scenarios can happen at the interface [20]:

1. An electron in the vapour is moving towards the interface and $V_0 > 0$. Although the force from the image charge is attractive, the electron will encounter a potential barrier of V_0. Depending on the kinetic energy of the electron, it can either be trapped on the surface or jump through the barrier and enter the liquid.

2. An electron is moving from the vapour to the liquid with $V_0 < 0$. In this case, the transfer should occur immediately.

3. A delocalised electron in the solution is approaching the interface and $V_0 > 0$. Although the electron is repelled by the image charge, the potential barrier, V_0, is dominant over the image potential. Electron transfer should occur without any additional energy.

4. An electron is in the liquid with $V_0 < 0$ and moving towards the interface. The image force is repulsive and the potential barrier prevents the electron from transferring to the vapour. Then either the electron already has enough kinetic energy to overcome the barrier or the transfer process is thermally activated.

2.4 Charge generation in liquids

Dielectric liquids are considered as good insulators at low fields with a full valence band and empty conduction band. Under extreme electric field conditions (above 10^8 Vm^{-1}) charges can be produced into the liquids by various mechanisms. At the breakdown voltage, the fluids will become conductive. The charge generation processes are different depending on the polarity of the applied field which is the reason for the difference in the phenomena observed during cathode and anode pre-breakdown.

Mechanisms for charge production can be separated into two categories, bulk and interface. Interface processes include field emission and ionisation which are responsible for injection of electrons and positive ions respectively. The mechanism for charge generation inside the liquid bulk is by field dissociation. Unlike interface processes, the bulk process produces both positive and negative charge carriers.

2.4.1 Field emission

In metals, a majority of electrons are bound to the positive ions of the crystalline lattice and possess a discrete energy level (band). The band diagram of a metal consists of valence and conduction bands which overlap each other. The Fermi level lies between the overlapping section. At absolute zero, electron energy is below the Fermi level. When the temperature increases, electrons can be thermally excited to an energy level high enough to remove itself from the atomic structure. The work that must be done to completely force an electron out of the metal is called the work function, in other words, this is the amount of energy that must be added to overcome the electrostatic force of crystalline lattice. This quantity is defined as the difference in energy between an electron resting outside the metal surface and the Fermi-level.

Consider an electron at a distance x from conductor, the image charge theorem states that the force acting on the electron in front of an infinite conducting sheet is given by:

$$F = \frac{1}{4\pi\epsilon_0} \cdot \frac{q_1 q_2}{r^2} = \frac{-e^2}{16\pi\epsilon_0 x^2} \tag{2.7}$$

The potential energy (energy required to move electron to infinity) can be expressed as:

$$W(x) = \int_x^{\infty} F(y)dy = \frac{-e^2}{16\pi\epsilon_0 x} \tag{2.8}$$

A plot of W(x) as a function of distance from metal surface is shown in Figure 2.5 (1). Without external field, the work function is given as:

$$W = E_{vacuum} - E_{Fermi} \tag{2.9}$$

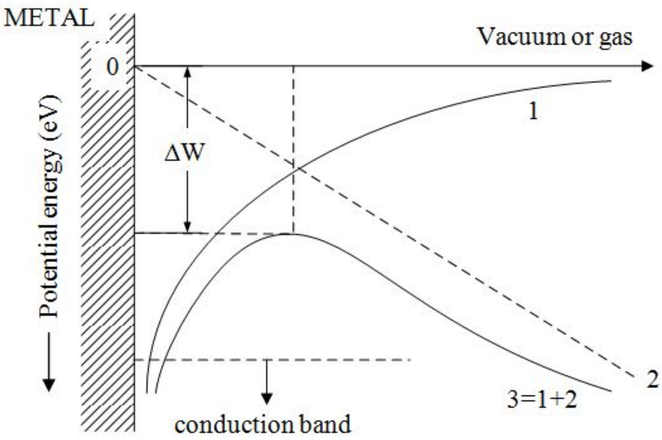

FIGURE 2.5: Energy band model in liquid (reproduced from [10]).

When electric field is applied, the electron will experience a force equal to qE. The potential energy caused by this is shown in Figure 2.5 (2). It can also be seen that the work function is reduced. Clearly, there is a maximum and it is at:

$$\frac{dy}{dx}\left(\frac{-e^2}{16\pi\epsilon_0 x} - eEx\right) = 0 \tag{2.10}$$

The solution is:

$$x_0 = \sqrt{\frac{e}{16\pi\epsilon_0 E}} \tag{2.11}$$

Using equation (2.11), the maximum value of potential barrier can be calculated from equation (2.10) :

$$y_{max} = -e\sqrt{\frac{eE}{4\pi\epsilon_0}} \tag{2.12}$$

Therefore, the reduction of work function is:

$$\delta W = |y_{max}| = e\sqrt{\frac{eE}{4\pi\epsilon_0}} \tag{2.13}$$

And effective work function:

$$W_{eff} = W - \delta W \tag{2.14}$$

The value of W depends on the properties of metals, for tungsten this value is: 4.5 eV [36].

As can be seen, the work function is reduced by an external electric field. For example, for the field of 0.1 MVmm^{-1} and 1 MVmm^{-1} , the value of δW is: 0.379 eV and 1.199 eV respectively. When the electric field is higher than 1 MVmm^{-1}, the value of δW becomes comparable to the work function of tungsten (also aluminium and copper). Moreover, it can also be seen in Figure 2.5 that increasing electrical stress will result in a thinner potential energy barrier. The result is an exponential increase in the possibility of electrons tunnelling through.

A theory for charge injection at the solid/vacuum interface due to an intensive field was originally developed by Fowler and Nordheim in 1928 [37]. Under this regime, current density was suggested to be independent of temperature. The required field might be lower in the experiments due to irregularities of the electrode surface finishing. The field emission current was expressed in the following form:

$$J = AE^2 exp(-\frac{B}{E}) \tag{2.15}$$

$$where \quad A = \frac{e^3}{8\pi hW} \quad and \quad B = \frac{8\pi\sqrt{2m}W^{3/2}}{3he}$$

In which, e and m are electron charge and mass and h is Planck's constant. The derivation of equation (2.15) has not taken into account the lowering of image force barrier. Another form of Fowler-Norheim current is given as [38]:

$$J = AE^2 exp(-\frac{B}{E}) \tag{2.16}$$

$$where \quad A = \frac{e^3}{8\pi hWt^2(y)} \quad and \quad B = \frac{8\pi\sqrt{2m}W^{3/2}}{3he}v(y)$$

The difference between equation (2.15) and (2.16) is the introduction of $t^2(y)$ and $v(y)$ with $y = \delta W/W$. Both of these functions are field dependent and take into account the modification of the image barrier. Values for $v(y)$ and $t^2(y)$ can be approximated as $0.95 - y^2$ and 1.1 [38].

The theory of the work function at the metal/vacuum interface can also be applied to liquid dielectrics. Due to different molecular structures, the adaption requires certain justifications. The first one is the replacement of ϵ_0 by ϵ since liquids have different permittivity than vacuum. Secondly, the work function in liquid cannot be equal to that in vacuum. In fact, the relationship between the two quantities is given by:

$$W_{liq} = W_{vac} + V_0 \tag{2.17}$$

Where V_0 is the electron affinity as defined previously.

Field emission current following the Fowler-Nordheim relationship has been observed in many non-polar liquids, e.g. the plot of $ln(I/V^2)$ against V^{-1} is in the form of a straight line. However, these results are only valid for very sharp needle tips ($r_p < 0.2$ μm) and with an electric field above 10^9 Vm^{-1} [39] [40]. When $r_p > 0.5$ μm, Trichel-like discharge pulses were observed [14]. Pulse current regimes can only occur if electron avalanches reach a critical size which can only be achieved in the case of a larger tip radius. In addition, bigger needle tips will lead to a larger amount of electrons being emitted. As a result, the current will quickly become space charge limited. Heat dissipation can also result in the formation of gaseous bubbles in which case the measured current will no longer follow the Nordheim-Fowler regime.

The current profile as in Fowler-Nordheim theory has not been observed in the case of LN_2. Consider a tip/plane configuration, at a certain applied potential, the electric field at the tip is high enough for the field emission regime. Electrons, after being injected into the liquid move towards the anode due to the electrostatic force, the velocity of which depends on the drift mobility of the charge carriers. Space charge starts to accumulate at distances from the tip where the electric field is much lower. Attachment, trapping of electrons may be possible at this point. Accumulated space charge lowers the field strength at the tip which results in lowering the amount of electrons injected and therefore reduces current. This effect is related to the mobility of charge carriers and the level of current injection. For liquid nitrogen which has low electron mobility (of the order of 0.1 $\mathrm{cm^2V^{-1}s^{-1}}$ [20]), space charge can be developed much faster than other high-electron-mobility liquids. Therefore, field emission current quickly becomes space charge limited and the Fowler-Nordheim plot cannot be observed [40].

2.4.2 Field ionisation

The field emission process can only be applied for a negative needle from which electrons are injected into the liquid. In the case of a positive needle, a similar ion-injection phenomenon is often referred as field ionisation. As shown in Figure 2.6, an electron from a liquid molecule at the liquid/solid interface can tunnel into the metal and create a positive ion. Field ionisation can be treated in two ways: via the liquid band model or simply the tunnelling of individual molecules and disregard of the band structure. The latter process appears to be more applicable for liquid dielectrics due to the weak intermolecular force and the absence of a long range structure [41]. It is also worth mentioning that the product of field ionisation in this case can either be a positive hole or a positive ion. Again due to the difference between the liquid structure and the solid phase, generation and movement of positive ions are more likely to be the dominant phenomena. Under the assumption that tunnelling of electron occurs in a non-interacting manner, field ionisation current has been derived by Halpern and Gomer [41].

$$I \sim p\frac{(I_{liq}-W_{liq})^2}{\sqrt{I_{liq}-W_{liq}}} \quad exp(-C\frac{\sqrt{W_{liq}}(I_{liq}-W_{liq})}{E}) \tag{2.18}$$

$$where \quad C = -2\frac{\sqrt{2\frac{m*}{h^2}}}{e}$$

In which, p the density of valence electrons, and m^* is the mass of a liquid molecule. However, field ionisation current following equation 2.18 has only been observed for LAr and LH_2. In other dielectric liquids, the current quickly become space charged limited, e.g. $\sqrt{I} \sim V$, due to the low mobility of positive ions.

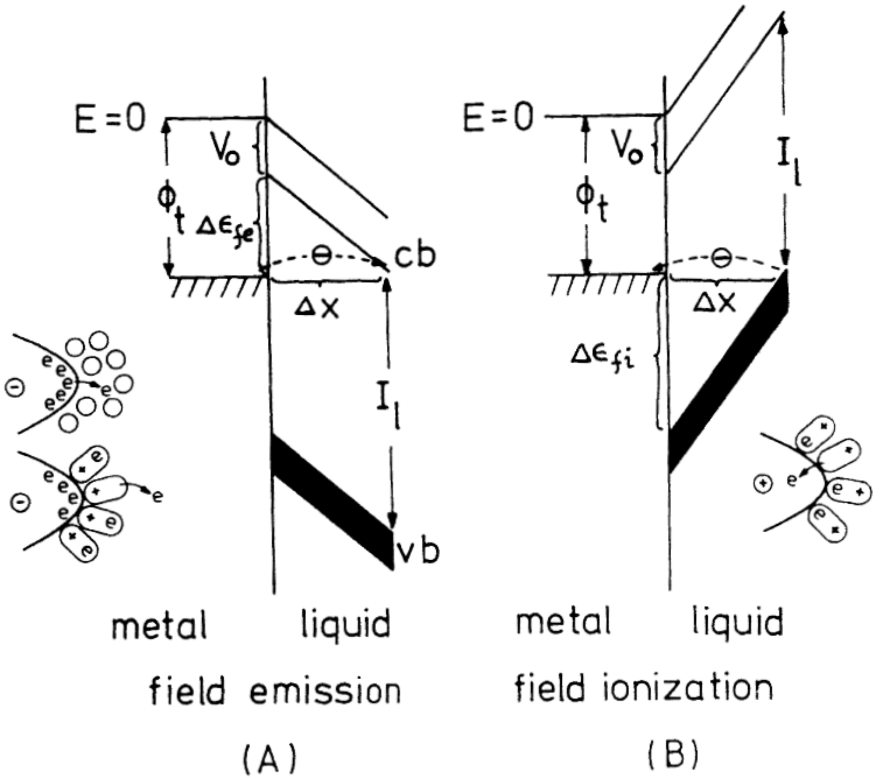

FIGURE 2.6: Schematic diagram of the energy levels at liquid/metal interface: (A) field emission, (B) field ionisation (reproduced from [29])

The energy barrier in the case of cathode emission is given as $W_{vac} + V_0$ where as in the case of field ionisation, the barrier is defined as $W_{fi} = I_{liq} - W_{vac} - V_0$. Consider a tungsten needle of which the work function is 4.5 eV, for cyclohexane, the value of W_{fi} can be estimated at 4.25 eV whereas for LH_2 $W_{fi} \sim 10$ eV. The corresponding threshold electric field for the two liquids are $1.2{\cdot}10^9$ and $7{\cdot}10^9$ Vm^{-1} respectively [42]. Thus, field ionisation occurs at a much higher electric field than field emission. In the case of LN_2, the value of W_{fi} can be calculated at 11.01 eV which proposes a threshold electric field close to 10^{10} Vm^{-1}.

2.4.3 Ionic dissociation

In electric field dependent ionic dissociation theory, a liquid contains a certain concentration of neutral ion pairs, c (m^{-3}), and an equal amount of positive and negative ions, $n_{\pm 0}$ (m^{-3}). Without an external electric field, the dissociation rate and recombination rate of neutral and charge ions depends on two kinetic rate constants, K_D and K_R respectively. Onsager [43] developed a theory explaining the effects of external field on the conductivity of liquid from a dissociation and recombination point of view. The dissociation rate, K_D, is influenced by the electric field while the recombination rate, K_R, is electric field independent. Consequently, the concentration of free charge carriers in the liquid increases as the electric stress increases. The dissociation rate, K_D, as a function of electric field is given as:

$$K_D(E) = K_D^o F(E) \tag{2.19}$$

where K_D^o is the rate at zero electric field, $F(E)$ is a function of electric field is defined as:

$$F(E) = f(b) = \frac{I_1(4b)}{2b} \tag{2.20}$$

where,

$$b = \sqrt{\frac{e^3 E}{16\pi\epsilon k^2 T^2}} \tag{2.21}$$

where, I_1, is the modified Bessel function, k is Boltzmann constant, ϵ is the permittivity of the liquid and T is the liquid temperature in Kelvin.

In thermal equilibrium without an external field, the relation between dissociation and recombination can be described:

$$cK_D^0 = n_{\pm 0}^2 K_R \tag{2.22}$$

where c is the concentration of neutral ion pairs and $n_{\pm 0}$ is the free charge concentration without an external electric field. Langevin recombination can be used to describe recombination of positive and negative ions [43]:

$$K_R = \frac{e(\mu_+ + \mu_-)}{\epsilon} \tag{2.23}$$

where μ_+, μ_- denote the mobility of positive and negative ions respectively. The conductivity of liquid at zero electric field is directly related to free charge concentration as follows:

$$\sigma = e(\mu_+ n_{+0} + \mu_- n_{-0}) \tag{2.24}$$

Because dissociation results in the generation of both negative and positive ions, negative and positive ion concentration should be equal, therefore:

$$n_{\pm 0} = \frac{\sigma}{e(\mu_+ + \mu_-)} \tag{2.25}$$

Therefore, the electric field dependent ionic dissociation can be expressed as:

$$cK_D = (\frac{\sigma}{e(\mu_+ + \mu_-)})^2 K_R F(E) \tag{2.26}$$

The Osanger theory shows good agreement with experimental data for conduction in various liquids when the electric field is below $5{\cdot}10^7$ Vm^{-1} [42]. At higher electric fields, conduction current does not show dependence on conductivity because other charge multiplication processes take place. Ionic dissociation is the process in the bulk liquid compared to field emission which is a boundary process dominant at the metal liquid interface. Therefore, the theory presented in this section is applicable for both negative and positive polarities.

2.5 Initiation pre-breakdown streamers in dielectric liquids

Breakdown in a liquid dielectric is the result of initiation and propagation of prebreakdown phenomena either in a uniform or divergent field, AC, DC or impulse voltage [44] [45]. Prebreakdown phenomena includes partial discharge currents, light emission, density change channels (often referred as streamers) which propagate towards the other electrode [46] [14]. This section focuses on the initiation process of positive and negative streamers in liquid dielectrics.

2.5.1 Electron avalanche

Electron multiplication processes based on collision ionisation were originally developed for gases. When moving under the influence of a field, electrons can ionise atoms from collisions. To cause impact ionisation, the energy acquired by an electron must be at least equal to the ionisation energy of the molecules. Electrons with lower energy can only excite the particles and further collision is required for excited particles to be ionised. Furthermore, not every electron with high-enough energy can cause ionisation since the process is governed by the probability of impact. The energy of an electron with a free path x is given by:

$$W = e \cdot E \cdot x \tag{2.27}$$

The fraction of electrons that can travel a distance, x, in the field direction without any collision is:

$$f(x) = e^{\frac{-x}{\lambda}} \tag{2.28}$$

Where λ denotes mean free path of electron in gases, r is molecule radius and N is density number:

$$\lambda = \frac{1}{\pi r^2 N} \tag{2.29}$$

This process can repeat as long as electrons can gain enough energy for ionisation. The avalanche process is characterised by the Townsend first ionisation coefficient, α, defined as the number of electrons produced by one electron per unit length. Then, the total number of electrons produced is given by:

$$n = n_0 e^{\alpha d} \tag{2.30}$$

where n_0 is the number of primary electrons generated at cathode and α is a function of applied field and density number:

$$\frac{\alpha}{N} = A_i e^{-\frac{B_i N}{E}} \tag{2.31}$$

Where

$$A_i = \sigma_i; B_i = V_i \sigma_i \tag{2.32}$$

σ_i and V_i are cross section constants for ionisation (relating to the possibility of ionised atoms) and ionisation energy of the gas. The values of A_i and B_i are normally acquired experimentally.

The Townsend breakdown model for gases has been extrapolated for liquids by considering the liquid phase as a dense gas. The ionisation coefficient, $\alpha(E, N)$, can be estimated by using the liquid density number, N. However, the value obtained from experimental data, $\alpha_L(E)$, is always higher than the extrapolated estimation $\alpha(E, N)$ for many liquid rare gases [47] [48], LN_2 [49], and cyclohexane [50]. Similarly, the estimated breakdown strength calculated from the Townsend gas model using the liquid density number is also higher than the measured values as shown in Table 2.2. This is because of lower ionisation energy in the liquid phase. As shown in the case of LN_2 (Section 2.2.2), the energy required to promote an electron from the valence to conduction band in the liquid phase is 1 eV lower than that in the gas form due to the low value of V_0 and polarisation energy P_+. Therefore, the avalanche process in a liquid can produce more electrons than in a dense gas with the same density number. The extrapolated calculation, $\alpha(E, N)$, thus, will tend to underestimate the ionisation coefficient, $\alpha_L(E)$. A similar explanation can be adapted for the difference between the theoretical breakdown voltage of a dense gas and measured values for a liquid.

Liquid	E_B **experimental (Vmm^{-1})**	E_B **calculated (Vmm^{-1})**	**Reference**
LAr	0.05	0.12	[51]
LN_2	0.38	0.55	[8]
LHe	0.2	0.3	[8]
CH	0.19	0.4	[52]

TABLE 2.2: Breakdown electric fields for different dielectric liquids.

2.5.2 Generation of gaseous bubbles

Gaseous bubbles can be produced thermally or electrically. LN_2 is normally used close to its boiling temperature. Because of its low latent heat (199 kJkg^{-1} [53]) and narrow liquid range (66.15 to 77.36 K), LN_2 is very susceptible to vaporisation. The presence of bubbles will reduce the dielectric strength of the liquid due to the lower breakdown strength of the gas phase. The effects of thermally induced bubbles which are the results of quenching or cooling are important [54] but are not considered in this thesis. On the other hand, electrically induced micro bubbles and their effects on breakdown in LN_2 are discussed.

The generation of microscopic bubbles in dielectric liquids due to electrical effects has been reported frequently in the literature. Nelson et al [55] proposed the existence of a threshold electric field for bubble formation in hydrocarbon liquids. The change in refractive index of the captured shadow graphs confirms the occurrence of phase change within tens of nanoseconds of the voltage application [56]. In cyclohexane, gaseous cavities were found to be developed from tiny filaments about 40 ns after applying voltage [57].

Denat et al [46] investigated the initiation and behaviour of electrically induced bubbles in LN_2 with point-plane experiments. Above a threshold field, E_s, electrons injected from a cathode can cause avalanche close to the point electrode where the electric field is at its maximum. The heat dissipation from collision with atoms has been considered as mechanism for bubble formation. Bubbles are recorded in the microscopic scale (several μm) and rebound several times before collapse into the surrounding liquid. The maximum radius of the bubble before collapsing is given by:

$$R_{max} = k\frac{{W_i}^3}{P} \tag{2.33}$$

where P is the applied pressure and W_i represents the amount of energy dissipation. W_i can be calculated by the product of the apparent charge and applied voltage. The charge can be acquired by integrating the current or via calibration methods. Gaseous bubbles can grow up to several micrometers before collapsing depending on the experimental conditions, such as pressure and applied voltage.

The required electric field for the formation of bubbles in LN_2 has been estimated by Peier [15]. After being injected, an electron will move under the influence of electric field due to Colombic force. The energy gained by the electron before its collision with an molecule is given by equation (2.27). At high field conditions, there will be large number of electrons injected into the liquid from cathode. Therefore, for a limited volume in front of the micro tip, it can assumed that the number of collisions per unit volume is equal to liquid density which is around $2.2{\cdot}10^{22}$ (cm^{-3}) at 77 K and atmospheric pressure. Then the dissipated energy density can be calculated by:

$$W = neE\lambda \tag{2.34}$$

where λ is mean free path of electron in LN_2 and has been approximated at $5{\cdot}10^{-10}$m [15]. In order to overcome the latent heat per volume of nitrogen (200 J/cm^3), the minimum electric field for bubble nucleation is given as:

$$E \geq \frac{W}{ne\lambda} \sim 10^8 \quad (Vm^{-1}) \tag{2.35}$$

This calculation seems to underestimate the threshold electric field, E_s, which has been obtained from the experimental data to be in the order of $1.1{\cdot}10^9$ Vm^{-1}. There are two reasons contributing towards this difference. First, the assumption that every molecule in the LN_2 structure will collide with electrons might not be relevant. Second, each collision does not necessarily result in heat dissipation, e.g. impact ionisation can occur if an electron has gained enough energy from the electric field.

2.5.3 Development into prebreakdown streamers

Considering an electrically induced bubble in LN_2 with a radius of several micrometers, the temperature inside the bubbles can be assumed to be equal to surrounding liquid which is at 77 K. Figure 2.7 shows uniform breakdown strength of gas nitrogen at 77K as a function of gap distance. The breakdown of gaseous bubbles can be estimated from the Paschen curve with the gap distance of several micrometers, e.g. bubble diameter. Thus, the electric field required for bubble breakdown should not exceed $0.5{\cdot}10^9$ Vm^{-1}. Since these gaseous cavities are generated at the needle tip, the electric stress across the bubble is similar to the threshold electric field of $1.1{\cdot}10^9$ Vm^{-1}. In addition, taking into account the different permittivity between the two substances, the field inside a gaseous cavity must be 1.44 times higher than the surrounding liquid. Thus, after being generated, gaseous bubbles will experience an electric field higher than that required to create breakdown. However, in order to start the avalanche process, a seed electron must be present inside the cavity. In the case of LN_2, the transfer of an electron from vapour to liquid phase can happen without any additional energy due to the positive value of V_0. The development of a discharge event is determined by the availability of a delocalised electron close to the nucleation site.

2.5.4 Negative streamers

With the presence of a gaseous cavity, the development into a density change streamer from a cathode point is a well understood process. Seed electrons can be supplied from the needle tip due to field emission. Once entering the bubble, due to the high electric field across the bubble, an avalanche can be initiated which results in breakdown of the gaseous cavity. Heat dissipation from the discharge will result in further vaporisation which increases the size of the gaseous filaments. The process is accompanied by current

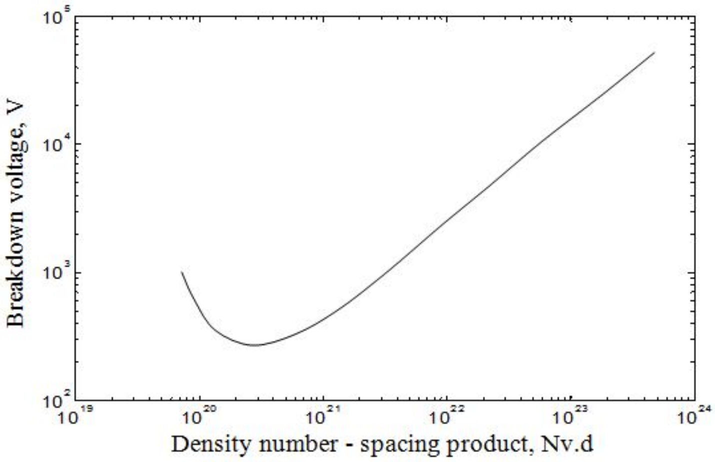

FIGURE 2.7: Paschen curve for nitrogen [10].

pulses, light emission and a shock wave [31] [8]. The occurrence of light emission indicates excitation of molecules which cannot be produced by charge generation process such as field emission, ionisation and dissociation. From the observed spectrum, an average electron energy within gaseous filaments in LN_2 has been found to be around 18 eV [58]. This value is higher than that required to ionise LN_2 molecules.

Lewis [19] suggested a mechanical model for electrical breakdown in liquids. Under high electric fields, liquid molecules will experience a force acting against the cohesive force in the direction perpendicular to the field. This force will act on the interface between metal and liquid and reduce the surface tension hence increase the molecular separation there. Moreover, the forces will increase the generation of vacant sites in the liquid (theory of holes in liquid). As a result, the liquid density is expected to be lower due to the electric field. Mechanical forces and holes can further develop as cracks similar to those of a solid. The cracks can be thought of as a region without any atoms which enable electrons to travel and gain massive energy. Therefore, at the end of the crack impact ionisation is feasible. Electrons produced at the tip of the cracks are considered to be localised and enhance the local field there. Further cracks can develop from that point and result in the development of a bush-like streamer.

The main question in the initiation of streamers from a cathode point is how the initial cavities are generated. Lewis proposed that the process of cavitation must occur before discharge due to mechanical effects [19] or reduction of surface tension in the double layer [59]. Whereas, other authors such as Denat [42], Lesaint [17] and Kattan [60] argue differently. These experimental results show the occurrence of a current pulse together with light emission before the formation of initial cavities. The process is the result of an avalanche in the liquid phase due to electrons injected from cathode. Although the feasibility of avalanche in liquid dielectrics is debatable due to much the lower mean free path than a gas phase, many recent experimental studies have produced results that support this phenomenon. In addition, results from nanosecond breakdown events suggest a similarity between impact ionisation processes of gas and liquid nitrogen [61]. Since the pulsed voltage is only for a few nanoseconds, no bubbles or streamers were recorded. Therefore, the breakdown occurs due to an electron avalanche in the liquid phase. The reduction of liquid density at high field proposed by Lewis [19] might play an important part in impact ionisation since it helps increase the mean free path of electrons.

2.5.5 Positive streamers

Streamer initiation mechanisms under a positive polarity are much less clear than for negative polarity. The field emission process which is the precursor for an avalanche in the case of negative streamers is not relevant. Electrons cannot be supplied from the planar electrode because of its much lower electric field. Moreover, with the configuration consisting of a solid barrier, even if there were some injected electrons, it would not be logical for these electrons to move across the barrier and take part in the prebreakdown process. In addition, experimental results under DC voltage are not necessarily reproducible. Current pulses have been recorded at much lower electric fields than those required for field ionisation [62]. In cyclohexane, current pulses were observed around $0.5{\cdot}10^9$ Vm^{-1} while a field of $1.2{\cdot}10^9$ Vm^{-1} is required to ionise the liquid. These pulses are also irregular and randomly distributed.

Under impulse voltages, the initiation of anode streamers was found also not to be reproducible. Effects of additives on the initiation of prebreakdown in cyclohexane were found inconsistent [44]. Hydrostatic pressure on the other hand has clear influence on the inception of anode streamers. Obtained results suggest that a lower density region was formed before the first current pulse [63]. The evaporation process is more difficult at higher pressure, consequently, the initiation voltage increases with hydrostatic pressure.

Measurements of conduction current prior to anode prebreakdown detected an increase of continuous current without light emission before partial discharge current pulses were detected [44][62][63]. This current was found to be too small to create cavitation of the liquid. The continuous current before the onset of discharge events could be due to ionic dissociation mechanisms. As discussed previously in Section 2.4, the dissociation rate is a function of the electric field. Close to the needle tip, the electric field is very high and the dissociation rate exceeds the combination rate. Consequently, free charge carriers can be produced. After being generated, negative ions then drift towards the positive point and enhance the local electric field here. This might explain the occurrence of current pulses well below field ionisation threshold [62]. Current produced by liquid ionisation can create heating as well as the formation of initial cavities [42]. Another suggestion is the possibility of a distribution of avalanches at a distance from the anode tip also having the ability of vaporising the liquid [44]. Initial cavities may also be formed due to mechanical forces. Generation of positive ions or holes can also occur which becomes more effective after discharge occurs due to the tunnelling of hot electrons from a cavity into the anode [59].

In summary, the initiation of prebreakdown phenomena at the cathode is better understood than at the anode. Field emission from a negative electrode can be the precursor to electron avalanche including multiple impact ionisation between electrons and liquid molecules. Local heat dissipation leads to the formation of gas cavities. Avalanches inside the cavities occur if the two conditions are met. First, there is a high enough electric field and second, there is a seed electron. Bubbles which do not breakdown or collapse will move under the electrodynamic effect of convection [44]. For an anode point, the formation of a low density region is a more complex phenomenon. Continuous current detected before discharges suggests conduction mechanisms such as ionic dissociation and liquid ionisation play an important role providing free electrons and local energy dissipation. Other theories such as electromechanical breakdown [19] also are considered as a primary step, or at least support, the formation of a lower density phase.

2.6 Streamer propagation in dielectric liquids

This section discusses the propagation of streamers in liquid dielectrics for both polarities under DC, impulse and AC voltages. Streamer propagation can be classified according to its velocity. Following this analysis, there are four modes in which mode 1 is the slowest, and mode 4 is the fastest. This thesis adopts a more conventional classification based on streamer shape: bush-like and filamentary or tree-like. In relation to velocity, bush-like streamers are slower, e.g. subsonic, whereas filamentary streamers can propagate at supersonic velocities.

2.6.1 Negative streamers

Yamazawa [64] observed both filamentary and bush-like streamers in LN_2 at the same voltage and pressure. The filamentary shape however is found to propagate from a bush-like structure at the tip, Figure 2.8. Therefore, it is suggested that there is no intrinsic difference between the two shapes since one of them seems to develop from the other. The difference is the number of spikes from the structure. A larger number of spikes is equal to a reduction in the local field at the tip of the spikes. As a result, the injected energy is more dispersed and a bush-like structure is formed. On the other hand, if the number of spikes is small, only the spike with highest field strength will grow. The injected energy will focus on forming the filament and results in filamentary shapes.

The streamer shape is found to be dependent on applied voltage. Near the inception point, a negative streamer only has a bush-like shape. As the voltage is increased,

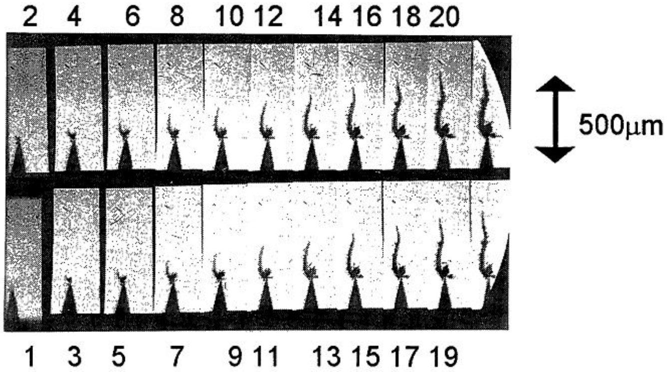

Figure 2.8: Negative filamentary streamer at 17.6 kV impulse voltage (reproduced from [64]).

the probability of bush-like streamer reduces while the appearance rate of filamentary streamers rises. At a certain point, filamentary shapes are more likely to be created than bush-like shapes.

The propagation speed of bush-like structures is slower than filamentary ones. The velocity of filamentary streamers is not constant over the discharging period. It consists of fast parts (300-400 ms^{-1}) and slow parts (30-60 ms^{-1}). Yamazawa [64] attempted to estimate the velocity of the fast part using a mobility equation:

$$v = \mu E \tag{2.36}$$

where v is streamer speed, μ is charge carrier mobility and E is electric field. The value of E is approximated at the maximum field at the tip. However, this estimation appears to be irrelevant since the local electric fields at the point will be affected by the local space charge in front of the streamers. In addition, the change of mobility under high field conditions can also affect the calculation of streamer velocity.

Swaffield et al [65] investigated streamers under applied AC voltages in LN_2. The results also suggest the appearance of bush-like structures near the inception point and filamentary streamers at higher applied voltages. However, the filamentary streamers reported in this work do not necessarily require a bush-like structure; which is distinct from reported research mentioned above. This can be seen by comparing Figure 2.8 and Figure 2.9. The paper also suggests that due to the development of space charge, the Laplacian field profile can be affected. Therefore, it is possible for streamers to grow in a direction not aligned with the field causing branching. For a filamentary structure, it is suggested that due to higher electric field the ionisation and propagation happens fast enough to prevent space charge build up. The result is that much less branching occurs during filamentary streamer propagation.

Denat [8] suggests that the negative streamer process in liquids in general is strongly related to the formation of an initial bubble at the tip due to electron avalanche. The

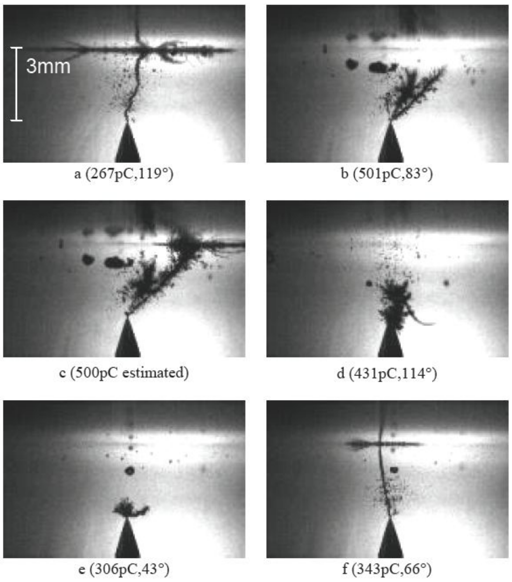

Figure 2.9: Negative filamentary streamer at 26.4 kV AC voltage at 75.7K, atmospheric pressure (reproduced from [65]).

electrical discharges can be observed inside the bubble depending on bubble life time. A sequence of current pulses correlated to bubble growing and merging is experimentally reported. This shows a resemblance with characteristics of bush-like streamers. The discharges in the vapour can quickly develop new bubbles due to intensive localised energy [46]. Recently generated bubbles will coalesce with existing ones thus creating more and more filaments. Because of the field distortion which is the result of charge accumulation, the direction of filament growth does not necessarily have to be aligned with the electric field. The initial velocity of the streamers in hydrocarbon liquids is in the order of 100 ms^{-1} [8]. However as the streamer propagates, the velocity can increase such that:

$$v \sim \sqrt{\epsilon / s\rho} E_{tip} \tag{2.37}$$

where s is a drag coefficient, ρ is the liquid density and E_{tip} denotes electric field at the streamer tip. When E_{tip} is greater than a certain voltage threshold, E_f, a new propagation mechanism needs to be considered since streamer shapes change from bush-like to tree-like.

Similar results have been reported for cyclohexane [45]. The slower mode or bush-like streamer is the result of bubble-like cavity with repetitive expanding and collapse. Electron bombardments in front of the streamer head induce vaporisation due to electron and molecule interactions. Streamer propagation is restricted by the ability to discharge in the gas phase which is an important process to ensure the supply of electrons for further advance. A model for a faster mode of negative streamers is also suggested. Electrons entering into the liquid can be trapped within cavities which result in the development of a space charge region in front of the streamer head. As the local field increases up to 1.5 MVmm^{-1} for cyclohexane, liquid molecules can be directly ionised. The propagation velocity then is not affected by the gas discharges but rather by the lifetime of electrons in traps.

2.6.2 Positive streamers

Bush-like and filamentary shapes are both observed in LN_2 pre-breakdown phenomena with a positive point electrode [64] [58]. Similar to negative streamers, a bush-like shape is observed at lower voltages than for filamentary structure. The bush-like structures of both polarities are not very different from each other. Denat [8] suggests that these streamers can also be initiated with liquid vaporisation and propagated due to electrical discharges inside the bubbles.

Lesaint et al [17] studied the propagation of positive streamers in hydrocarbon liquids. Under DC voltage, both bush-like and filamentary streamers are observed. Two inception voltages have been defined in this study, V_s for slower streamers and V_p for faster ones. Results show that under the same conditions, the value of V_p is always higher than V_s. Above the filamentary streamer inception voltage, streamers propagating follow a tree-like structure. Light emission was detected for both bush-like and filamentary shapes. Transient currents recorded during streamer propagation show distinct differences between bush-like and filamentary shapes with the former one consisting of a series of fast pulses and the latter one having a continuous component.

Swaffield et al [65] observed light emission in the vapour columns during the positive streamer process. This leads to the suggestion of a conductive plasma channel bridging through the liquid. The formation of this column is thought to be because of liquid ionisation in contrast to electron emission. Filamentary streamers in this case show more branches than negative filamentary streamers. The branching appears to increase for increasing applied voltage. The maximum propagation velocity has also found been found to be much higher than negative streamers: more than 1 kms^{-1} compared to 300-400 m^{-1} [64].

The discharge currents recorded during the positive streamer process consist only of several high magnitude pulses compared to lower magnitude but a higher repetition rate current seen with negative streamers. The current pulses seem to be unaffected by the pressure up to 0.4 MPa [65] [8].

In summary, both bush-like and filamentary streamers are observed during prebreakdown processes for both anode and cathode point electrodes. In general, the bush-like propagation mode is dominant at lower electric fields. The model for this mode is based on the formation and coalescence of gas cavities due to electron bombardments with liquid molecules. Measurements of transient current show a series of fast pulses which can be linked to the branch structure of the streamer shape. During propagation, the electric field at the tip of the streamer needs to be maintained at high level either by space charge electric field or by formation of a conductive filament bridging streamer channels. Positive filamentary streamers propagate at a much faster velocity than negative ones which is due to different propagation mechanisms as suggested above. Similar to the discussion in Section 2.5, prebreakdown phenomena under a positive polarity is more complex than that under a negative polarity.

2.7 Summary

The inception electric field for partial discharges in LN_2 is somewhere around 1 $MVmm^{-1}$. Below that level, the current is negligibly small. Uniform field breakdown results are not of interest since such experiments can only be undertaken at high applied voltages and very small gaps. The results from which might not be practical since pre-breakdown phenomena is influenced by volume [11]. Instead, the majority of investigations on prebreakdown phenomena in LN_2 utilise point-to-plane experiments with the benefits of intense field at the point tip. The electric field has a Laplacian distribution with the maximum value at the needle tip and decreases rapidly as away from the point. Even though the field can be calculated, or simulated theoretically [66], it is difficult to acquire the actual value since distortion happens as soon as electrons are emitted. Moreover, Bonifaci et al [14] suggests that the behaviour might depend on the tip radius. Experiments were undertaken with tip radius varying from as low as 0.1 μm to 10 μm. A systematic study on the effect of tip radius on the inception electric field has not been found in the literature. Therefore, the calculated values for the inception field from measured voltages are not necessarily in good agreement between different authors.

For a negative polarity needle point, the initiation process is thought to be due to cold emission from the electrode. At low fields, electron injection is low and thermally activated. At higher fields, the effect increases and is suggested only to be a function of applied voltage only. This implies the low-operating temperature of cryogenic liquid will not affect the field emission regime. However, current emission following Nordheim-Fowler theory only exists or appears for low current densities before becoming space charge limited.

After being injected, electrons accelerate due to the electric field and collide with other molecules after gaining a certain amount of energy. If the energy is high enough, ionisation can occur and result in an avalanche. The heat dissipation caused by collisions is highly localised around the tip of the needle. As a result, the energy produced can be high enough to create phase change [15]. The injected energy has also been characterised from the apparent charge and the applied voltage [46]. The bubble radius is then estimated from the injected energy. It is assumed that electron avalanche happens first in the liquid at the tip of needle causing discharges from which a bubble is formed. The avalanche is this case is similar to Townsend criterion for gas breakdown.

Initial cavities can also be formed by mechanical effects [19]. However, experiments to confirm an electromechanical theory are difficult to achieve for several reasons. First of all, the crack is of sub-micrometre size which is difficult to observe optically. Second, the development of a crack can quickly lead to electron avalanche and streamers. The process occurs in nanometre scale which makes it even more difficult to observe. On the other hand, pressure changes due to molecule separation might be measured. However, the change only happens around the tip of the electrode where the electric field is high. Such measurement would require very sensitive data acquisition.

Nevertheless, it is agreed that bubbling occurs during partial discharge activity in dielectric liquids. Bubbles which are visible with the naked eye have been observed [67]. Smaller bubbles, in the micrometer range, have been recorded [46]. Even bubbles with nanometre radius have been suggested [28]. This type of bubble is discussed as a void free of molecules rather than a gaseous nitrogen substance. The terminology is in many ways similar to that used for "voids" in liquid (see section 2.2.1). Both holes and bubbles can both increase the free path of an electron but avalanches or partial discharges can only initiate in bubbles.

Discharge within gaseous bubbles occur if two conditions have been satisfied: the electric field across the bubble is high enough and a seed electron is available. The condition of electric stress can be achieved since cavitation occurs close to to needle tip where the electric field is the highest. Seed electrons can be readily supplied due to field emission from a cathode point, whereas in the case of a positive needle, the availability of an initial electron remains unclear. This might explain why experimental results from a cathode point are more reproducible than from an anode one. Discharge inside a bubble will lead to further vaporisation of the liquid and result in the formation of density change channels propagating through the liquid; which are referred to as streamers.

Negative and positive streamers behave differently. In general, negative streamers are slower and bushier than positive ones. Partial discharges initiated from a negative polarity needle tip are often higher in quantity, but lower in magnitude. Positive streamers appear with only several high density current pulses. In LN_2, reported experimental data for pre-breakdown phenomena under AC voltages is still very limited. Streamer initiation and propagation has yet to be well understood. In addition, the step-wise growth of negative streamers has not been reported since previous work has only used low bandwidth PD measurement. For that reason, wideband PD detection method using a UHF sensor has been applied in this study to help clarify the step-wise development of negative bush-like streamers.

Chapter 3

Experiment to Measure PD Behaviour in Cryogenic Liquids

3.1 Introduction

Pre-breakdown phenomena in liquid nitrogen is sensitive to experimental conditions such as temperature, pressure and impurities. Therefore, it is important for any analysis of experimental results that laboratory conditions are well controlled. An experimental system, followed by a set of procedures, has been developed in order to control the test conditions such that any obtained data is both reliable and repeatable. Details of the experimental arrangement are provided in this Chapter.

The first section in this Chapter explains the design of the cryostat in which all experiments were conducted. This equipment is essentially a thermal insulated vessel with optical ports for streamer observation. In addition, it is also capable of thermal and pressure control and is PD free up to 50kV. The experimental arrangement requires a PD source that consists of a sharp tungsten needle, which has been electrochemically etched, an insulation barrier and a high voltage electrode which is connected to a HV supply through a bushing system. Narrowband and wideband PD measurement techniques were used simultaneously to provide a further understanding of discharge process during streamer initiation and propagation. An imaging system consisting of a high speed camera and a light source that illuminates the examined objects through the available optical ports is used to obtain images of streamers. Lastly, the experimental procedure is discussed with the emphasis on removing impurities and filling the cryostat with LN_2.

3.2 The cryostat

The pre-breakdown and breakdown behaviour of LN_2 is strongly influenced by the temperature and hydrostatic pressure of the liquid [7] [11]. In addition, streamers in LN_2 are accompanied with partial discharge current and density change in the liquid which can be observed optically. Therefore, the study of dielectrics for HTS applications requires optical observation, partial discharge measurement as well as monitoring of variations in temperature and pressure. In order to meet these requirements, a unique cryostat was designed and manufactured by the Tony Davies High Voltage Laboratory in cooperation with the Institute of Cryogenics at the University of Southampton. The details of the design and construction of this equipment can be found in D.J. Swaffield's thesis [10]. However, for the purpose of understanding how the experiments operate, this section summarises the structural details of this cryostat as well as the changes made to fit the purposes of this study.

Figure 3.1 shows a schematic diagram of the cryostat. The main structure of the cryostat consists of an inner pressure vessel (1) and a outer jacket (2) which are thermally insulated from each other by a vacuum inter-space. The two vessels, flanges and top plate (3) are made of 316L stainless steel. Sapphire windows (4) and BK7 glass windows are aligned so that images of the density change can be captured. A copper thermal lead-through (7) is placed at the bottom of the cryostat and connected with a helium cryo-cooler (6) through a copper flexible coupling (8). A filled epoxy resin bushing (9) cast by Pirelli SPA is earth screened inside the inner vessel by semi-conducting paint and terminated (10) at the bottom end. The top of the bushing is terminated outside the vessel with paper tape insulation and a voltalit encased stress relief cone. High voltage is applied from the top of the cryostat via two corona shields (12).

The only modification in this project from the original design is the replacement of sulfur-hexafluoride gas by air in the gas chamber (11). The reason for this is sulfur-hexafluoride gas can be hazardous after discharges. Such a modification leads to a slight reduction of the pd free level for applied voltages from 50kV to 40 kV.

3.2.1 Temperature control

There are various designs to achieve temperature control for LN_2 such as sacrificial pool boiling jacket, continuous flowing loop of LN_2 or a cryo-cooler system with the coldhead fitted (shown in Figure 3.2) between the two vessels and underneath the inner vessel. The cryostat use the latter method. The cryo-cooler system consists of a coldhead, model RGS120T, which is connected to a helium compressor pack by insulated hoses. A flexible copper coupling which is compatible with local displacement due to thermal contraction is used to transfer the heat from LN_2 inside the inner vessel to the cryo-cooler system. The coldhead receives cold high pressure helium (up to 2.1 MPa) from

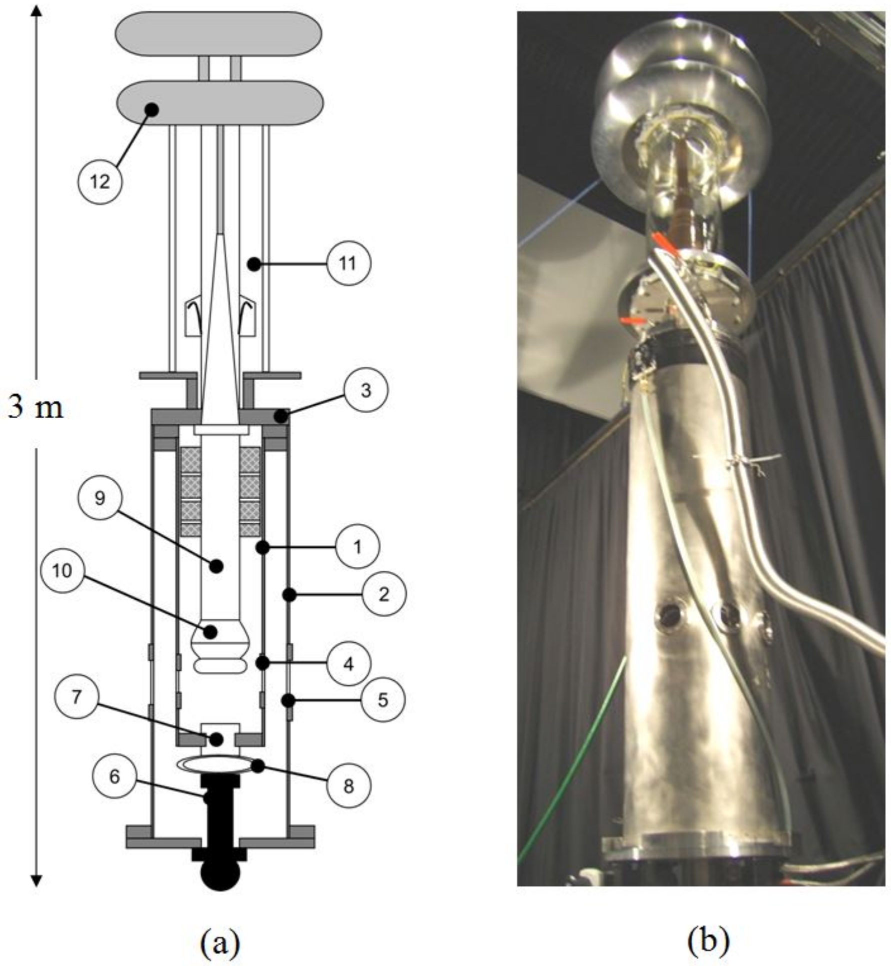

FIGURE 3.1: The cryostat : (a) schematic diagram (b) overview from the outside (reproduced from [4]).

the coolpak 6000 through high pressure gas pipe and therefore absorbs the heat coming out of the inner vessel. Hotter helium gas is then delivered back to the coolpak for re-compression before being transferred back to the coldhead to complete a full cycle. This system requires an external cooling loop, in this case water, to remove the heat taken from the inner vessel.

The water cooling loop utilise an 11 kW water chiller in order to cool, and pump cold water below 18^0 C into the coolpak. After being warmed by heat from the helium cooling system, the hot water is circulated around the outside of the cryostat via three parallel copper loops. This design has two purposes. Firstly, the top plate is normally at low temperature since LN$_2$ is filled through a valve which is directly connected the plate. This will help lower the temperature of the hot water and therefore keeping it cool when entering the laser. Secondly, since the top plate is at low temperature, there is a risk that the PTFE o-rings, which are used to ensure vacuum tight seal, get too cold and lose their integrity as a seal between the two vessels as well as between the inter-space region and the inner vessel. The heat transmitted by the water via the three cooper

FIGURE 3.2: Leybold coldhead RGS120T (reproduced from [8]).

loops increases the temperature of the rings and help the system remain vacuum tight. Cold water after being fed to the laser will do its job of cooling the heat produced by discharges in the copper vapour laser. Hotter water then is connected back to the water chiller to form a closed loop system as shown in Figure 3.3.

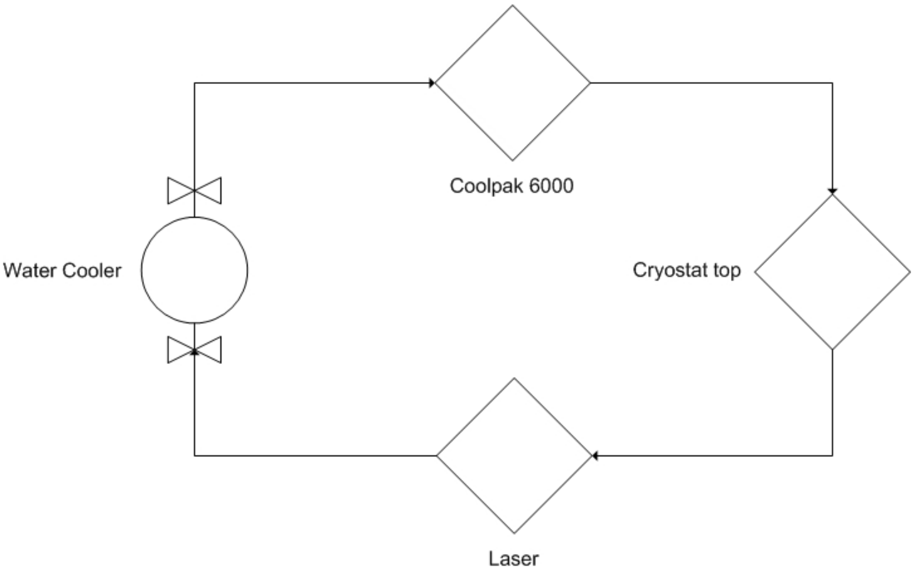

FIGURE 3.3: The diagram of the water cooling loop.

The inner vessel is thermally insulated by keeping the pressure of the inter-space below 10^{-5} Torr. In addition, the vessel is wrapped with multiple layers of aluminium to provide radiation reflection barriers. Additional insulation is provided by buffets located just underneath the top plate. Temperature control is achieved by continuously running the cryo-cooler to remove heat out of LN_2. Two 100 W electric heaters is mounted on the copper coupling with the purpose of control the amount of cooling power. A pt-100 platinum thermistor is also mounted on the coupler to measure its temperature. The system allows continuous temperature measurement and control of the liquid inside the inner vessel.

It is important that LN_2 must not solidify during the experiments since solidification would lead to major damage to the device. A suggested solution is an interlock system whereas the cryo-cooler will be switched off when the temperature goes below a critical value for example 65 K. However, since this project only focuses on LN_2 close to its boiling temperature, the risk of solidification is minimised. Thus, the safety system to prevent solidification of LN_2 has yet to be implemented.

The cryo-cooler, as stated previously, is located at the bottom of the inner electrode while the sample is about 20-30 cm above. For the reliability of the results, the temperatures at discharge locations must remain constant. However, it is possible that PD in LN_2 can create changes in local temperature, e.g. at the discharge sites. The temperature at the needle tip is closely measured using two different sensors, namely a pt-100 and a carbon ceramic sensor (CCS) supplied by Lake Shore Ltd and Temati Ltd respectively. Their resistance versus temperature profiles are plotted in Figure 3.4.

According to the given data sheets, CCS has better accuracy than that of pt-100 sensor (0.01 K versus 0.5 K). Information about sensitivity and time response, on the other hand, are not supplied by the manufacturers. These two parameters are of interest because heat dissipation during streamer discharges in LN_2 can result in local changes in temperature at the incident sites. Such events only happen in a small volume of the liquid during a short period of time, therefore, it would not create a significant change in the liquid temperature but rather a transient variation. For applied voltages below 30 kV, the measured temperature remains almost unchanged at 77.8 ± 0.3 (K). However, during the study of solid dielectric degradation, at 35 kV, variations could be up to several Kelvin as shown in Figure 3.5. After turning off the high voltage supply, the liquid temperature immediately returns to its steady state value. Results obtained from this study show that transient changes in temperature could only be observed by the CCS whereas readings from the pt-100 remained constant. The important factor contributing towards the difference between the two sensors is likely to be the time constant of each device. Pt-100 sensors consist of platinum film inside a ceramic substrate of which purpose is to improve the sensor's physical strength, therefore, the time it takes to heat up the ceramic structure is the main factor decide the response time rather than the sensor itself. Meanwhile, the CCS is allowed to directly contact to the environment

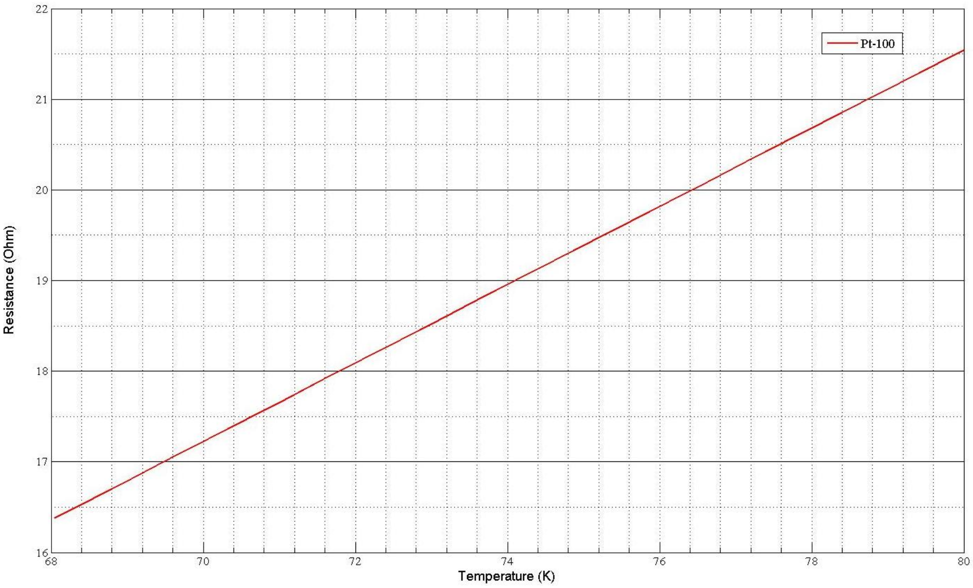

(a) Pt-100

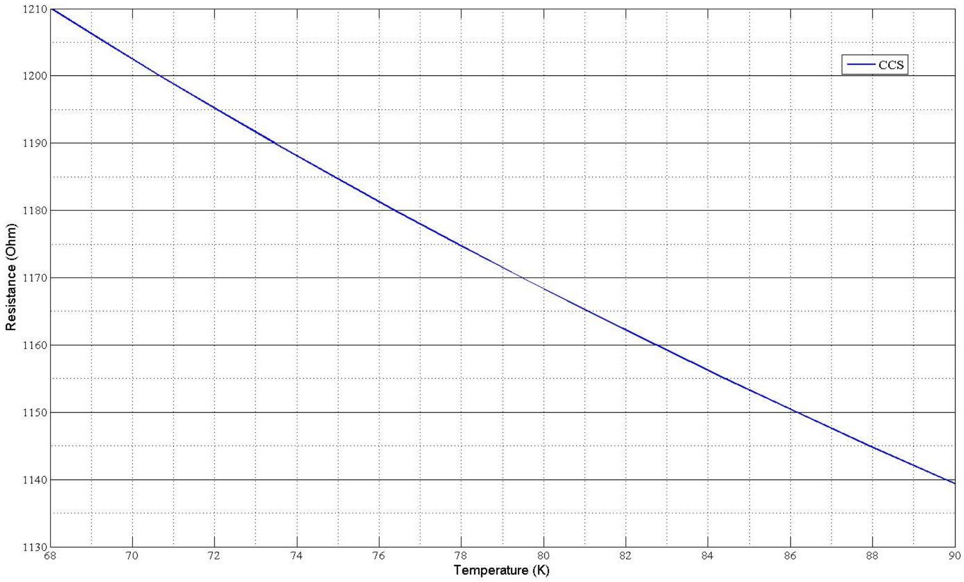

(b) CCS

Figure 3.4: Temperature versus resistance plots of (a) Pt-100 (given by Lakeshore Ltd) and (b) CCS (given by Temati-uk Ltd).

which could mean that it has a much shorter time constant than the pt-100 sensor.

3.2.2 Pressure control

The cryostat has been designed to work up to an inner vessel pressure of 2 MPa [10]. This research has not investigated the effects of pressure on the behaviour of streamers in LN_2, therefore, the focus is on keeping the liquid at atmospheric pressure while preventing impurities such as oxygen and water from entering the inner vessel.

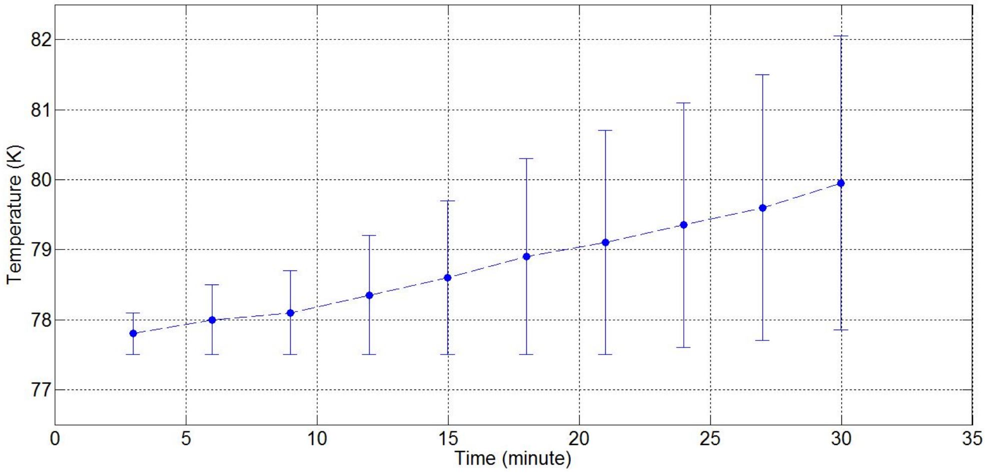

FIGURE 3.5: Temperature variation at 35 kV over 30 minutes.

The top plate and the pressure vessel are held together by thirty two stainless steel bolts in order to form a vacuum-tight seal. These bolts are tightened to a calculated torque of 95 Nm [10]. With the bolts in place, the inner vessel then can be vacuumed below 10^{-3} Torr to remove most impurities. A pressure gauge supplied by Thompson Valves Ltd is mounted on top on the cryostat to monitor pressure during the experiments. During the experiments, a large amount of LN_2 can be potentially vaporised causing an increase in pressure inside the cryostat. In order to maintain the pressure of the inner vessel at atmospheric level, the filling valve on top of the cryostat was kept open. However, at the same time, it is undesirable to allow air to enter the vessel since oxygen can greatly affect experimental results. The solution is to connect a rubber tube to the filling valve. This tube has been specially designed with a closed end, and a small split close to this end. In its normal condition, the tube is close and does not allow air to enter. As the pressure inside the cryostat increase, the small split will be open and allow ventilation of gaseous nitrogen. The pressure of the inner vessel was closely monitored and remain at 0.1 MPa during the tests. For additional safety measure, a safety (1 bar) blast valve is mounted on the top of the cryostat so that in the event of over-pressure it will be open to protect the equipment.

3.3 Experimental arrangement

The schematic diagram of the experimental apparatus is shown in Figure 3.6. The configuration consists of three major parts: a PD source, measurement system and imaging system.

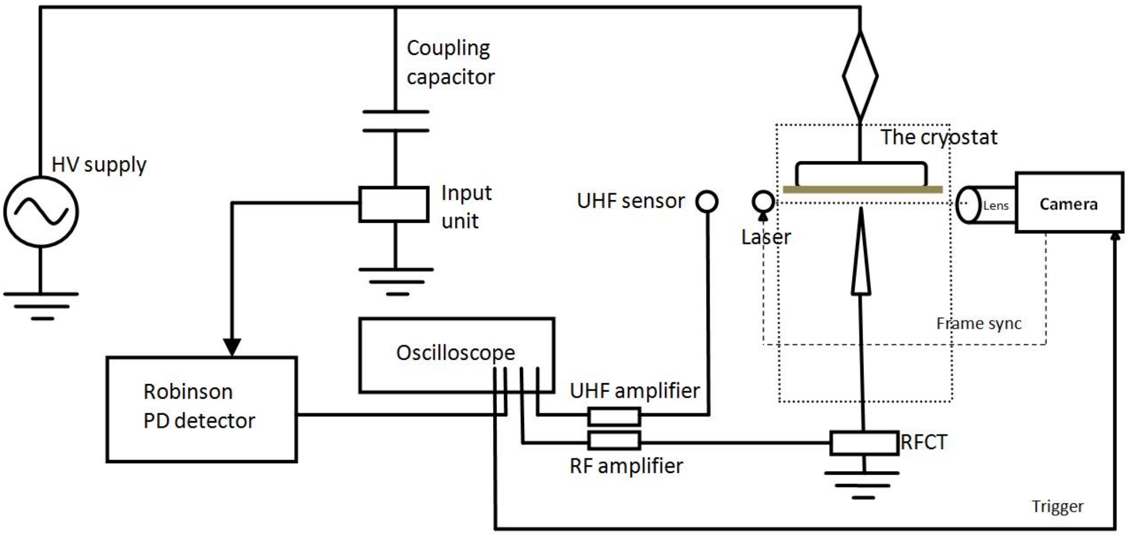

FIGURE 3.6: Schematic diagram of experimental arrangement.

3.3.1 PD source

The PD source primarily consists of a very sharp needle pointing towards a round electrode which is connected to the HV supply via the cryostat bushing. This set up, which is normally referred as point-to-plane configuration, is widely used when an extreme electric field is required. The sharper the needle, the higher the electric field at its tip. Likewise, the maximum electric field increases as the gap distance between the needle and the opposite electrode reduces. It is very difficult to measure the exact maximum stress, however, under the assumption that the needle tip is a hyperboloid, this value can be mathematically estimated as a function of tip radius, applied voltage, and gap distance [68]:

$$E_{max} = \frac{2U}{r_p ln(\frac{4d}{r_p})} \tag{3.1}$$

where U is the applied voltage, r_p is the tip radius, and d is the gap distance between the two electrodes.

The aim of point-plane configuration is to create a very high electric field while applying a much lower voltage. The required sharpness of the needle depends on the experimental conditions such as the HV source and the gap distances as well as the materials being investigated. A material will experience pre-breakdown or breakdown phenomena when the electric field across it exceeds a certain value. The term inception voltage is defined as the applied voltage at which detectable discharges initiate. From the experimental configuration, the inception electric stress then can be calculated. For LN_2, the initiation of pre-breakdown PD requires high electric fields in the order of 1 $MVmm^{-1}$ [46]. With the cryostat PD free up to 40 kV, it would be preferable to able to initiate PD below

20 kV so that behaviour well above inception point can also be investigated. Therefore, if the gap distance is taken as 20 mm, then from equation 3.1 the tip radius must be smaller than 5.9 μm.

Among many methods to produce sharp needle tips, this research employs electrochemical etching to fabricate tips from tungsten wires with a shank diameter of 1 mm. The basic principle of the method is that a tungsten wire placed inside a sodium hydroxide bath is etched by a DC current while being slowly pulled out of the solution. Details of the design can be found in Appendix A. This apparatus can produce tips as sharp as 0.1 μm in radius. However, this study only used needles with tip radius of 2.5±0.5 μm since sharper needles were found to be easily bent or damaged at cryogenic temperatures. An example of a tip that was used in an experiment is show in Figure 3.7. Because discharges in LN_2 can cause erosion or bluntness to the sharp end of the needle [60] [67], tungsten tips were carefully monitored and re-etched if required after each experiment.

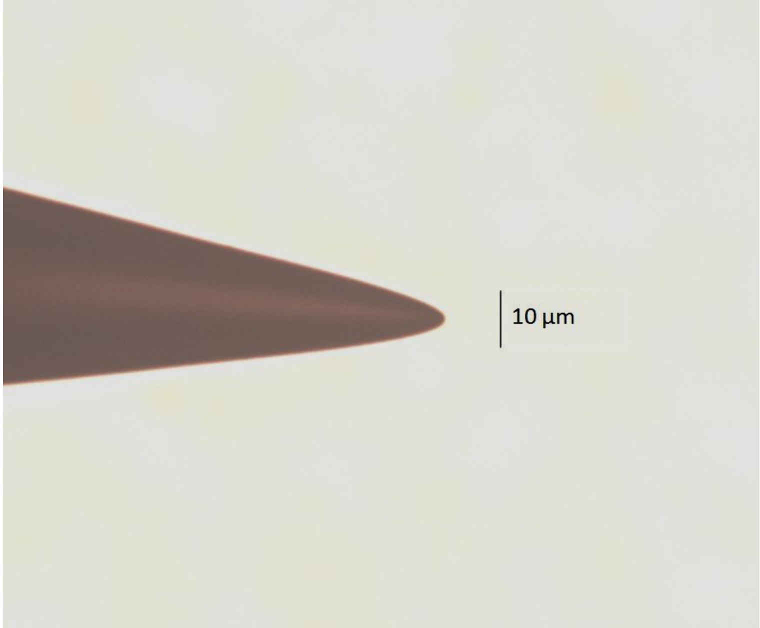

FIGURE 3.7: A needle tip produced by the electrochemical etching method.

In the event of complete a breakdown, streamers in LN_2 can cause significant damage to the plane electrode as well as the needle tips. While the needle tips can be easily re-etched, recovering the plane electrode to its original state after a breakdown is much more difficult. Since the focus remains on the pre-breakdown phenomena, an insulation plate is placed over the top of the plane electrode to protect it from erosion cause by excessive discharges. Various materials had been used for the barrier including fluorocarbon based polymer (PTFE), glass fibre reinforced resin (GRP), and cotton fibre weave impregnated with resin (6F/45). The whole configuration is hold together by a structure made of nylon screws and bolts as shown in Figure 3.8. The plane electrode is connected to the HV source through the cryostat bushing while another connection is made between the needle and the cryostat bottom vessel which then is earthed to a HV earth. Gap distance is measured by optical devices by capturing an image of the PD source and comparing with a calibrated scale.

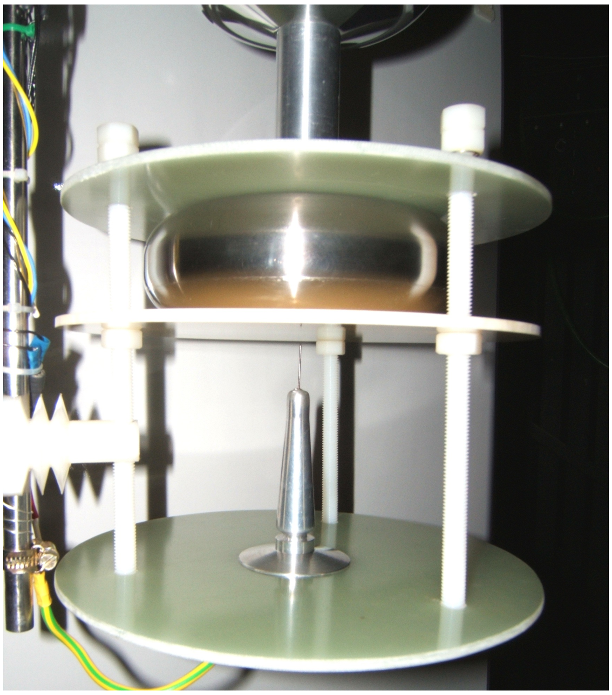

Figure 3.8: PD source with a tungsten needle and a PTFE barrier.

Previous work using the similar configuration [10] has shown that streamers in LN_2 can cause severe damage to the insulation barrier. This phenomenon is of interest since LN_2 can recover it self after discharge if sufficient cooling power is provided, erosion of solid insulation on the other hand is irreversible and degrades the material over time. The consequence is premature failure of the insulation system, which may prove to be very costly. Therefore, it is important to understand how materials deteriorate under cryogenic conditions. A part of this research will utilise this experiment configuration to study how streamers damage the solid insulation and the causes of such behaviour. Using the experimental techniques described in this section, the study of solid dielectric erosion was undertaken by using different materials for the insulation barrier. The damage region after each test was analysed by means of microscopic imaging and Raman spectroscopy. Together with the discharge data and shadow images, the erosion phenomenon of solid dielectrics in LN_2 are presented in Chapter 6.

3.3.2 Measurement systems

Pre-breakdown streamers in LN_2 in this research have been studied by conventional as well as high frequency PD measurement techniques. The problem with wideband methods is that a very high sampling rate is required. By using multiple detection simultaneously, the maximum memory capacity of the measuring device is quickly reached. Therefore, in some cases, a lower sampling rate was used so that a longer measurable period is available. Phase resolved analysis of PD in LN_2 under AC voltages was achieved by the means of ϕ-q-n plots. The plots only use the measurement data following the IEC standard since high frequency measurements cannot be calibrated in terms of apparent charge.

3.3.2.1 Narrowband and wideband measurement

A digital oscilloscope, Tektronix 7254, is used to measure PD signals from three PD measurement methods simultaneously. Two trigger systems are considered. This first one is based on the Robinson pulses so that even if PD currents did not excite UHF signals, PD pulses from the Robinson unit would still be recorded. This set up allows capture of PD signals of short duration, 50μs, which requires less memory and allows storage of multiple events using the fast frame function. However, the phase or the position of the discharge on a 50 Hz cycle is unknown. The other arrangement utilises a signal from a trigger box which is plugged in the main supply. This system allows the identification of the phase at which discharges occur. Measurements of UHF signal require high resolution, 5 GSs^{-1} or 10 GSs^{-1} for a bandwidth up to 2.5 GHz or 5 GHz. At 5 GSs^{-1}, recording a whole cycle, 20 ms, needs 100 MB of data per channel which reaches the limit of the oscilloscope. At 10 GSs^{-1}, only half of a 50 Hz cycle can be captured at a time.

Partial discharge activity inside the LN_2 excites electromagnetic waves which can be captured by the UHF sensor mounted on the outside wall of the cryostat via the dielectric windows (BK7 glass and sapphire) (as shown in Figure 3.9). The closed cylindrical structure of the metal cryostat wall contains all radiated waves inside causing reflections. An aluminium cylinder thickness 1 mm covers the sensor to shield it from airborne noise. The frequency response of the UHF sensor, which is measured using a UHF calibration system [69], is shown in Figure 3.10 (a). A wideband amplifier (+21 dB gain) is connected to the sensor output to boost the signals to allow capture by the oscilloscope Figure 3.10 (b).

The relationship between UHF signals and the apparent charge followed IEC 60270 standard is of interest. One of the most convenient methods to quantify UHF signals is to compute its energy content from the captured waveform [70]. The energy of a UHF signal, U, is calculated by integrating UHF voltage waveform over the signal duration:

$$U = \frac{\Delta t}{R_L} \sum {V_i}^2 \tag{3.2}$$

where V_i is the ith sample of the waveform, R, is the termination impedance which is

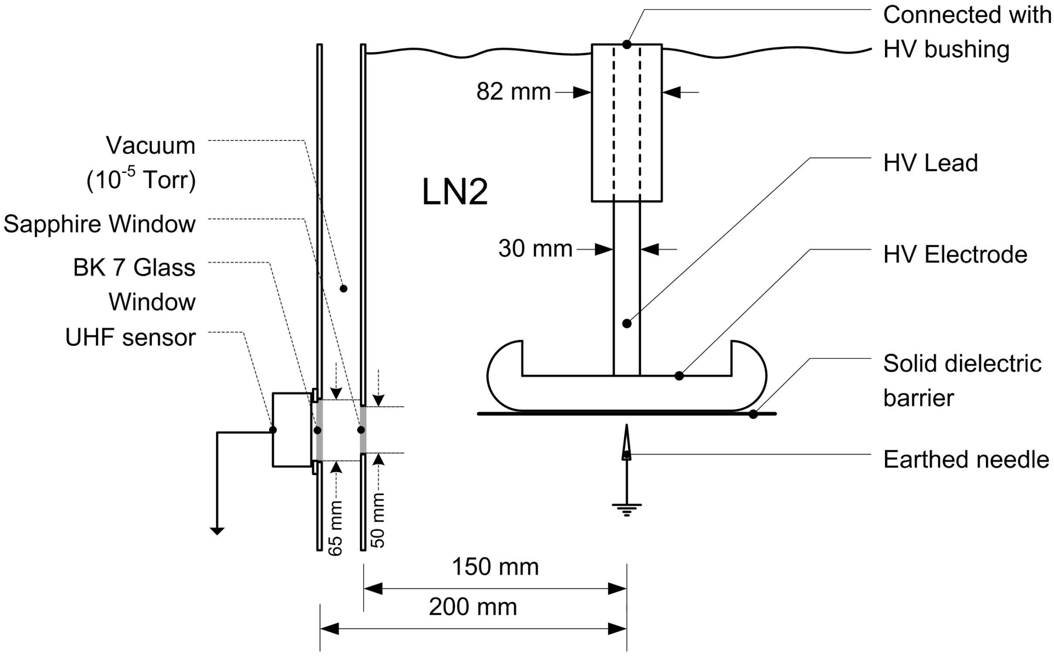

FIGURE 3.9: Mounting arrangement of the UHF sensor with respect to electrode arrangement.

50 Ω, and sampling time interval $\Delta t = 100$ ps. The plot of UHF energy and apparent charge suggests how the UHF signal relates to charge movement at the discharge site.

Because radiated signals are generated by electrons accelerating within a PD current pulse, the rise time of a current pulse will strongly influence the energy received by UHF sensor. However, if only one discharge source in a fixed location is investigated, the relationship can be predicted. Any voltage seen by the sensor, V_i, will be proportional to the electric field incident on UHF sensor, E, since the sensor is a passive device. If the shape of the pulses is considered to be constant, di/dt will scale proportionally to the peak current, I_p. In addition, $I_p \propto q$ due to calibration by the IEC 60270 standard. Therefore, V_i will increase as charge, q, increases. Finally, since the UHF energy is calculated from ${V_i}^2$, U is proportional to q^2 [70]. Certainly, this suggestion is valid under a set of assumptions listed above.

3.3.2.2 The ϕ-q-n plot

ϕ-q-n plots present apparent charge, phase position and cumulative number of recorded discharges in one figure. It provides a visual characterisation of PD pulses, which can be useful to obtain information about discharge sources. In this study, there are two methods for ϕ-q-n plotting: using PD pulses obtained by the oscilloscope from Robinson Detection unit and a Omicron Mtronix MPD600 PD measurement system. Both of them are compliant with the IEC 60270 standard.

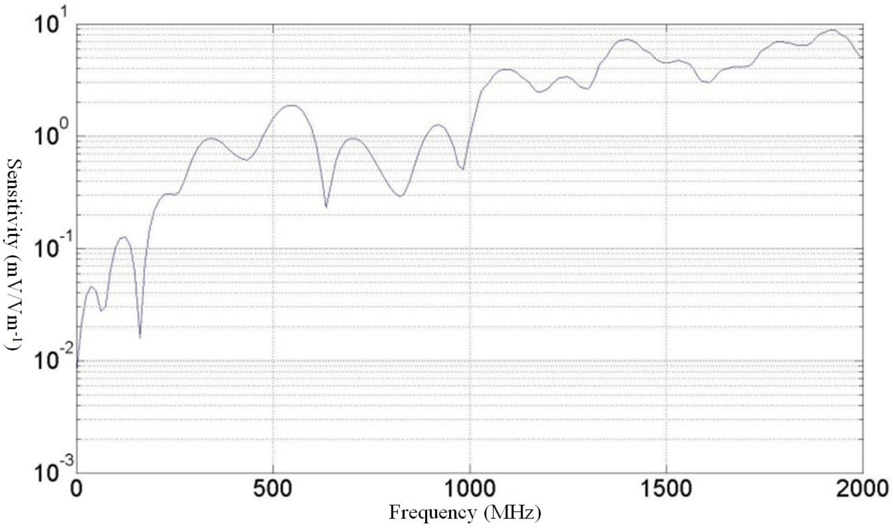

(a) Frequency response of UHF sensor.

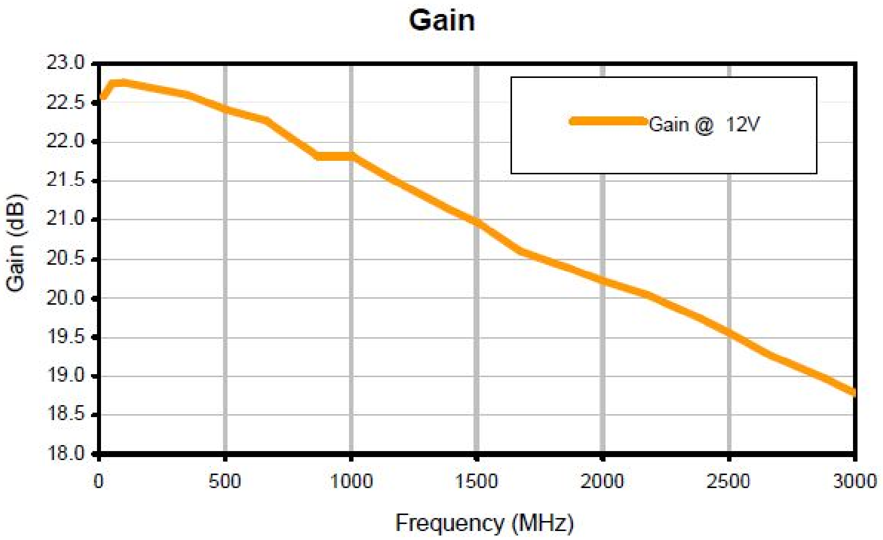

(b) Gain against frequency plot of ZX60-3018G+ amplifier (supplied by Mini-Circuits Ltd)

Figure 3.10: Frequency response of UHF sensor and amplifier.

The Mtronix MPD600 system is a commercially available package for PD measurement. Its principle is the same as any other conventional methods which is to detect PD pulses via a HV blocking capacitor (1 nC in this case). The signals are acquired via a Quadripole unit which also acts as a digital processing unit as well as an electro-optic converter. Optical signals then are transmitted to a computer by optical fibres for data storage and analysis. The system has its own calibrator unit which injects known apparent charge pulses into the experimental apparatus with magnitudes up to 100 pC. The bandwidth of the detection unit was selected to be 100 kHz to 600 kHz for this study.

The Mtronix measurement system includes a software package which can record PD data continuously for a long period of time depending on the capability of the computer. However, obtained data is presented as a phase resolved diagram where each point shows a single PD event (Figure 3.11 (a)). Although the ϕ-q-n plotting option is available from the software, the figures are very difficult to analyse as shown in Figure 3.11 (b). ϕ-q-n plots used in this research were produced using Matlab from the phase resolved diagrams provided by the Mtronix software. One issue with the Mtronix package is that only figures representing PD events can be obtained but not the actual PD pulses. Therefore, this system can neither be used in parallel with wideband measurements nor in a phase correlated image technique. In this research, the Mtronix system is the primary tool for the investigation of erosion of solid insulation while the study of streamer phenomena uses the Robinson system in conjunction with wideband measurement techniques.

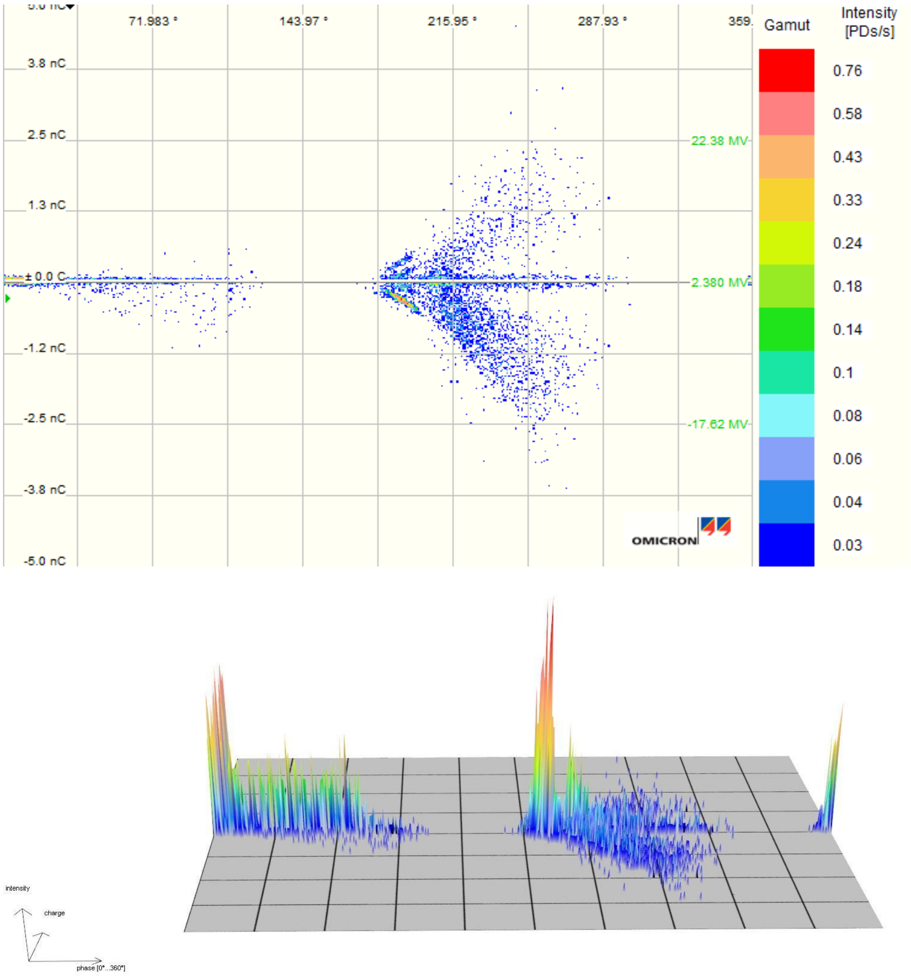

FIGURE 3.11: An example of phase resolved analysis by Mtronix system: (a) phase resolved diagram (b) 3D version of (a).

Data acquisition to IEC 60270, requires detection units that utilize a zero crossing detector which is connected to the power supply. This trigger unit provides a signal that is in phase with the HV source; therefore, the phase at which discharges occur can be identified. With its fast frame function, an oscilloscope can capture 500 50-Hz cycles for ϕ-q-n plotting. Bearing in mind that the fast frame function does not necessarily record adjacent events due to the time required to process data, this should not affect

ϕ-q-n analysis since the accumulated discharge pulses are of interest not the pulse to pulse sequence of these events. It is also worth mentioning that the zero crossing unit after connecting to the power supply has a variation of approximately 20 μs. This error is either from the supply or the unit itself; however, with a power cycle of 20 ms, this represents a phase error equivalent to 0.36^0. Over a large amount of samples, e.g. 500 cycles, such an error can be neglected.

The ϕ-q-n plot algorithm is, in principle, a function to analyse PD pulses across a 20-ms, or 360^0, cycle. First, a threshold level, below which data is considered as noise, needs to be defined. In this study, a computational threshold level of 30 pC was used unless stated otherwise. The function then scans across the data until a point with value higher than the threshold is found. Within a hold-off period, a local maximum is found. This period is simply equivalent to the duration of a PD signal, 60 μs in this case. An example of a PD pulse including the threshold level and hold-off time is shown in Figure 3.12. The maximum value of a PD pulse will represent the apparent charge while the point at which the peak occurs will be the phase of the discharge. After storing the processed data, the programme continues to look for the next PD pulse. This process is repeated for 500 cycles. The combined data is then used for ϕ-q-n plotting.

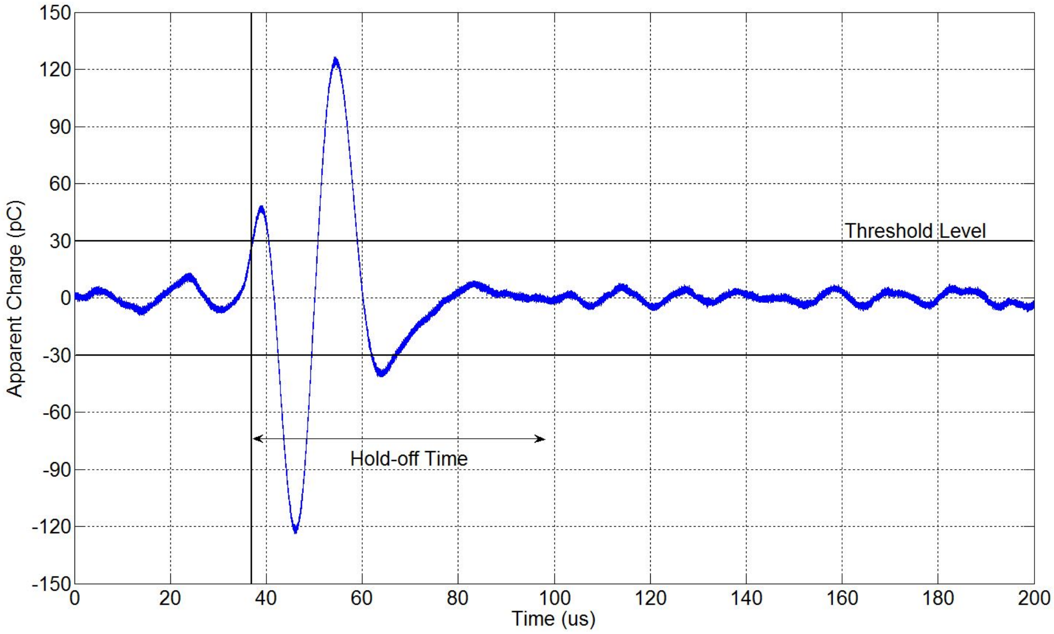

FIGURE 3.12: Threshold level and hold-off time of an PD pulse measured by the Robinson unit.

The hold-off time sets a limitation to the measurable repetition rate. If the appearance frequency of PD pulses is greater than one over the hold-off time, in this case: 16667 pulses per second, the plotting algorithm might not be able to discriminate them. Close to the inception voltage, this should not be a problem since the appearance frequency is low. As voltage increases, more PD pulses occur and are closer to each other in time, therefore, the issue of repetition rate becomes important. This matter is discussed in detail in the Chapter 4.

3.3.3 Imaging system

Understanding the pre-breakdown streamer phenomena in LN_2 is one of the primary objectives of this research. Although PD measurements can provide useful information on the subject, the observation of streamer propagation gives further details on how streamers behave under various conditions. For this purpose, a phase correlated imaging technique has been developed such that images of streamers can be linked to corresponding PD magnitudes as well as the phase at which the events occurred.

Over the past decades much effort has been devoted to the subject of observing density change streamers in liquid dielectrics. Two methods have been suggested, both of which have given very promising results. The first one employs an image intensifier such as streak cameras to capture the changes in light intensity with time inside streamer channels [71] [72]. Variations in light intensity are caused by charge excitation and decitation during the discharge process. The advantage and disadvantage of this method lie within the fact that streak cameras can only capture images for a short period of time, in nanoseconds. Therefore, these cameras can observe streamer movement in great detail but are less effective when recording a longer sequence of activities. The second method for visual characterisation of streamers is often referred as shadow imaging techniques. This method relies on the fact that streamers consist of multiple density change channels which have different refractive index than the liquid itself. Therefore, if the viewing area is to be illuminated by a light source, streamers will appear with a different colour, in most cases: darker than the surrounding liquids. A high speed camera is used to capture the images which can be stored in a computer for further analysis. Therefore, this technique has no issue with measuring long sequence of events, in fact, continuous monitoring is possible. Its limitation is the speed at which image can be captured. This number normally comes in the form of frame per second (fps). Basically, it defines a period of time from which two events can be discriminated. This technique was initially applied for dielectric liquids by Faramund [73] and Chadband [74]. However in their research, a conventional light source was used which limits the quality of the recorded images due to prolonged exposures. The use of a high power laser as a light source [75] has proven to provide much better results since the camera is only illuminated for a much shorter period. Over the last decades, shadow imaging with laser light sources has become an important tool in the study of the initiation and propagation of density-change streamers [64][44][45][76].

3.3.3.1 High speed camera

This research employs the shadow graph technique for streamer observation in LN_2. The selected camera is an HG100K from Lake Image Systems Ltd. The maximum frame rate is 100,000 fps and the maximum resolution is 1504x1128 pixels. The higher the frame rate, the lower the resolution and vice versa. Details of this relationship are shown in Table 3.1.

Frames per second	4:3	1:1
1,000	1504x1128	1120x1120
2,000	1056x792	896x896
3,000	832x632	704x704
5,000	640x480	544x544
10,000	416x320	352x352
20,000	256x192	224x224
30,000	192x152	160x160
50,000	96x72	96x96
100,000	32x24	

Table 3.1: Frame rates and resolutions of the HG100K Camera.

The fastest imaging speed available is 100,000 fps, however, experimental results suggest that above 50,000 fps image quality reduces significantly. At the highest frame rate, streamers cannot be recognised at all due to low resolution of the images. Therefore, the capturing rates were selected from 5000-50,000 fps depending on the purpose of the experiments.

Two optical lenses, QM100 microscope and Nikon, were used for image magnification. The QM100 lens has a good magnification but only a small area can be viewed at any one time. The other lens, on the other hand, provides less focus but can record images over a much larger field of view (FOV). The difference in viewing area between the two lenses is shown in Figure 3.13. Both images have the same resolution, 200x200 pixel^2.

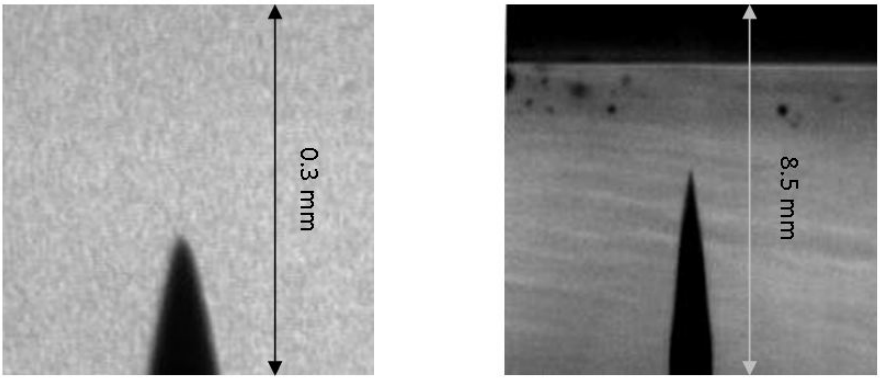

Figure 3.13: The difference in FOV between the two lenses.

3.3.3.2 Light sources

The two lenses require different light sources. For the wider FOV lens, a 500 W filament lamp can provide sufficient light intensity for streamer observation. This light source, however, cannot provide enough illumination for the QM100 lens. In this case, a very intensive light source is required. A class four LS20 50 copper vapour laser supplied by Oxford Lasers Ltd was selected as a stroboscopic light source for the camera. The frequency of the laser can be controlled from external pulse source up to a the maximum pulse rate of 50 kHz. Light from the laser has a pulse width of 25-30 ns and the wavelengths are 510.6 nm, green, and 578.2 nm, yellow.

Because the filament lamp produces continuous light, it can be used simply by pointing it at the area of interest. The focus of the lens then can be adjusted to produce satisfactory images. Its drawback is that the any blur of the captured image is very much dependent on the shutter speed of the camera. The speed determines how long the optical sensor is exposed to light. The shorter this time is, the less blur within the image. In this research, this time was set as 5 μs.

The laser light source system is much more complicated. Since the laser can be extremely dangerous when in contact with human eyes, a safety system needs to be developed before any experiments can be carried out. There are two viable options, either include all experimental apparatus inside a interlocked room or design a system such that laser beams are contained from the output of the device through the sample to the camera. The latter method was chosen since the experiments require a lot of space, therefore, constructing a room including all the equipment is very difficult. A schematic diagram of the laser interlock system is shown in Figure 3.14.

The most important element of the interlock system is a wooden ring which is painted black to minimise light refection. This ring was made from two semicircular sections which are overlapped with each other. The ring has 4 windows that are aligned with optical ports of the cryostat. Laser light is transmitted from the device into a diffuser, for reduction of light intensity as well as to broaden the lighting area, by optical fibre. Laser beams then shine on the object with the camera capturing images from the opposite side. The other two viewing ports are used for monitoring LN_2 condition and mounting the UHF sensor. Two black wooden boxes were constructed to confine the output of the laser and the diffuser within. The path between the copper laser and HG100K camera is fully enclosed to ensure heath and safety.

There are five interlock switches within the system. The first one is mounted on the box covering laser output. This interlock is connected to the laser so that if the box is open, the laser radiation sequence will shut down. The other four switches are mounted on the viewing windows on the ring. There are connected in series which means if one of them is open the laser shutter window cannot be open. With this window closed,

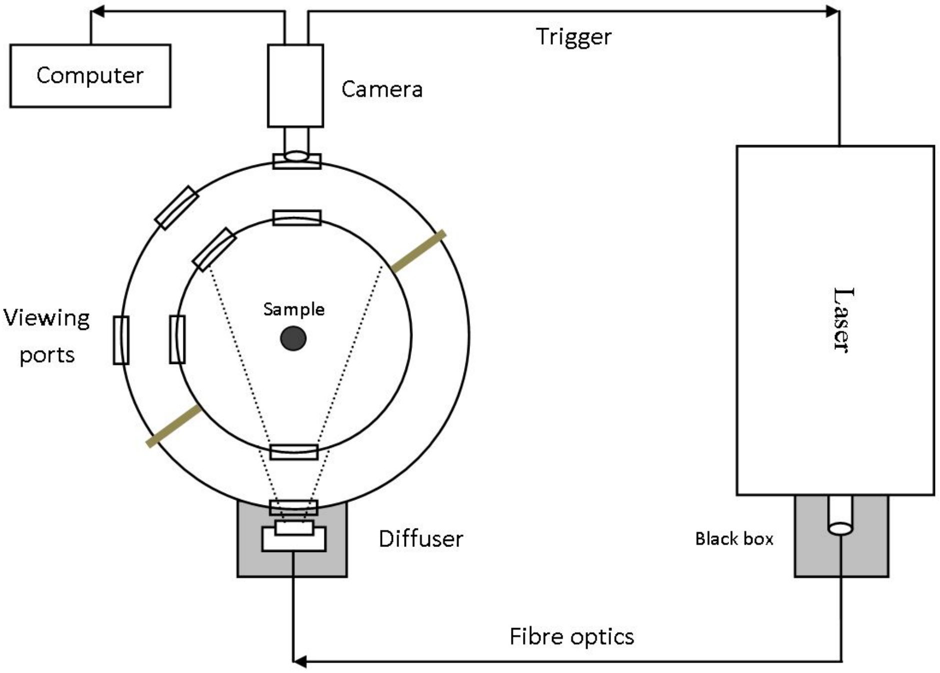

Figure 3.14: Schematic diagram of the laser interlock system.

even though radiation sequence is on, there will be no laser light transmitted outside. With the interlock system in operation, risk of exposure to laser radiation is effectively eliminated for the operator as well as people in the surrounding environment.

If an internal clock is used, the laser fires beams at a frequency of 10 kHz. This optimum frequency can be adjusted by changing the coupling capacitor inside the device. Operation following an external clock signal is also viable via a pulse generator unit. This unit can work from 0 to 50 kHz. However, the laser can only operate within half of the optimum frequency. For example, if the internal clock is at 10 kHz, the laser can only produce radiation in a frequency range of 5-20 kHz. In addition, output power at either 5 or 20 kHz will be reduced in half. This is equivalent to a camera speed from 5000 to 20000 fps.

It is important to ensure that the laser pulse is synchronised to the open period of the camera shutter. Although both camera speed and laser firing rate can be set to the same value, such as 10 kHz, there is a possibility that the object is not illuminated by the beams since the camera shutter is only open for a period of 5 μs. In order to ensure laser and camera operate at the same time, the laser is activated from a signal sent by the camera. Therefore, during the 5 μs shutter opening duration, a pulse laser with duration of 20-30 ns can effectively backlight the sample. Moreover, since only 30 ns of a streamer event is recorded by the camera, motion blur of images can be effectively removed.

One concern is the effect of laser radiation on the measurement results. A simple calculation of laser photon energy shows that the laser beam cannot effect the charge generation process in LN_2. The laser has wavelengths of 510 nm and 578.2 nm. Therefore, the amount of energy that may be transferred to other molecules by photons can be calculated as:

$$E = \frac{hc}{\lambda} = 3.89 \times 10^{-19}(J) = 2.43(eV) \tag{3.3}$$

For an electrode surface, tungsten has a work function of 4.35 eV which is significantly above the value given in Equation 3.3. Thus, the energy of a laser photon incident is not sufficient to excite electrons out of the needle surface. Similarly, for nitrogen molecules, more than 10 eV is required to promote an electron from the valence band to the conduction band. This value is also much larger than that calculated in Equation 3.3. In addition, the laser output is triggered by PD pulse activity. Therefore, the discharge happens before laser photons start interacting with liquid molecules. Consequently, the laser beam should not interfere with the obtained experimental results.

3.4 Experimental procedure

Replacement of needles and samples requires removing the top plate out of the bottom vessel. A folk lift was selected for that purpose. It has a weight capacity of 150 kg which is well above the weight of the top plate, 130kg. Before lifting, the top plate is securely clamped to the folk lift's skies by two M12 bolts. The lift is checked frequently for user safety. With the top plate lifted, the needle can be removed for re-etching.

With the needle in place, the point-plane configuration is reassembled to a desirable gap distance. The gap between the needle and the insulation barrier is reduced by 3-4 mm after filling LN_2 because the sample holder shrinks at low temperature. This behaviour must be taken into account when placing the needle, otherwise the tip might collide with the solid barrier if the gap distance at room temperature is too small. Such an event would damage the needle tip or even break the tungsten wire. The exact liquid spacing gap is measured using optical devices.

The top plate is then returned to its original position inside the bottom vessel. A vacuum tight seal is created by applying torque of 95 Nm to thirty two bolts connecting the top pate and bottom vessel together. A two-stage vacuum pump is used to remove impurities (mostly water, dust and oxygen) out of the inner cylinder. It takes more than eight hours for the vacuum level to go below 10^{-3} Torr. In most cases, the vacuum pump was left running for twelve hours.

It is important to keep a fine vacuum level between inner and outer vessels. This inter-space region acts as a thermal insulation layer. Because of the cryogenic temperature of the tests, the outer walls facing the air can be much cooler than ambient temperature in the case of poor insulation. Consequently, water can condense on the optical ports severely reducing the quality of the images taken by the camera. The solution to the problem is to maintain a fine vacuum level between the two vessels during each experiment. The vacuum pump was left running during the testing period in order to maintain a vacuum level below 10^{-5} Torr.

3.5 Summary

This Chapter discusses the experimental techniques used to investigate the behaviour of dielectrics under cryogenic conditions. The central apparatus of this investigation is a cryostat which has been specifically constructed to meet the aims of the research [10]. Besides its objective as an insulating vessel, the cryostat also has optical ports for streamer imaging and a HV bushing which is PD free up to 40 kV.

Experiments in this thesis employ a point-to-plane configuration in order to achieve high levels of electric fields for streamer initiation while maintaining low applied voltages below the PD free level of the cryostat. The sharp point is made from tungsten wire using electrochemical etching. Due to erosion caused by PD in LN_2, needles were re-etched after each test. A barrier made of solid insulation is placed on top of the plane electrode to prevent total breakdown and protect the electrode from excessive discharges. In [10], these barriers were found to be damaged by accumulated streamer discharges. Eroded material could affect the reliability of the insulation system. The erosion phenomenon was studied using a similar experimental configuration but under much higher applied voltages.

The design of the experimental apparatus focuses on controlling laboratory variables since the behaviour of streamers in LN_2 is greatly affected by the test conditions [11]. Temperature and pressure was continuously monitored during each experiment to ensure the experimental conditions remain unchanged. Impurities are effectively removed by vacuum before each experiment. An experiment procedure has been proposed to ensure that results are repeatable.

The imaging system requires a high density light source such as a laser to backlight the area of interest. This raises a safety issue since direct exposure of a class IV laser can cause severe damage to the naked eye. This problem was tackled by designing an enclosed path from laser output to the camera such that all laser beams are contained within. The system also has interlock switches which are connected in series. In the event of opening a safety switch, the laser operation will stop.

Chapter 4

Partial discharge Detection at Cryogenic Temperature

4.1 Introduction

Partial discharge is defined as a localised discharge within an insulation system. It is restricted to the region of insulation under stress. Although a single PD event might not necessarily lead to complete breakdown of the material, the discharge can deteriorate dielectric materials due to impact with high energy electrons or ions. Damage accumulation caused by repetitive PD pulses can eventually result in complete failure of insulating materials and therefore, the high voltage component. Recognising the significance of PD on lifetime of insulation, various methods have been developed for the purpose of detecting and measuring PD events. The main requirement is to capture the effects caused by high energy electrons and ions during discharges. These effects are: dielectric losses, light radiation, noise, pressure variation, chemical reaction and electrical current pulses. Among those, detection techniques based on current pulses are the most common and widely applied. This is due to the fact that these approaches provide good sensitivity together with a possibility of continuous on-line monitoring.

The IEC 60270 standard provides definitions and descriptions of a current measurement technique which permits a measured PD pulse to be quantified in apparent charge (in picoCoulombs). This conventional technique has been well developed over many years. From the experience gained, a set of specifications for the measurement has been defined and accepted internationally. However, there are several limitations to the conventional system. First, apparent charge is not the amount of charges transferred at the discharge sites; therefore, the actual PD current cannot be determined. Secondly, the pulse resolution time of a PD detection method which indicates the ability of distinguish successive PD events, is inversely proportional to its bandwidth. Due to the narrow bandwidth of IEC 60270 techniques (typically less than 600 kHz), multiple discharge events, between which the time intervals fall below the resolution threshold, cannot be resolved. Instead, a slowly damped output is recorded which shows the integration of successive pulses. Finally, the conventional system only takes into account the amplitude but not the waveform of the pulse. As a result, two PD pulses with different characteristics in the time domain can appear to have the same apparent charge value. Therefore, wide bandwidth PD measurements methods such as the use of UHF sensors can provide useful information that is otherwise missing from the IEC 60270 standard approach.

The limitations of the conventional method have been recognised when measuring PD in dielectric liquids [9] [77] [78]. The current pulses generated during streamer propagation in dielectric liquids such as mineral oil have been found to appear in bursts with short duration (in nanoseconds) and adjacent to each other, e.g. less than several microseconds apart. The IEC 60270 method produces a slowly damped pulse which presents the integration over time of many faster current pulses [77]. On the other hand, wideband detection methods have the problem of quantifying measurement results. Therefore, combining the conventional method and a wideband measurement, such as using a UHF sensor, can provide a better understanding of the discharge mechanisms as well as better detecting and testing tools. The IEC 60270 technique can quantify the apparent charge at the terminals while the non-conventional wideband method provides details about individual events.

The wideband measurement methods used in this work are RFCT and UHF sensors with the focus on the latter method. The details of experimental apparatus can be found in Chapter 3. This chapter discusses on the application of UHF sensors in detecting and measuring PD in LN_2. The RFCT method, which is a more commonly-used wideband measurement technique than the UHF sensor, was also applied to further confirm the reliability of the UHF measurements of PD in LN_2.

4.2 The excitation of UHF signals

During a discharge event, electrons and ions are constantly accelerated due to the high electric field or decelerated when impacting with molecules. Electromagnetic radiation occurs when charged particles move with inconsistent velocity. Therefore, during a PD pulse, electromagnetic waves can be radiated and spread from the source in all directions. The further away from the source, the more the electromagnetic energy dissipates. If the PD source is located inside a confined space such as a transformer or a cryostat, reflections happen when the travelling waves came into contact with conducting surfaces. This creates a complex signal which can be measured by a sensor mounted at a dielectric window.

The optical windows in the cryostat used for this experiment have similar dimensions to those used in [79]. Results given in [79] suggest that the use of dielectric blocks with diameter greater than 100 mm and relative permittivity greater than 5 can lower the cut-off frequency of several propagation modes. However, dielectric material with very high relative permittivity, ϵ_r greater than 10, can create a problem of energy reflection due to significant difference in relative permittivity between one medium and another. The windows of the cryostat are made of sapphire and borosilicate (BK7) which have relative permittivity of 9 and 4.6 respectively. Theses window were selected to satisfy the pressure requirement at the same time to be compatible with the imaging system.

4.2.1 Step input response

The technique for creating electromagnetic radiation which simulates PD events has been previously discussed [69][79][80]. The system consists of a pulse generator circuit which is connected to a monopole probe via a SMA (or BNC) connector. The monopole is simply a conducting wire as shown in Figure 4.1. The pulse generator circuit supplies the monopole with pulses of with rise time of a few in nanoseconds. Because the rise time is much shorter than the pulse duration, which normally is in microseconds, the input waveform can be considered as a step input. In this work, the pulse generator unit provided input waveforms with magnitudes of 3.7 V and rise time varying from 2 ns to 20 ns as shown in Figure 4.2.

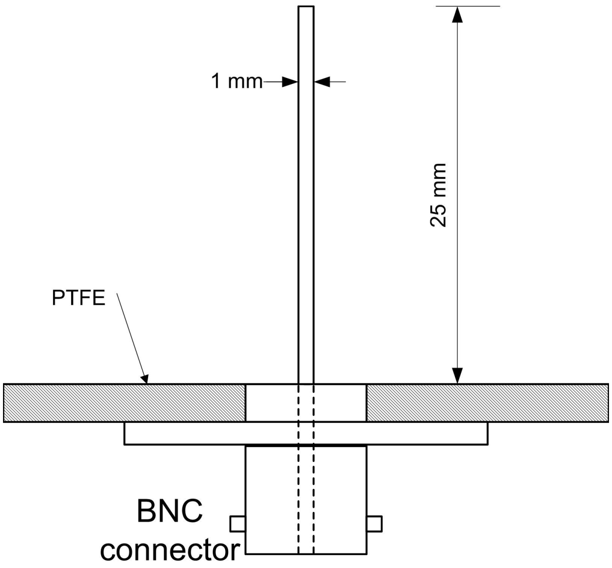

FIGURE 4.1: The input probe.

The monopole was placed in the centre of the inner vessel at the same height as the optical ports so that electromagnetic radiation could propagate through the insulating medium and reach the dielectric windows. This radiation is generated by a current pulse flowing through the conducting wire. The excited signals which are in the UHF range can be captured by the sensor as shown in Figure 4.3.

Initial results (Figure 4.3) show that the electromagnetic waves excited inside the cryo-

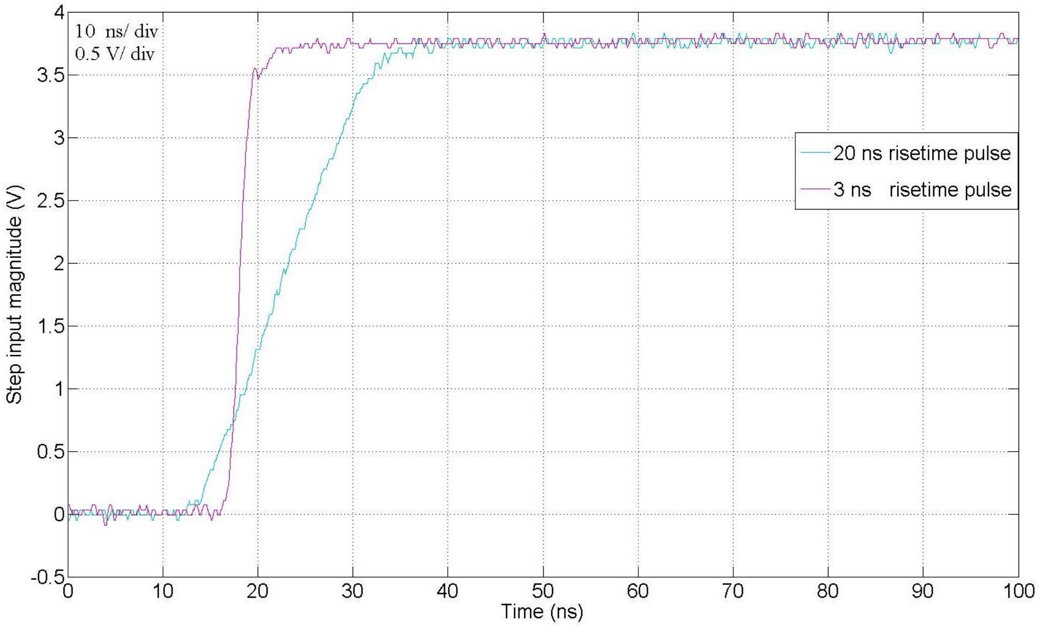

FIGURE 4.2: The input waveform.

stat can be captured by the UHF sensor mounted on the outside wall. The output amplitudes of the 3-ns and 20-ns inputs are 4 mV and 2 mV respectively. The noise level was defined as the peaks of the measured signals before applying the voltage. The value is ±1.75 mV in this case as shown in Figure 4.3. When the rise time of an input waveform is more than 25 ns, the radiated signals fall below the noise level and therefore cannot be measured by the device. An approximately 50-ns delay was measured between the input and the UHF sensor waveform output. This is due to the length of the cable transferring the input waveform to the monopole. Since the pole is located inside the cryostat, an 8-meter cable is required. If the signal travels with a velocity of half of the speed of light, it would take the signal 40 ns to reach the monopole. The other 10 ns delay may be the result of electromagnetic wave propagation and the time delay produced by the electronic measurement devices.

The relationship between the rise time and output amplitudes is shown in Figure 4.4. The faster the input voltage rises, the higher the amplitude of the signal detected by the sensor. This is due to the fact that a shorter rise time results in higher magnitude of current pulses being generated. More current flowing through the wire means stronger electromagnetic radiation.

4.2.2 PD in air

Results from the previous section have established that electromagnetic wave radiation within the cryostat can propagate through its structure and be captured by the UHF sensor. Before carrying out experiments in LN_2, a set of experiments were undertaken to

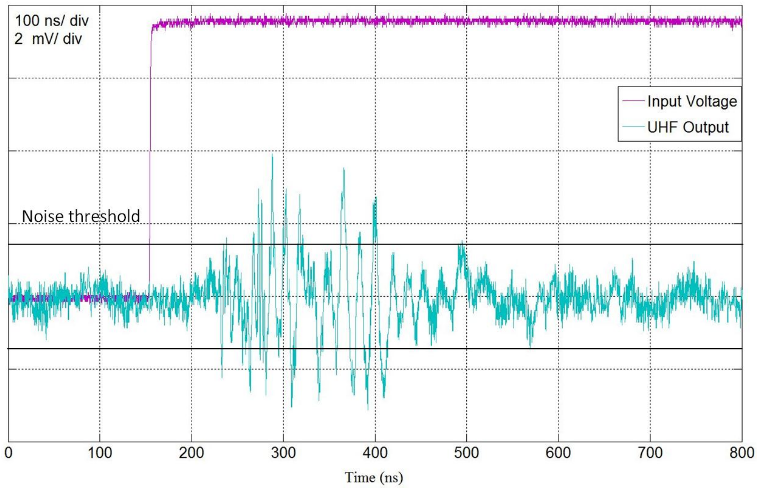

(a)

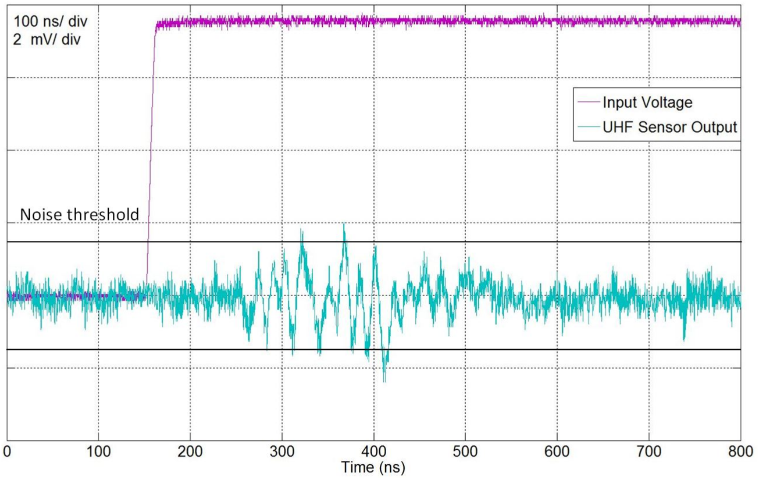

(b)

Figure 4.3: Typical UHF sensor output of step input voltage, (a) 3 ns rise time, (b) 20 ns rise time.

study the response of the sensor to PD pulses in a gaseous environment, e.g. air, and the effects of the cryostat structure on the electromagnetic radiation propagating through it. These tests utilised a point-to-plane configuration as discussed in Chapter 3. The PD source was placed inside the cryostat during the first experiment and outside during the second one. In both cases, relative position of the sensor and the needle was kept constant so that experimental results would show the effects of the cryostat structure on any propagating electromagnetic waves.

Measurement results from the sensor with the PD source inside and outside of the cryostat are shown in Figure 4.5 and Figure 4.6 respectively. The excitation voltage was 4 kV for both experiments. Although the apparent charge level was not measured in this particular test, the two waveforms were the UHF responses from PD pulses which were excited from the same experimental conditions. The only difference was the location of the PD source. In addition, corona in air using sharp points has a distinct characteristic

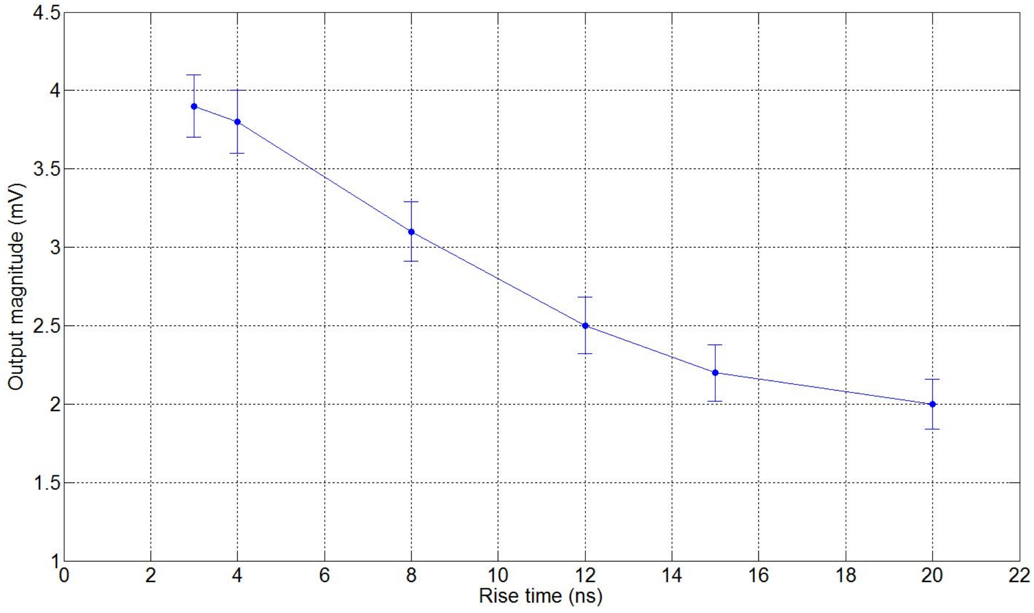

FIGURE 4.4: The relationship between input voltage's rise time and sensor amplitudes.

of producing similar magnitude pulses repeatedly. Therefore, it can assumed that the UHF waveforms presented here were excited from PD pulses which have similar apparent charge levels. Moreover, since the relative position of the sensor and the wave radiated point was kept unchanged, the difference between the results showed in Figure 4.5 and Figure 4.6 is merely caused by the cryostat structure.

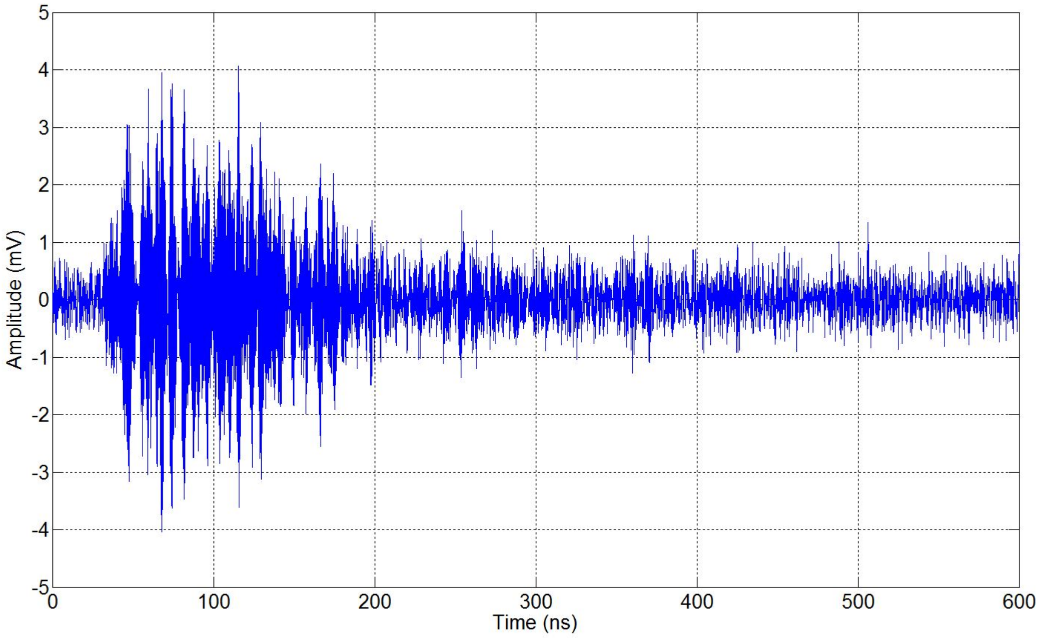

FIGURE 4.5: Typical UHF sensor output of PD in air inside the cryostat.

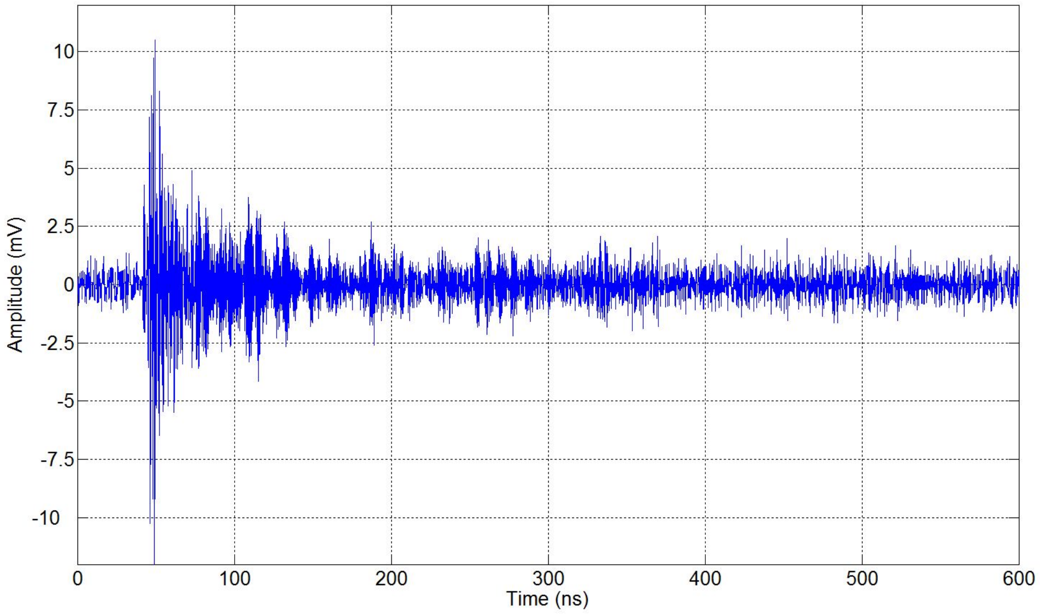

Figure 4.6: Typical UHF sensor output of PD in air outside the cryostat.

When the PD source was placed inside the cryostat, multiple peaks are observed in the measured output waveform. Meanwhile, in the other case, only one important peak is seen. The cryostat is essentially two aluminium vessels. Reflections occur when travelling waves are in contact with conducting surfaces such as the cryostat's wall. Reflected signals then propagate in the opposite direction and possibly bounce off the walls several times before reaching the dielectric windows. As soon as the electromagnetic wave is radiated, one part of the wave travels directly toward the window where the sensor is mounted while at the same time another part propagates towards the opposite direction and is therefore reflected by the conducting wall before making it way back to the sensor. The difference in the travelling distance between these two components is equal to one diameter of the inner vessel. Therefore, if the first and second peak of the UHF waveform is assumed to present theses two parts of the radiated waves, the difference in the travelling distance should be equal to the inner vessel diameter, 35.6 cm. Assuming that the electromagnetic wave travels at the velocity of light, such distance would cause a delay of 11.9 ns between the two waves. This hypothesis explains the 12-ns difference between the first and second peak of the UHF output as shown in Figure 4.5. Subsequent peaks in this waveform occur at inconsistent time intervals since the wave bounces of the metal surface at different angles. During propagation, interaction between electromagnetic waves can happen either constructively or destructively. This might explain the fact that the maximum amplitude does not necessarily occur at the first peak of the UHF waveform when the discharge source was placed inside the cryostat. In fact, as can be seen in Figure 4.5, the highest output voltage is observed over 80 ns after the starting point of the waveform while in the case of PD outside the cryostat, maximum amplitude occurs almost instantly (Figure 4.6).

The amplitude of the output was more than two times greater when the test was carried out outside of the cryostat, indicating that attenuation does occur during propagation of the UHF signals through the material structure. When electromagnetic waves enter a medium with a difference in permittivity, some of the energy will be transferred through the medium at the same time reflection occurs at the contact surface. The greater the difference in permittivity, the more energy that will be reflected [79]. On its path to the sensor, electromagnetic wave travels through two different windows that both have a permittivity much greater than that of air. Therefore, signal attenuation in the case of PD source inside of the cryostat is as expected.

A model has been developed by A. M. Ishak from University of Strathclyde in order to further investigate the effects of the cryostat on the UHF signals propagating through it. The details of this model can be found in Appendix B. The results from this work suggest that the attenuation is minimum for very fast current pulses while for PD of a longer duration the cryostat structure severely attenuates the radiated signals. This phenomenon is believed to be the consequence of internal reflection since the windows only allow signals with short wavelengths to efficiently propagate through. The behaviour can be observed by analysing the frequency spectrum of UHF outputs of the electromagnetic radiations inside and outside the cryostat. As shown in Figure 4.7, the main difference between the signals lies within the lower frequency spectrum (range of 0.3-2.3 Ghz). FFT amplitude within this range is much lower in the case of PD source inside the cryostat due to the attenuation of the lower frequency components.

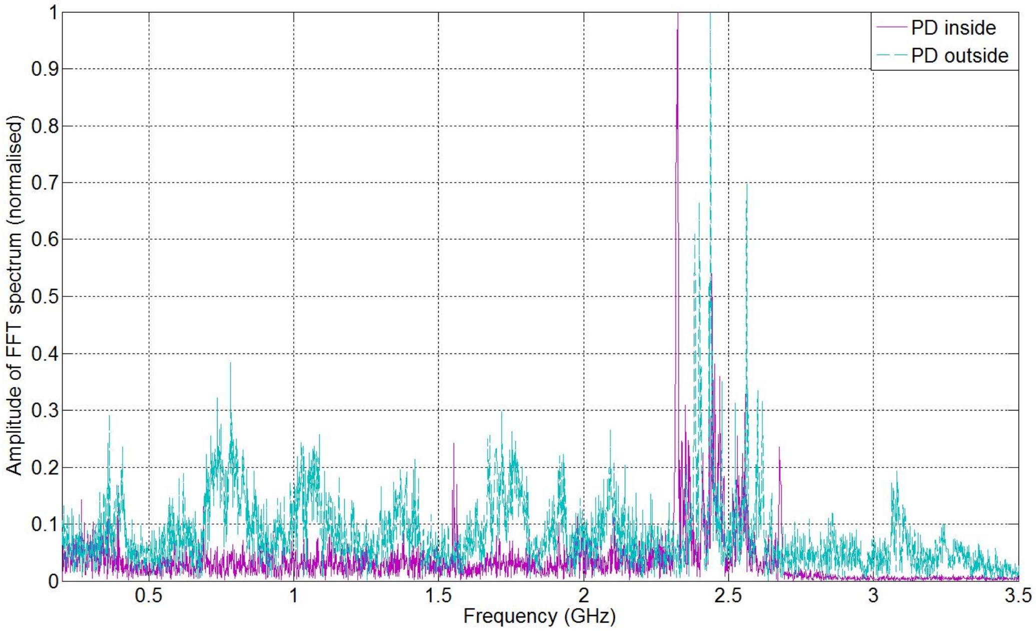

FIGURE 4.7: Frequency spectrum of UHF sensor signal during PD in air inside and outside the cryostat

4.2.3 PD in LN_2

The use of UHF sensors in monitoring PD in liquid dielectrics is much less common than that in gas insulated system (GIS). For LN_2 in particular, only a few published works have been found on the application of UHF sensors, and most of them are involved with free particle discharges [81] [82] [83]. In this research, a point-to-plane configuration was used in order to study the prebreakdown phenomena in LN_2 under AC applied voltages. The point-plane set up can be thought of as a sharp protrusion defect which causes PD in high-voltage equipment. Since the PD source is submerged in LN_2 inside the cryostat, it is expected that radiated waves reflect at the metal walls when in contact. Such reflections can occur multiple times before the signals attenuate completely. Experiments which generate electromagnetic waves radiated within a confined metal tank simulate what happens in HTS power devices. The inter-space vacuum technique used in the cryostat structure is a very common method for thermal insulation of LN_2 filled equipment. Therefore, the results presented here contribute towards the understanding and application of UHF monitoring for future HTS power apparatus.

It has been shown that UHF radiation inside the cryostat by step voltages and PD in air can be captured by a UHF sensor mounted on the outside wall. The next objective is to investigate the feasibility of using UHF sensors to measure PD pulses generated during pre-breakdown phenomena in LN_2. Figure 4.8 shows a typical UHF waveform observed by the sensor during negative streamer discharges. Figure 4.8 reveals that current pulses produced during LN_2 streamer discharge can radiate UHF signals enough to be measured by the sensor with a good signal to noise ratio.

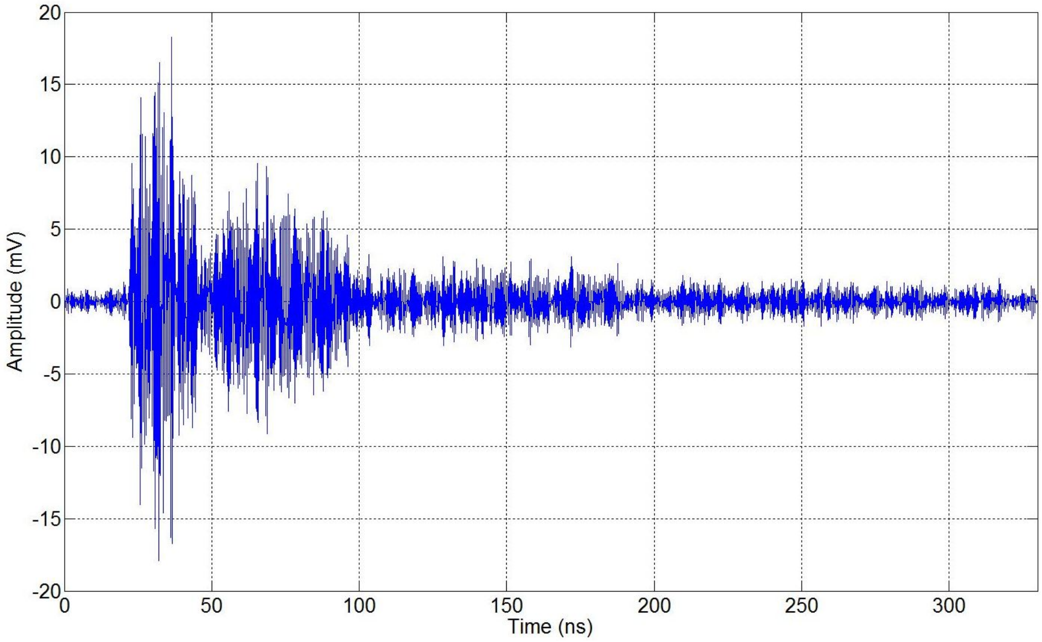

FIGURE 4.8: Typical UHF sensor output during negative streamer discharges.

Similar to signals radiated by PD in air, the UHF waveform in this experiment also experienced reflections and interference before detection by the sensor. However, the frequency spectrum plots of PD in air and in LN_2 show different characteristics (Figure 4.9). Firstly, the highest amplitude in the spectrum is 0.5 Ghz lower when the PD source was submerged in LN_2. Secondly, it appears that UHF waveforms radiated by PD in LN_2 have a wider spectral content compared with discharges in air. It is hypothesised that the PD process in LN_2 involves the generation and collapse of bubbles which is far more complex than the case of PD in air. Bubbles generated during pre-breakdown phenomena in LN_2 undergo variations in pressure and size during the process which could be the reason for the difference in the observed spectral content.

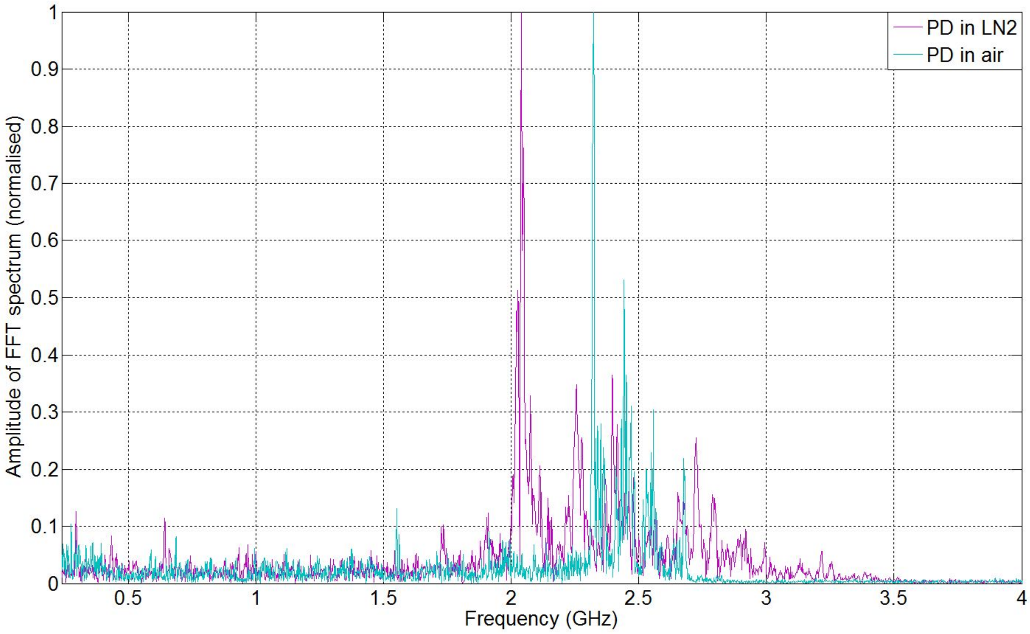

FIGURE 4.9: Frequency spectrum of UHF sensor signal for PD in air and in LN_2.

4.3 Wideband and narrowband PD measurements

Figure 4.10 shows captured PD signals during a 50 Hz ac cycle measured simultaneously by the following measurement methods: IEC 60720 standard, UHF and RFCT sensors. Thermally induced bubbles were not observed before and after the experiment so it may be assumed that there were no thermal effects on pre-breakdown streamers. The applied voltage was at 19 kV rms and the gap distance between the needle and insulating barrier was 15 mm after filling with LN_2. The UHF sensor is capable of detecting PD in both positive and negative half cycles while the RFCT technique in this case suffers from very high background noise from the earth connection and therefore failed to detect lower magnitude PD pulses during the positive half cycle when the needle was negative to the plane electrode. It is difficult to comment on the sensitivity of the UHF sensor

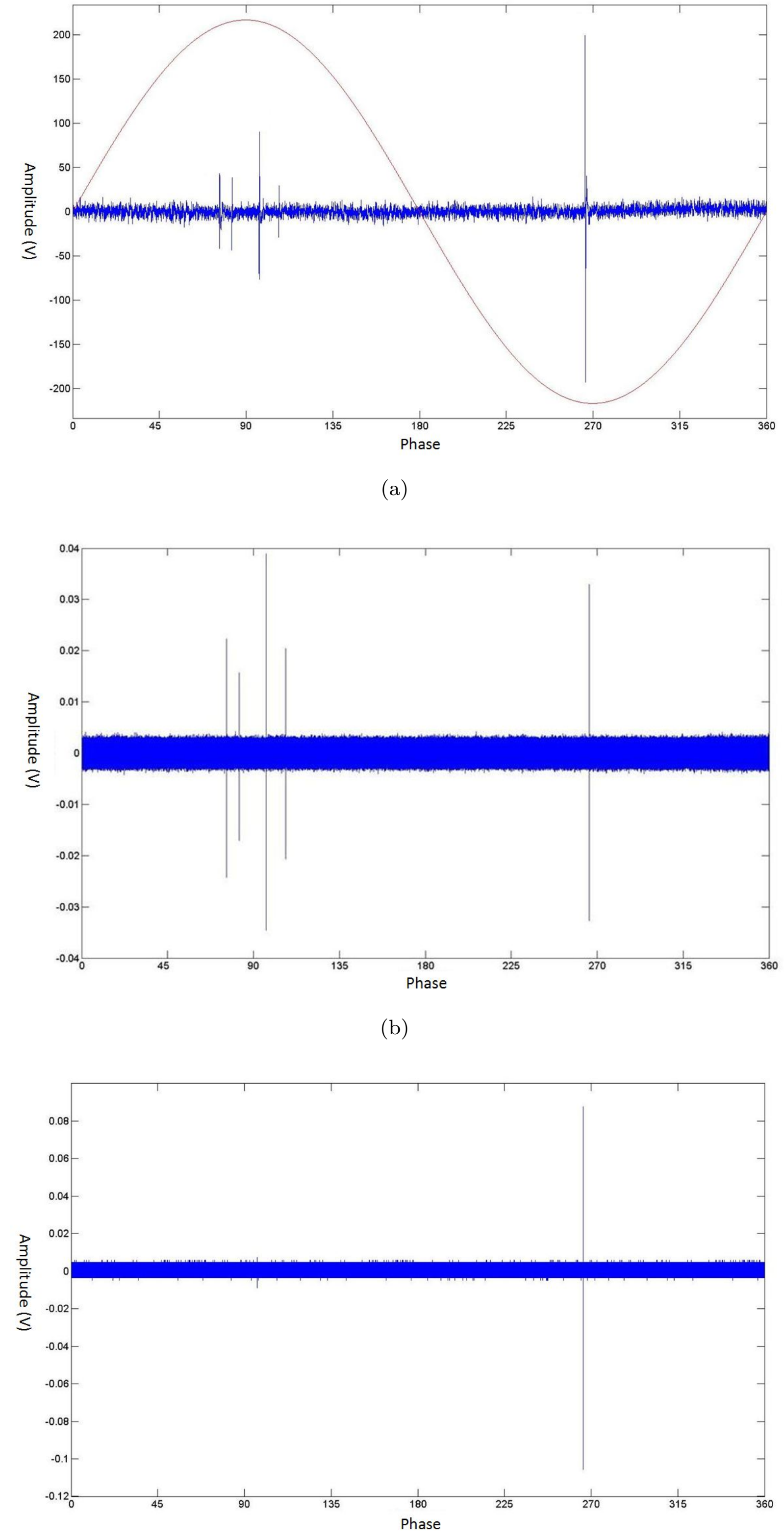

(a)

(b)

(c)

FIGURE 4.10: PD measurement results from (a) IEC 60270, (b) UHF sensor, (c) RFCT at 19 kV, 77.8±0.3 K, atmospheric pressure, liquid gap distance 15mm.

since a relationship between UHF signals and apparent charge has yet to be established, however, it can be seen that PD pulse with an apparent charge level as low as 25 pC can be detected.

Streamer discharges in LN_2 excited UHF signals which were captured by the sensor are shown in Figure 4.10(b). Results from the UHF sensor are in phase with IEC 60720 pulses. However, the magnitudes of the UHF measurements do not appear to be proportional to the corresponding apparent charge. Even though the magnitude of the UHF measurement increases linearly with apparent charge in LN_2 during free metallic particle discharges under AC voltages [82], the linear relationship for a point-to-plane arrangement cannot be implied. The UHF signals are related to the rate of change of current. Therefore, the linearity of this relationship is dependent on the variability of the current waveform. In fact, previously published results of UHF measurements in mineral oil [70] suggest that current waveforms during free metallic particle discharges are more consistent than during needle-to-plane discharges. Similarly, the difference between this work and [82] in the relationship of UHF magnitude and charge transferred can be explained by the fact that current waveforms show more variation during point-to-plane discharges than free particle discharges.

4.3.1 Pulse burst behaviour during negative streamer discharges

Figure 4.11 shows a typical pulse train sequence recorded during the formation of a negative bush-like streamer at 17 kV. Simultaneous measurements by the IEC technique and the RFCT sensor are also displayed in the same figure. The narrowband detection method following the IEC standard does not resolve multiple discharge events close to each other in the time domain. Instead, a slowly damped output is recorded which shows total amount of charge transferred by integrating the successive pulses. The burst sequence of PD observed here in LN_2 has also been observed for many other dielectric liquids [77] [78] [84]. This phenomenon is common for discharge in liquid mediums because the PD process in liquids involves the generation and collapse of bubbles. Each discharge in a bubble would be equivalent to a single pulse in a pulse burst sequence. Therefore, any attempt to measure PD in a liquid-filled system using narrowband detection will result in a single integrated signal of a pulse train which otherwise can be observed by wideband measurement methods such as the UHF sensor in this case. RFCT sensors, in theory, should be able to observe this burst behaviour since the bandwidth of the sensor is large enough to distinguish those PD events. However, signals measured by the RFCT do not show as much detail as the UHF sensor since the bandwidth of RFCT is lower and the sensor is detecting currents in the earth connector. This means that the signal to noise ration is effected by other external events.

The pulse burst behaviour was observed for negative streamers as for all the gap distances studied (from 2 mm to 20 mm). It can also be seen from Figure 4.11 that the waveform from the IEC standard measurement is delayed by several μs compared to RFCT and UHF signal. The time delay is due to the amplifier inside the Robinson PD detector unit.

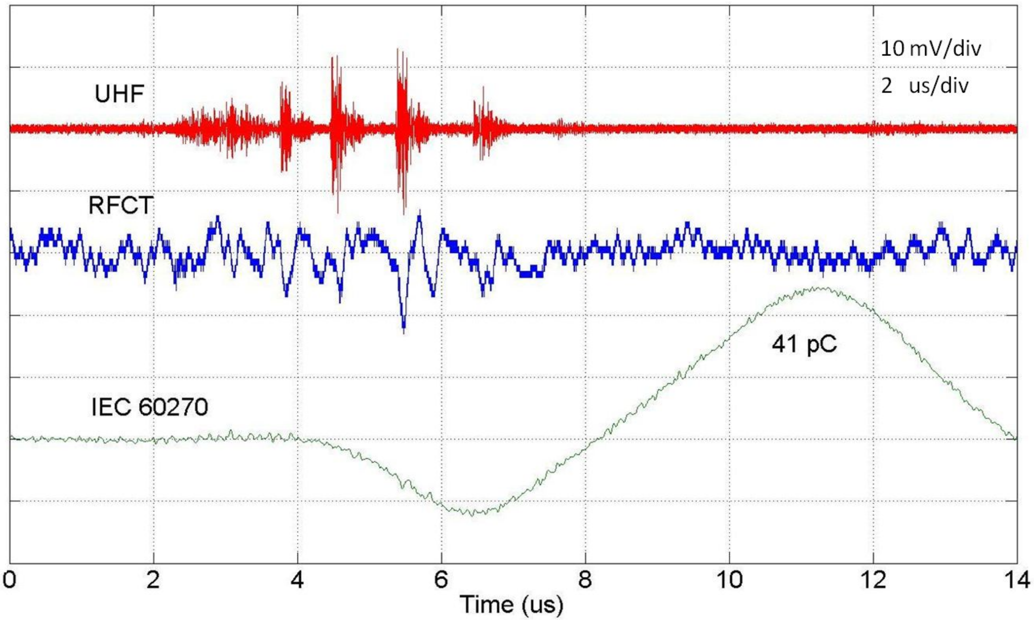

FIGURE 4.11: Typical point cathode PD bursts in LN_2, gap distance 20 mm, at 17 kV, LN_2 at atmospheric pressure, 77.8±0.3 K

Figure 4.12 shows another PD event during the development of streamers from a negative polarity tip. Two peaks were observed by the conventional IEC60270 capacitively coupled signal which can be thought of as two PD pulses, the time difference between them being long enough for the conventional method to recognise but still too short to distinguish into two separate pulses. This behaviour is known as superposition error which occurs when the time between two adjacent PD pulses is less than the duration of a single output waveform. The consequence is that an overlapping response is recorded. Superposition errors can either be additive or subtractive, and it would be very difficult to predict the nature of the errors. In this case, from the UHF sensor waveform, it would appear that the superposition was subtractive.

The pulse resolution time, T_r, is the shortest time interval between which two consecutive PD pulses that can be distinguished, e.g. the amplitude of the resulting pulses is no more than 10 % of that for a single pulse. By definition, it is inversely proportional to the bandwidth of the measurement method. In this case, the Robinson PD detector cannot seperate pulses that are less than 80 μs away from each other while for the UHF sensor the pulse resolution time is in the order of a few hundreds nanoseconds. Waveforms from both RFCT and UHF sensor (in Figure 4.12) show different current pulses with the latter one almost double the previous pulse in amplitude.

The results in Figure 4.11 and Figure 4.12 show the two distinct discharge signatures observed during negative streamer process. The appearance rate of the events which are

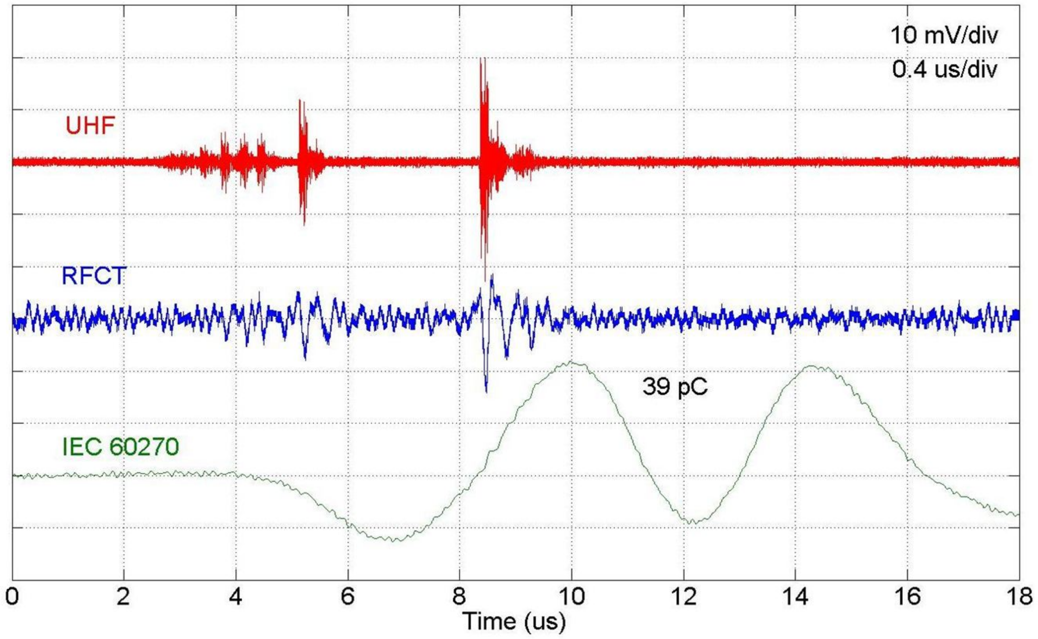

FIGURE 4.12: Dual point cathode PD pulses, gap distance 20 mm, at 17 kV, LN_2 at atmospheric pressure, 77.8±0.3 K

similar to that shown in Figure 4.11 is higher than those following Figure 4.12. This ratio reduces with the applied voltages: 16.5:1, 9.4:1 and 7.2:1 at 17, 19 and 23 kV respectively. Correlation between these discharge signatures and streamer propagation modes will be discussed in Chapter 5 which emphasizes on streamer characterisation in LN_2. The discussion in this chapter focuses on PD measurement methods for condition monitoring of future HTS power apparatus.

The number of pulses in a sequence as well as the amplitude of the discrete pulses increases under higher applied voltages as shown in Figure 4.13. The rise in PD magnitude can be explained by the increase of electric field across the incident area which would lead to more charges being generated. Thus, stronger current pulses generating more electromagnetic radiation were observed. In addition, streamers in LN_2 tend to branch out more under the influence of higher electric fields. Since propagation of density-change channels is accompanied with discharge pulses, an increase in the number of branches would result in more discrete pulses in a burst sequence. It is worth noting that waveforms presented in Figure 4.13 were the responses of PD pulses with different charge values. In fact, the apparent charge measured by the conventional technique of the UHF waveform in the figure was 60 pC, 120 pC, 150 pC at 17 kV, 21kV and 23 kV respectively. The phenomenon in which charge transfer at the terminals increases with applied voltages in dielectric liquids has been observed by many authors [45] [62] [84].

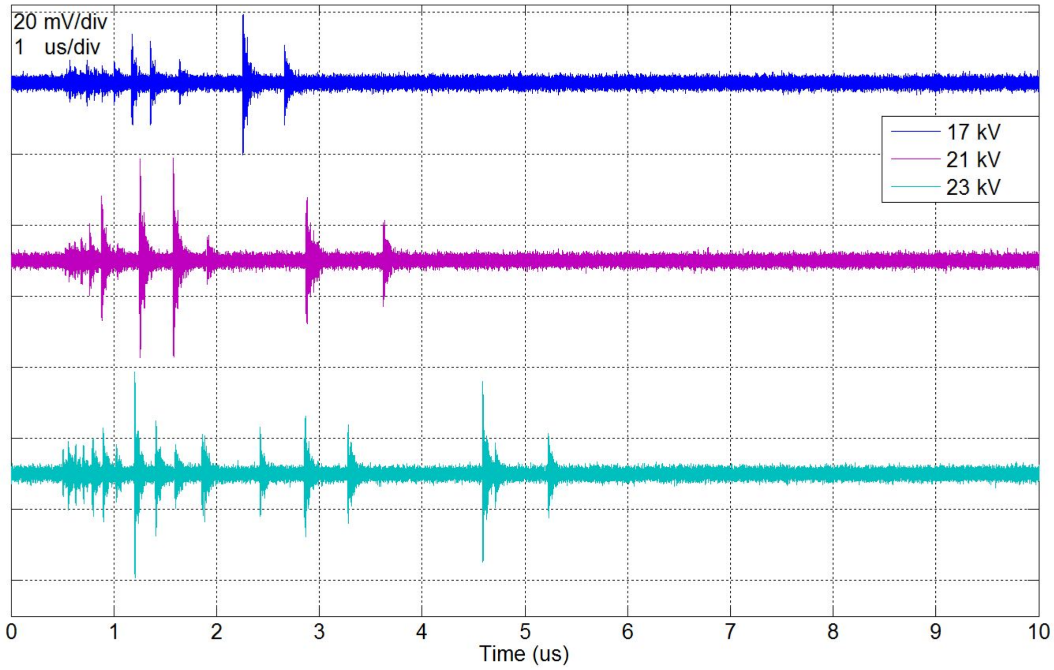

FIGURE 4.13: PD burst behaviour during negative streamers at different applied voltages. The gap distance was 15 mm and LN_2 was at 77.8±0.3 K, atmospheric pressure.

4.3.2 UHF waveforms during positive streamer discharges

Partial discharges from a point anode, Figure 4.14, captured by the UHF sensor are observed to display a different pattern compared with the point cathode discharges. Only one single event is seen and no additional pulses are observed. Waveforms recorded by the RFCT show a similar behaviour. This implies a difference in the mechanisms governing the pre-breakdown phenomena of a point cathode and anode. These results are in line with previous observations [10] [8], in which the propagation of a filamentary positive streamer are accompanied by a PD pulse with higher apparent charge than that recorded for negative streamers.

On some occasions, three out of 200 PD signals, two pulses have been observed by the UHF sensor in a PD event during positive discharges as shown in Figure 4.15. Considering the branching phenomenon of positive filamentary streamers [10], the behaviour here can be thought of as a consequence of the formation of additional filaments. Unfortunately, in order to capture the growth of multiple filaments from a positive streamer, the required frame rate of the camera must exceed 1,000,000 fps (less than 1 μs between each frame) which is much greater than the imaging system maximum rate of 50,000 fps. Therefore, the shadow graph technique in this research can only confirm the shape of a streamer correlated to a particular PD event rather than observe the development of the density-change channels. The results in Figure 4.15 also show a time resolution error in the detection method using RFCT sensor. Thus, for PD measurement in LN_2 in particular, the UHF sensor can provide better detection of adjacent current pulses

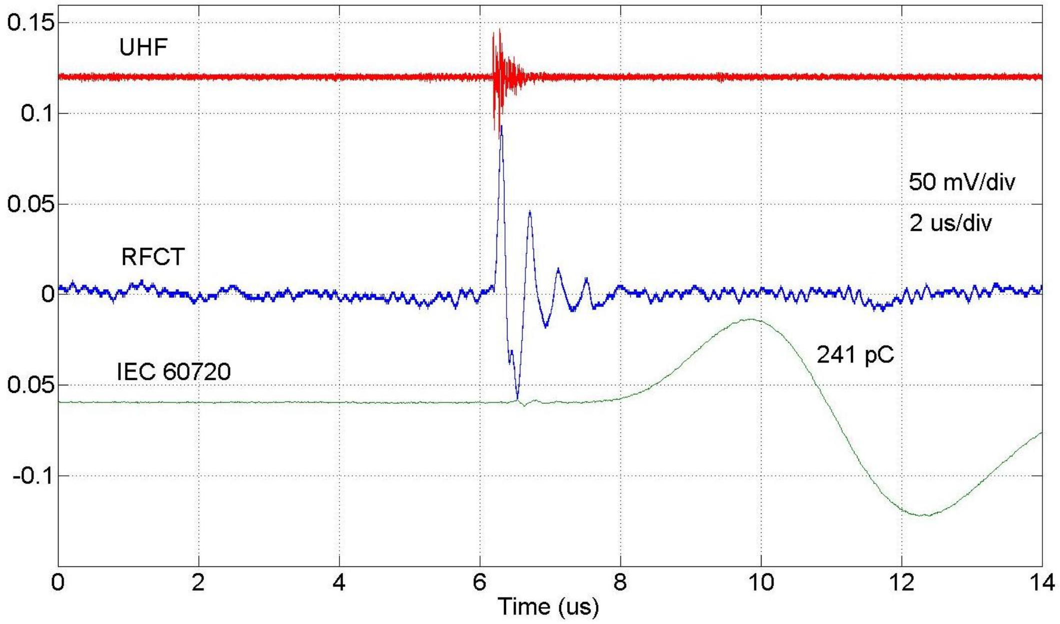

FIGURE 4.14: Typical point anode PD pulse in LN_2, gap distance 20 mm, at 17 kV, LN_2 at atmospheric pressure, 77.8±0.3 K

than the conventional method and other wideband techniques such as RFCT.

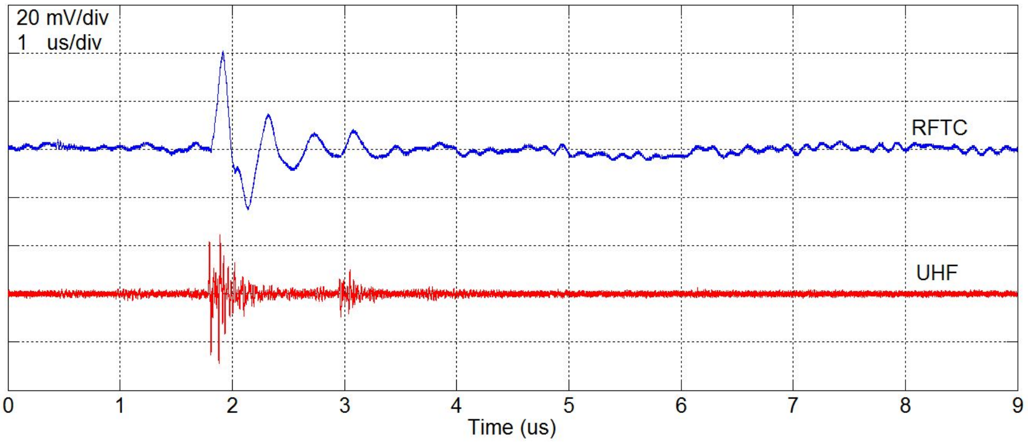

FIGURE 4.15: A PD event during positive discharge measured by UHF and RFCT sensor, 245 pC, gap distance 20 mm, at 17 kV, LN_2 at atmospheric pressure, 77.8±0.3 K

The influence of applied voltage on the signals measured by the UHF sensor is shown in Figure 4.16. Similar to the results from negative streamers, the measured amplitudes increase significantly when the PD source was subjected to higher applied voltages. Apart from the increased amplitude, other characteristics of the recorded waveforms appear to be similar across the range of testing voltages. The observation differs from that of UHF pulses detected during negative polarity in which the characteristics of the pulse sequence were greatly affected by the increase of the applied voltage.

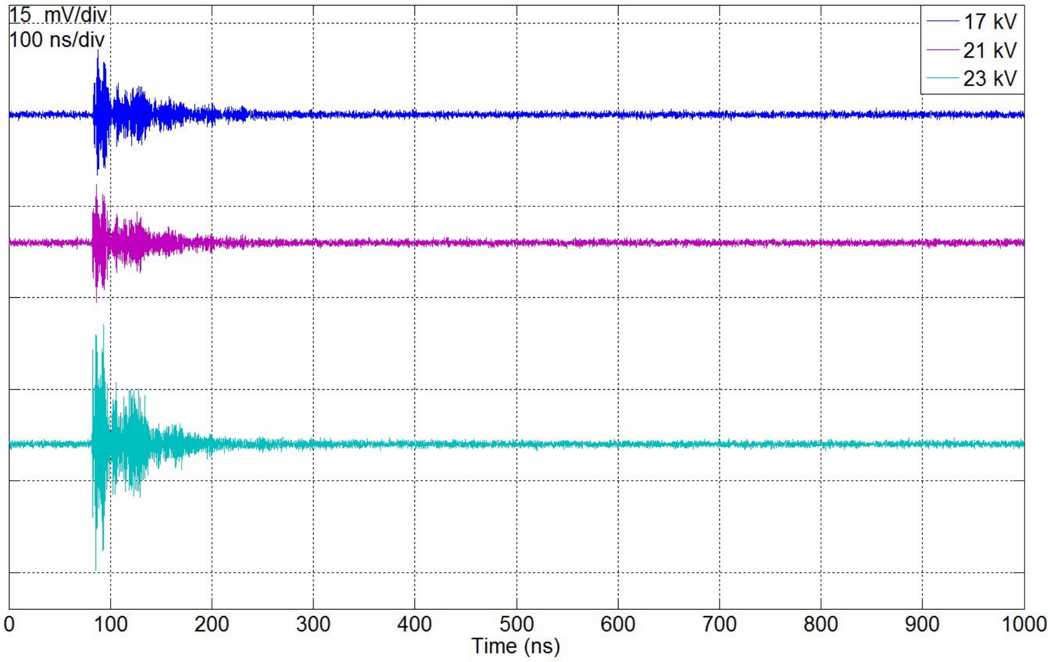

FIGURE 4.16: Waveform observed by the UHF sensor during positive streamers at various applied voltages. The gap distance was 15 mm and LN_2 was at 77.8±0.3 K, atmospheric pressure.

4.3.3 Current pulses and UHF measurement during streamers in LN_2

Since the RFCT sensor shows poor results when the needle is negative to the planar electrode, measurements of current pulses during negative streamer propagation are required in order to confirm the pulse train phenomenon observed by the UHF sensor. PD current pulses during pre-breakdown process in LN_2 can be measured via a 50-Ohm resistor placed in the earth connection. The voltage drop across the resistor will be proportional to the current following to it according to Ohm's Law. The experimental arrangement is shown in Figure 4.17. The only difference between this and previous studies is the replacement of the RFCT sensor by a 50-Ohm resistor.

During cathode pre-breakdown phenomena, PD events appear in the form of multiple current pulses as shown in Figure 4.18. The fast current pulses excited electromagnetic radiations which were captured by the UHF sensor. Each current pulse corresponds to a single waveform recorded by the sensor. The behaviour is less clear at the beginning of the sequence due to a cluster of current pulses. Therefore, it can be concluded that the typical sequence recorded by the UHF method is the result of current pulses due to streamer propagation. The overlapping phenomenon seen using IEC standard detection is again observed here. If the sequence of current pulses is the result of a single streamer propagation, the concern is that the corresponding measured charge by the conventional method, in this case, is inaccurate. Therefore, characterisation of streamers in dielectric liquids, LN_2 in particular, based solely by apparent charge levels will have many shortcomings. As a PD measurement method, the application of

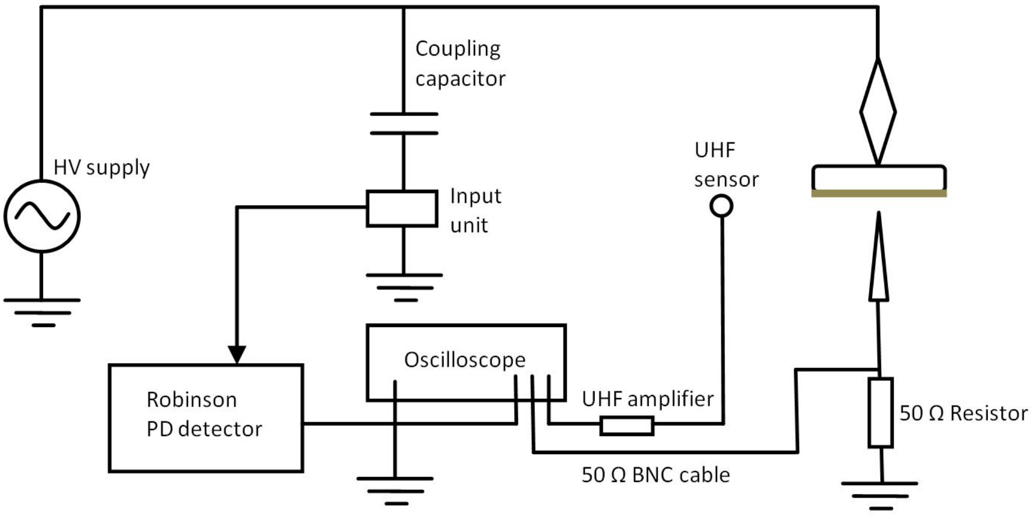

Figure 4.17: Schematic diagram of current pulse measurement.

a UHF sensor will certainly give a better resolution in the time domain compared to the conventional method in which a coupling capacitor is used and solve the problem of narrowband bandwidth detection.

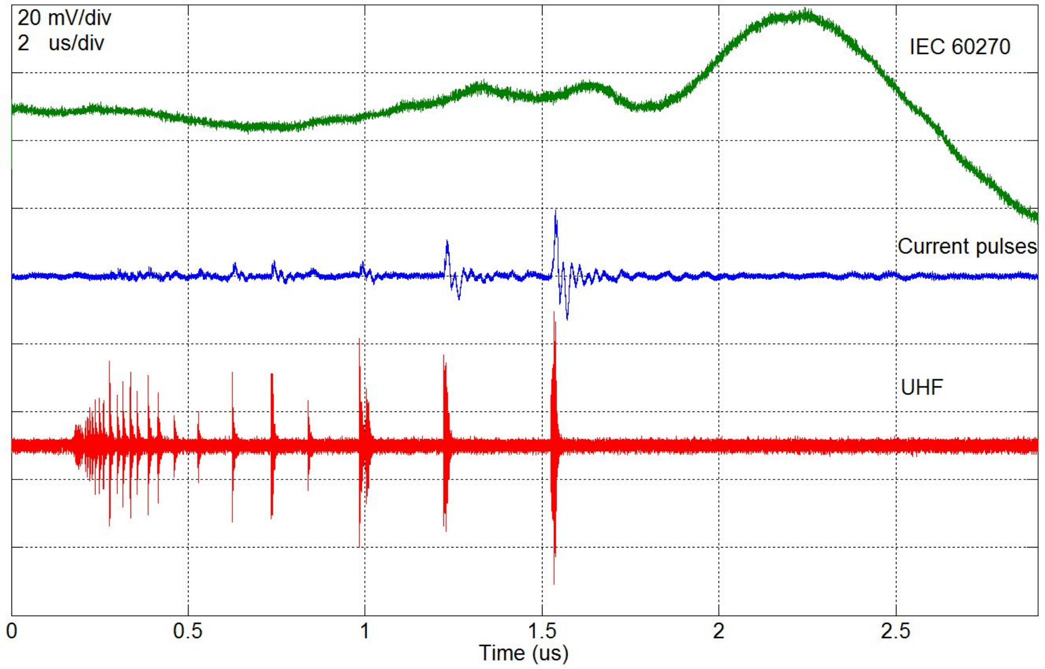

Figure 4.18: Current pulses during negative streamers in LN_2, gap distance 20 mm, at 23 kV, LN_2 at atmospheric pressure, 77.8±0.3 K

4.3.4 Correlation between narrowband and wideband measurement signals

The apparent charge value given by the IEC standard is not the actual charge transferred at a discharge site but relates to the amount of charge transferred at the terminals. It is impossible to access the real charge involved during a PD event. Wideband measurement methods are relatively new and there is a lack of in-field experience as well as any form of standard to quantify the measurement results. By using narrow and wideband detection simultaneously during pre-breakdown PD in LN_2, a relationship between the conventional method and high frequency techniques can be investigated in order to quantify wideband measurement waveforms in terms of apparent charge.

In gas insulated systems, UHF signal amplitude has been suggested to be proportional to the apparent charge magnitude [85]. In LN_2, a similar correlation has been suggested during free particle discharges [82]. However, with a point-to-plane configuration, this relationship is not accurate as illustrated in Figure 4.19 and Figure 4.20. Large variations in the plot of the UHF peak-to-peak voltage against the corresponding charge were observed during the positive half cycle when the needle was negative to the plane electrode. For positive discharges, although a correlation can be seen, the scatter in the recorded data is too high to draw any useful conclusion. The observed variations can be explained by multiple reflections at the cryostat walls due to the fact that a peak of a UHF waveform can be the result of interference between various reflected components as discussed in Section 4.2.

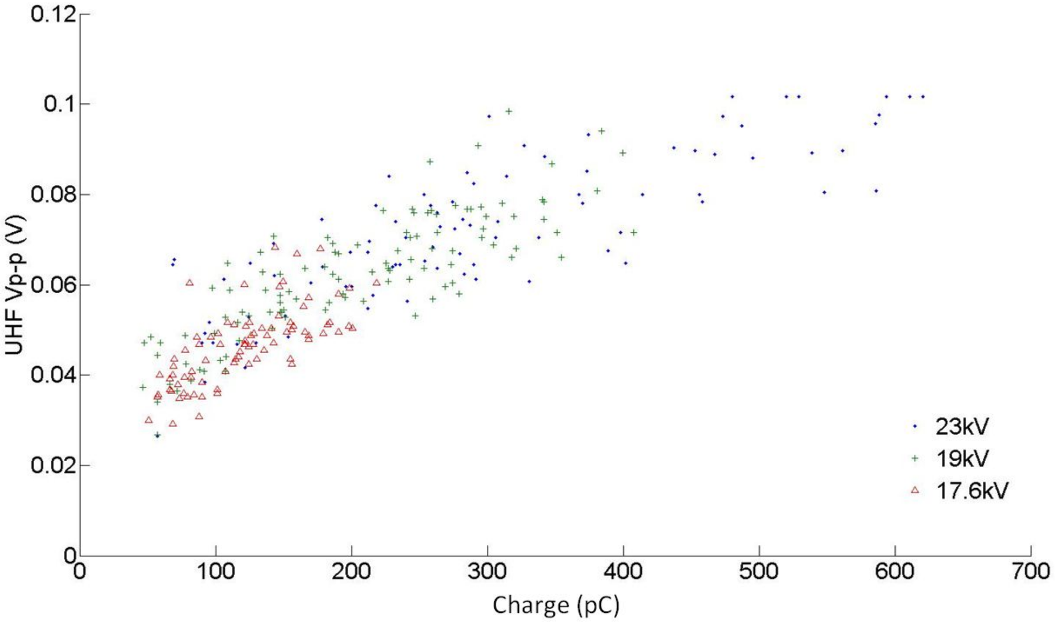

FIGURE 4.19: UHF peak-to-peak values plotted against apparent charge during positive discharges cycle at 17.6 kV, 19 kV and 23 kV.

Figure 4.21 and Figure 4.22 present the relationship between the energy received by

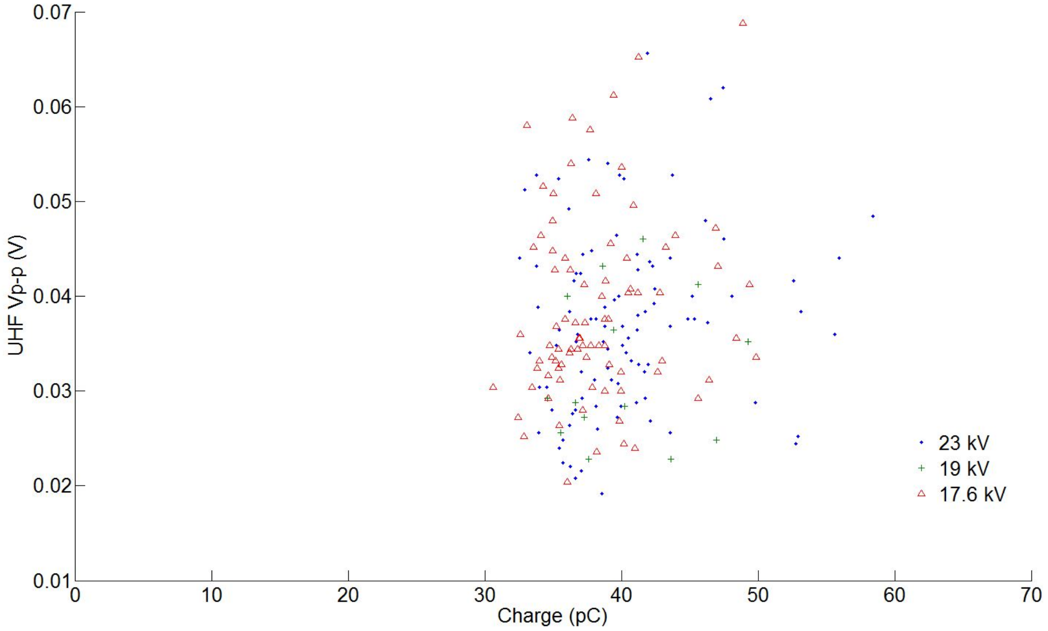

FIGURE 4.20: UHF peak-to-peak values plotted against apparent charge during negative discharges cycle at 17.6 kV, 19 kV and 23 kV.

the sensor and apparent charge from the IEC standard measurements for positive and negative pre-breakdown discharges respectively. It can be seen that UHF energy has a positive correlation with the corresponding charge during both half cycles. During positive discharges, a correlation can be observed however it is difficult to define the nature of this relationship due to the variations of the results (Figure 4.21). On the other hand, data for negative streamers in Figure 4.22 shows even more variation especially when the applied voltage increases to 23 kV. Similar observations have been proposed for transformer oil [70]. The UHF energy received during positive streamers is only a few times higher than during negative streamers in LN_2 while in oil this ratio is more than 300 times. The reduction in consistency of the wideband and narrow band measurements (Figure 4.22) can be explained as a consequence of the pulse burst sequence during negative discharges. Meanwhile, only a single event was observed for positive discharges. More pulses during a sequence would imply additional variations in pulse waveforms, which further reduces the consistency in the energy and apparent charge relationship.

Data for the peak-to-peak amplitudes of RFCT waveforms relative to apparent charge following IEC 60270 standard at 17.6 kV, 19 kV and 23 kV are shown in Figure 4.23. For PD pulses with magnitude below 330 pC, the peaks of RFCT waveform are proportional to the apparent charge, q. However, when the PD magnitude determined using the conventional method exceeds 400 pC, the recorded data becomes more variable and diverts away from the linear relationship. Similarly, in Figure 4.21, more variations are also introduced when the apparent charge increases over 330 pC. The results during negative discharges are not considered, since the noise level of the RFCT is too high to be able to detect lower magnitude pulses.

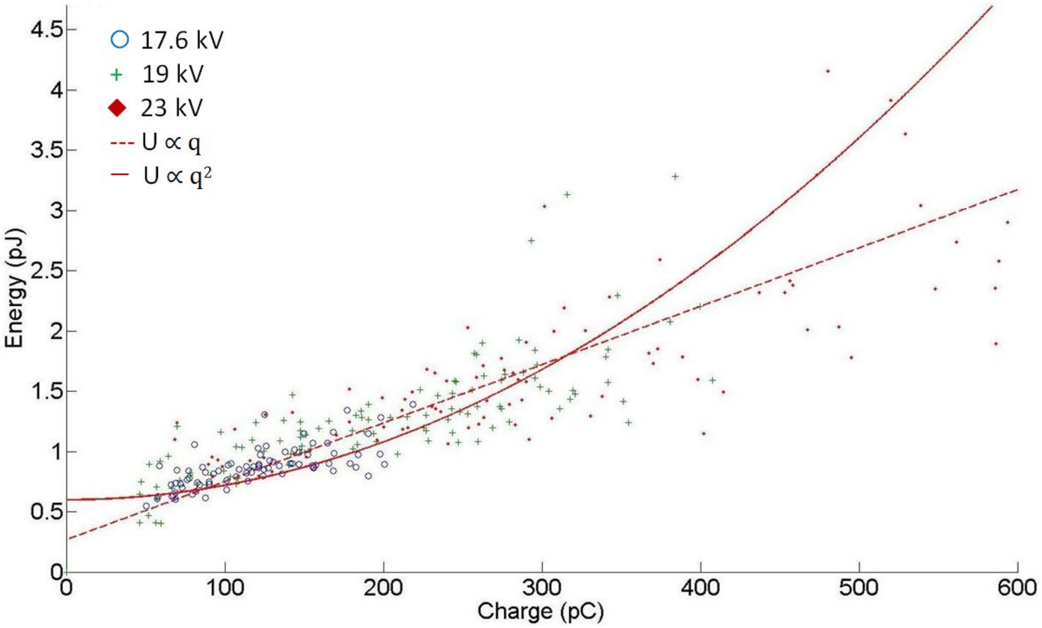

Figure 4.21: UHF energy plotted against apparent charge during positive discharges cycle at 17.6 kV, 19 kV and 23 kV.

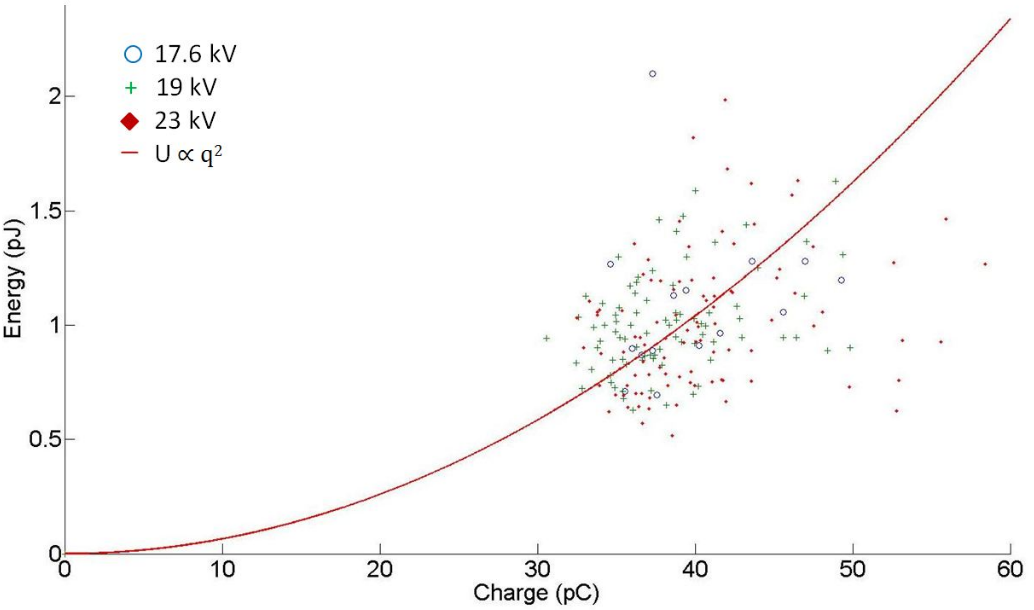

Figure 4.22: UHF energy plotted against apparent charge during negative discharges at 17.6 kV, 19 kV and 23 kV.

Pompili [78] suggests an indirect method to calibrate wideband PD measurement. The IEC apparent charge provides an integration of the series of pulses recorded by wideband measurements such as the UHF sensor. Assuming that the shape and duration of a discrete pulse remain unchanged during this period, the charge of each pulse then should be proportional to its peak value. Therefore, an indirect calibration can be achieved by solving a set simultaneous equations with the number of unknowns equal to numbers of discrete pulses during the event. Applying this method for Figure 4.11 and Figure 4.12,

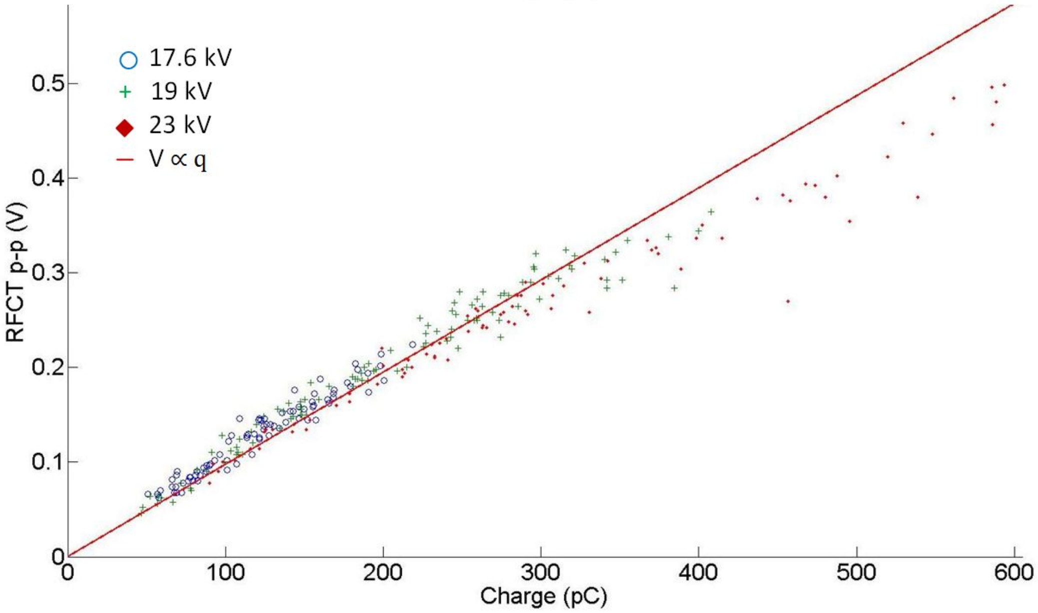

FIGURE 4.23: RFCT peak-to-peak values plotted against apparent charge during positive discharges at 17.6kV, 19kV and 23kV.

the results are shown in Figure 4.24 and Figure 4.25 respectively.

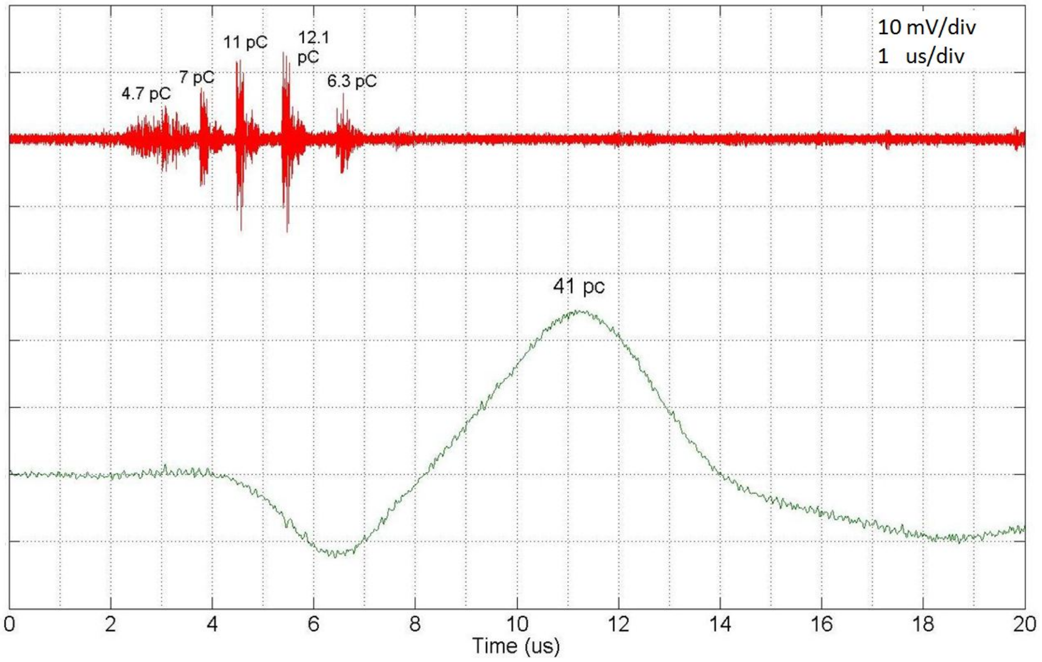

FIGURE 4.24: Indirect calibration of UHF pulse sequence, gap distance 20 mm, at 17 kV, LN_2 at atmospheric pressure, 77.8±0.3 K

The calibration method proposed here can be applied for any pulse series as long as the IEC standard and UHF measurements are taken simultaneously. The parameter of interest here is the ratio of UHF signal and the equivalent charge, V_p/q. From the computation mechanism, the ratio between the peak value of each individual pulse and its corresponding apparent charge level should be the same for all of the discrete pulses

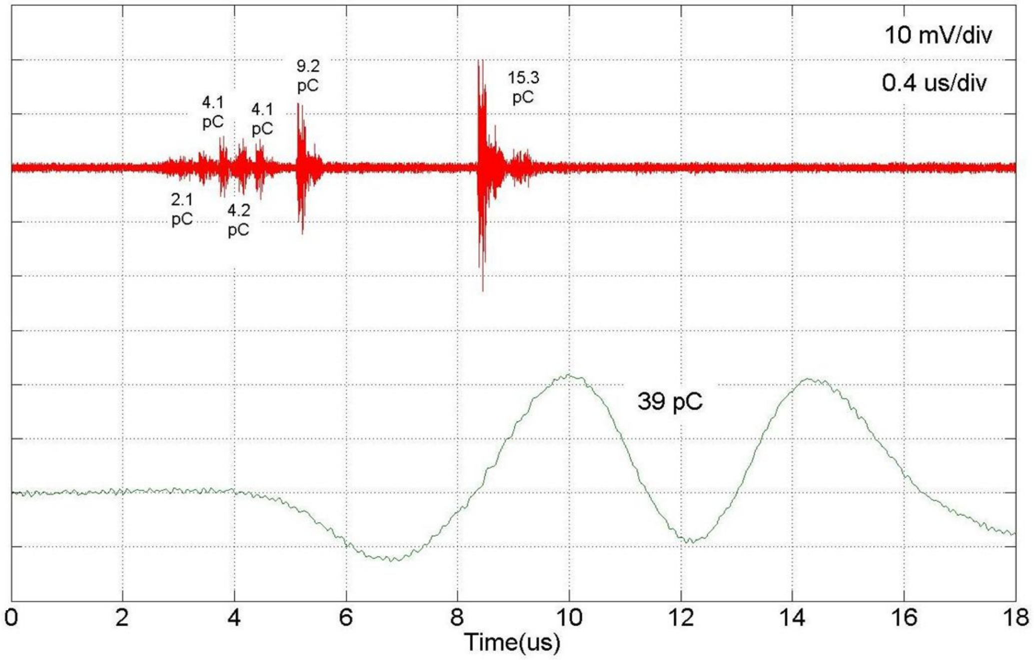

FIGURE 4.25: Indirect calibration of UHF pulse sequence, gap distance 20 mm, at 17 kV, LN_2 at atmospheric pressure, 77.8±0.3 K

in in a pulse burst sequence. The next question is the consistency of the values of V_p/q between each streamer discharge event. In the two examples presented here, for the case of Figure 4.24, the value of V_p/q is equal to 1.09 (mV/pC) and Figure 4.25, $V_p/q = 2.6$ (mV/pC). The ratio changes more than two times. However, this observation is not surprising since IEC measurement in Figure 4.25 suffers from the overlapping phenomenon and therefore the measured apparent charge is inaccurate. In fact, it should be less than the amount of charge transferred at the terminals during this PD event. This observation can explain a much higher ratio of V_p/q compared with that in Figure 4.24. Disregarding the scenarios in which time resolution error occurs, the values V_p/q calculated for each voltage level are presented in Table 4.1.

Applied Voltage	V_p/q_{min}	V_p/q_{max}	V_p/q_{ave}
17 kV	1.2 mV/pC	1.7 mV/pC	1.4 mV/pC
19 kV	0.9 mV/pC	1.4 mV/pC	1.2 mV/pC
23 kV	1.0 mV/pC	1.5 mV/pC	1.1 mV/pC

TABLE 4.1: Minimum, maximum and average values of V_p/q at 17 kV, 19 kV and 23 kV.

On average the ratio of UHF signals and IEC standard measurements decreases with the increase of the applied voltages. Variations in the values of V_p/q reduce significantly compared with the results in Figure 4.24 and Figure 4.25, e.g. when overlapping error occurs. By considering the apparent charge as a summary of the charge involved in each individual pulse, the method has taken into account the number of pulses within a sequence and therefore provide much better result than that shown in Figure 4.20 in which only the maximum of a pulse burst event is used. However, due to the changes of the current waveforms, the calibration approach still has an error within ± 33 % of the average value for each voltage level. If the data for the three voltages are combined, the value of V_p/q for negative discharges in LN_2 is estimated at 1.23 ± 40 % mV/pC.

4.4 Summary

This Chapter discusses the application of wideband measurement PD monitoring for LN_2. The UHF sensor provides a low cost, easy to apply, wideband PD detection method for condition monitoring of HTS power equipment. An experiment has been designed to measure pre-breakdown discharge currents in LN_2 under AC voltages using wideband, UHF and RFCT, sensors and the conventional IEC 60270 standard.

The results from this study provide support for the application of UHF sensors in PD monitoring of HTS power apparatus. Current pulses during streamer discharges with short rise time excite signals in the UHF domain which can be captured by the sensor mounted on a dielectric window. Signal to noise ratio under this condition is likely to be very good since the metal walls of the HTS device will act as a Faraday cage reducing any external noise. The details in the time domain detected by the UHF sensor were not seen by conventional detection due to its limited bandwidth. Instead, a damped integrated signal was observed using the conventional method. An RFCT sensor could be used for wideband PD measurement. However, in this particular study, noise from RFCT measurement was found to be significantly high. Consequently, poor sensitivity was observed, which reduced the effectiveness of this approach for PD detection especially during negative discharges.

In the case of free metallic particle discharges, previous work suggests that the amplitude of UHF sensor signal showed a linear relationship to apparent charge [83]. However, this relationship does not hold for a point-to-plane configuration. Experimental results have shown that neither peak-to-peak nor total energy of UHF data has a consistent relationship with IEC standard measurements. Correlation during anode streamers shows a more defined trend compared to cathode streamers due to larger variations of UHF waveforms. This observation has been reported for mineral oil under a similar experimental configuration [70]. The behaviour can be explained as a consequence of the pulse burst sequence which was observed only during negative discharges. More pulses during a sequence would imply additional variation in pulse shapes, which further reduces the consistency in any proposed energy and apparent charge relationship.

Since a narrowband measurement gives an integration of a pulse sequence, the apparent charge correlated to each individual pulse can be estimated providing that PD measurements using wideband method and IEC standard were carried out simultaneously. This computational method takes into account the total number of pulses involved in a discharge event and therefore has shown to be more effective for calibration of negative discharges. However, even with such a method, variations in the ratio between UHF signals and apparent charge still exist due to the inconsistency of the current pulses. Therefore, the assumption of constant current waveform during the prebreakdown period is incorrect. The conclusion can be drawn here is that as a detection method, the UHF sensor has proven to be effective during this investigation. As a measurement method, many difficulties in quantifying the UHF signals occur due to the variations of the current waveforms between different streamer events.

Chapter 5

Behaviour of Partial Discharge Streamers in Liquid Nitrogen under AC Applied Voltages

5.1 Introduction

HTS power apparatus generally uses liquid nitrogen as the coolant as well as part of the insulation system [7] [11]. Partial discharges in LN_2 are accompanied by density change streamers which are the precursor of electrical breakdown of the liquid. With the aim of characterising PD streamers in LN_2 under AC voltages, pre-breakdown phenomena has been studied by the means of high frequency PD measurements and phase-correlated high-speed imaging utilising the cryostat and the experimental configuration described in Chapter 3.

The appearance of phase-change channels has been observed by many researchers in various dielectric liquids [16] [75] [76] [84] [86]. The evidence is often presented in the form of shadow images which indicate the change in phase due to different colours between the channels and surrounding liquid. Current pulses have also been observed during initiation and propagation phases of streamers in liquid dielectrics [87] [88]. Discharges during pre-breakdown create local heating which results in the vaporisation of the liquid. Light emission has also been observed during streamer development [58] [89] which indicates excitation and decitation of charge carriers.

The study of PD pulses by various measurement techniques (Chapter 4) has shown that discharge events during negative streamers appear in the form of pulse burst sequence while during positive polarity, the pulse burst phenomenon was not observed. This is the result of difference propagation modes and mechanisms between the two polarities. With the help of a technique that allows correlating streamer images and PD signals, streamer propagation can be characterised by its shape as well as by corresponding discharge waveforms. The recorded shadow graphs have shown that phase change streamers can propagate with two main shapes, bush-like and filamentary. Both of these types were observed during positive and negative half cycles. The predominance of each mode is very much dependent primarily on the applied voltage as well as the polarity of the needle. From the observed results, mechanisms behind the pre-breakdown phenomena for each polarity and streamer propagation mode in LN_2 are proposed and discussed.

Although a considerable amount of research has been published on the subject of streamer initiation and propagation in dielectric liquids, the study of PD patterns in LN_2 during AC cycles is much less focused. In a HTS device, composite insulation systems including LN_2 and solid insulation impregnated within the liquid are commonly used. For the purpose of characterizing PD behaviour in a solid/liquid point-plane system, a comprehensive investigation was undertaken with different cryogenic solid dielectrics, applied voltages and gap distances. ϕ-q-n plots have been used to analyse PD patterns since it provides information of discharges over multiple cycles. The plot consists of the phase position, ϕ, the apparent charge magnitude, q, and the accumulation number, n, of the PD pulses measured to IEC60720. The discharge pattern is studied for different applied voltages, gap distances and solid barrier materials.

5.2 Pre-breakdown streamer inception voltage

Depending on the experimental arrangement, a PD measurement will have a certain noise level. Partial discharge inception voltage (PDIV) in this research is defined as the lowest voltage level at which a sudden change in PD activity was observed [90]. Streamer inception voltages (SIV) on the other hand are the lowest voltage level at which a streamer is detected by the optical devices, e.g. a high speed camera. In dielectric liquids, the two terms PDIV and SIV are closely related [91]. This is because at a critical voltage level, electron tunnelling from the needle becomes more effective. The excessive electrons then transfer their energy into the liquid and create a low density region or bubble. Therefore, a dramatic increase in numbers of detected PD signals is often accompanied with density change streamers. In the case of toluene, ditolyl ether and perfluoropolyether oils [91], the values of PDIV and SIV although very close to each other have different values.

Under the experiment conditions described in Chapter 3, discharges of magnitude as low as 15 pC can be measured. However, in order to ensure that the measured results are PD in LN_2, a threshold level was set at 30 pC. Therefore, the term dramatic change used in PDIV definition means the occurrence of PD pulse of which the apparent charge value is above the noise level of 30 pC. Detection of a streamer via the shadow graph method, on the other hand, is restricted by the resolution and shutter closing rate of the camera.

With a magnifying lens focusing at the needle tip, the sensitivity of the photograph technique is around 1 μm per pixel. This means streamers which are smaller than the resolution of the imaging system cannot be detected. Although the highest frame rate of the available camera is 100,000 fps, the shutter speed for SIV measurement was chosen at 50,000 fps due to the inverse proportionality between the imaging speed and quality. The frame rate in this research is very much lower than that used in [91], up to 20,000,000 fps, for SIV measurement. However, this concern is not important due to the fact that the camera is synchronised with the PD measurement device. The shutter is open as soon as a PD pulse is detected. The delay which is caused by the time for the triggering signal to travel from one device to another can be neglected. Therefore, although a relatively lower frame rate is used in this work, the triggering mechanism ensures that density change streamers which are the result of PD events are captured.

Throughout the study, any PD pulses above a set threshold of 30 pC were observed with streamers formed at the tip of the needle. This observation confirms the same values of PDIV and SIV. Previous published work by Takahashi [67] suggests a similar phenomenon in which PD in LN_2 under AC voltages were also recorded with bubbles appearing out of the needle tip. It is hypothesized that since experiments were carried out at LN_2 boiling temperature, the liquid is very susceptible to phase change due to local heat dissipation by electron collisions. These values of PDIV and SIV were found to be equal in LN_2 under applied AC voltages.

The occurrence of streamers or PD in liquids under AC voltages is intermittent, especially at low voltages. Although PDIV has been defined as the lowest voltage at which PD events appear, this does not mean that pre-breakdown phenomena occur for each 20-ms AC cycle. The intermittent occurrence of discharge streamers is a common phenomenon in dielectric liquids [90]. Many factors can contribute towards this randomness such as the required conditions for discharge in the vapour cavities and the influence of space charge on the local electric field. A quantitative model has yet to be been found to represent this phenomenon. PD and streamer appearance was monitored during a period of 3 minutes which is equivalent to 6000 cycles before increasing the applied voltages. The PDIV values then were determined by whether or not PD occurred during the 3 minute period.

As mentioned in Chapter 2, pre-breakdown phenomena in a liquid appears when the electric field reaches a high enough value to allow field emission, for the cathode, or field ionisation, for the anode. The maximum stress at the needle tip can be estimated as a function of tip radius, applied voltage, and gap distance:

$$E_{max} = \frac{2U}{r_p ln(\frac{4d}{r_p})} \tag{5.1}$$

where U is the applied voltage, r_p is the tip radius, and d is the gap distance between the two electrodes which is the liquid gap spacing plus the thickness of the insulation barrier. Rearranging Equation 5.1 gives:

$$U = \frac{1}{2} E_{max} r_p ln(\frac{4d}{r_p}) \tag{5.2}$$

Streamers in a liquid occur when the maximum electric field at the needle tip reaches a certain threshold, E_s, which will allow electrons tunnelling into the liquid and initiating discharges. Therefore, the values of PDIV can be estimated as the gap distance increases, by keeping r_p and E_s unchanged. A factor of $\sqrt{2}$ was introduced, since the measured values are recorded as rms voltages:

$$PDIV = \frac{1}{2\sqrt{2}} E_s r_p ln(\frac{4d}{r_p}) \tag{5.3}$$

PD inception voltages when gap distances vary from 4 mm to 23 mm are shown in the Figure 5.1. The voltage required for streamer initiation increases as the distance between two electrodes changes from 4.2 mm to 23 mm. A similar trend was also presented in [67]. The estimated values of PDIV were calculated from equation (5.3) with Es=1.55 MVmm^{-1}.

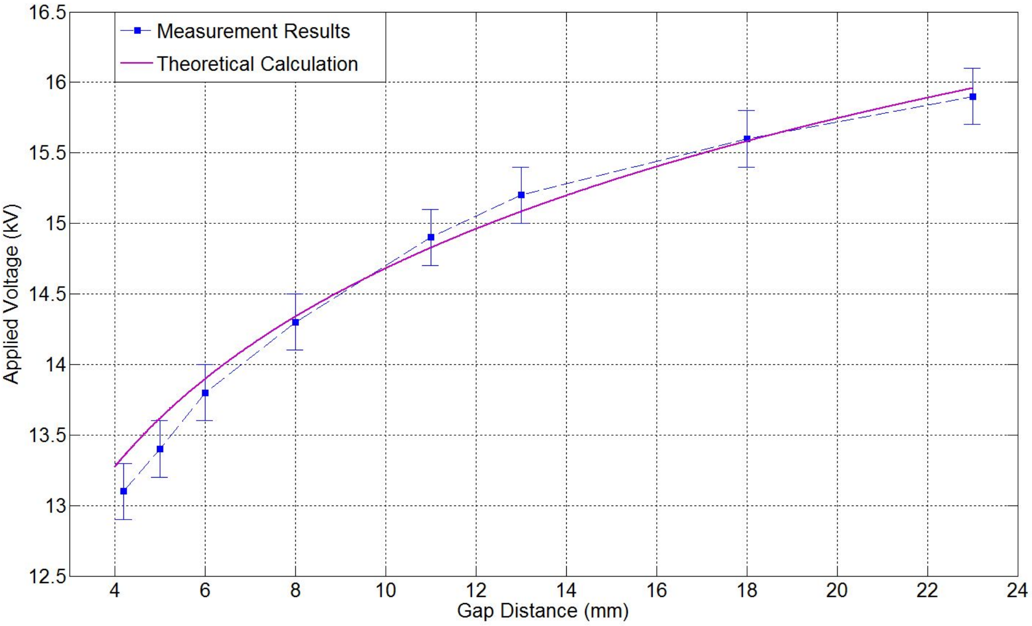

FIGURE 5.1: PD inception voltage, tip radius 2.5 μm, LN$_2$ at atmospheric pressure, 77±1 K.

Calculation of electric field using equation (5.2) does not consider the effects of the difference in permittivity between the solid dielectric barriers and liquid nitrogen. Plots shown in Figure 5.2 detail the fields seen at the maximum and minimum separations between the needle tip and plane electrode used in this experiment. Note that in both cases the electric field is greater than the value of E_s (1.55 MVmm^{-1}) which is sufficiently high enough for streamer initiation. The difference in the fields caused by a higher permittivity of the solid barrier board compared with LN2 reduces when the electrode separation distance increases. This would explain the variation in experimental and theoretical results shown in Figure 5.1 in close gaps. Another factor contributing towards this deviation is believed to be the variation in the geometry of the needle tip. Nevertheless, the results obtained in Figure 5.1 support the argument of a threshold electric field, E_s. When the electric field at the tip exceeds this value, avalanches appear due to field emission and electron multiplications which result in partial discharges and bubbles. The value of E_s was found to be of the order of 1.55 MVmm^{-1} which is similar to previously published work [58] in which the threshold field for negative and positive streamer initiation was reported at 1.4 and 2.0 MVmm^{-1} respectively. Whereas the threshold field for electrically induced bubbles in LN2 was found slightly lower, of the order of 1.1 MVmm^{-1} [46].

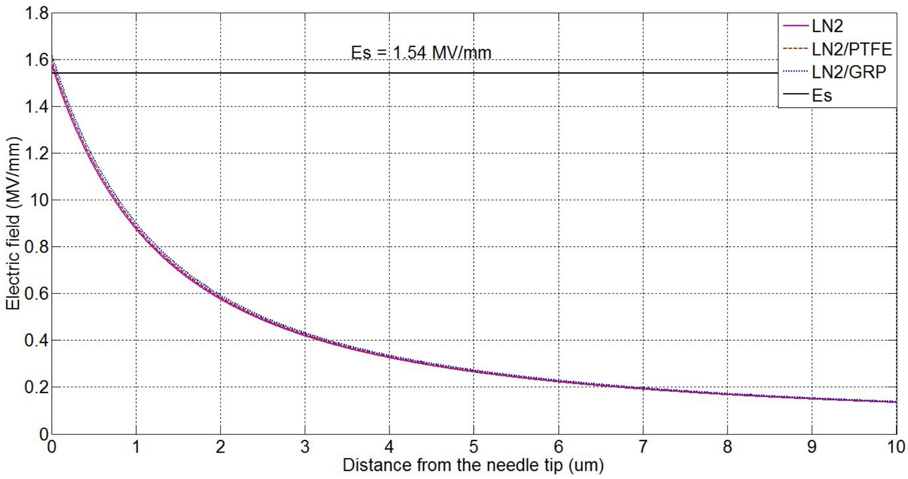

(a) 23 mm gap distance

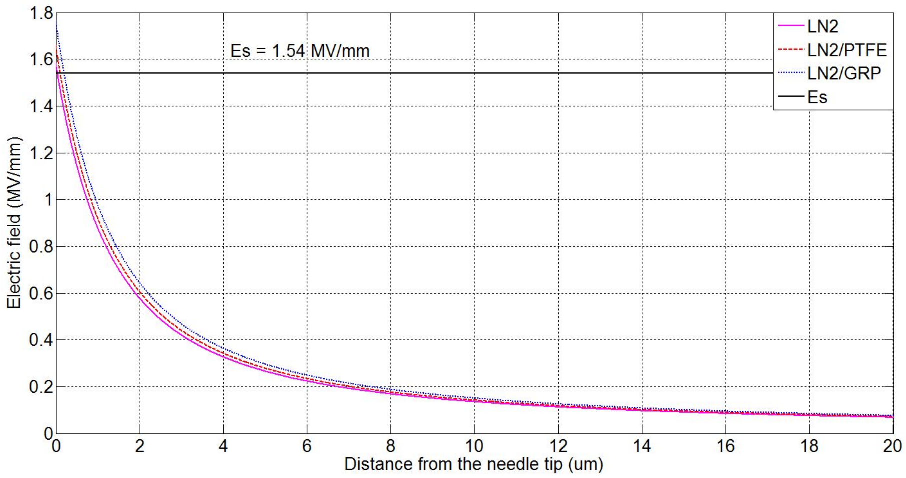

(b) 4 mm gap distance

FIGURE 5.2: Electric field at a distance from the needle tip with and without solid dielectric barrier for maximum (a) and minimum (b) electrode separation.

5.3 Initiation and propagation of cathode streamers

Figure 5.3 shows PD signals measured by the conventional method and the UHF sensor during a positive half cycle when the needle is negative to the plane electrode. Measurements were taken at the inception voltage of 13.7 kV. Both conventional and UHF measurements show PD in LN_2 at inception voltage has similar characteristics to corona discharges in air. Each discharge occurs after a similar time interval as well as having almost the same apparent charge.

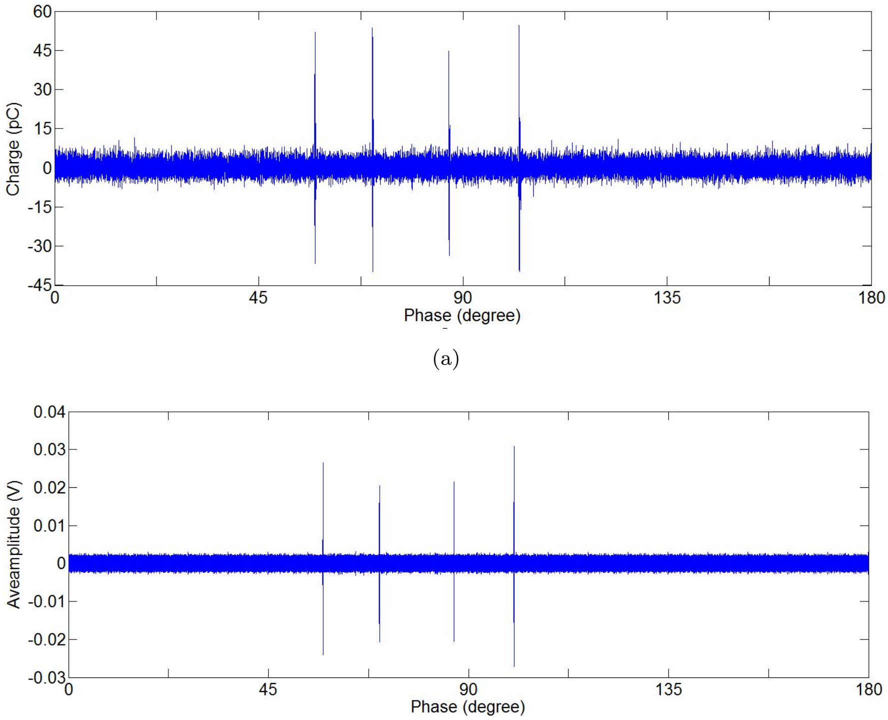

(a)

(b)

FIGURE 5.3: PD from a cathode point measured by (a)IEC 60270 standard (b) the UHF sensor. At 13.7 kV, 77.8±0.3 K, atmospheric pressure, liquid gap distance 3 mm.

Since many similarities can be found between negative corona in LN_2 and in gas, the same mechanism may be proposed to explain the behaviour of PD during a cathode point discharge. Initially, discharges happen when the electric field is high enough to create avalanches. The electrons produced from the discharge move under the influence of the applied fields. A space charge then is formed in front of the needle which reduces the local electric field and stops further discharges from happening. The extinction of discharge means that additional charges cannot be generated while the existing ones move away towards the other electrode. This results in the recovery of the electric field in front of the needle tip until it reaches a point when a new discharge can be initiated. The result is a regular occurrence of PD pulses as shown in Figure 5.3. The corona pulse regime has also been observed in liquid argon [92], liquid xenon [93], and other hydrocarbon liquids [50][62].

The corona-like discharge pattern is typical for discharges from a negative needle across the studied gap distances. The subject of corona discharges in dielectric liquids has been previously discussed under AC, DC voltages [67] and with different tip radius [94]. In LN_2, gaseous filaments created due to corona pulses only exist close to the needle tip and result in bubbles which moved away from the high electric field region.

Above the inception voltage, partial discharges from the cathode point also appear in the form of multiple pulses; however, the discharges appear in a more erratic manner. As can be seen in Figure 5.4, the magnitude of each discharge pulse and the time between two consecutive events show more variation than that recorded at an applied voltage just above the inception voltage (Figure 5.3). Under higher applied voltages, the liquid experiences more intense external electric fields. Therefore, more charge carriers can be generated together with an increase in the number of streamer branches. In addition, different modes of streamer propagation in LN_2 at well above PDIV has been reported in [65] [89]. Streamers propagating with filamentary shapes tend to have higher PD magnitude than bush-like ones. The increase of the applied voltage, therefore, creates more variations in the space charge profile between streamer events. As a result, the time required for the electric field at the needle tip to recover is very much different from one streamer event to another. This might explain the randomness in the PD pattern recorded during the positive half cycle of the applied voltage.

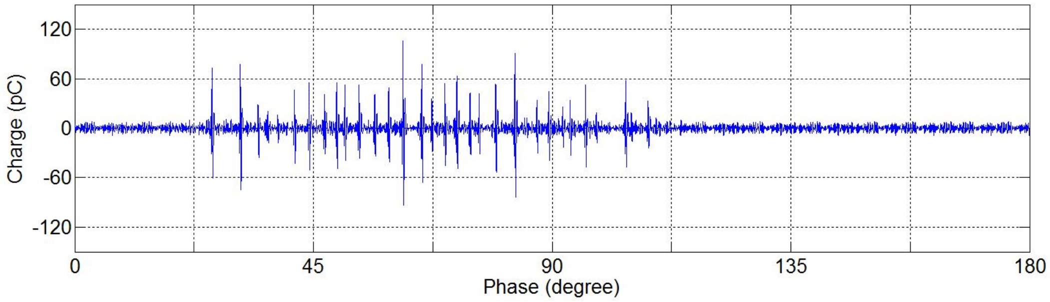

(a)

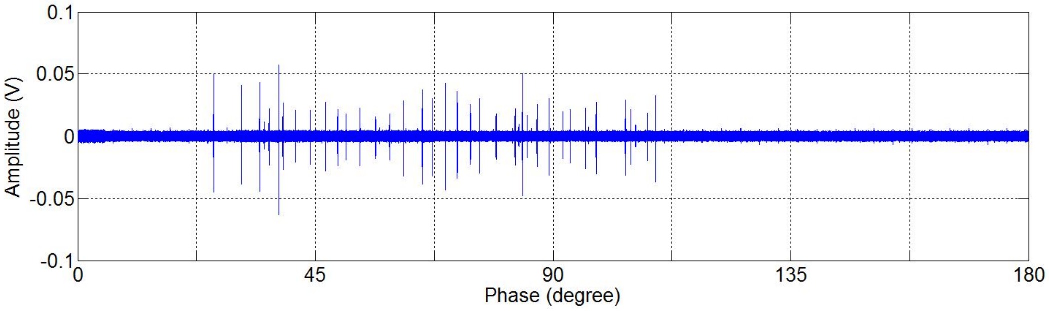

(b)

FIGURE 5.4: PD discharges from a cathode point measured by (a)IEC 60270 standard (b) the UHF sensor. At 22 kV, 77.8±0.3 K, atmospheric pressure, liquid gap distance 3 mm.

5.3.1 Negative bush-like streamers

PD activity during negative bush-like streamers appears in a pulse burst sequence as illustrated in Figure 5.5(b). While the narrowband measurement only shows a single pulse, the results from the UHF sensor contain multiple discrete pulses that increase in magnitude over 2 μs and then decrease. In liquid dielectrics, when the electric field at the needle tip exceeds a certain threshold, electrons can be effectively injected into the material from the needle electrode. Once entering the liquid, due to the extreme electric field, electron avalanches can occur and result in generation of initial cavities. Once the bubbles have been formed, providing that seed electrons are available and the electric field across the bubble is sufficient, breakdown of gaseous cavities will happen [16] [95] [96]. The low magnitude pulses at the start of the sequence can be thought of as the result of the initial discharge in the liquid phase. After that, the following pulses are responding to the activity in the gas phase. Due to the growth of the channels, more charges can be generated each time the bubble breaks down which results in the ascending magnitude of the pulse sequence. As the channels grow, a higher voltage is required to create breakdown. In addition, space charge accumulating in front of streamer head further reduces the voltage across the streamer channels [97]. When the electric field across a gaseous channel is not sufficient to create breakdown, a streamer cannot continue to propagate. The last events of the sequence observed during negative slow streamers often appear to have lower magnitudes than previous pulses. This phenomenon can be explained either by partial breakdown of the long gaseous channels or the fluctuation in the growth of the streamer which results in its continuation to create discharges before its collapse [98], as shown in Figure 5.5(c).

The corresponding streamer images of this particular PD event are shown in Figure 5.5(c). This sequence of images were taken at 5000 fps which means each frame was 200 μs apart from each other. In this case, as well as other results presented in this chapter, PD pulses (Figure 5.5(a)) occurs between the first and second frame of the image sequence (Figure 5.5(c)). Due to the limitation in the camera speed, the growth of streamer cannot be observed. Instead, only the final structure of the streamer can be recorded. The existence of phase change during PD from a high voltage cathode needle is evident by the darker area at the tip of the needle. The last picture of this sequence shows that if no further discharge occurs, the gaseous channels cannot sustain and breakdown into clouds of bubbles which propagate toward the other electrode. There are two factors contributing towards the movement of bubbles. The first is buoyancy force causing bubbles to rise up. The second force acting on the bubbles is dielectrophoretic force which act to move the bubbles towards the less intensive field region, e.g the planar electrode [99].

During the positive half cycle when the needle polarity is negative, each PD event is followed by the generation of a density-change streamer. Close to the inception voltage,

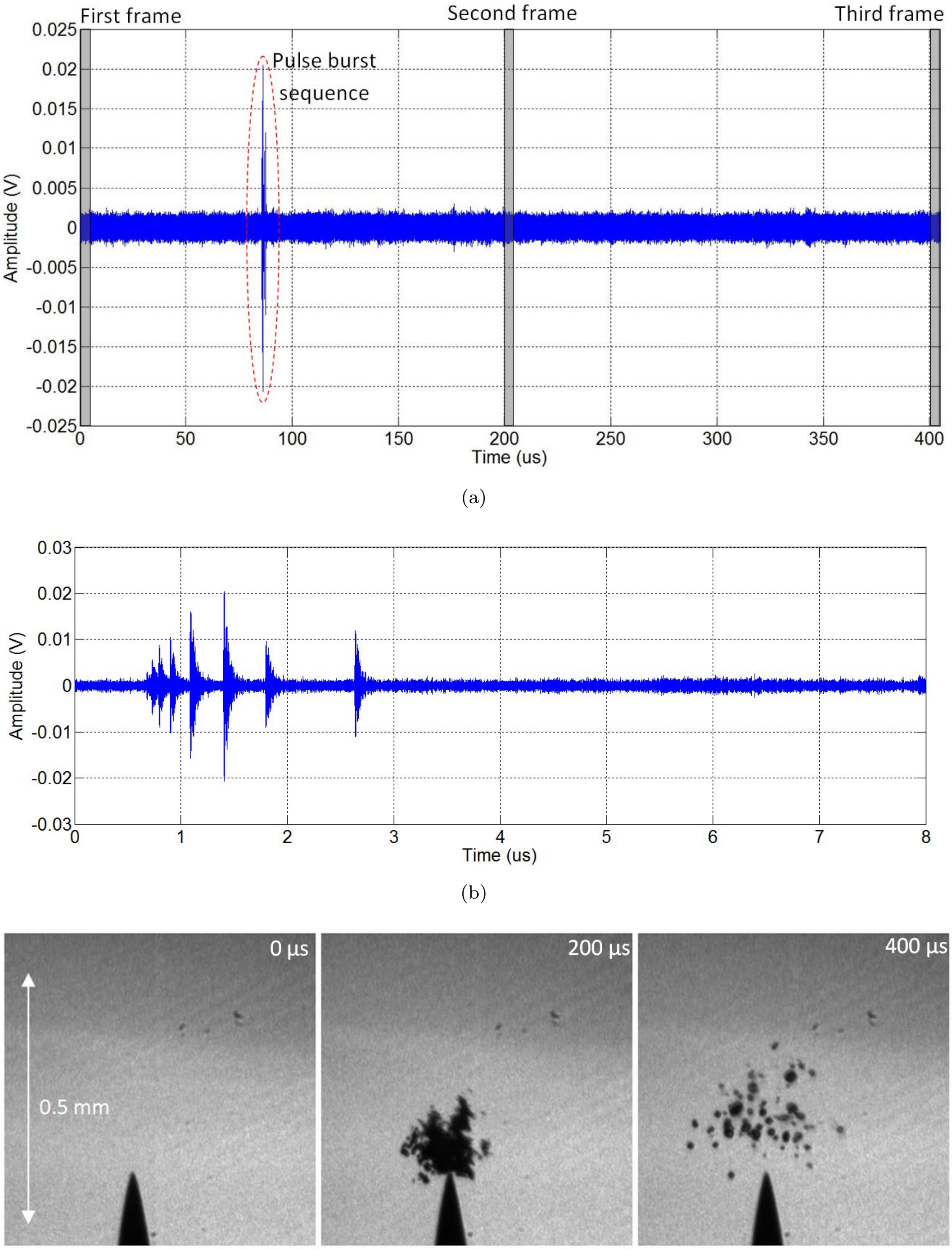

(a)

(b)

(c) 52 pC

Figure 5.5: An example of cathode bush-like streamer in LN_2 (a) the first event in Figure 5.3 observed by the UHF sensor, (b) details of the pulse burst sequence (c) the corresponding images taken at 5000 frame per second. At 13.7 kV, 77.8±0.3 K, atmospheric pressure, liquid gap distance 3 mm.

only the bush-like propagation mode was observed. Figure 5.6 illustrates the last PD pulse train in a four-event sequence recorded during a 10-ms half cycle (shown in Figure 5.3). UHF waveforms show a pulse train sequence indicating the growth of streamer channels. Phase change is also evident by the recorded images. The main difference to the streamer in Figure 5.5 is that the gaseous bubbles exist in the liquid before the discharge process starts. These bubbles are the result of the previous streamer. However, it is very unlikely that these vapour cavities would affect the observed results. The first reason is that the characteristics of discharge pulses and shadow graphs are very similar to that of the bush-like streamer shown in Figure 5.5, e.g when bubbles are not recorded before streamer formation. Secondly, initiation of a negative bush-like streamer occurs at the needle/liquid interface. The bubbles which are the results of the previous streamer have already moved far away from the needle tip. Lastly, the further away from the needle point, the lower the electric field is. Therefore, close to inception voltage, it is impossible to electrically breakdown these cavities which have moved into the lower field region.

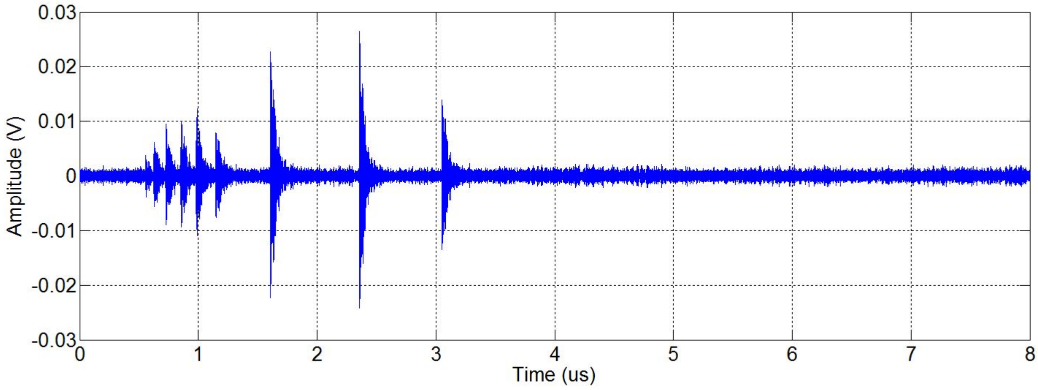

(a)

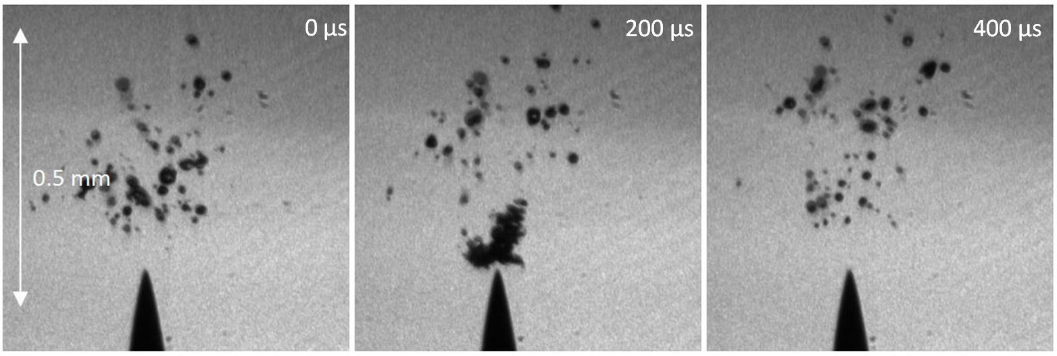

(b) 44 pC

FIGURE 5.6: An example of cathode bush-like streamer in LN_2 (a) PD pulses observed by the UHF sensor, (b) the corresponding images taken at 5000 frame per second. At 13.7 kV, 77.8±0.3 K, atmospheric pressure, liquid gap distance 3 mm.

Bush-like streamers were observed during negative pre-breakdown phenomena for all of the the studied gap distances. Figures 5.6 and 5.7 show examples of negative bush-like streamers captured by the UHF sensor and the high speed camera with liquid spacing gaps of 1.5 mm and 13 mm respectively. Streamer propagation was accompanied by a pulse train sequence indicating the growth of the streamer channels. Similar to the results obtained when the needle was 3 mm away from the barrier, pulse trains were observed with smaller pulses at the start of the sequences. The general trend of the recorded sequences remained unchanged. Phase change was also evident by the correlated shadow graphs showing a darker area with bushy shape in front of the needle tip (Figure 5.9). The discharge characteristics of bush-like streamers observed by the UHF sensor and the high speed camera were consistently found across this study. Therefore, it can be hypothesized that the governing mechanisms for bush-like negative streamers remain unchanged regardless of applied voltage or gap distance.

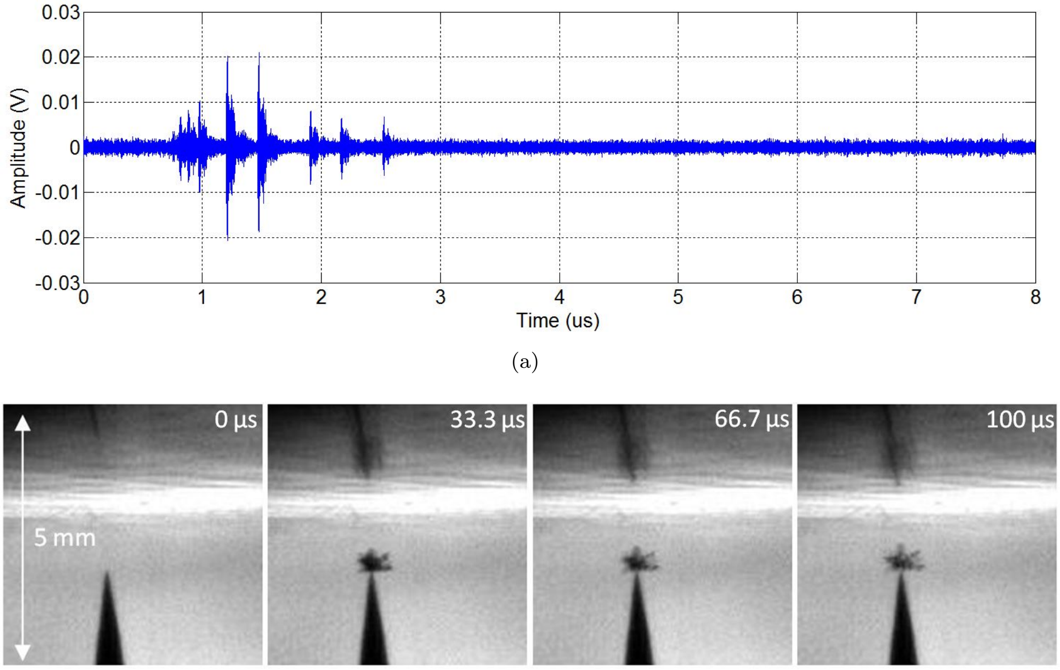

(a)

(b)

FIGURE 5.7: An example of cathode bush-like streamer in LN_2 (a) PD pulses observed by the UHF sensor, (b) the corresponding images taken at 30000 frame per second. At 14 kV, 77.8±0.3 K, atmospheric pressure, liquid gap distance 1.5 mm.

Across the gap distances studied, the propagation length of negative bush-like streamers was found to vary between 200-300 μm. Under the assumption that propagation time of a streamer is equal to the duration of the pulse burst sequence, the velocity of the observed streamers was in the order of 100 m/s. This result is similar to that recorded for LN_2 under a step impulse voltage [64].

The images presented in the above cases were taken with a wide field of view lens. As can be seen the frame size in these scenarios are more than 5 mm while in the previous shadow graphs (Figure 5.5 and Figure 5.6), the dimension of the captured photos were around 0.5 by 0.5 mm^2. With this lens, the camera speed can be increased significantly up to 30000 fps. At this rate, recorded images are 33.3 μs apart in real time from each other. A faster shutter closing rate means that the streamer process can be observed in greater detail. The density change region was found to last for approximately two frames which is equivalent to 66.7 μs (Figure 5.8). Meanwhile, the pulse train sequence

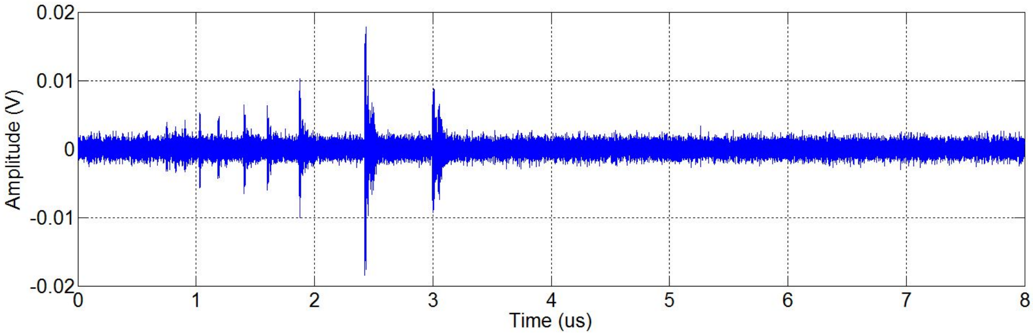

(a)

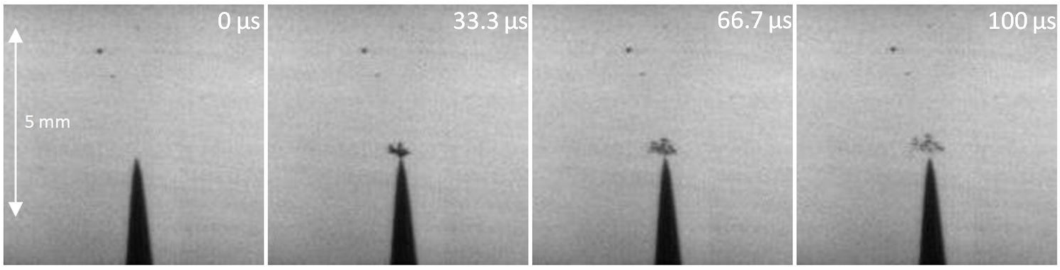

(b) 45 pC

FIGURE 5.8: An example of cathode bush-like streamer in LN_2 (a) PD pulses observed by the UHF sensor, (b) the corresponding images taken at 30000 frame per second. At 14 kV, 77.8±0.3 K, atmospheric pressure, liquid gap distance 13 mm.

normally lasts for 2-4 μs. After the current deceases, the gaseous channels can remain for a few tenths of microseconds before ultimate collapse. The collapse of a channel happens when the vapour pressure falls to or lower than the hydrostatic pressure of the surrounding liquid [78].

Above inception voltage, negative streamers also dominantly propagate with bush-like shapes although the appearance of filamentary shapes increases with the applied voltages. Pulse burst behaviour was observed by the UHF sensor during the streamer events showing a higher number of individual pulses as well as a longer sequence duration. Under a higher external electric field, additional streamer channels can be formed on top of a bush-like base due to the intensive electric field at the channel tips. As can be seen in Figure 5.10(b), two bush-like structures were observed with one on top of the other. The pulse sequence (Figure 5.10(a)) also showed discrete activities with the first part, from 1 to 2.5 μs, having similar characteristics to bush-like streamers at lower voltages while the second part, from 2.5 to 4 μs, appears to be more random. The hypothesis is that the starting component of the sequence corresponds to the bushy base of the streamer and the latter part relates to the additional branches formed on top.

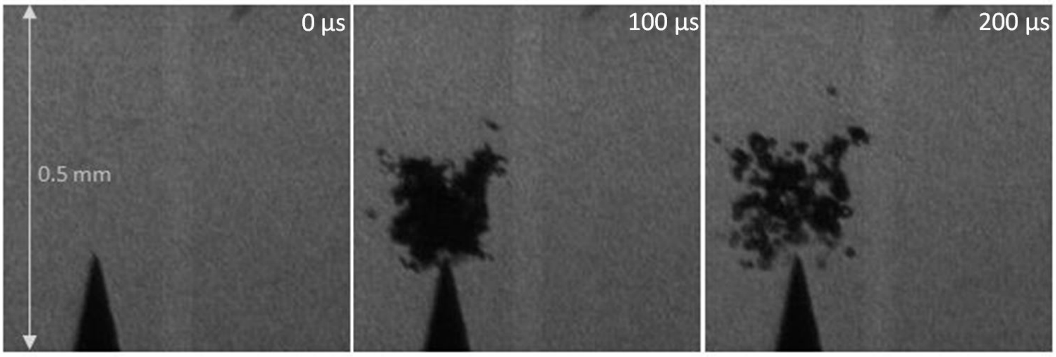

(a) 52 pC

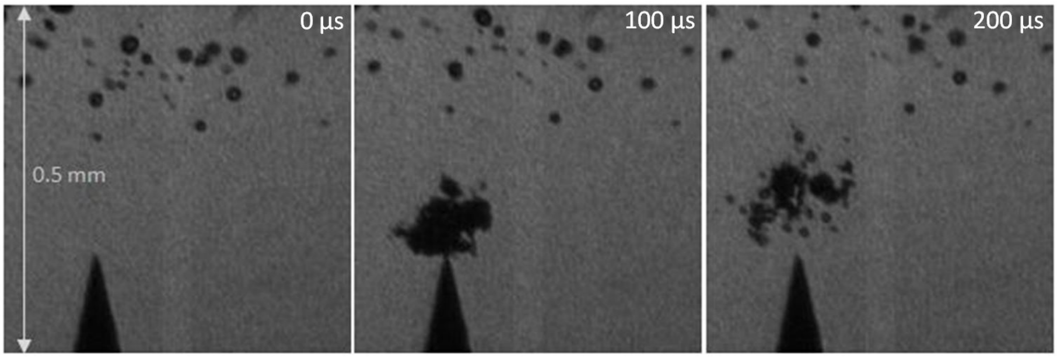

(b) 43 pC

FIGURE 5.9: Examples of cathode bush-like streamer taken at 10000 frame per second. At 16 kV, 77.8±0.3 K, atmospheric pressure, liquid gap distance 15 mm.

5.3.2 Negative filamentary streamers

Although the bush-like propagation mode is dominant during pre-breakdown from a cathode point, at higher applied voltages, filamentary streamers have been observed in LN_2 under step input voltages [89] as well as AC voltages [65]. Figure 5.11(b) illustrates an example of filamentary streamer taken at 5000 fps, 22 kV and 3-mm gap spacing. Streamers propagating with tree-like shapes can be distinguished as they have more defined filaments. The streamer presented here emerges from a bush-like structure close to the needle tip. This particular result shows almost the same structure as negative filamentary streamers under impulse voltage. Due to a very high framing rate of 100 ns, the propagating sequence of the streamer can be observed in detail. The reported streamer was found to have a filament growing out of a bushy structure which was formed initially [64].

Figure 5.11(a) shows a pulse burst sequence measured by the UHF sensor during the propagation of the filamentary streamer. From the discharge sequence, it can be hypothesized that the growth of the density-change channels happened in two phases. During the first phase, from 0.5-2.2 μs, signals from UHF measurement appear to have similar properties to discharges during negative bush-like streamers, such as multiple pulses adjacent to each other. The second phase of the pulse train is a single pulse with

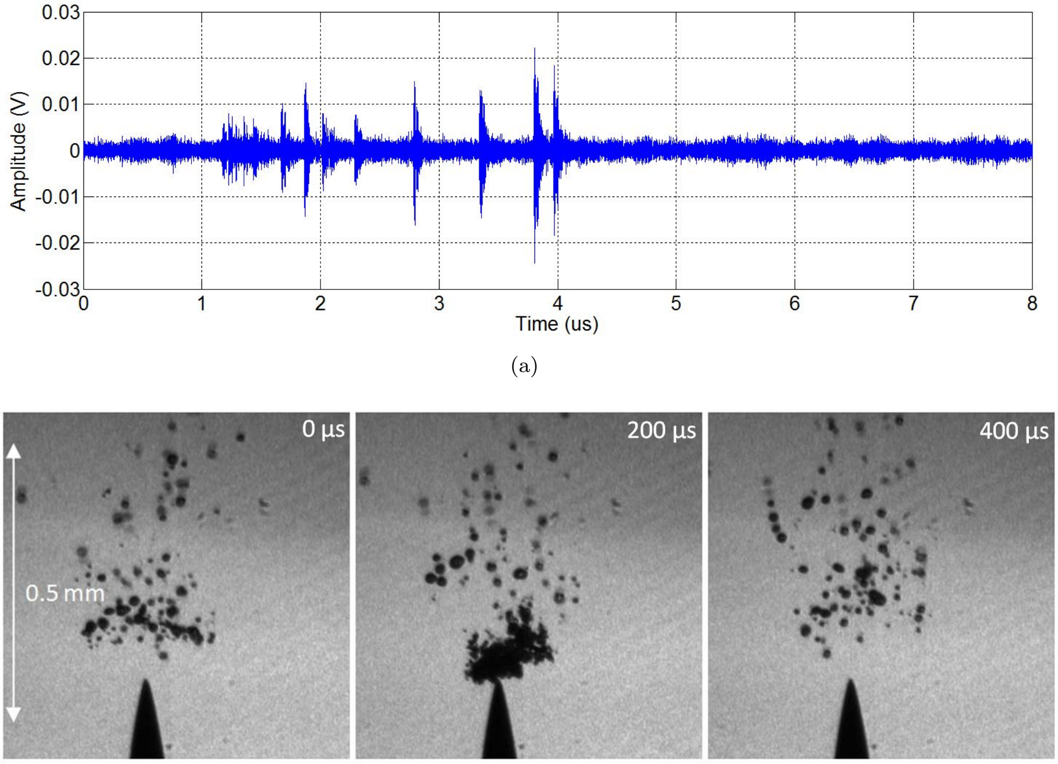

(a)

(b) 44 pC

FIGURE 5.10: An example of cathode bush-like streamer in LN_2 (a) waveforms observed by the UHF sensor, (b) the corresponding images taken at 5000 frame per second. At 22 kV, 77.8±0.3 K, atmospheric pressure, liquid gap distance 3 mm.

higher magnitude than its predecessors. This individual pulse can be related to the single filament propagating toward the other electrode as shown in Figure 5.11(b). The different characteristics between the two parts of the discharge process suggest that an altered propagation mechanism must be governed by the filamentary streamer events. The growth of the single filament corresponds to a single UHF waveform, therefore, cannot be explained using the step-wise development of bush-like streamers. In addition, the need to provide initial cavities is no longer required due to the bushy structure underneath. A more direct mechanism such as molecular ionisation is more likely in this case. The argument then is that in order to ionise liquid a very high electric field is required while the filamentary streamer situated at a distance from the point where the external field had been reduced. However, the local electric field at the tip of the streamer channel where the filament originated could be significantly enhanced due to any space charge developed there.

Filamentary streamers were also observed during experiments at 15-mm gap distance (Figure 5.12(b)). A bush-like structure exists at the needle tip similar to that in Figure 5.11(b), however, the area of this region is smaller than the previous result. The filament in this case also has propagated longer with better defined branches. The pulse trains recorded by the UHF sensor (Figure 5.12(a)) show typical characteristics of nega-

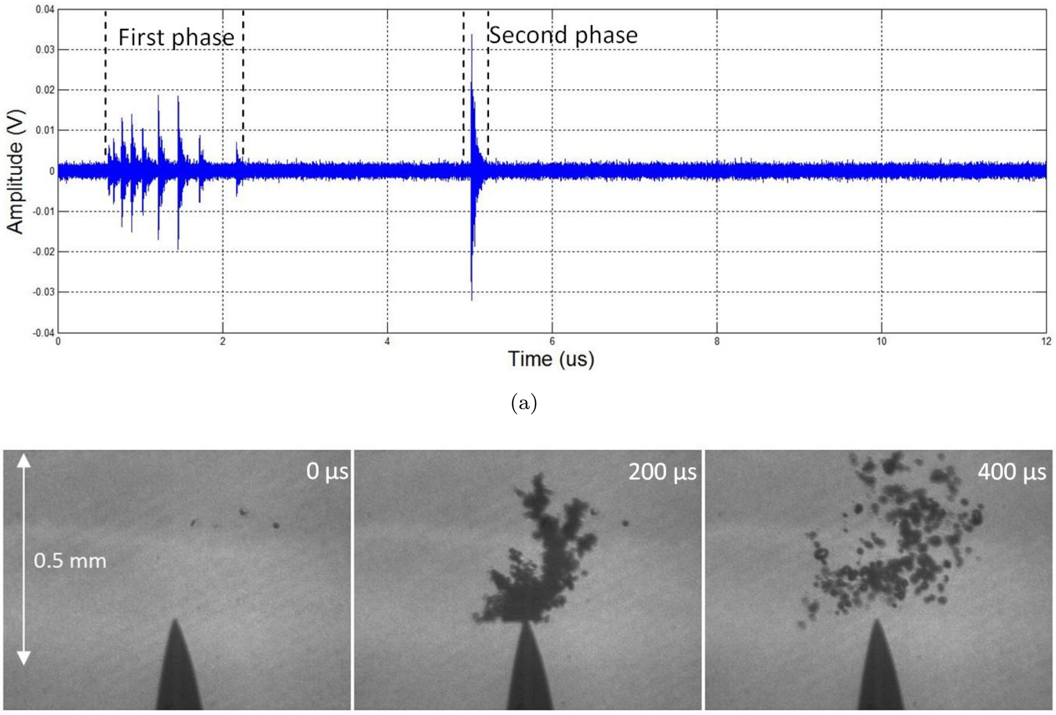

(a)

(b) 110 pC

FIGURE 5.11: An example of cathode filamentary streamer in LN_2 (a) waveforms observed by the UHF sensor, (b) the corresponding images taken at 5000 frame per second. At 22 kV, 77.8±0.3 K, atmospheric pressure, liquid gap distance 3 mm.

tive filamentary streamer with a bush-like discharge at the start of the sequence followed by a much higher amplitude pulse.

The negative filamentary streamer in Figure 5.13 appears to have different characteristics than the two previous results. Instead of one, multiple filaments have developed from the bushy structure. The propagating distance is also shorter than that of the streamer in Figure 5.12. The increase in the number of branches tends to reduce the streamer length due to the effect of local space charge in front of the streamer heads. The branching phenomenon is also evident in measured UHF waveforms by the occurrence of multiple pulses after the formation of bush-like structure at the needle tip. In addition, the magnitude of these pulses are less than half of the single pulse which was responsible for the single filament observed in Figure 5.12(a). In this case, the propagation length of the streamer filament appears to have a positive relationship with the magnitude of the UHF pulse. A higher current pulse will result in more vaporisation of the liquid, and therefore, longer density-change channels.

This observation supports the hypothesis that propagation modes of streamers are dependent on the local electric fields at the tip of the streamer channels. The resultant field is a combination of the applied voltage and space charge built up during the streamer discharge. Because the duration of the whole event is typically less than 10 μs, which is equivalent to 0.18 degree of a 50 Hz cycle, the potential of the needle tip can be

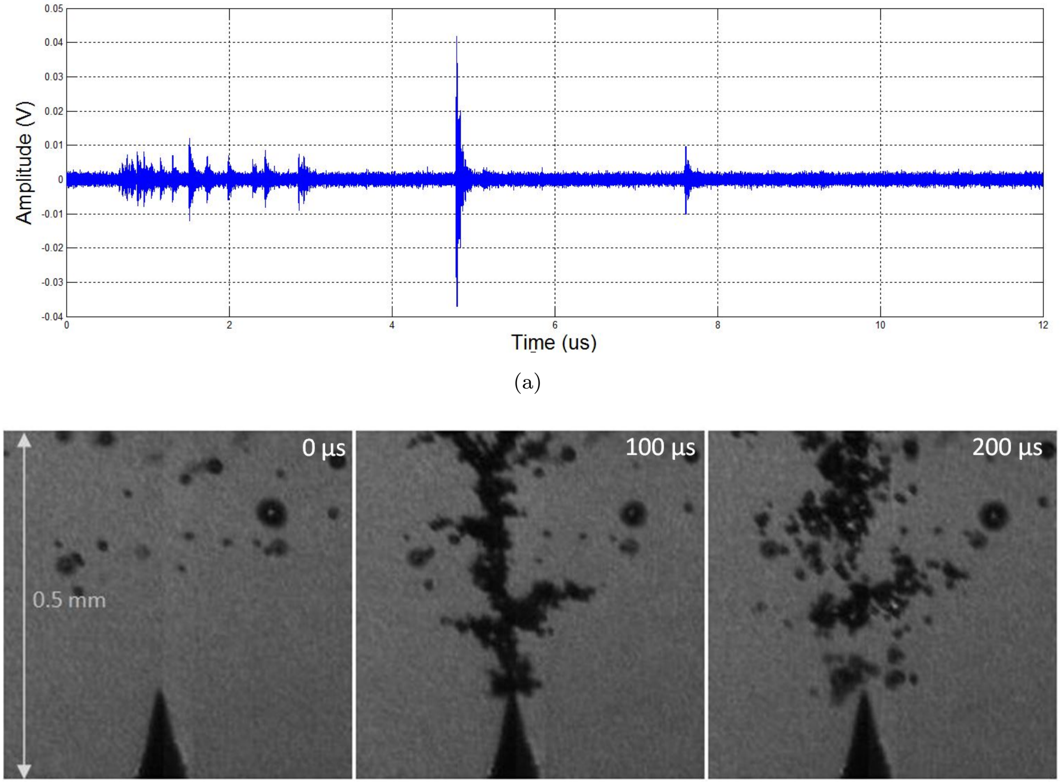

(a)

(b) 90 pC

FIGURE 5.12: An example of cathode filamentary streamer in LN_2 (a) waveforms observed by the UHF sensor, (b) the corresponding images taken at 10000 frame per second. At 18 kV, 77.8±0.3 K, atmospheric pressure, liquid gap distance 15 mm.

assumed to be constant over this period. Therefore, any variation in local field must be due to the accumulation of space charge at the top of the streamer branches. If the field enhancement is sufficient, new propagation mechanisms, such as liquid ionisation, can then be considered [8].

The amount of charge transfer at the terminals during the filamentary streamer process is almost double that of bush-like streamer discharges. This is because the propagation of negative tree-like streamers has two phases: bush-like structure and filaments grown from it. Each stage has each own current pulses as shown by the UHF sensor measurements. Since the conventional method integrates the pulse sequence, the integrated apparent charges show higher values than in the case of bush-like propagation only. An increase in the gaseous area is also observed during a filamentary streamer compared with the bush-like mode due to higher energy dissipation into the liquid causing more liquid to be evaporated.

The details in time domain recorded by the UHF sensor show good agreement with the observed shadow graphs. The growth of filaments out of a bush-like structure can be observed in the UHF pulse trains which show two parts with different characteristics. Each part of the UHF pulse sequence can be related to each phase of the streamer

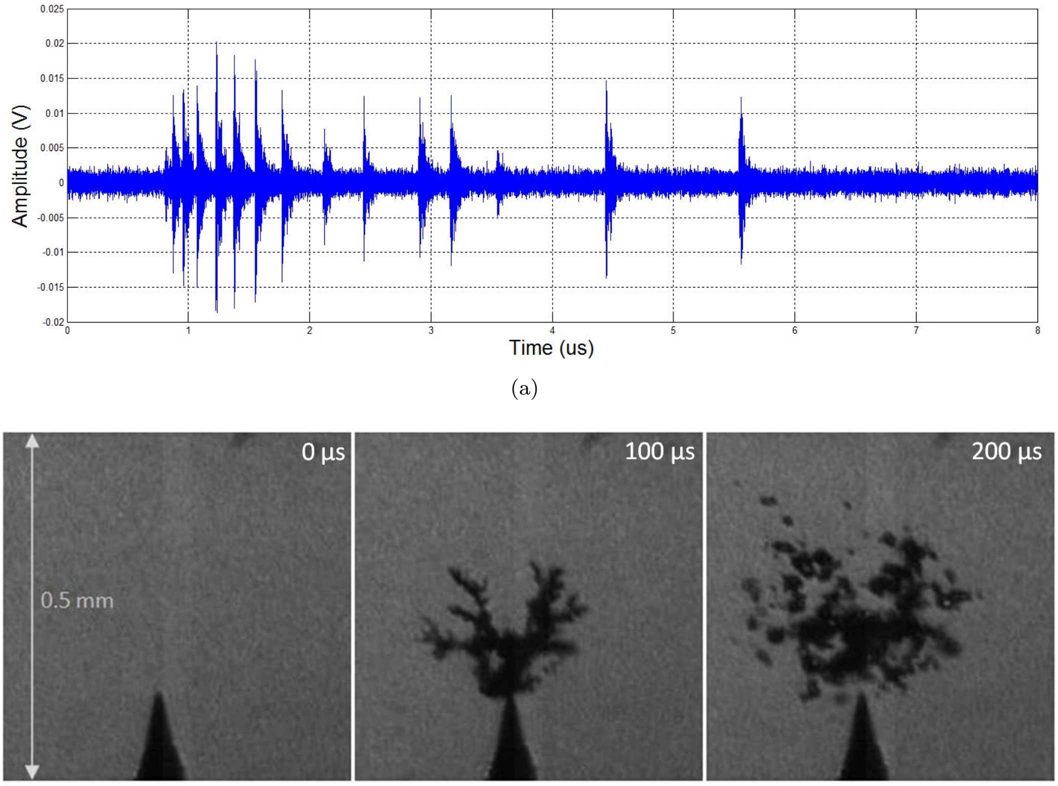

(a)

(b) 75 pC

Figure 5.13: An example of cathode filamentary streamer in LN_2 (a) waveforms observed by the UHF sensor, (b) the corresponding images taken at 5000 frame per second. At 18 kV, 77.8±0.3 K, atmospheric pressure, liquid gap distance 15 mm.

development. Similar to bush-like streamer discharges, the details in the time domain are lost using conventional PD detection due to its narrow bandwidth. This information has shown to be useful to distinguish propagation modes as well as understand the development of the streamer as illustrated from these results.

As the voltage increases, more space charge is formed in front of the needle tip by repetitive partial discharges. Under these conditions, the generated streamers do not necessarily propagate perpendicularly or even towards the planar electrode. The observed density-change channels tend to move away from the cloud of bubbles in front of the tip where the space charge has accumulated (Figure 5.14(a), (b), (c)). In the cases of streamers presented in Figure 5.14(b) and (c), there are streamer branches that propagate parallel to the planar electrode. This phenomenon indicates the dominance of the space charge field over the external electric field under extreme applied voltages. In contrast, close to inception voltage, the external field is dominant because of all the observed streamers propagate following the bush-like mode and the strongest field direction. As the applied voltage increases, an extension out of the bush-like structure is observed, this additional vapour region can either have bushy or filamentary shape. The propagation of filamentary streamers far from the needle tip, where the external electric field is reduced significantly, indicates the role of space charge in local electric field enhancement. Further rise of the applied voltages leads to the dominance of the space charge field causing a change in the direction of streamer branches.

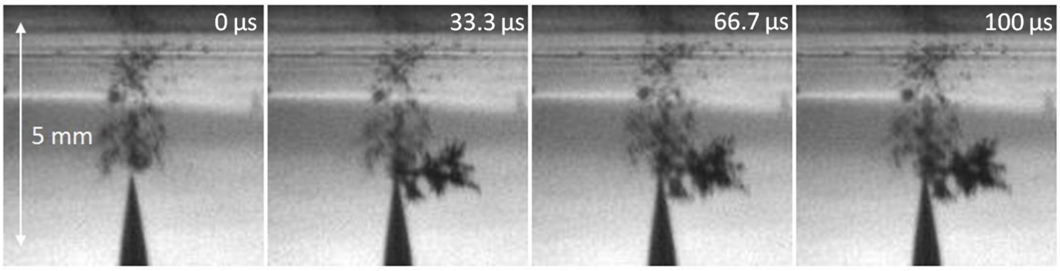

(a) 658 pC

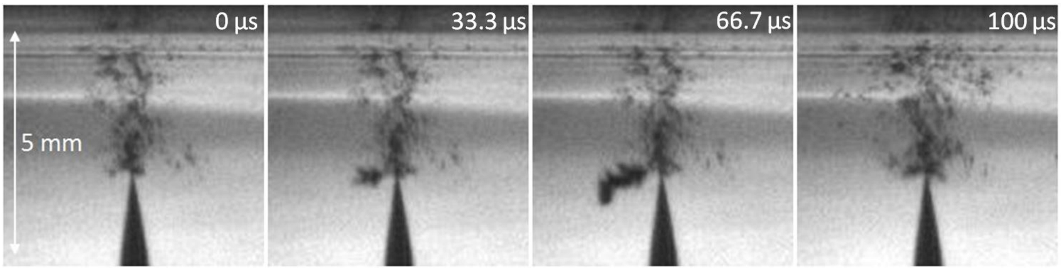

(b) 552 pC

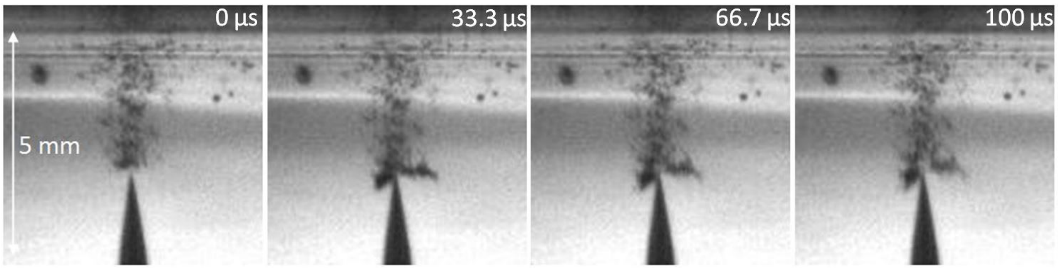

(c) 435 pC

FIGURE 5.14: An example of cathode filamentary streamer in LN_2 (a) waveforms observed by the UHF sensor, (b) the corresponding images taken at 30000 frame per second. At 25 kV, 77.8±0.3 K, atmospheric pressure, liquid gap distance 3 mm.

At 35 kV, PD with magnitude in the nC range occur during the positive half cycle, e.g when the needle is negative. These streamers completely propagate across the gap. Due to the existence of the solid insulation barrier on top of the planar electrode, complete breakdown does not occur. On the streamer meeting the barrier, charge carriers created inside the streamer channels are deposited on the surface of the barrier and create a local space charge. The charges, electrons, move away from the attachment point under the influence of the local field . Consequently, heat dissipation and vaporisation of the liquid, which is evident by the low density region, occur on the surface of the solid dielectric barrier as shown in Figure 5.15. One may argue that the phenomenon observed could be due to bubble movement across the area, however, from Figure 5.15(b), a darker region is observed in the form of streamer channels before breaking down into many smaller bubbles. The question is that whether or not further electron avalanches occur. In some cases, Figure 5.15(a) and (c), further electron avalanches are evident by the additional branches of streamer propagating from the surface of the solid dielectric towards the needle tip.

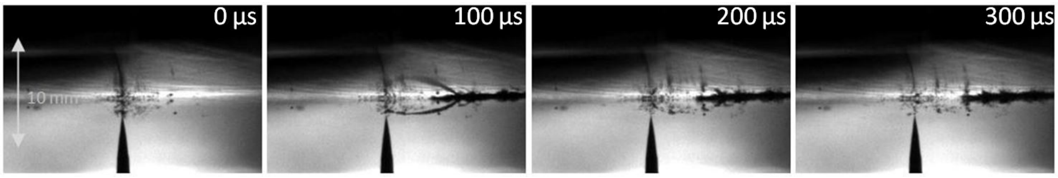

(a) 25 nC

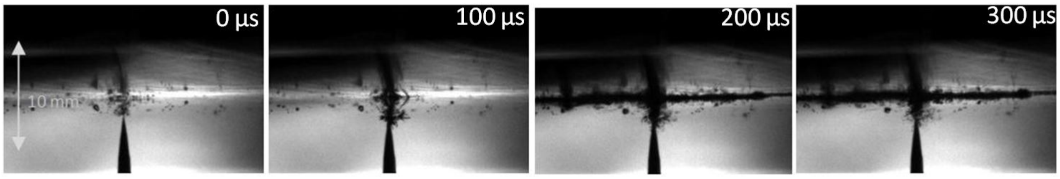

(b) 38 nC

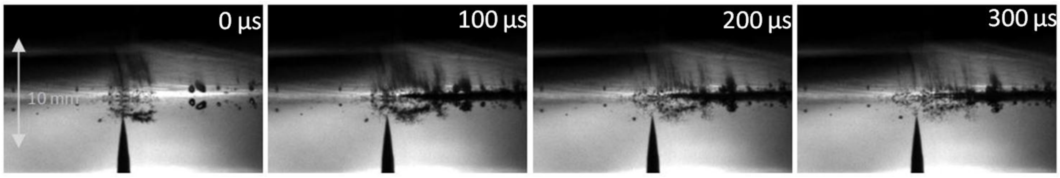

(c) 36 nC

FIGURE 5.15: An example of cathode filamentary streamer in LN_2 (a) waveforms observed by the UHF sensor, (b) the corresponding images taken at 10000 frame per second. At 35 kV, 77.8±0.3 K, atmospheric pressure, liquid gap distance 1.5 mm.

5.4 Initiation and propagation of anode streamers

Streamers in LN_2 during the negative half cycle, when the needle polarity is positive, are observed less frequently than during the positive half cycle. Both bush-like and filamentary shapes were recorded; however, the filamentary mode is dominant. Bush-like positive streamers appeared most frequently just above the inception voltage. As the applied voltages increases, the likelihood of a filamentary streamer increases.

Partial discharges from a point anode captured by the UHF sensor display a different pattern to negative streamer discharges. The pulse train phenomenon of PD from a point cathode was not observed during positive polarity. Waveforms recorded by the RFCT show the same behaviour. This implies different mechanisms governing the pre-breakdown phenomena initiating from positive and negative needles. The first case is linked to the formation and expansion of gaseous cavities and the latter suggests a more direct mechanism such as ionization of the liquid.

Unlike the case of cathode streamers, the subsequent discharge current flowing to earth from the development of an anode streamer can be detected by the RFCT. The commercially available RFCT used in this study has been used to detect PD in plant such as medium voltage PILC cable circuits and high voltage transformers. In both cases, the required minimum detection sensitivity is of the order of a few hundred picoCoulombs.

5.4.1 Positive bush-like streamers

An example of bush-like streamer development during discharges from a point anode is shown in Figure 5.16. Although the streamer appearance is similar to negative bush-like streamers, measurement from the UHF sensor only shows one single event in contrast to pulse burst behavior during cathode discharges. The observation is also different to bush-like positive streamer in transformer oil [97] [88] [100], where multiple current pulses were recorded during the propagation of a bush-like streamer. However, other streamer characteristics such as length and shape are similar.

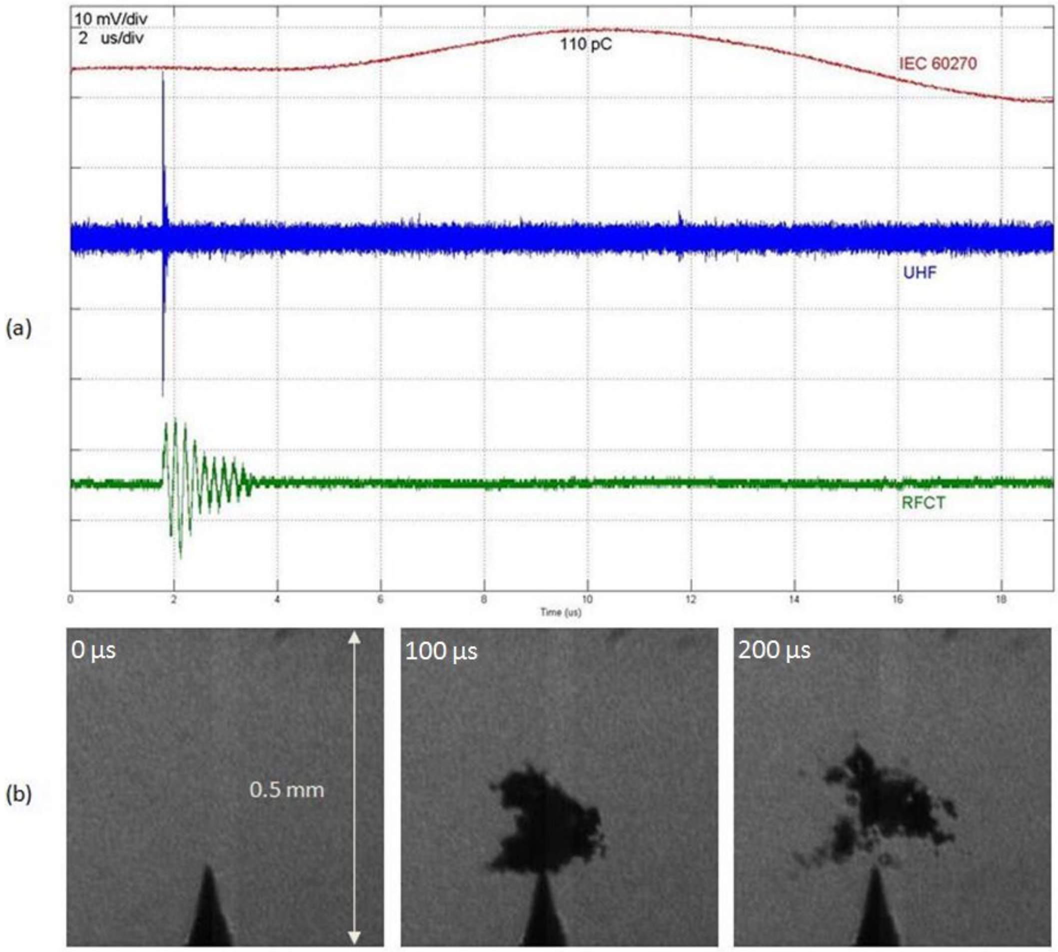

FIGURE 5.16: An example of anode bush-like streamer in LN$_2$ (a) UHF and IEC 60720 measurements, (b) the corresponding images taken at 20000 frame per second. At 17 kV, 77.8±0.3 K, atmospheric pressure, gap distance 15 mm.

Another bush-like streamer from a positive point is shown in Figure 5.17. A single pulse was observed by the UHF sensor similar to the result from Figure 5.16. A bush-like vapour region appeared in front of the tip for about one frame before dissolving into a cloud of bubbles. Although the structure remains unchanged, the dark area from the shadow graphs caused by positive bush-like streamers is bigger than that from negative ones. The propagating length in general is also longer. The observation is in agreement with the higher current pulses measured during positive PD.

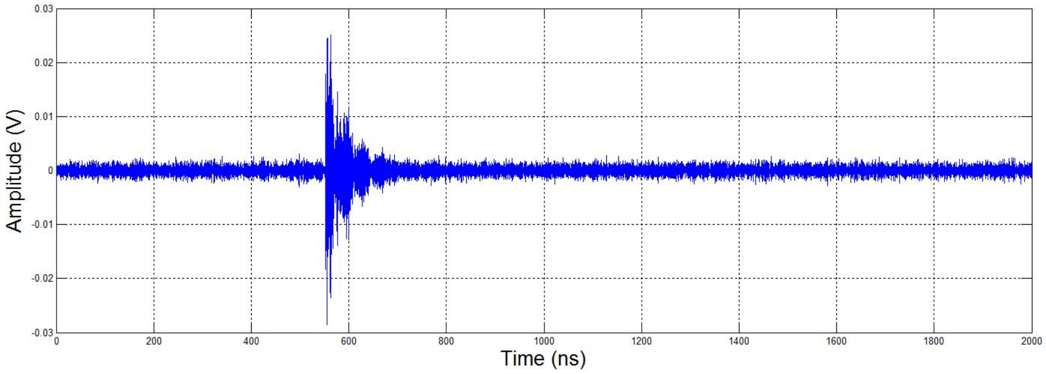

(a)

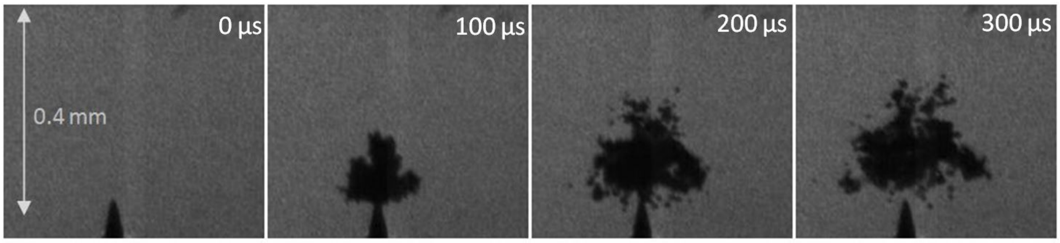

(b) 85pC

FIGURE 5.17: An example of anode bush-like streamer in LN_2 (a) waveforms observed by the UHF sensor, (b) the corresponding images taken at 20000 frame per second. At 17 kV, 77.8±0.3 K, atmospheric pressure, liquid gap distance 15 mm.

Bush-like streamers were observed for all gap distances studied as shown in Figure 5.18 close to inception voltages. The existence of positive bush-like streamers does not seem to be affected by the gap between the needle and the planar electrode. Applied voltage, however, greatly affects the phenomenon since as the voltage increases, bush-like streamers were observed less frequently. Above a certain threshold voltage, a filamentary shape was found to be dominant during positive PD in LN_2. The same conclusion has been drawn for hydrocarbon liquids [84] and LN_2 under impulse voltages [64]. Needle tip radius also influences the occurrence of positive bush-like streamers. It has been observed for liquid cyclohexane and propane that there is a critical tip radius, r_c, above which anode streamers only propagate with filamentary mode [50]. The tip radius used in this work (2.8 ± 0.5 μm) has always been smaller than the given value of r_c, 6 μm.

Although many similarities can be found in the shapes of bush-like positive and negative streamers from the captured shadow graphs, the mechanism behind the negative discharges cannot be applied for pre-breakdown phenomena from an anode point. Firstly, the pulse burst behaviour which explains the step-wise growth of vapour channels was not seen in this case but instead a single current of which magnitude is much higher

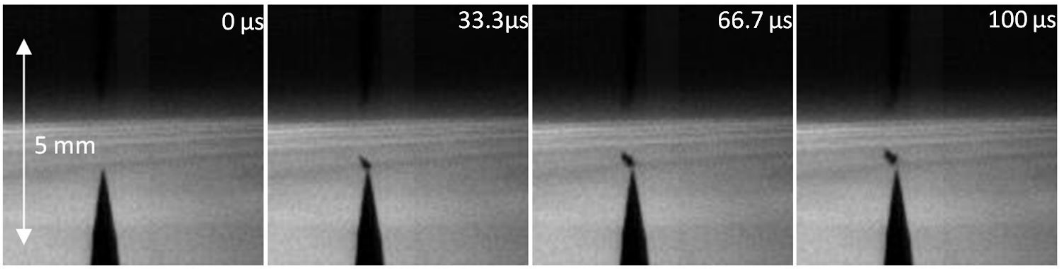

(a) 56 pC

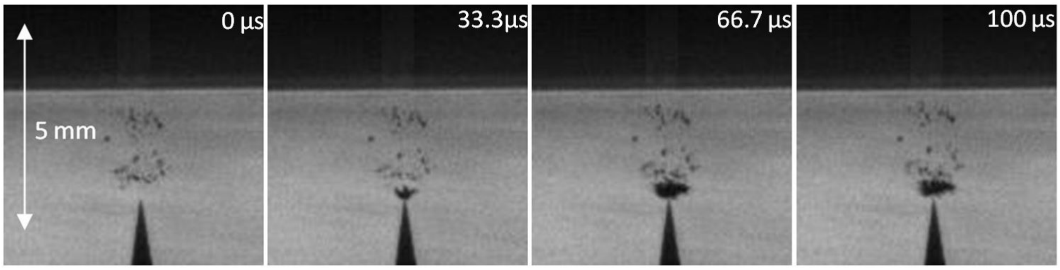

(b) 95 pC

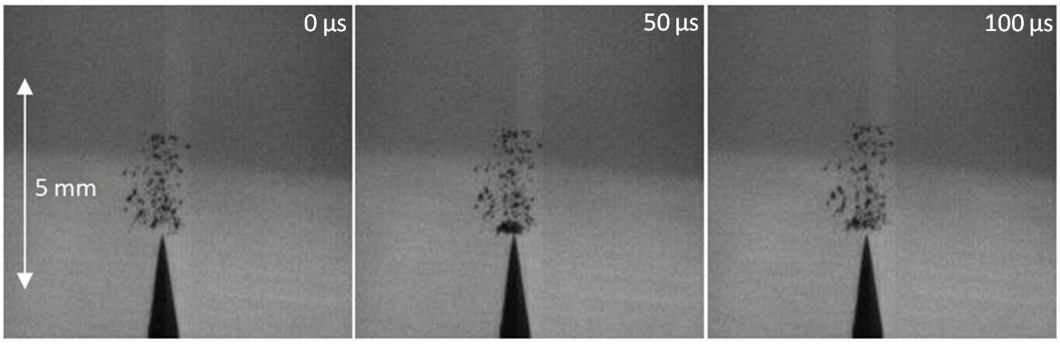

(c) 71 pC

FIGURE 5.18: An example of anode bush-like streamer in LN_2 (a) 1.5 mm liquid gap distance (b) 3 mm liquid gap distance (c) 12 mm liquid gap distance. At 22 kV, 77.8±0.3 K, atmospheric pressure.

than the discrete pulse in the negative pulse sequence. Secondly, field emission which is believed to be the primary charges provider for negative streamers does not occur for a positive point electrode. Electrons cannot be supplied from the planar electrode because of the very low electric field there. Without the initial cavity and seed electron, the streamer cannot be initiated.

5.4.2 Positive filamentary streamers

Filamentary streamers were recorded during positive pre-breakdown process for all the applied voltages and gap distances studied. The tree-like structure observed has defined branches as shown in Figure 5.19, Figure 5.20 and Figure 5.21. In contrast to cathode filamentary streamers, the growth of density change channels from an anode point does not necessarily require a bushy structure at the needle tip. This is because of differences in the mechanisms governing the process of streamer development from the two polarities. In the case of a negative point, a bushy base is quickly formed due to field emission and electron avalanches before a filamentary mode can be initiated. Meanwhile PD from an anode point is the result of more direct charge generation mechanisms such as liquid ionization. In addition, continuous current was observed before discharge pulses during positive streamers [44] [45] [84] [63]. The movement of negative charges towards the positive needle enhances the local electric field there high enough for propagation in filamentary mode. Meanwhile, from a cathode point, field enhancement is due to the space charge developed at the tip of the bush-like structure. In terms of PD measurements from the UHF sensor, the discharge signature of positive filamentary streamers and the second phase of the negative tree-like streamers, which indicates the growth of the filaments, have similar characteristic: a high-magnitude pulse. It is hypothesised that both processes are governed by a similar mechanism which is ionization in the liquid phase. In this work, PD pulses were measured rather than continuous current. Therefore, whether or not field-enhanced dissociation happened cannot be confirmed. Other mechanisms such as electromechanical generation of nano-scale cavities [19] or pressure reduction due to repulsion force between charges [101] would be important to or at least assist the generation of initial cavities.

The streamers presented in Figure 5.20 and Figure 5.21 propagate with more filaments than that in Figure 5.19. Because these streamers branch out more, their propagation length is shorter than in the case of a single filament. Streamer development can be affected by the surrounding space charge and decrease their propagation length. In both cases presented here, it can be observed that the tip of the filament become blunt prior to streamer propagation ceasing. This may suggest that the ionisation process, driven by the electric field stress at the filament tip, may have stalled due to the effects of space charge from the surrounding filaments. In addition, further away from the point the electric field can be reduced to a value too low to continue vaporising LN_2.

Although multiple branches were observed, only a single pulse was measured by the UHF sensor. It appears that there is not a relation between the number of branches of a positive filamentary streamer and the number of pulses recorded by PD measurement methods. It is possible the growth of multiple filaments occurs adjacent to each other in the time domain such that even wideband detection using the UHF sensor fails to distinguish individual events.

As the applied voltage increases further, PD events having magnitudes in the nC range are observed. The recorded density channels completely bridge the liquid gap and propagate along the surface of the insulation barrier (Figure 5.22). Similar to negative filamentary streamers under similar voltage levels, the space charge created from previous streamers can affect greatly the Gaussian electric field profile. As a result, streamer channels do not necessarily propagate in a perpendicular direction to the planar electrode especially in extremely high voltages when more charges may be presented in the

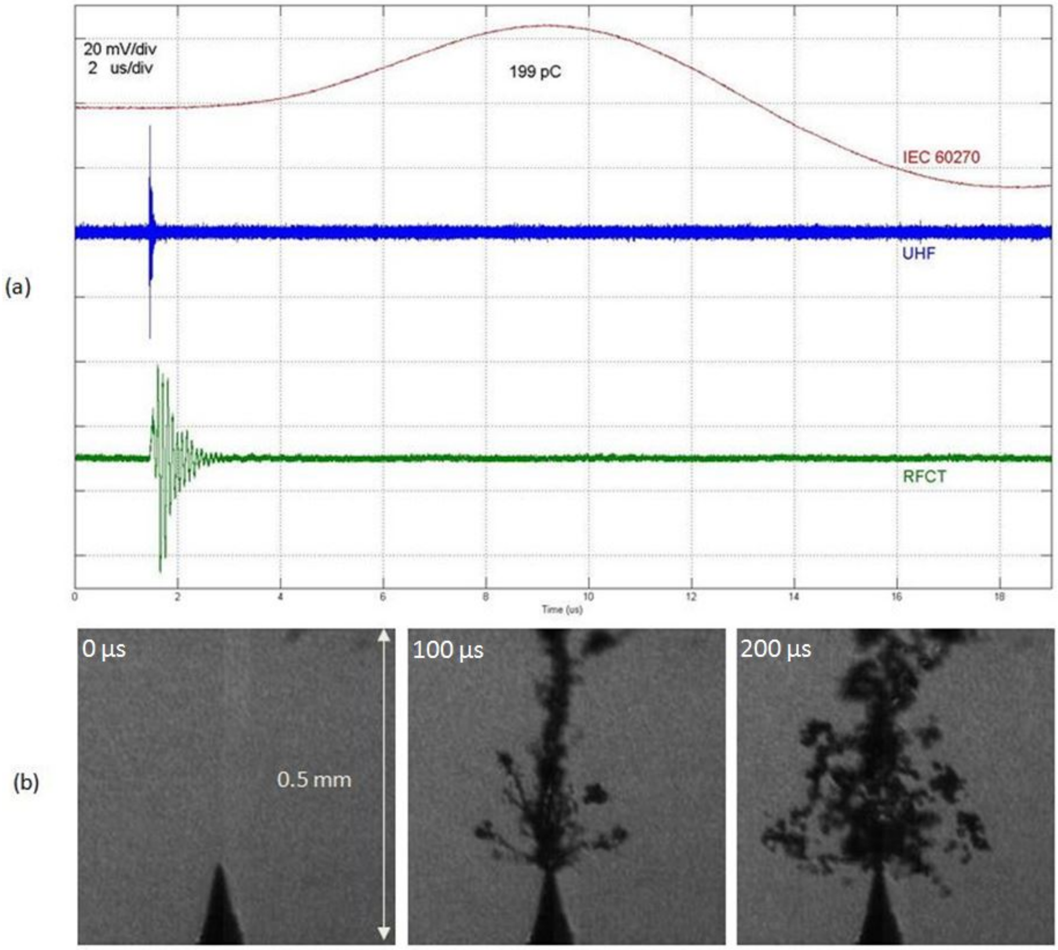

FIGURE 5.19: An example of anode filamentary streamer in LN$_2$ (a) UHF and IEC 60720 measurements, (b) the corresponding images taken at 20000 frame per second. At 17 kV, 77.8±0.3 K, atmospheric pressure, gap distance 15 mm.

liquid (Figure 5.22 and Figure 5.23). The streamer appeared to branch out more when it reached the insulation barrier creating multiple attachment. A similar characteristic has been observed in LN$_2$ under AC voltages for larger tip radius and shorter gap distance [10]. On its attachment to the insulation barrier, density change regions were also observed on the surface of the barrier. Similar to negative streamers, charge carriers will be spread out across the surface of the barrier. The charge then will move across the weakest dielectric path which is the interface rather than penetrate to solid dielectric. The result is the vaporisation of liquid on the surface as observed.

The colour of the streamer channels is brighter during propagation than during the post PD process of breaking up into clouds of bubbles. This indicates a decrease in pressure of the filaments due to the expansion of the streamer channels. Since the current pulses were observed for less than the duration between each frame while the existence of the density change channels lasts much longer, it can hypothesized that the thin filament was a result of the observed current pulses. When the discharge stops, e.g. no further current is recorded, the streamer filaments expand while their pressure reduces. The

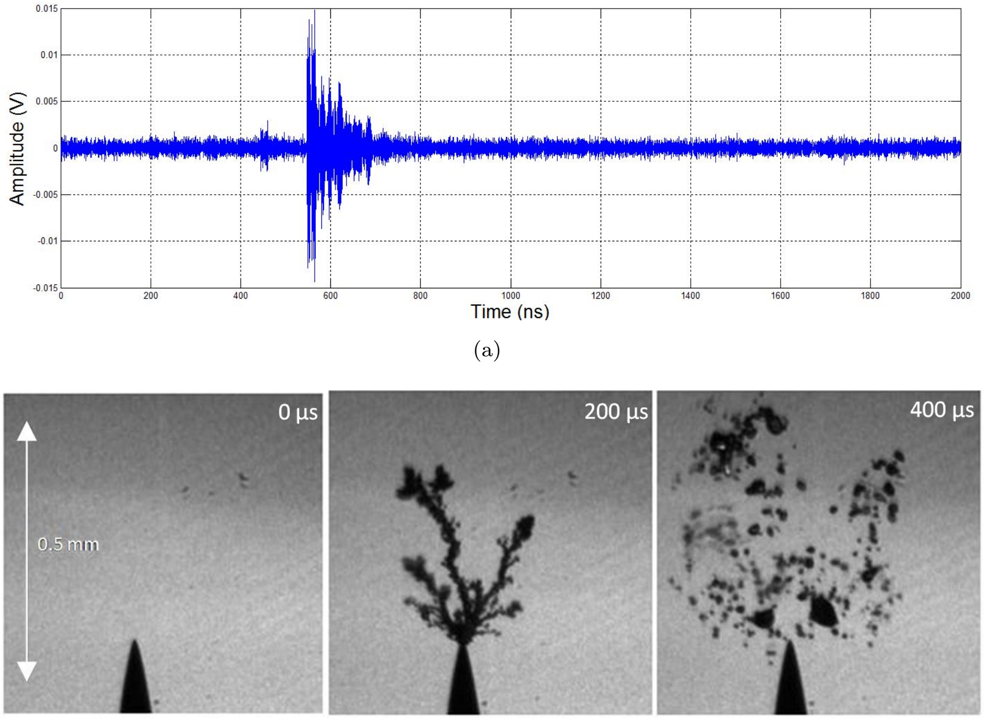

(a)

(b) 21pC

FIGURE 5.20: An example of anode filamentary streamer in LN_2 (a) waveforms observed by the UHF sensor, (b) the corresponding images taken at 5000 frame per second. At 22 kV, 77.8±0.3, atmospheric pressure, liquid gap distance 5 mm.

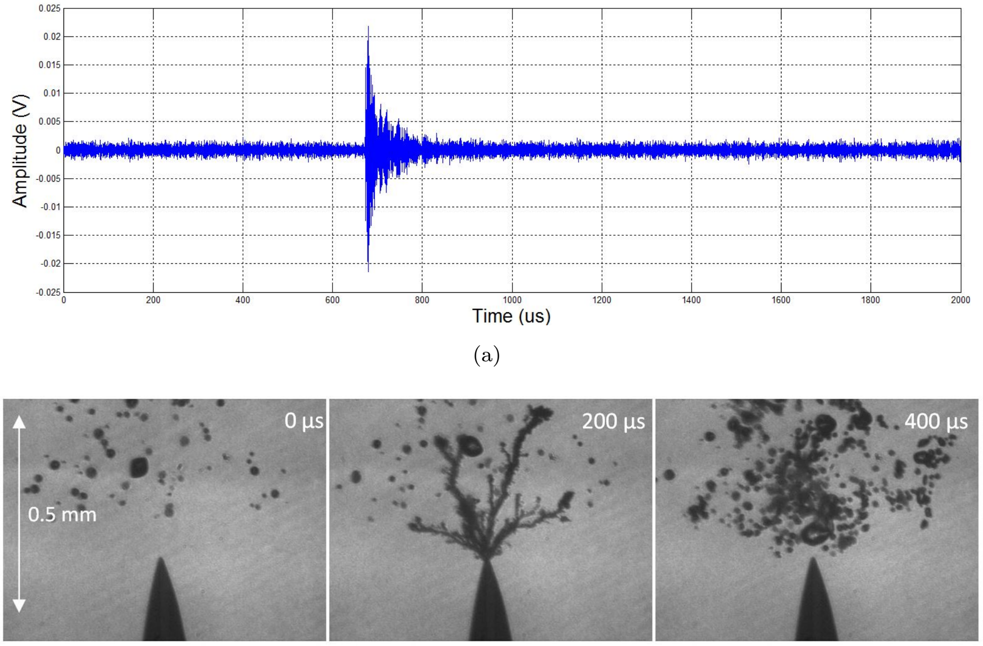

(a)

(b) 223pC

FIGURE 5.21: An example of anode filamentary streamer in LN_2 (a) waveforms observed by the UHF sensor, (b) the corresponding images taken at 5000 frame per second. At 22 kV, 77.8±0.3 K, atmospheric pressure, liquid gap distance 5 mm.

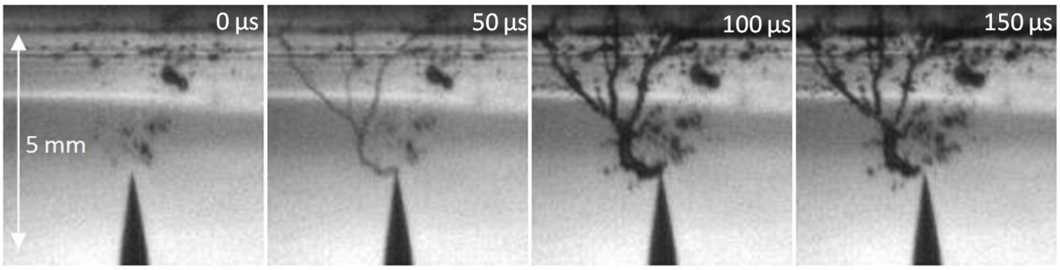

(a) 32 nC

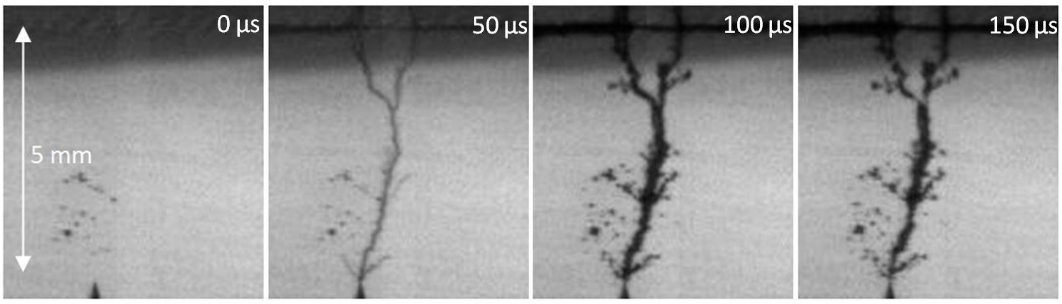

(b) 12 nC

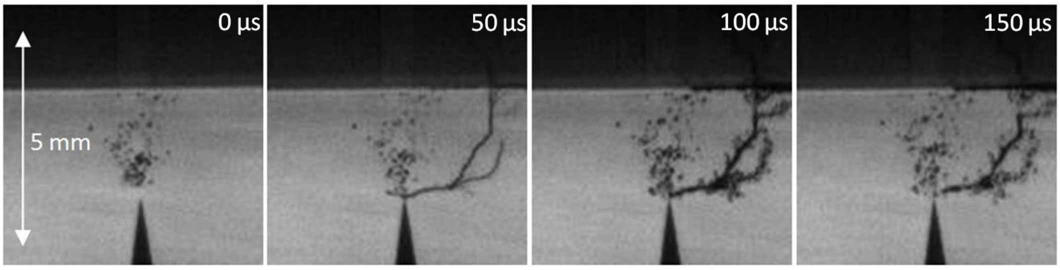

(c) 8 nC

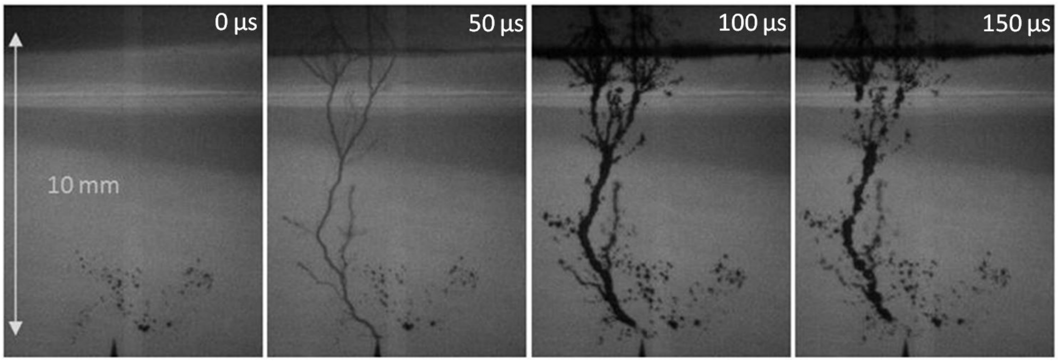

(d) 13 nC

Figure 5.22: Anode filamentary streamers in LN_2 at 30 kV, 77.8±0.3 K, atmospheric pressure, liquid gap distance: (a) 3 mm (b) 2.8 mm (c) 5.5 mm (d) 10 mm.

filaments can exist for a further 100 μs or so before breaking up due to lower pressure. The collapse of the streamers occurs randomly along the filaments. The resulting bubbles of discharges with magnitude in the nC range tend to exist until the next cycle of the applied voltage.

Further examination of streamer filaments reveals that the development of positive filamentary streamers in which the length of gaseous channels exceed a few millimetres is discontinuous. Branching tends to occur and form a junction as shown in Figure 5.23. Most of the time, a change in a direction of the streamer was observed. This change can either be over a range of a few to 40 degrees (Figure 5.24). The longest single filament, before branching, was measured at 6.2 mm. This behaviour was observed more frequently for long gap distances, e.g. above 5 mm. The limitation of the camera speed makes it difficult to analyse the the development of the streamer in these scenarios.

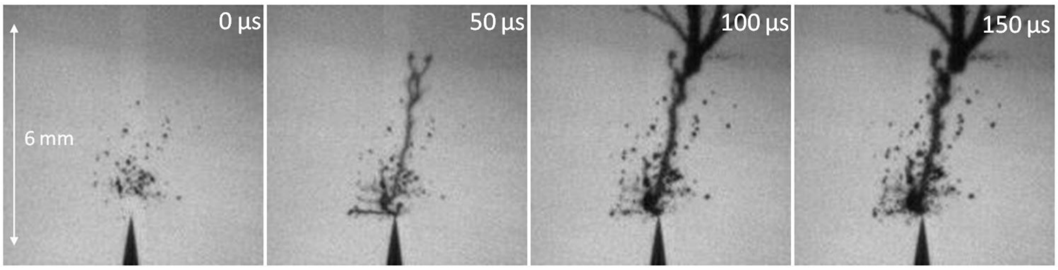

FIGURE 5.23: An example of anode filamentary streamer in LN_2, images taken at 20000 frame per second. At 30 kV, 77.8±0.3 K, atmospheric pressure, liquid gap distance 11 mm.

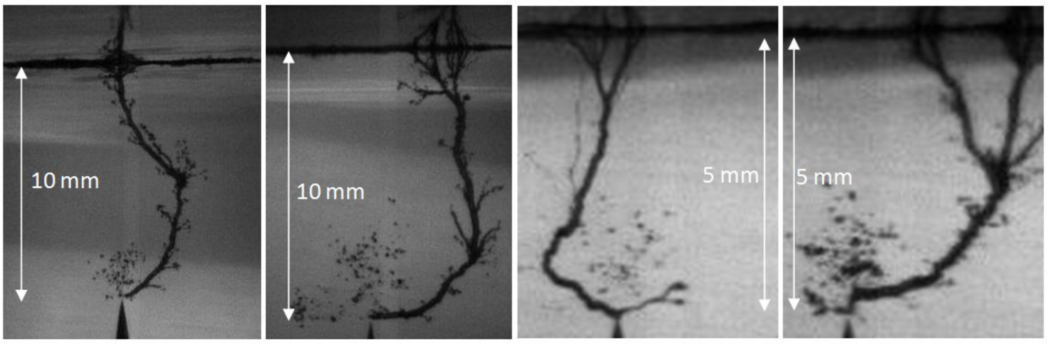

FIGURE 5.24: Branching phenomenon of positive filamentary streamers for various distances.

In mineral oil positive filamentary streamers tend to propagate continuously up to a gap distance of 20 mm [102] [71]. Rain [100] studied pre-breakdown phenomena in mineral oil in large gaps and concluded that when a streamer develops more than 20 mm, many of its filaments stop while only a few of them continue propagating. Filaments longer than 20 mm are subjected to periodic re-illuminations which keep connecting the filaments with the electrode and result in further propagation of the streamer. Similar branching phenomenon to that shown in Figure 5.24 has also observed. However, in LN_2, the continuity of streamer propagation is only observed up to a few millimetres.

5.5 Phase resolved analysis of partial discharges in LN_2

This section presents a characterisation of partial discharges in LN_2 under AC voltages by the means of phase resolved analysis. The construction of ϕ-q-n plots has been discussed in detail in Chapter 3. In this case, a typical signal lasts for approximately 60 μs which is equivalent to 120 data point at 2 Msample/sec. Thus, this sets a maximum measurable repetition rate of 17 discharge pulses per millisecond. On the occasion that the occurrence of PD events exceed this rate, the PD measurement method would fail to distinguish the adjacent PD pulses and results in an overlapped waveform as shown in Chapter 4. Although this concern might not be important close to the inception voltage, the increase of number of pulses due to higher applied voltages may eventually lead to overlapping of PD waveforms. Therefore, the number of PD pulses recorded under extreme conditions, e.g. above 25 kV, might not be the exact number of PD events due to the limitation of the measurement device. Thus, the focus here is not the exact number of events but rather a comparison between different experimental conditions such as gap distances and materials in order to investigate the PD patterns for a composite insulation system using LN_2.

5.5.1 10G/40 Results

Figure 5.25 shows the PD pattern in LN_2 for an AC inception voltage (50 Hz) of 14.3 kV. The liquid gap spacing between the needle tip and the 10G/40 insulation barrier was 5.5 mm. The plot was constructed from data recorded over 500 cycles which is equivalent to 10 s in real time. More activity can be seen during negative discharges than positive ones however the PD magnitudes of positive streamers are of greater magnitude than negative events. The observation demonstrates the typical difference between the two polarities: anode discharges are less frequent but have higher measured apparent charge than PD from a cathode point [65]. When the needle polarity is negative, electrons can be readily supplied from the needle tip where the electric field is the highest. Once entering the liquid, collision between electrons and liquid nitrogen creates heat which results in a creation of an initial cavity that can eventually develop into a bush-like streamer. Meanwhile, the process from an anode point faces difficulty of finding available electrons close to the needle tip where streamer can be initiated. Therefore, the probability of PD occurrence during positive polarity is lower than negative polarity which explains lower numbers of PD pulses recorded during a positive applied AC field.

With reference to Figure 5.25(a), it can be seen that PD during positive discharge appear in two groups. The first group has the magnitudes below 60 pC and the charge transfer per discharge in the second group varies between 60 and 460 pC. Previous work on streamer behaviour in LN_2 under AC voltages [65] has shown that both bush-like and filamentary streamers exist during anode discharges in LN_2. Streamers propagating

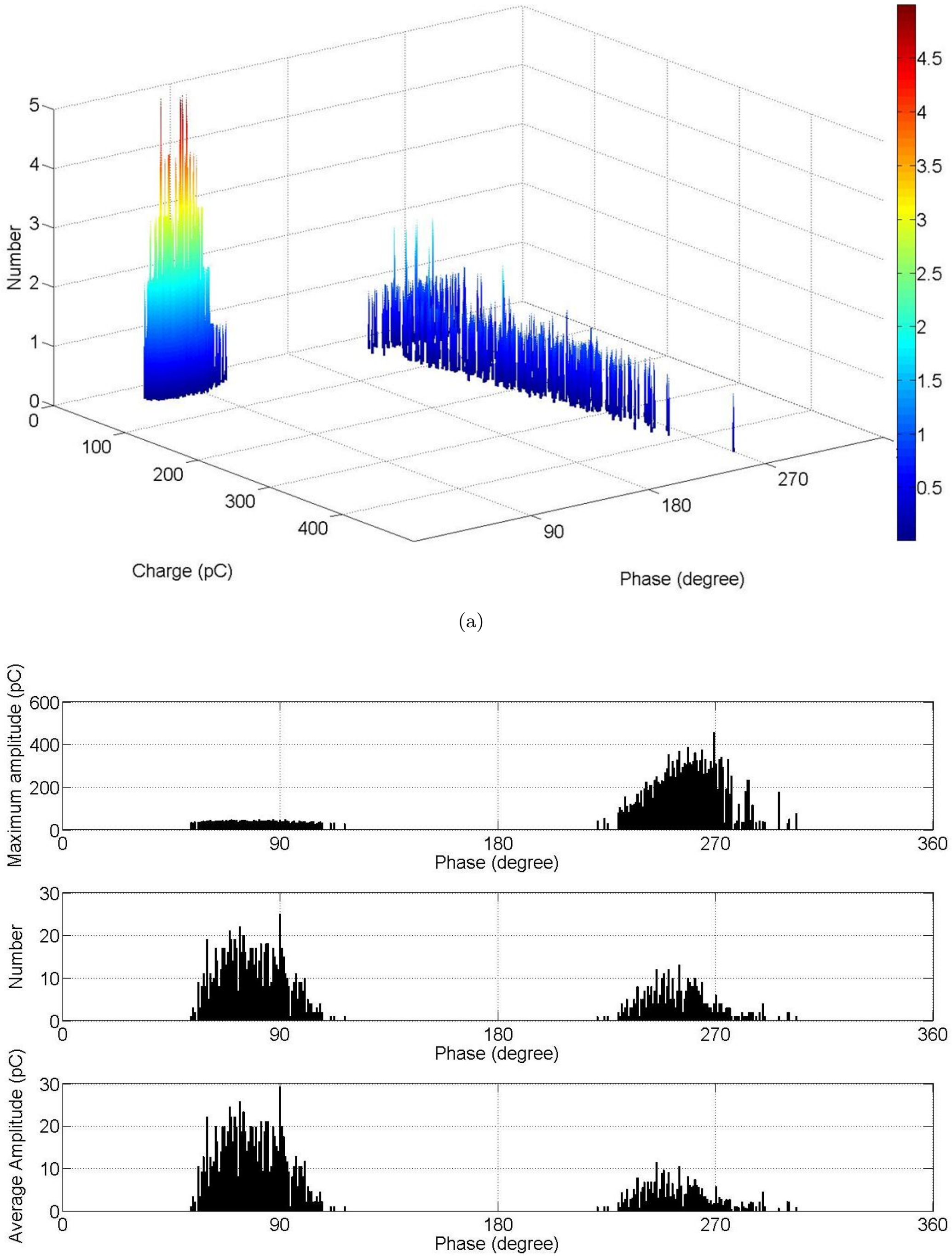

(a)

(b)

Figure 5.25: (a) ϕ-q-n plot, (b) maximum charge, cumulative number, average charge by phase window at 14.3 kV, 5.5 mm gap distance, 10G/40 sample, 77.8±0.3 K, atmospheric pressure.

in tree-like shapes tend to have longer filaments and higher discharge magnitude than those having bushy shapes. Therefore, it can be hypothesized that the two groups of PD pulses observed in Figure 5.25 correspond to the two propagation modes of streamers: bush-like and filamentary. The hypothesis is confirmed by the analysis of the shadow graphs captured by the camera as shown in Figure 5.26.

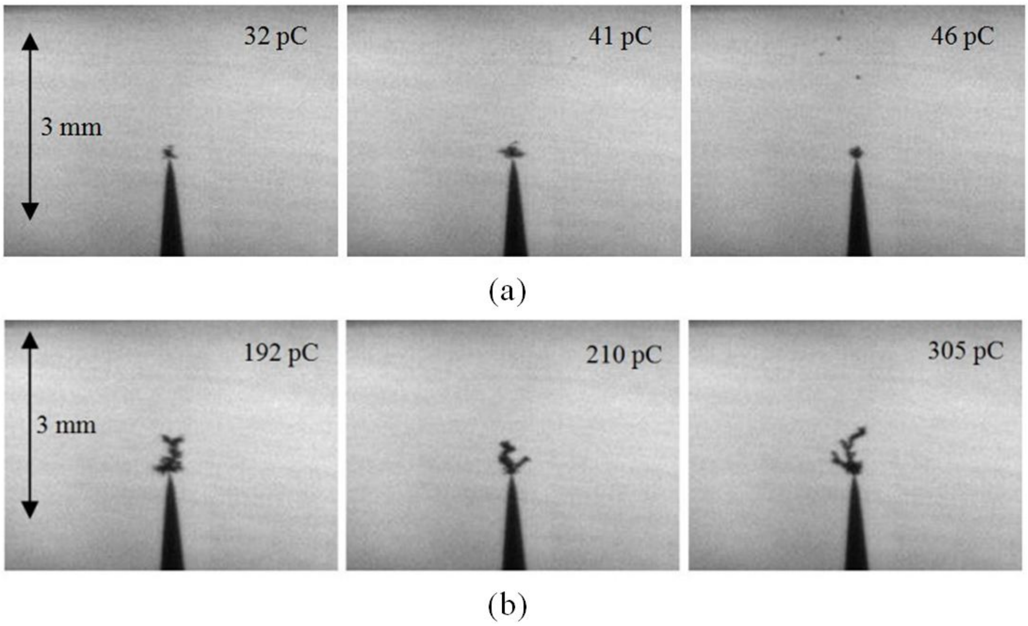

FIGURE 5.26: Examples of positive (a) bush-like and (b) filamentary streamers in LN_2 at 17.1 kV, 5.5 mm gap distance, 10G/40 sample, 77.8±0.3 K, atmospheric pressure.

As the applied voltage rises to 17.1 kV, the number of PD pulses recorded increases significantly during both positive and negative half cycles (Figure 5.27). The main characteristics of the PD pattern from the two polarities remain unchanged: positive discharges are higher in magnitude but less frequent than negative ones. The maximum magnitude of PD from an anode point increases by almost four times compared with positive streamer discharges at the inception voltage. The maximum charge transfer during negative discharges is also higher than those at lower applied voltage, rising from 44 pC to 72 pC. The cumulative number and the average charge transferred in each phase window also increase significantly due to the higher rate of change of the applied voltage.

The active phase band also widens from 51^0-117^0 to 38^0-123^0 for negative discharges and from 220^0-303^0 to 207^0-318^0 for positive discharges when the applied voltage rises from 14.3 to 17.1 kV. In both cases, the PD pulses are not distributed evenly around 90^0 and 270^0, e.g. the peaks of the AC sinusoidal voltage wave. Instead the discharge occurrence shifts more towards the first and third quadrants. During streamer discharges, space charge can be developed in front of the needle tip. The charge carriers drift towards the planar electrode under the influence of the electric field. This layer of charge creates an electric field superimposed on the external field from the applied voltage and prevents additional streamers from being initiated. As the potential of the needle tip increases following the voltage waveform, the external electric field becomes dominant over the superimposed field and breakdown occurs the liquid. A new streamer can be formed and the process repeats till the applied voltage reaches its maximum. Shortly after the

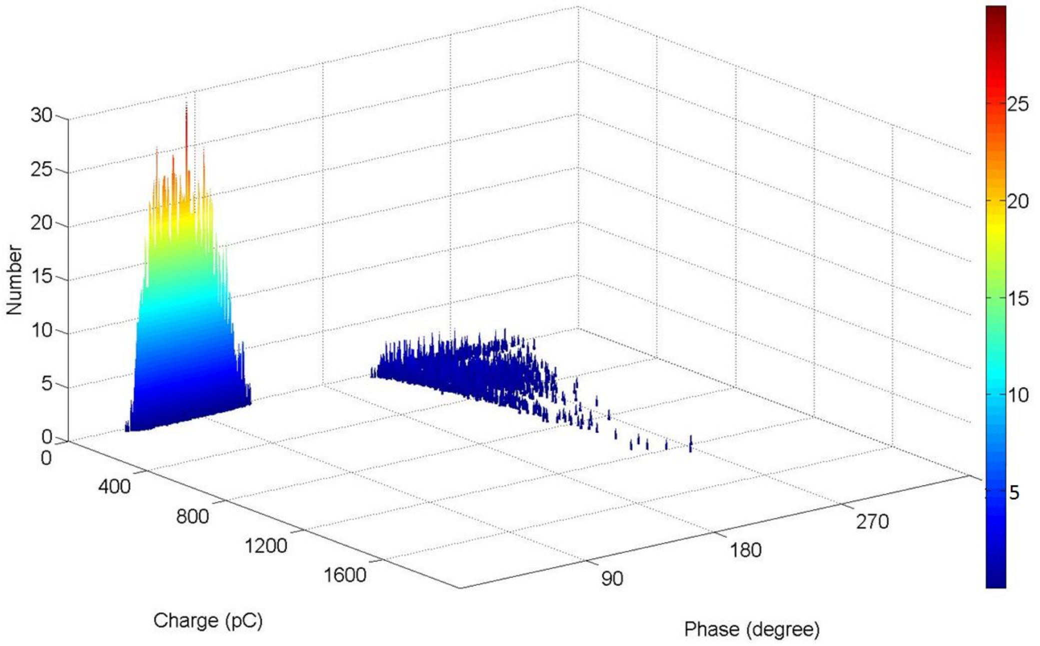

(a)

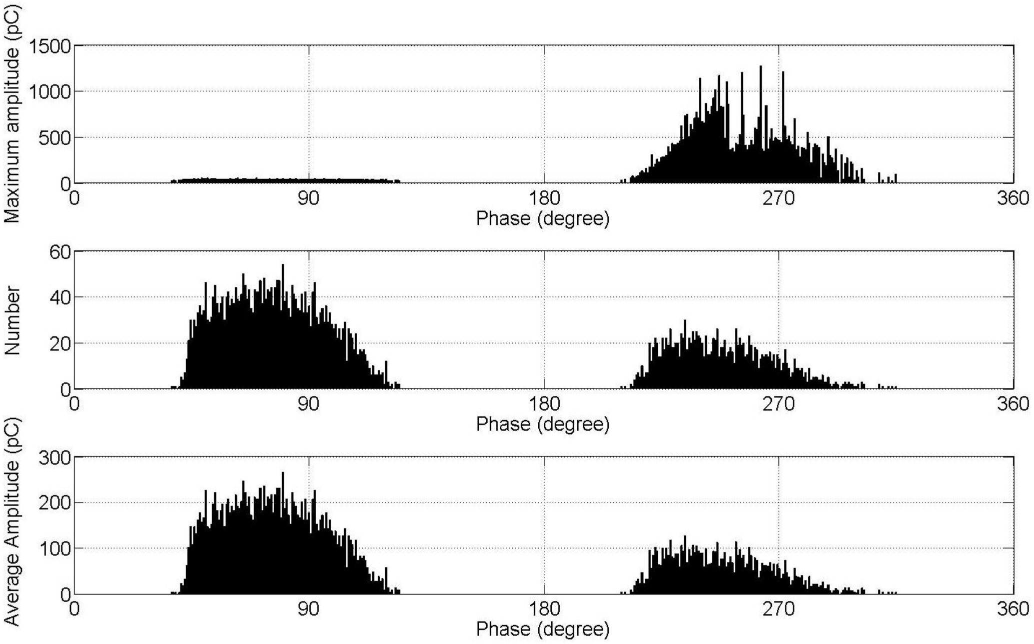

(b)

FIGURE 5.27: (a) ϕ-q-n plot, (b) maximum charge, cumulative number, average charge by phase window at 17.1 kV, 5.5 mm gap distance, 10G/40 sample, 77.8±0.3K, atmospheric pressure.

peak, the external electric field is no longer sufficient to initiate PD which leads to the extinction of discharge activity. The space charge in the liquid due to PD in a half cycle can exist in the system until the next half cycle. The charge carriers can either remain in the liquid or on the surface of the insulation barrier. At the point of the zero crossing, the charge remaining from a previous half cycle starts moving towards the needle tip due to electrostatic force and enhances the local electric field. Therefore, PD can be initiated earlier in the applied phase. The process repeats for each half cycle and results in the pattern observed. This observation is different to the PD pattern in oil at larger gap distances [9] [103] in which PD pulses were found around the peaks of the voltage waveforms.

Above 20kV, streamers which completely bridge the liquid nitrogen gap between the needle and the insulating barrier were observed. The discharge magnitudes of these events were measured just below 9 nC at 20 kV and in the order of tens of nC at 30 kV as shown in Figure 5.28.

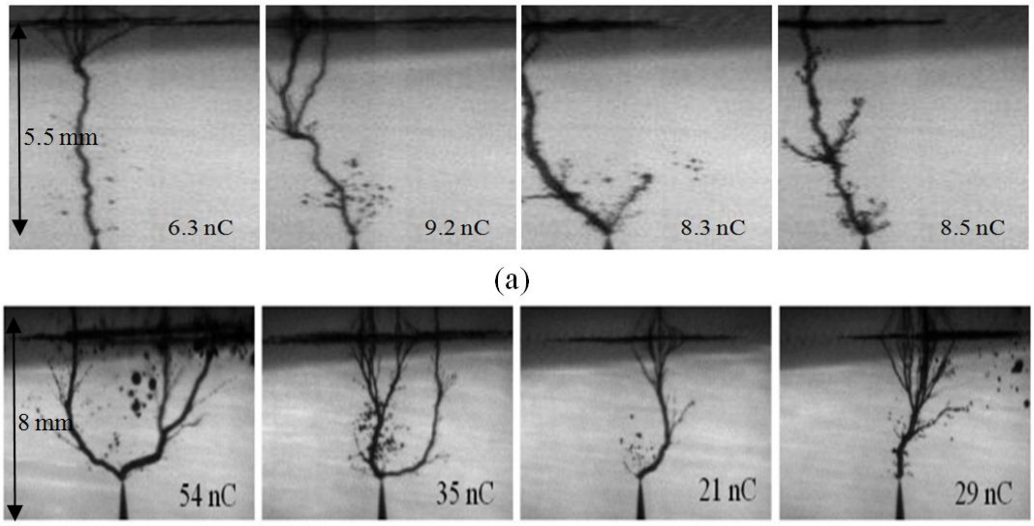

(a)

(b)

Figure 5.28: Positive filamentary streamers that reach the insulation barrier and the corresponding apparent charge at (a) 20 kV, (b) 29 kV, 5.5 mm gap distance, 10G/40 sample, 77.8±0.3 K, atmospheric pressure.

Figure 5.29(a) and (b) show ϕ-q-n plots for streamer discharges at 20 kV and 29 kV respectively. The threshold level was set to 200 pC such that PD with magnitude in the order of tens of nC can be measured. With this configuration, the bush-like part of the ϕ-q-n of which magnitudes are typically below 100pC (Figure 5.25 and Figure 5.27) are not included in the graphs. Instead the high-magnitude PD pulses are of interest. At 20 kV, positive streamer channels can reach the barrier surface. This type of event can be separated in the ϕ-q-n plot from the filamentary streamers that only partially breakdown the liquid by a dramatic increase in the measured charge. Positive streamers that reached the solid insulation occur close to the peaks of the sinusoidal waveform when the applied potential is at its highest. Negative streamers which have tree-like shapes were seen with magnitude of the order of a few hundreds pC. At 30 kV, the probability of positive streamers reaching the other electrode and the corresponding charge transfer increase dramatically. Under this applied voltage, negative streamer channels can also travel to the solid insulation barrier but the occurrence rate is much less than that for the positive streamers.

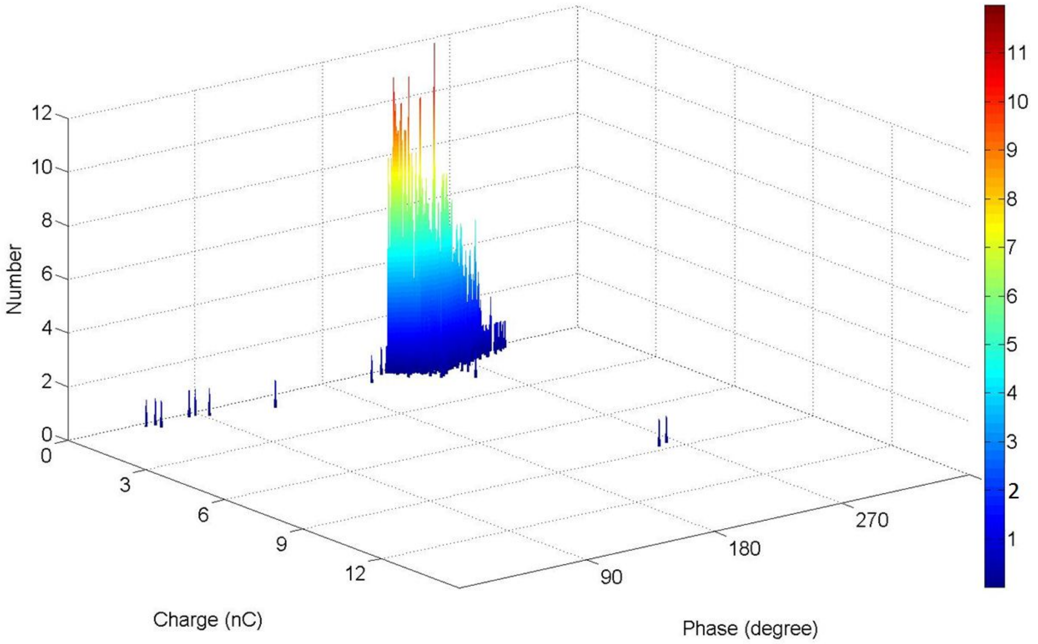

(a)

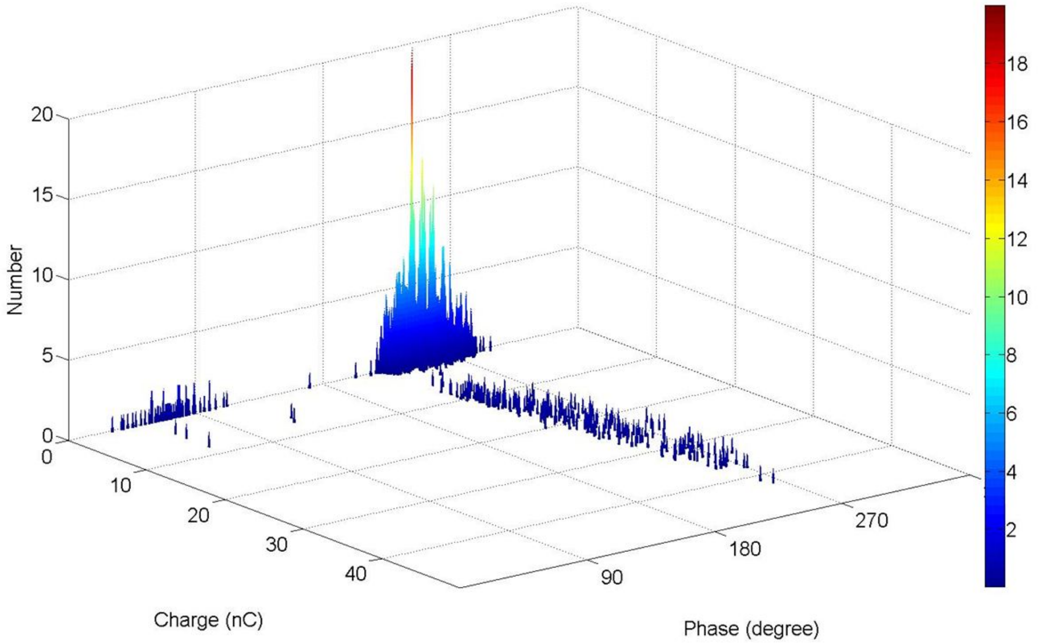

(b)

FIGURE 5.29: ϕ-q-n plots of PD in LN_2 at (a) 20 kV, (b) 29 kV, 5.5 mm gap distance, 10G/40 sample, 77.8±0.3 K, atmospheric pressure.

At closer gap distances, the overall discharge pattern is very similar to PD in larger gaps. The results presented in Figure 5.30 were measured at 15.4 kV at 1.9 mm liquid spacing gap. The applied voltage here gives a similar maximum electric field at the needle tip to that of Figure 5.27. The shadow graphs in Fig. 9b show that at this voltage level, positive streamers had reached the insulation barrier with discharge magnitudes between

2-8 nC. Meanwhile, at 5.5 mm gap distance, the applied voltage and the minimum charge required for PD events to completely bridge the gap was found to be much higher. Previous work has shown that the streamer volume and the apparent charge have a positive relation [17]. Therefore, when the needle is further away from the barrier, in order to reach the solid surface, longer filaments are required which results in the higher PD magnitudes. The increase in the required applied voltage, on the other hand, can be the result of the voltage drop across the streamer channels [104] and the reduction of the external field away from the needle tip [66].

The active phase band shown in Figure 5.30 is also wider than in Figure 5.27 for negative discharges. Although the calculated external electric field is similar in the two scenarios, the lowest initiation phase reduces to 20^0 from 32^0 when the gap distance was 3.6 mm closer. In order words, discharges can be initiated at a lower potential in the case of a closer gap distance. This can be explained by the effects of space charge from one half cycle to another. At 15.4 kV, positive filamentary streamers can reach the solid/liquid interface and possibly travel a few milimetres along the surface. The majority of the charges created during this process will remain on the surface of the solid insulation until the next half cycle. Streamer discharges which completely bridge the gap have higher magnitudes than others. In other words, the space charge built up in this case can be higher than that from PD between 5.5-mm gap and at 17.1 kV. The following result is that negative discharges can be initiated at a much lower phase voltage, e.g. at 20^0.

Figure 5.31 shows the ϕ-q-n plot and the maximum charge, cumulative number, average charge by phase window at 35 kV and 1.9-mm gap distance. The amplitude of the recorded PD pulses increases dramatically. The maximum value of charge transferred is found up to 245 nC. The probability of streamers reaching the barrier is also higher for both negative and positive streamers compared with the result during 5.5-mm experiments. Back discharge was observed for both polarities. The occurrence of discharge before the zero crossing is the result of charge accumulation on the surface of the solid insulation.

5.5.2 PTFE Results

With PTFE samples, the discharge pattern of the composite insulation system Figure 5.32 shows many similarities to that observed with G10 samples. Discharges appear more frequently in the first and third quadrant due to the effect of charge storage. Negative pulses are more frequent but less severe than positive ones. For the same applied voltages, the magnitude of positive filamentary streamers reaching the PTFE surface are in general smaller than the results presented during G-10 experiments. The average charge transfer per phase window, therefore, is also reduced.

When the applied voltage was increased to 35 kV (Figure 5.33), PD was recorded before

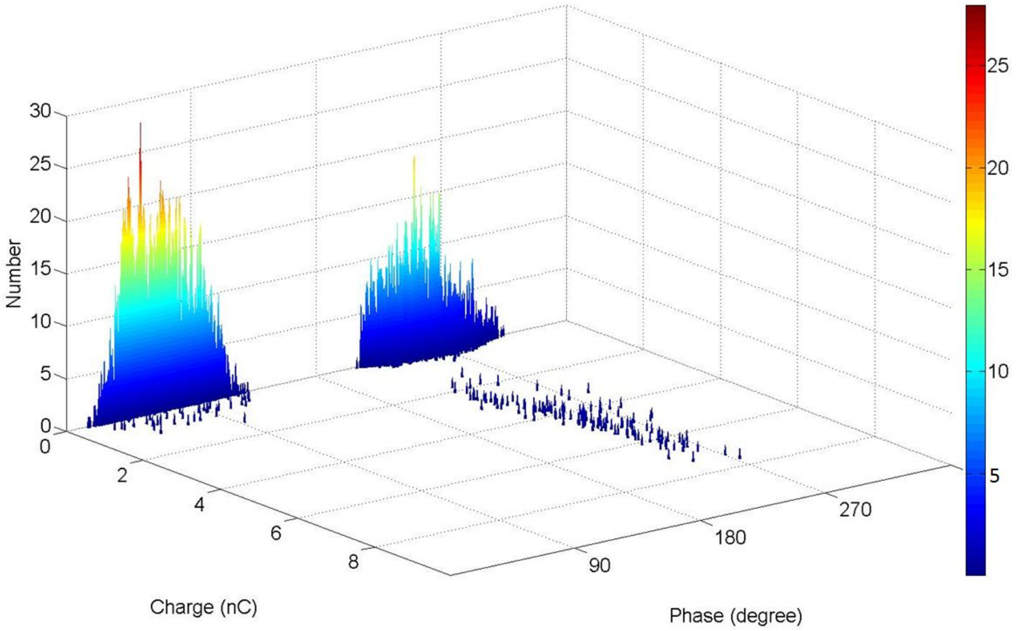

(a)

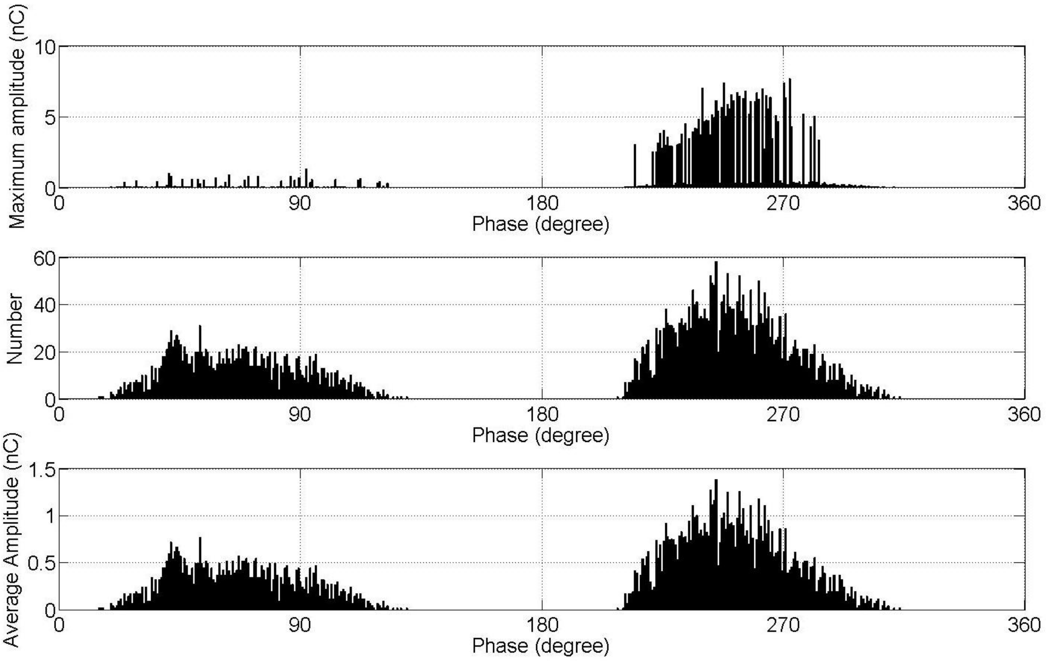

(b)

FIGURE 5.30: (a) ϕ-q-n, (b) maximum charge, cumulative number, average charge by phase window at 15.4 kV, 1.9 mm gap distance, 10G/40 sample, 77.8±0.3 K, atmospheric pressure.

the zero crossing. The back discharge phenomenon has also been seen during G10 sample experiments. Similarly, the number of pulses, maximum amplitude and average charge transfer per phase window also increase with the rise of the applied voltage due to the higher electric field at the needle tip.

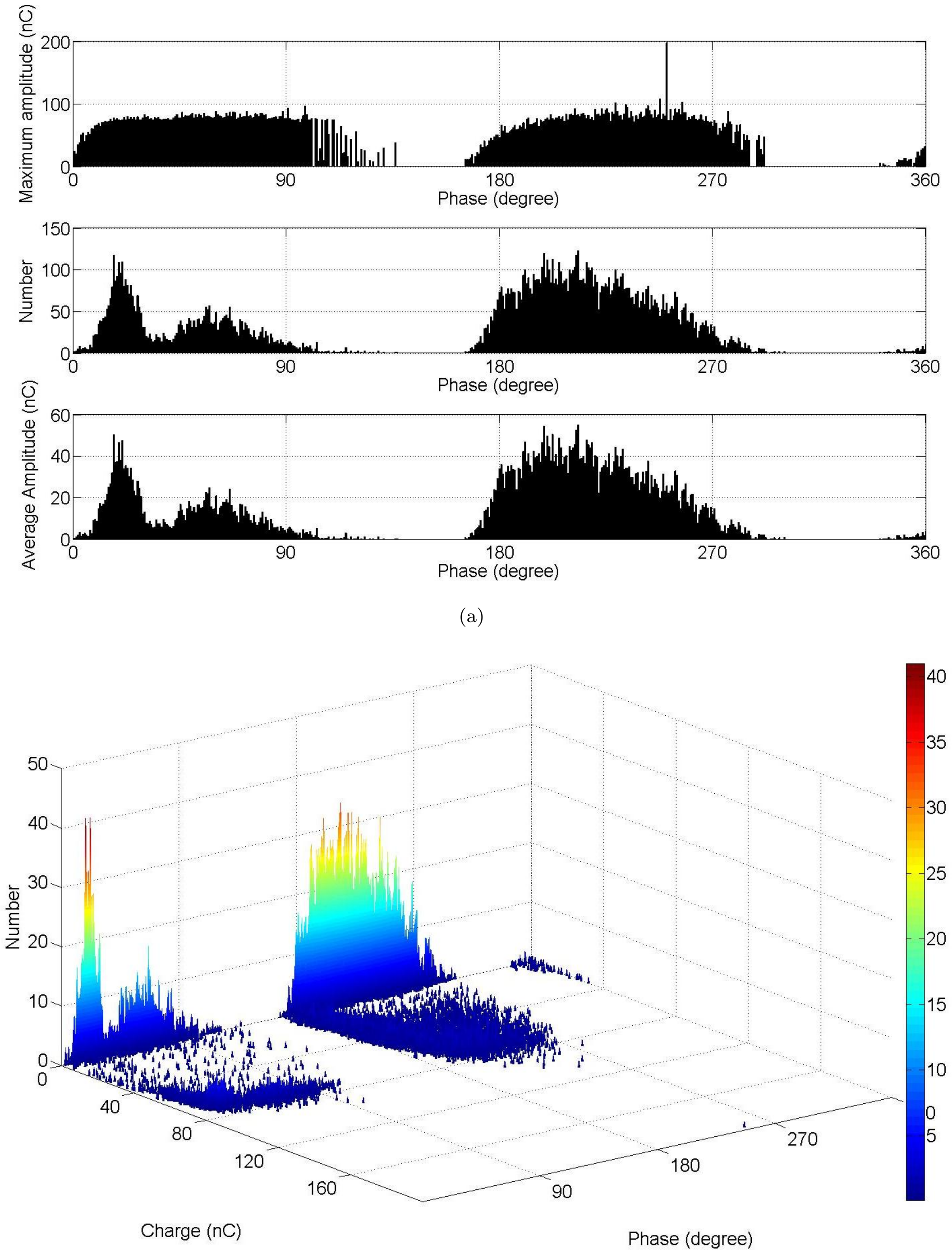

(a)

(b)

FIGURE 5.31: (a) ϕ-q-n, (b) maximum charge, cumulative number, average charge by phase window at 35 kV, 1.9 mm gap distance, 10G/40 sample, 77.8±0.3 K, atmospheric pressure.

The obtained experimental results suggest that higher charge amplitudes are recorded for streamers that reach the G10 samples under similar experimental conditions than PTFE ones. Meanwhile bush-like streamers which only involve liquid properties have almost the same apparent charge for the two tested samples. Therefore, it can be hypothesized that once the streamers attach the solid/liquid interface, the discharge profile is affected

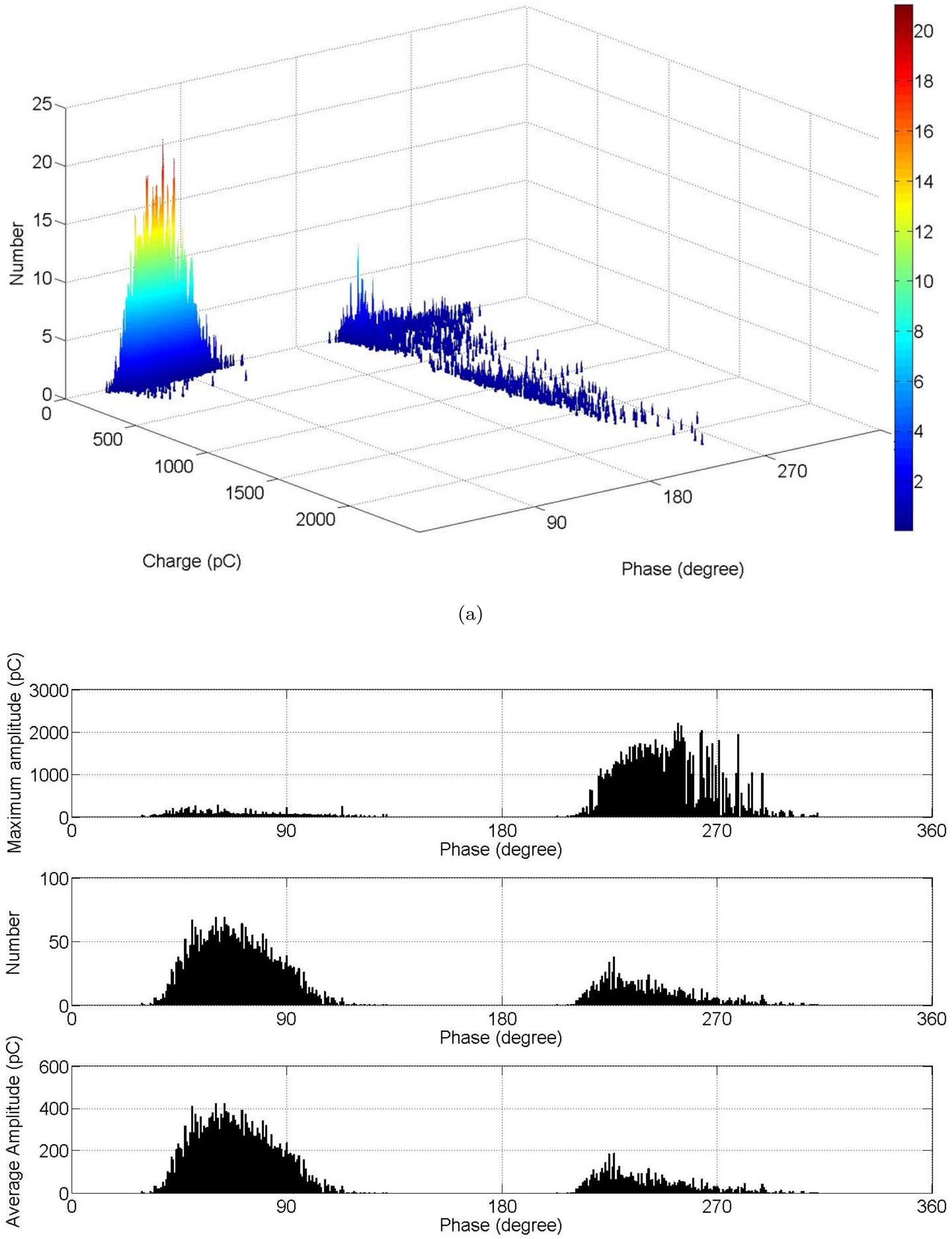

(a)

(b)

Figure 5.32: (a) ϕ-q-n, (b) maximum charge, cumulative number, average charge by phase window at 15.4 kV, 1.45 mm gap distance, PTFE sample, 77.8±0.3 K, atmospheric pressure.

by the solid insulation material. On the other hand, PD that is localised at the needle tips is not influenced by the barrier. Therefore, at 35 kV, streamers completely bridge the liquid gaps frequently and the PD pattern is very different for the PTFE and G10 samples as shown in Figure 5.31 and Figure 5.33. The reason why higher discharges were seen during G10 sample experiments remains unclear at this point but may in part be

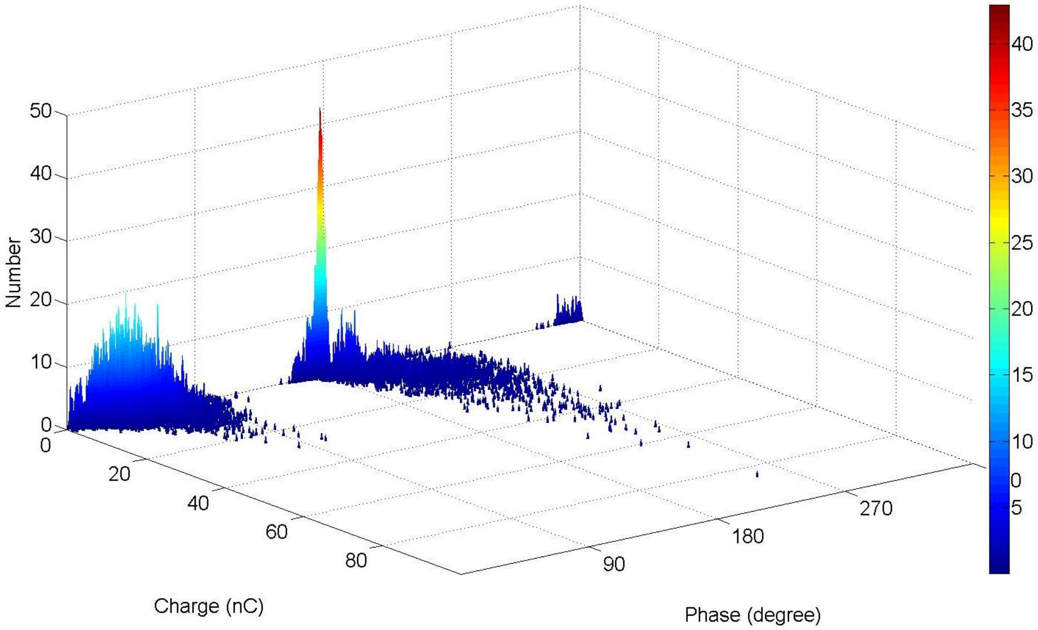

(a)

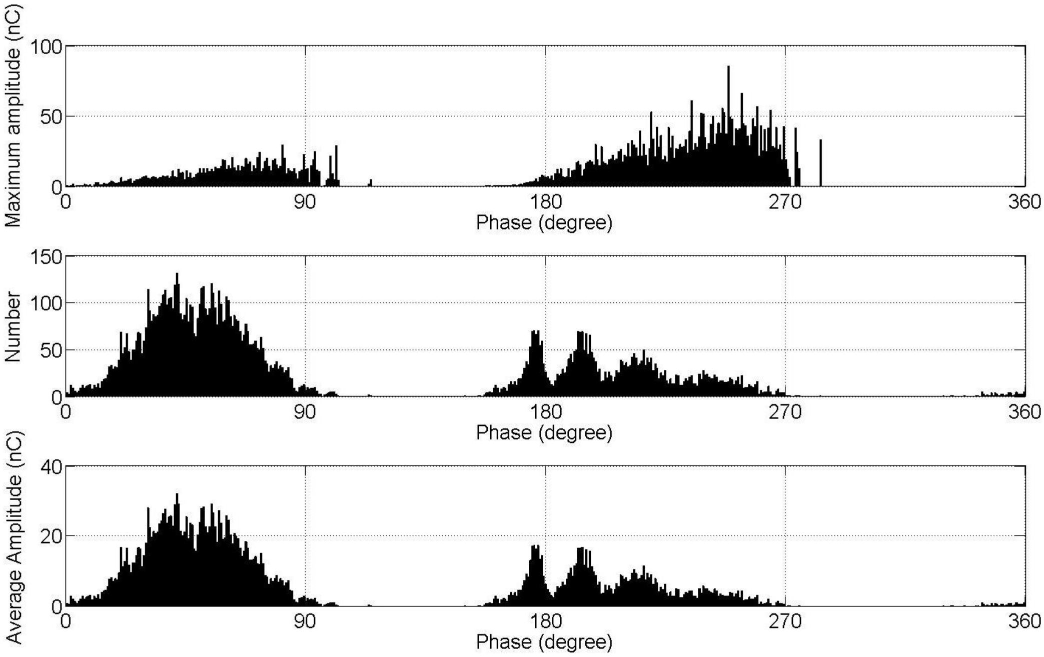

(b)

Figure 5.33: (a) ϕ-q-n, (b) maximum charge, cumulative number, average charge by phase window at 35 kV, 1.45 mm gap distance, PTFE sample, 77.8±0.3 K, atmospheric pressure.

due to its composite structure (e.g. non homogeneous) which may enhance local charge trapping. Further study on the charge storage and transfer at the solid/liquid interface is required.

5.5.3 Discussion on PD patterns in a LN_2/solid dielectric insulation system

PD in a LN_2/solid dielectric insulation system occurs more frequently in the first and third quadrant regardless of gap distances, applied voltage or the choice of solid dielectric barrier materials. The inception phase is also further away from the peaks of the applied waveform than the extinction phase. In some cases, discharges were observed before the zero crossing of the voltage waveform indicating that charge storage is a dominant factor. The question is whether charge was stored at the interface region or in the liquid. The shadow graphs of streamers show the attachments of the channels on to the surface of the solid dielectric barriers and this would suggest the charge carriers accumulate on the solid insulation surface [105].

The longer the gap distance between the two electrodes the higher the applied voltage required for the streamers to reach the barrier. The trend is shown in Figure 5.34(a). The phenomenon is the result of the voltage drop along the streamer channels and lower electric field away from the needle tip. Likewise, the minimum apparent charge recorded for the events that completely bridge the gap also increases as the gap distance increases, Figure 5.34(b). This is due to the fact that longer filaments are required for the streamers to propagate to the solid/liquid interface.

The amount of charge transferred per cycle increases as the applied voltage increases as shown in Figure 5.35. The increment is due to longer filaments in each event as well as the increased frequency of streamer appearance. A dramatic rise was observed above 18.4 kV due to the occurrence of streamer attachments to the solid barrier. As discussed previously, PD events associated with steamers that reach the barrier have much higher magnitudes due to the further propagation of the streamer channels on the surface of the solid dielectric.

5.6 Summary

The occurrence of density change channels during streamer propagation in LN_2 is evident by the dark area in the shadow graphs. This behaviour was observed for both half cycles and for different applied voltages. Density change streamers have been seen previously in LN_2 and other dielectric liquids [60]. The initiation of these streamers is better understood for cathode points than anode ones. It is widely accepted that negative streamers are initiated by field emission and electron avalanche due to high electric fields. The consequence is an initial cavity observed together with a current pulse [60] [42]. It also suggested that a current pulse occurs before a bubble is observed which could indicate that initiation happens during the liquid phase. A similar hypothesis has been proposed for transformer oil due to a smaller magnitude current pulse observed

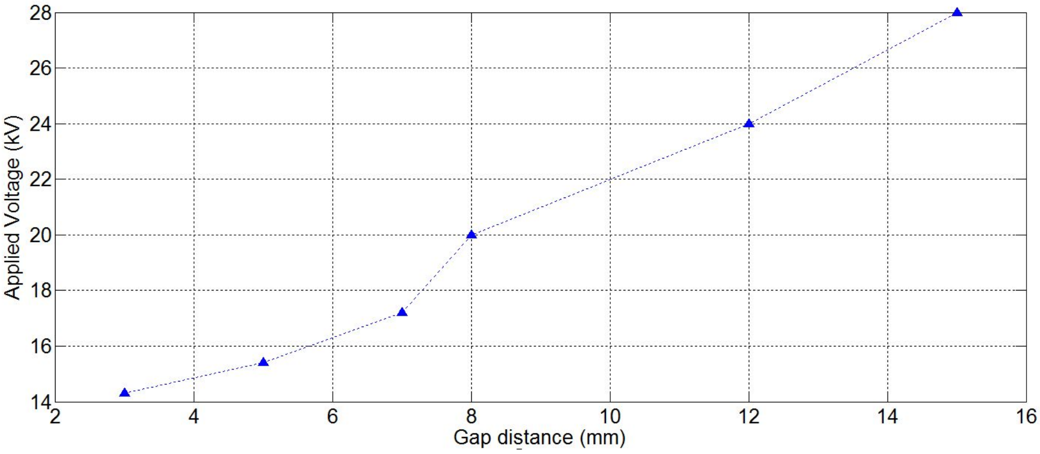

(a)

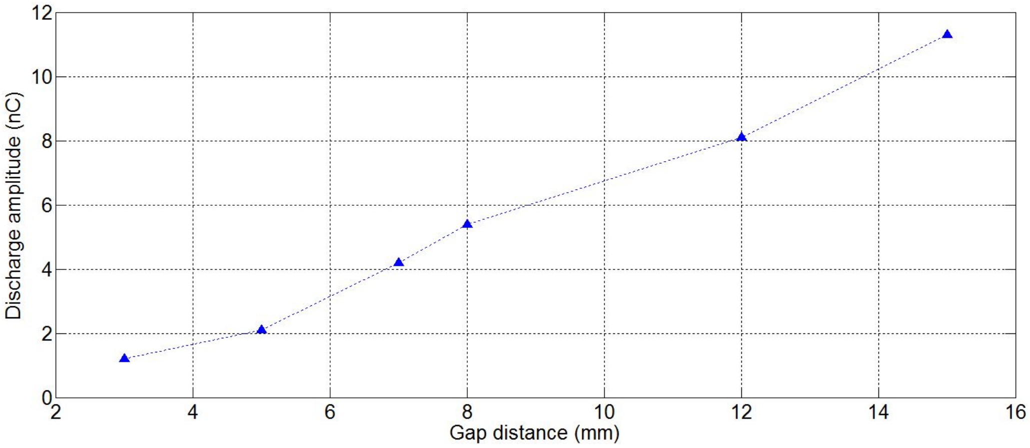

(b)

FIGURE 5.34: (a) Applied voltages and (b) minimum charge transferred of the streamers that reach the solid barrier.

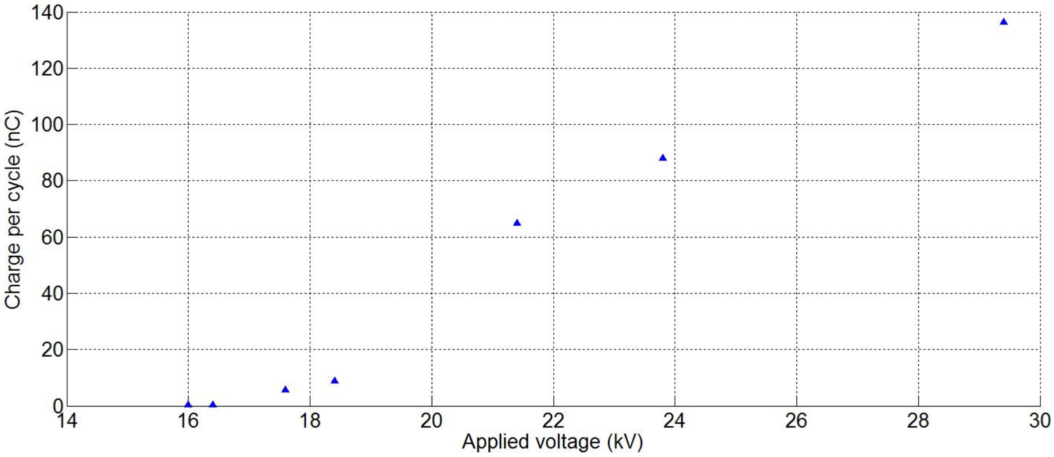

FIGURE 5.35: Charge transferred per cycle versus the applied voltage, 5.5 mm gap distance, 10G/40 sample, 77.8±0.3 K, atmospheric pressure.

in a pulse train during negative streamer discharges [78]. For LN_2, UHF results from this study also show a similar pattern, e.g. lower magnitude pulses observed during the beginning of a pulse train sequence. This could be interpreted in the same manner as in [78], e.g. discharge in liquid phase initiates bubbles which then grow and collapse as a negative streamer propagates in LN_2.

Both bush-like and filamentary propagation modes have been recorded by shadow images during each half cycle. The appearance rate of bush-like structures is more than filamentary ones during the positive half cycle, when the needle is negative to the plane electrode. Meanwhile, the filamentary mode is dominant for positive streamers. Filamentary negative streamers appear to grow out of a bush-like structure.

In the case of negative filamentary streamers, the correlated UHF waveforms contain two parts with the first one have the characteristics of a bush-like streamer while the later pulses are similar to pulses produced from filamentary anode streamers. This supports the proposed hypothesis that the enhancement of local electric field due to space charge can result in a change in propagation mode, from bush-like to filamentary [10] [64].

Partial discharges in a liquid nitrogen/solid dielectric insulation system have been investigated experimentally using a point-to-plane configuration. The inception voltage for PD in LN_2 can be estimated under the hypothesis that there is a threshold electric field above which PD streamers are initiated. In this study, this value was found in the order of 1.55 $MVmm^{-1}$.

Streamers appear more frequently from a cathode than an anode point regardless of applied voltages. This can be explained by the difficulty of ensuring a seed electron in the high electric field region, close to the needle tip during a negative half cycle when the needle point is positive. Meanwhile, during a positive half cycle, electrons can be supplied from the needle point, which in turn causes streamers to initiate [45].

Phase resolved analysis using ϕ-q-n plotting shows that PD events occur primarily in the first and third quadrants of the voltage waveform. The inception phase shifts towards the zero crossing as the applied voltage increases and eventually back discharge occurs. This indicates the importance of charge accumulation on the PD patterns in a composite insulation system. It is difficult to conclude on how the charge is stored. However, the difference in the PD patterns between PTFE and G10 barriers together with streamer attachments observed by the shadow graphs would suggest that charge carriers accumulate on the surface of the solid dielectric barrier.

One concern is the degradation of the solid materials due the streamers discharge in LN_2. The study has proposed certain voltage and charge levels in which streamer attachment happens. Below these values, the discharges only happen in the vicinity of the needle tips and do not affect the solid materials. Previous work at Southampton [106] has shown the presence of fields in excess of 2 $kVmm^{-1}$ can cause a reduction in the hysteresis between convection in the liquid and nucleate boiling. When combining this result with the findings here, it is possible to hypothesize that the presence, under fault conditions, of a very high electric field could have two significant effects: first the formation of filamentary streamers are associated with large PD events and second an increase in the number of thermally induced bubbles at or near to the high field point. Consequently, the need for early detection of any PD activity to ensure fail safe operation of HTS power apparatus is of paramount importance.

Chapter 6

Partial Discharge Streamer and Material Degradation Under Cryogenic Conditions

6.1 Introduction

In a HTS device, solid dielectrics are generally immersed in LN2. Due to its simple chemical composition, liquid nitrogen is not degraded after PD events or even complete breakdown. The only effect is the generation of clouds of gaseous bubbles which will gradually disappear providing that sufficient cooling is available. The damage caused by PD streamers on the solid part of a liquid/solid insulation system, on the other hand, is irreversible. Degradation of solid dielectrics can be accumulated over time which can result in premature failure of the materials. Therefore, besides dielectric, thermal and mechanical properties, erosion performance of the solid dielectric is also important in improving lifetime and reliability of the insulation system.

Previous work has shown that laser ablation is an effective method for studying surface erosion of insulating materials since it can be used to simulate the thermal degradation associated with electrical discharges [107] [108]. The use of laser radiation to characterise thermal degradation has also been suggested to be more sensitive than traditional Fourier Transform Infrared (FTIR) spectroscopy [109]. The principle of this method is to apply known energy to a localised region of the tested sample using a high power laser source. Two distinct processes have been suggested to be involved with ablation of materials namely photochemical and thermal [110]. UV radiation with short wavelength, e.g. 193 nm, can produce a chemical reaction which leads to bond breaking of the materials. Photons from a visible or infra-red lasers do not have enough energy to cause photochemical effects. Photon energy is transferred to the material in the form of molecular vibration which can be considered as a thermal process. In this research, thermal degradation is of interest, therefore a continuous infra-red laser source was used.

Discharge experiments utilise a point-to-plane configuration with an insulation barrier placed over the planar electrode. This arrangement was subjected to a 50 Hz AC voltage over a period of 30 minutes. The insulation barrier was either a PTFE or GRP sheet. Previous work [10] has reported a difference in surface erosion characteristics between the polymer and fibreglass. This believed to be is due to the structural difference of the two materials: homogeneous in the case of PTFE and in-homogeneous, e.g. glass fibre reinforced plastic. In this research, surface degradation was found for both tested materials indicating that PD streamers in LN2 can cause significant damage to a solid barrier between LN2 and a metal electrode. The damage caused by discharges has been compared with laser ablation results of the same materials in order to identify the mechanisms governing surface erosion under cryogenic conditions.

6.2 Laser ablation of cryogenic dielectrics

PTFE and GRP sheets were cut into 30x40 mm^2 samples for the laser ablation study. The prepared samples were radiated by a carbon dioxide laser with a wavelength of 10.5-10.6 μm. The laser was located inside a fully enclosed aluminium box with an interlock system that only allows the laser to be radiated when the cabinet is closed. Laser power output and duration is controlled from the outside of the interlocked box. The samples were located horizontally and at 200 mm away from the laser aperture. The radius of the laser spot was 3mm. The samples were tested at various laser powers (2 W to 28 W) and different time durations. The energy presented was calculated by multiplying the laser output and the exposure time. The surface damage was quantified by the pit-depth as well as the material weight loss. Each sample was weighed on a digital scale of which accuracy was 0.1 mg before and after the laser ablation test. A simple subtraction then determines the weight lost by laser radiation. After being weighted, the radiated samples were bisected in order to measure pit-depth. Similar laser ablation equipment has been used previously for the study of laser ablation in polymer [111] and silicon [112] composites.

6.2.1 PTFE Results

In the case of PTFE samples, ablation damage appears in the form of holes at the laser contact point as shown in Figure 6.1. The higher power and energy of the applied laser, the more material was ablated, indicated by an increase of the hole depth. In both cases presented in Figure 6.1, the tested samples show a V-shape profile which has been previously reported for unfilled materials in contrast to the spherical shape observed in laser ablation experiments with filled polymeric composites [111]. In all PTFE samples, laser ablation damage was from vaporisation of material, almost no carbonisation was observed. Figure 6.2 shows the variations of the erosion depth as a function of the laser energy. These samples were exposed to laser radiation for a fixed period of 10 s while the laser output increased from 3 W to 27 W. The hole depth increases almost linearly with laser energy. The linear relationship between radiated energy and hole depth has been reported for polypropylene and silicon rubber [111]. Compete puncture of a 3-mm PTFE sample occurred when the energy exceeded 350 J.

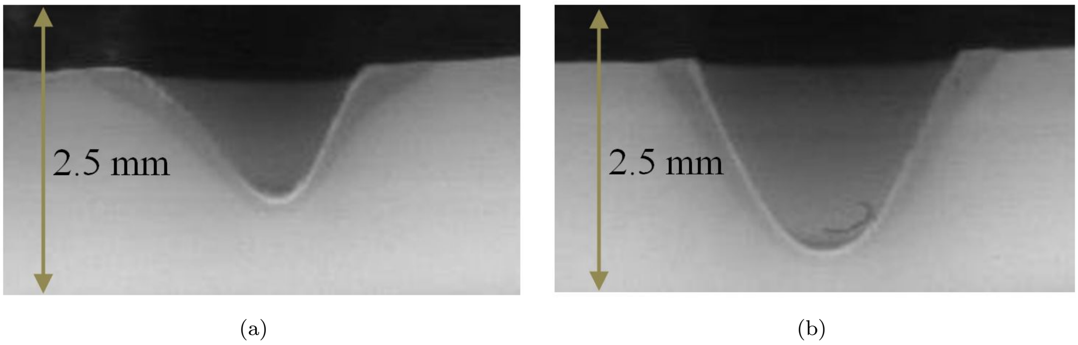

(a) (b)

FIGURE 6.1: Cross sections of erosion pits in PTFE formed by laser ablation at (a) 9 W, (b) 24 W.

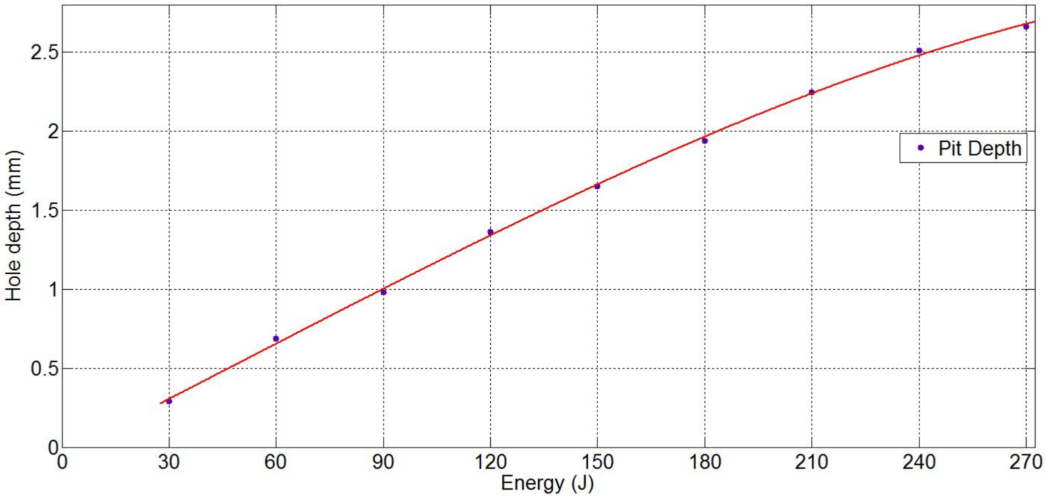

FIGURE 6.2: Hole depth as a function of laser energy.

Due to the long wavelength of the laser, the impact energy of laser photons on PTFE is not enough to break the polymer bonds nor create chemical reaction. Instead, the photon energy is transferred into the material in terms of thermal vibrations of molecules. The result is a local heating at the contact points of laser radiations. Due to the low thermal conductivity of PTFE, the local heating cannot be dissipated sufficiently which results in a dramatic increase of temperature. The increase of local temperature leads to liquidisation and eventually vaporisation of the PTFE samples. Laser ablation damage has been found to be less for materials which have higher thermal conductivity such as carbon fibre composites [111].

6.2.2 GRP Results

While the damage caused by laser ablation on PTFE was simply the removal of material, the observed phenomenon for the GRP samples was more complicated. This is because of the glass/epoxy structure of the composite. The epoxy resin can be degraded at much lower temperature, a few hundred degrees; meanwhile the degradation of glass fibre only occurs well above a thousand degrees [113]. Therefore, at lower laser energy (below 100 J), only the epoxy layer was removed as shown in Figure 6.3 (a) and (b). The size of the degraded hole increases with the radiated energy. As the energy increases above a few hundred Joules, melting of the glass fibre was also observed (Figure 6.3 (c) and (d)). Microscopic images of the eroded G10 samples show clearly the removal of epoxy resin which results in the exposure (Figure 6.4 (a)) and liquidation (Figure 6.4 (b)) of the glass fibre weave.

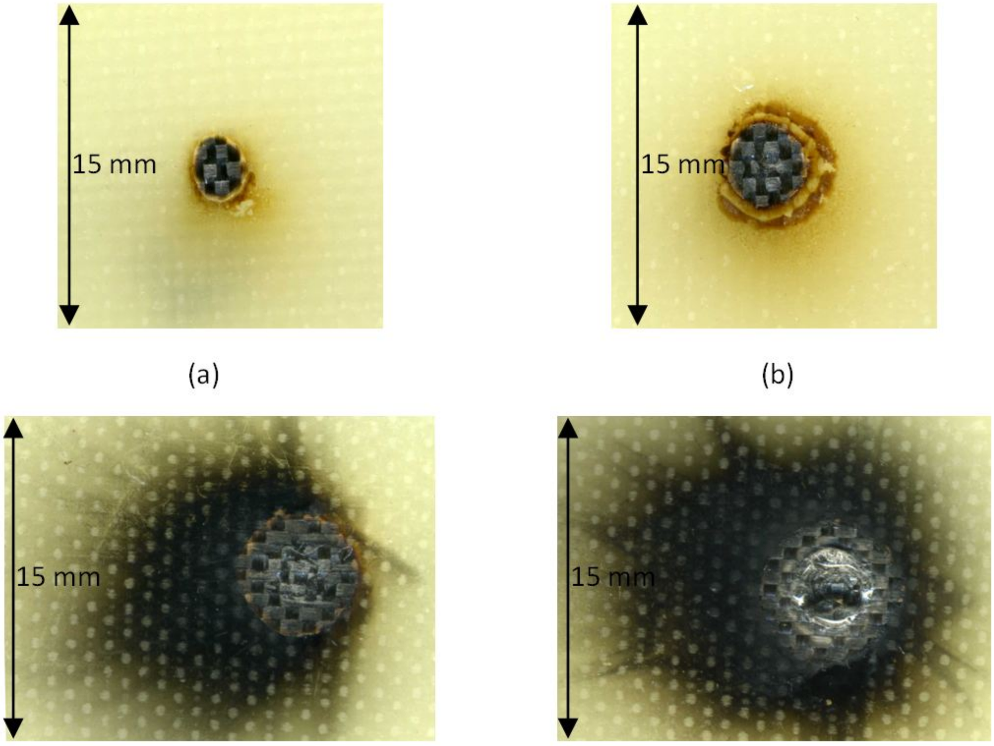

(a) (b)

(c) (d)

FIGURE 6.3: Laser ablation results of GRP samples at (a) 15 W and 15 J, (b) 15 W and 30 J, (c) 15 W and 240 and (d) 28 W and 420 J.

Different to the PTFE samples, carbonisation was observed on the surface as well as in the bulk of the GRP samples due to pyrolysis of the organic epoxy. When fibreglass

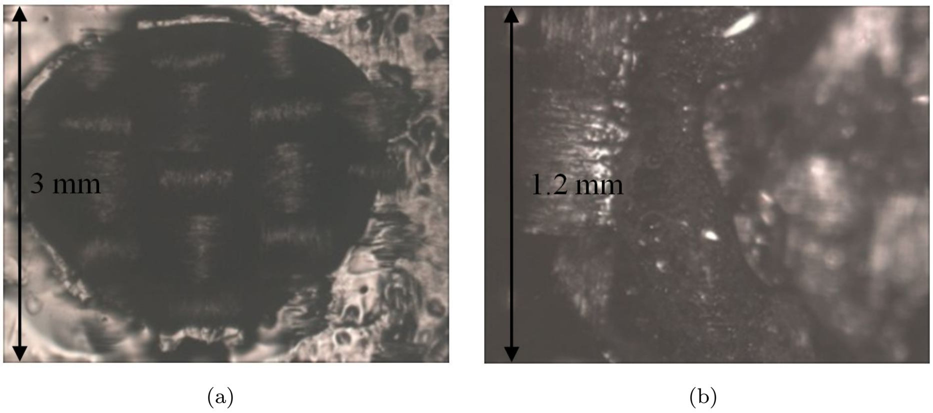

(a)

(b)

FIGURE 6.4: Laser ablation results of GRP samples at (a) 15 W and 15 J, (b) 28 W and 420 J.

sheets were exposed to high energy radiations, carbon products were found up to tens of millimetres away from the 3-mm radiated circle as shown in Figure 6.3 (c) and (d). On the other hand, using the same power and energy, vaporisation of PTFE was localised around the exposed region. Immediately after being radiated, PTFE was found softened or in a liquid form over a few-millimetres around the contact area. If the sample then was left at room temperature for a few minutes, liquid PTFE would return to its original solid form. The foregoing observation is the result of thermal conduction which leads to an increase in temperature of the surrounding environment. Although this rise in temperature is high enough to melt PTFE, it is not sufficient to cause vaporisation of the polymer. Meanwhile, in the case of GRP, the thermal conduction causes thermal decomposition of the epoxy resin which results in the carbon products observed far away from the laser contact point. Thermal decomposition of the epoxy resin is a irreversible process and very different to the softening of the PTFE sample which has the ability to recover.

The mass loss data for ablated GRP and PTFE samples are shown in Figure 6.5. The power laser was set at 50% and 95% of the maximum power corresponding to 15W and 28 W respectively. Below 800 J, for PTFE samples, the mass lost data is very similar for both power levels. As the energy increases, the results during 15-W tests saturated at just below 55 mg while the mass loss by 28-W laser continued increasing. For a given laser power and regardless of the radiated energy, PTFE samples experienced more weight reduction compared with the other material eventhough the infrared absorptivity of PTFE is higher than that of GRP: 1.3 [114] compared with 0.7 [115] respectively. The observation is the result of different ablating processes for the two materials. Under the same radiated conditions, PTFE samples experience a large amount of material removal due to material vaporisation while the glass fibre was hardly melted. In addition, the weight loss from the epoxy part of the GRP samples is very limited due to the fact that majority of the carbon products still remain on the samples.

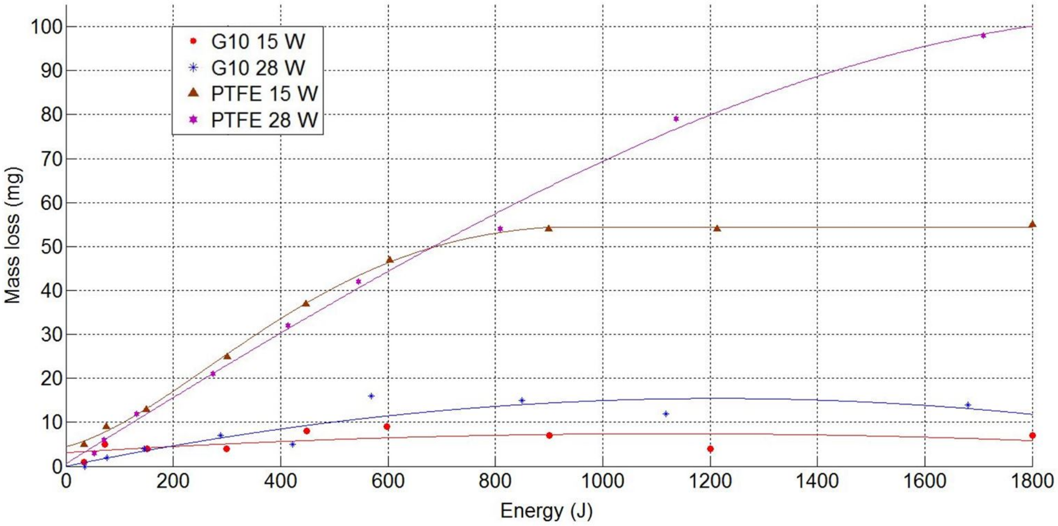

FIGURE 6.5: Laser ablation data for G10 and PTFE samples at 15 W and 28 W.

6.3 Degradation of solid dielectrics under cryogenic conditions

In the previous chapter, pre-breakdown streamers in LN2 were characterised as gaseous conducting channels propagating from the needle tip towards the planar electrode. Close to the PD inception voltage, density-change channels propagate less than 1 mm and do not reach the solid barrier. In fact, the requirements for fully-developed streamers have been discussed in terms of applied voltage and minimum apparent charge (Figure 5.34). For a distance of 4.5 mm between the needle and the planar electrode, applied voltage and charge transferred during a PD event need to be above 15.5 kV and 2 nC respectively. Figure 6.6 shows examples of streamers that localise at the needle tip (Figure 6.6 (a)) and completely bridge the liquid gap (Figure 6.6 (b)). Once reaching the solid insulation, the channels can continue propagating along the surface of the barrier. The attachment of streamer channels does not necessarily lead to degradation of the solid barriers. In fact, up to 30 kV and for 30 minutes of applying voltage, no significant damage was observed on the surface of the insulation barriers. Surface erosion on both materials were seen when the applied voltage was increased to 35 kV.

6.3.1 PTFE

Figure 6.7 (a) and Figure 6.8 (a) shows histograms of accumulated PD pulses in a LN2/PTFE configuration at 35 kV for 4.5-mm and 4-mm electrode gap distance respectively. The data were captured after 5 minutes of applying voltage and for a duration of 1 minute. The threshold level was set at 1.5 nC since PD pulse of which magnitude below this level only partially breakdown the liquid gap and only fully developed

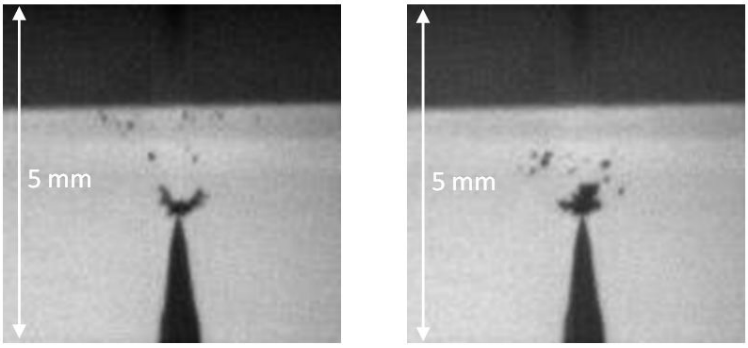

(a) Partial breakdown of the liquid

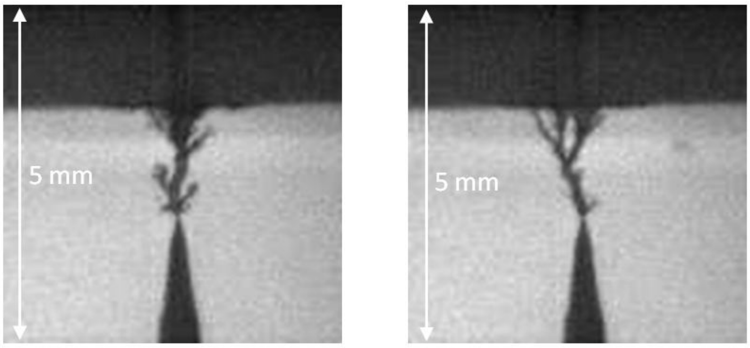

(b) Complete breakdown of the liquid

FIGURE 6.6: Examples of density change streamers in LN2 at (a) 15 kV (b) 20 kV, GRP sample, LN2 at 77.8±0.3 K, atmospheric pressure.

streamers are of interest. From the recorded data, streamers are accompanied with large PD events (tens of nC). PD patterns are found unchanged during the 30 minutes of the experiment. The ϕ-q-n plots (Figure 6.7 (b) and Figure 6.8 (b)) were constructed from unipolar charge data from which the charge transferred per cycle can be calculated. PD patterns are similar for the two gap distances with higher magnitude pulses observed during 4-mm gap experiments. Large PD events at 35 kV are followed by vaporization of a large volume of LN2 as shown in Figure 6.9. Gaseous bubbles of which diameters were in the order of millimetres were found after the discharges and could last for several half cycles. The shadow graphs recorded also show a continuity in propagation of density change channels on the surface of the insulation barrier. On contact with the barrier, although some of the charges from the streamers can penetrate into the material bulk, the majority of them must accumulate on the surface of the barrier and increase the tangential electric field. Eventually, breakdown occurs in the liquid along the surface and results in the observed phenomenon. It is possible that during this process, surface discharge characteristics, e.g. branched structures, occur, however, the imaging configuration in this experiment does not allow capturing such behaviour. In some occasions, the accumulation of charges on the surface of the PTFE barrier is dominant over the external field such that the local electric field is sufficient to ionise LN2 and initiate streamer filaments that propagate from the liquid/solid interface as shown clearly in

Figure 6.9 (b).

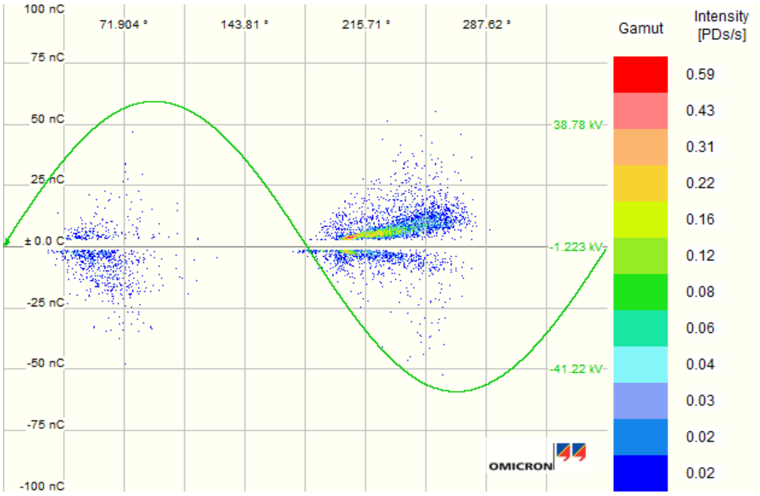

(a) Bipolar

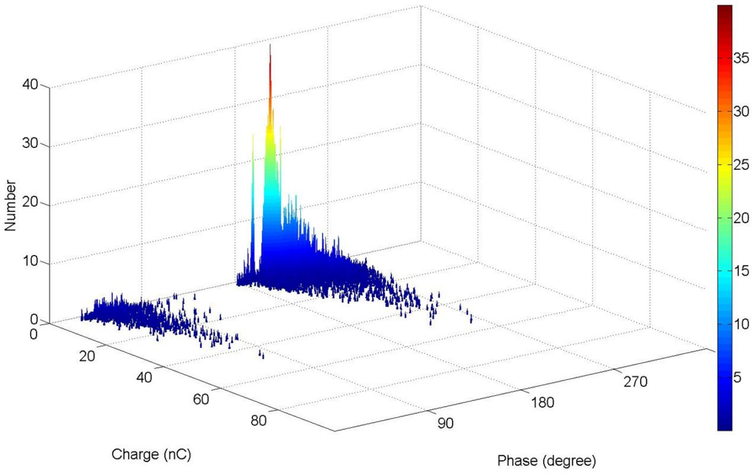

(b) Unipolar

Figure 6.7: Accumulated PD pulses during one minute, PTFE sample, 35 kV, 4.5 mm gap distance, 77.8±0.3 K, atmospheric pressure: (a) Mtronix histogram, (b) ϕ-q-n plot produced from (a).

6.3.1.1 Surface degradation of PTFE barriers

Typical erosion characteristics of a PTFE barrier after 30 minutes of applied voltage are shown in Figure 6.10. The damage remains only on the surface and does not penetrate into the bulk of the material. Laser ablation results, on the other hand, show significant vaporisation and mass loss while the damage from experiments in LN2/PTFE only appears on the surface and almost no weight loss was seen. Such differences suggest that thermal degradation is not an important factor because under cryogenic conditions, local thermal effects become less effective. Any localised heating produced by PD streamers can be quickly dissipated by the surrounding liquid nitrogen. The erosion level reduces when the gap distance between the two electrodes was increased. This could be because

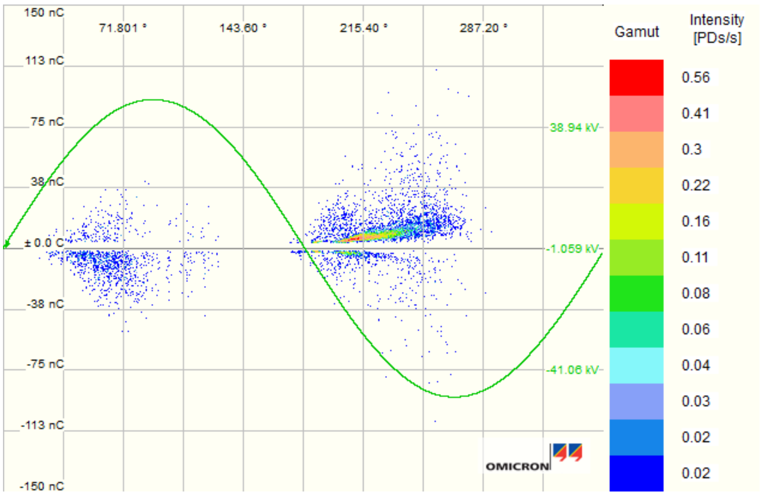

(a) Bipolar

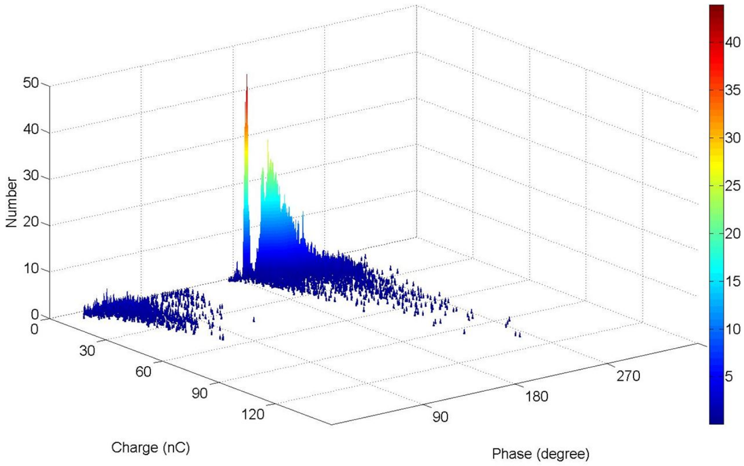

(b) Unipolar

Figure 6.8: Accumulated PD pulses during during one minute, PTFE sample, 35 kV, 4 mm gap distance, 77.8±0.3 K, atmospheric pressure: (a) Mtronix histogram, (b) ϕ-q-n plot produced from (a).

of a reduction in the maximum electric field at the needle tip as well as higher voltage drop due to longer streamer filaments. Both factors will lower the amount of charges and local electric field on the surface of the polymer and therefore, reduce the surface erosion.

For both gap distances, the damage profile is very similar. As can be seen in Figure 6.10, there appears to be an undamaged circle of which the centre is directly above the needle tip. Outside of the circle, degraded material is in the form of a darkened surface and observed up to 20 mm away from the centre. From the captured streamer images, the white circle in Figure 6.10, e.g. undamaged PTFE, is where the attachments between density change channels and the solid barrier occur whereas the eroded area corresponds to the propagating phenomenon of streamers along the liquid/solid interface. Therefore, it can be hypothesised that the damage is caused by the streamer propagation along the

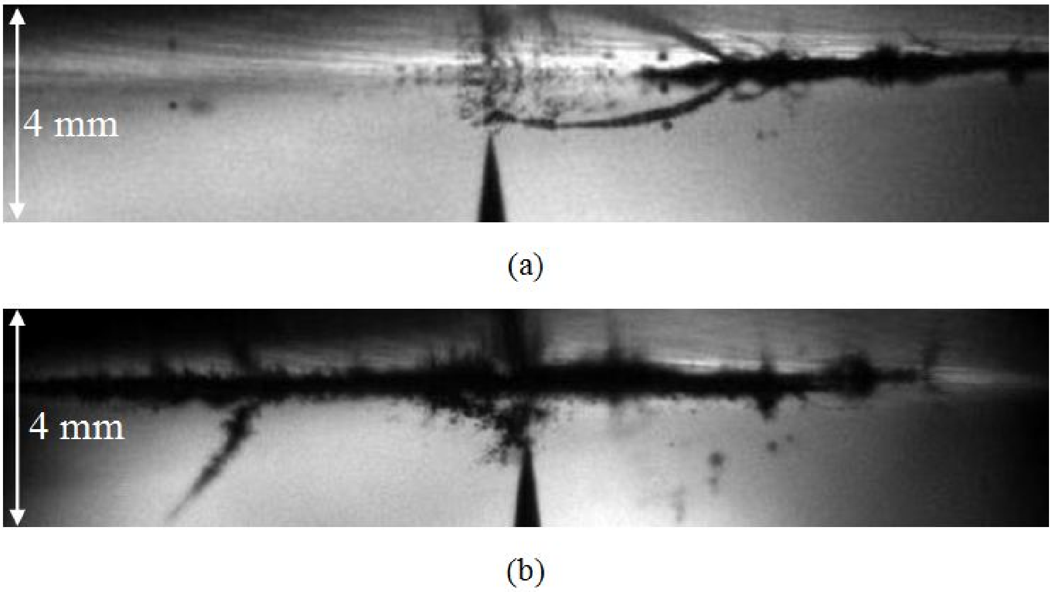

Figure 6.9: Filamentary streamers propagating along the surface, at 35 kV, 4.5 mm gap distance, PTFE sample, 77.8±0.3K, atmospheric pressure.

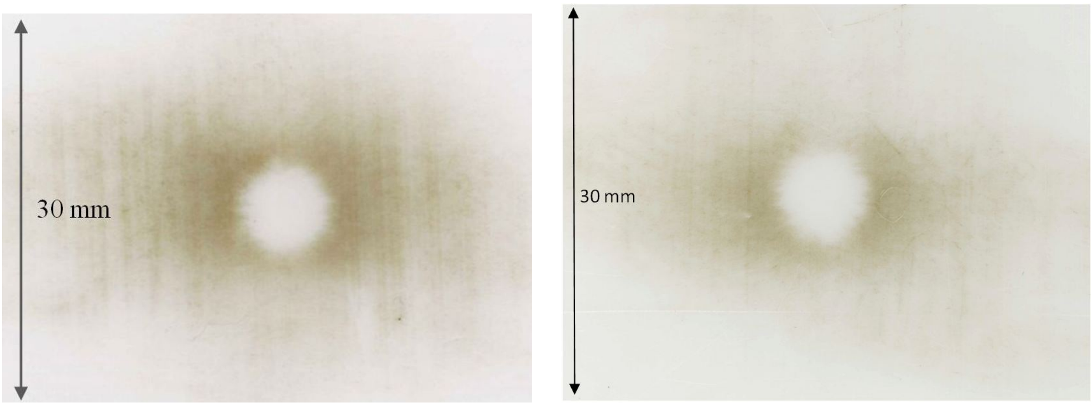

(a)

(b)

Figure 6.10: Surface degradation on PTFE samples (a) 4 mm, (b) 4.5 mm.

surface of the polymer rather than initial attachment.

6.3.1.2 Raman analysis of the damaged PTFE surface

Raman spectroscopy relies on inelastic scattering of monochromatic light from a laser source. Interactions between laser photons and molecules result in a shift in frequency of the scattered photons. The phenomenon is referred as the Raman effect [116]. The information obtained from the Raman shift can be used to analyse surface chemical compounds of the incident material. In a recent research, Raman spectroscopy has been used as a technique to characterise chemical components within electrical trees in polyethylene [117] [118]. In this work, the same method was applied to the eroded samples in order to study the chemical compounds produced during PD in LN2. The information provided by Raman spectroscopy can be used to analyse mechanisms governing the degradation phenomenon of a cryogenic solid dielectric. The details of the experimental apparatus are included in [118].

Figure 6.11(a) shows two Raman spectra, A and B, which were obtained from the points on the material surface illustrated in the top right corner of the Figure. From point B, all the main bands of PTFE are included such as peaks at 383 cm^{-1} (rotation of CF_2), 729 cm^{-1} (vibration of CF_2) and 1379 cm^{-1} which is the characteristics of C-C bond. Similar Raman spectra of PTFE has been reported in [119]. Therefore, the Raman spectra of the white circle, point B, shows only the characteristics of PTFE and no further degradation products are seen (Figure 6.11(b)). This supports the hypothesis given above that initial attachments of density change streamers may not be harmful to the PTFE barrier. For point A, the situation is rather complicated. Firstly, besides the characteristics of PTFE (peaks that represent F-C-F and C-C bond), a high level of fluorescence was observed. Although fluorescence cannot be used to analyse the actual chemical components since it superimposed most of the peaks, its presence suggest a production of new species different to PTFE during the discharge experiments. This then would indicate that the material has been degraded. The link between fluorescence and ageing of a solid dielectric has been suggested previously in various research [117] [118] [120]. The second phenomenon is the high intensity around 1300-1600 cm^{-1}. Previous work [121] has shown that Raman spectroscopy of carbon is characterised by two strong band 1360 and 1560 cm^{-1}, namely D and G band respectively. Due to the high intensity of fluorescence, the two bands cannot be distinguished. However, from the measure Raman spectra, it can be suggested that carbonised products were produced. Similar observations have been reported for electrical trees in polyethylene [118].

Carbonised products together with highly fluorescent species cannot be produced by thermal effects due to two reasons. Firstly, carbonisation was not observed during laser ablation experiments. Secondly, PTFE barriers were at cryogenic conditions, therefore, in order to degrade the material thermally, the amount of heat required is much higher than experiments taken at room temperature. Accumulation of thermal degradation from different streamer events is unlikely since the barrier was submerged in a large volume of LN2 of which temperature measured at the discharge location only showed a fluctuation up to a few Kelvins. The discussion is in agreement with previously published work [122] [123] in which thermal degradation is considered an unimportant phenomenon during ageing processes of cryogenic dielectrics.

In terms of chemical degradation, from the experimental procedure discussed in Chapter 3, the presence of oxygen in the system can be neglected. Previous work [124] [125] [126] has shown that oxidation plays an important role in the degradation of polymers by corona discharges in gas. Whereas in a pure nitrogen environment, e.g. without oxygen, scarcely any noticeable degradation of polyethylene was observed [126]. This is simply

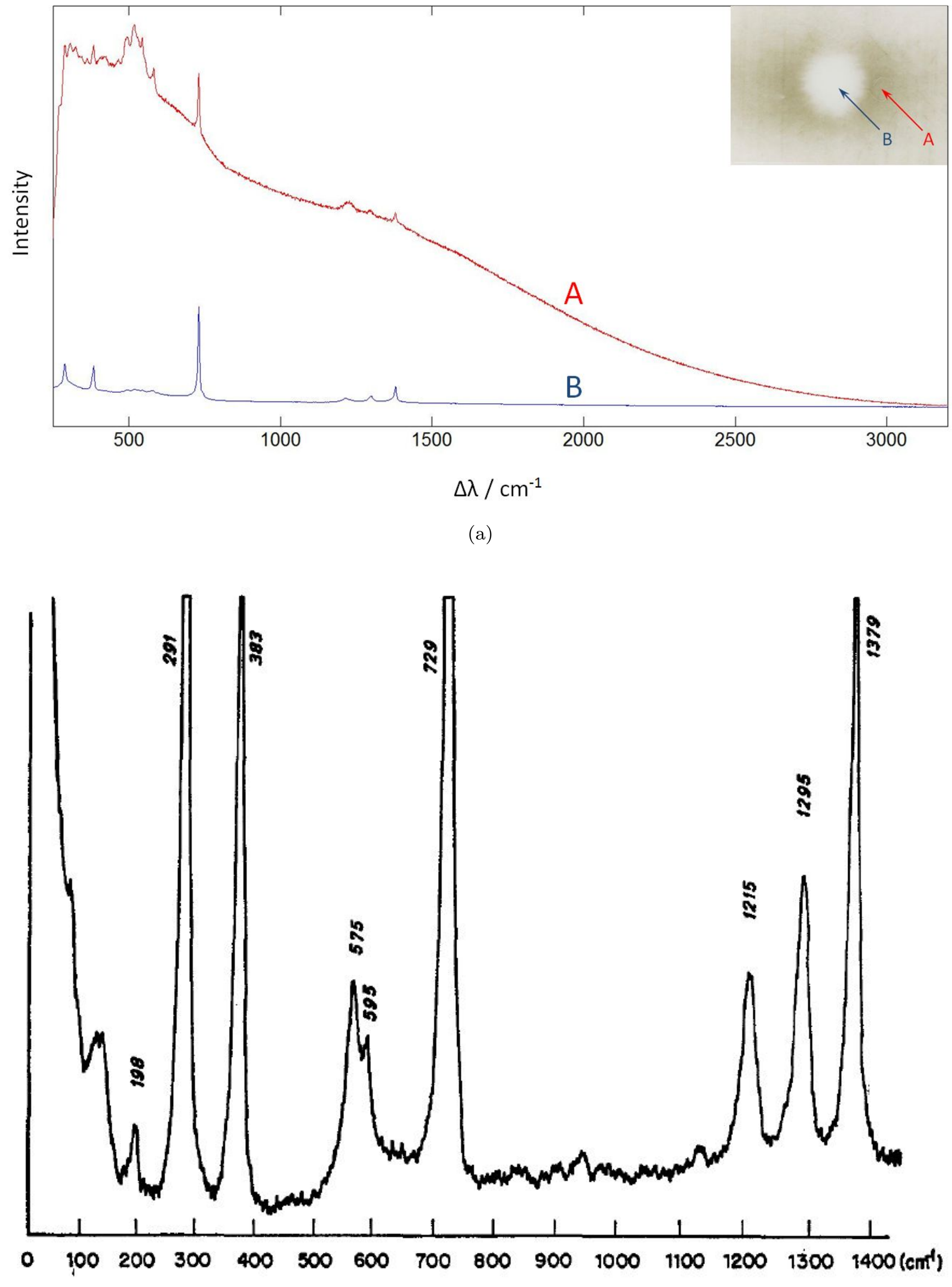

(a)

(b)

Figure 6.11: Raman spectroscopy of damaged PTFE barrier (a) and virgin PTFE (reproduced from [119]).

because nitrogen is a much less active gas compared to oxygen. Therefore, in a solid dielectric/LN2 insulation system, chemical degradation is unlikely to be an important factor [127]. Mechanical damage, although can be a significant process as will be shown later on, cannot affect chemical contents of a material. In a gaseous environment, previous work has shown that bombardment of charge carriers on an insulation can cause micro cracks [128], sputtering and damage to polymer chains [124]. The bonding energy of a C-C bond is 3.6 eV while a C-F bond is much stronger, $\sim$ 5.2 eV [129]. These bonds can be ruptured by electrons from LN2 streamers channels of which energy has been reported to be more than 10 eV [58]. Surface modification of PTFE due to nitrogen plasma has been reported to be in the form of high concentration of C-C as well as carbonaceous products as a consequence of sputtering of positive nitrogen ions on the surface of the polymer [130]. Whereas, the effects of electrons from a N2/H2 plasma treatment are the production of CHF-CHF and C=N groups [131]. Given that streamers in LN2 can be regarded as cold plasma filaments [58], the result presented here is in agreement with those obtained during nitrogen plasma experiments such as carbonisation of the polymer surface. However, in this work, the presence of C=N group was not found due to the high degree of fluorescence. Nevertheless, it can be hypothesised that the degradation phenomenon observed in a LN2/PTFE insulation system can be, predominantly, due to the interactions of streamer charges with the polymer surface.

6.3.2 GRP

Figure 6.12 shows the histogram (a) and ϕ-q-n plot (b) of PD data recorded for 3000 cycles, e.g. 1 minute, after 5 minutes of applying voltage. Similar to previous measurements, the threshold was set at 1.5 nC such that only streamer events that reached the solid barrier would be recorded. Much larger PD pulses were observed for GRP insulation barrier than PTFE with the maximum apparent charge reaching 250 nC. As has been discussed in Chapter 6, higher PD magnitude during discharges on a GRP barrier is partly due to the inhomogeneous structure of the material which produces local trapping sites [132]. The PD pattern is also very different between PD with fibreglass and PTFE barriers. In the case of fibreglass, large PD events exceeding 30 nC were seen before the zero crossing of the applied voltage. Meanwhile with PTFE barrier, PD at the zero crossing has significantly lower magnitude especially when the waveform changes from negative to positive, PD pulses above 1.5 nC were not observed. Since at the zero crossing, the external electric field is at a minimum, PD events occur near zero crossing point must be the result of charge storage on a surface of a solid barrier. The observation, therefore, would further confirm that more charges were trapped on the surface of GRP than PTFE barriers under similar experimental conditions. PD characteristics remain unchanged when the gap distance between the two electrodes were reduced to 4 mm as shown in Figure 6.13. The only difference, similar to the case of PTFE barriers, is the increase of apparent charge as well as the number of PD events.

Figure 6.14 and Figure 6.15 shows examples of filamentary streamers during experiments with GRP barrier at 35 kV. The images were taken at 30,000 and 20,000 fps respectively. The recorded streamers, in this case, are usually localised around the attachment points

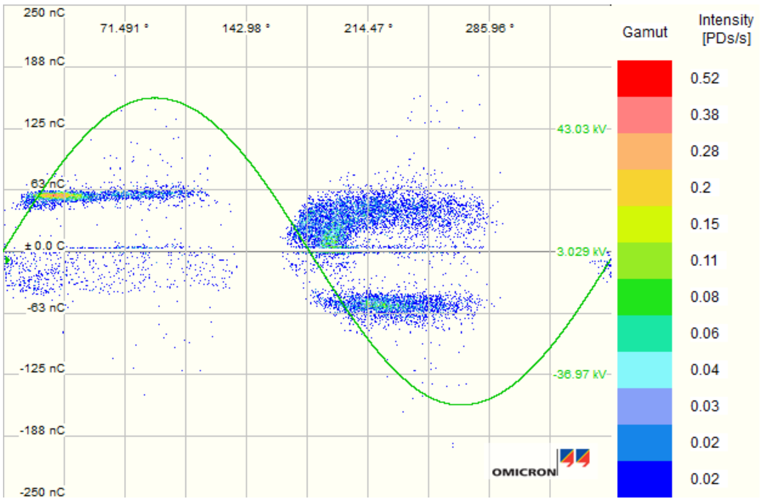

(a) Bipolar

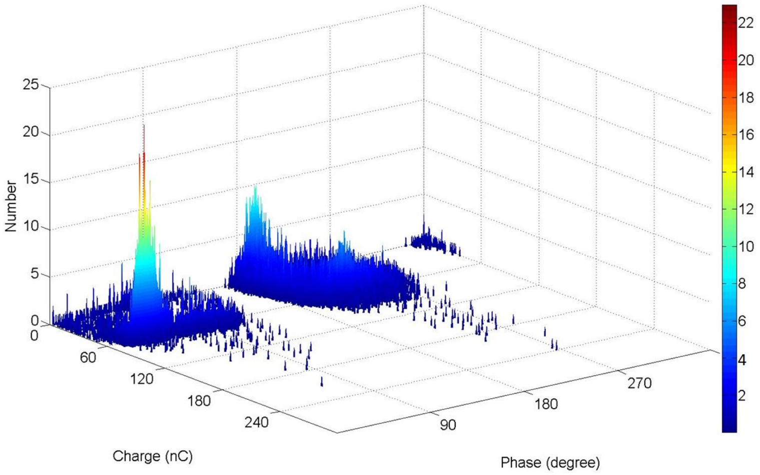

(b) Unipolar

FIGURE 6.12: Accumulated PD pulses during one minute, GRP sample, 35 kV, 4.5 mm gap distance, 77.8±0.3 K, atmospheric pressure: (a) Mtronix histogram, (b) ϕ-q-n plot produced from (a).

(except for Figure 6.15 (b)) whereas in the case of PTFE/LN$_2$ insulation system, gaseous channels tend to propagate along the surface of the barrier (Figure 6.9). Attachment of PD streamers on to the GRP surface results in a vaporisation of a larger liquid volume than that observed for PTFE samples. This characteristic is in agreement with Figure 6.12 in which more intensive PD pulses were seen during GRP/LN$_2$ experiments. The development of streamers into an arc discharge was also observed (Figure 6.14 (b) and Figure 6.15 (c)) but for GRP samples only. The reason why arcs were only seen during fibreglass tests can be because of the charge trapping phenomenon on the surface of the GRP barriers. The charges can be combined with those from the streamer channels and create a large amount of current which results in a glowing arc as observed.

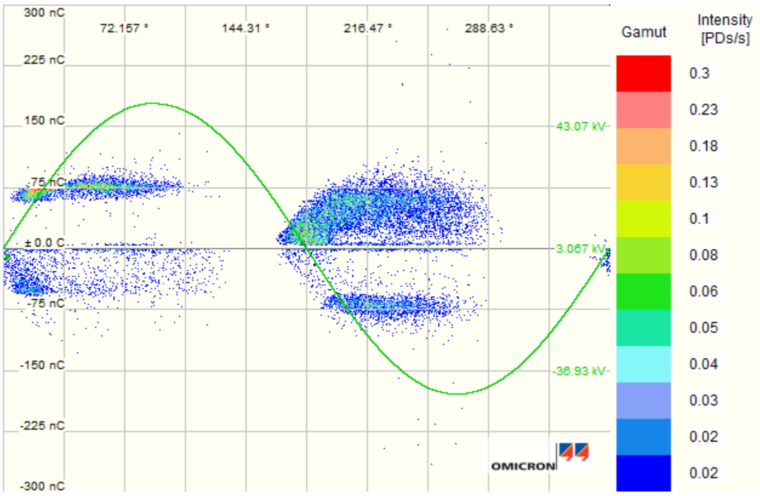

(a) Bipolar

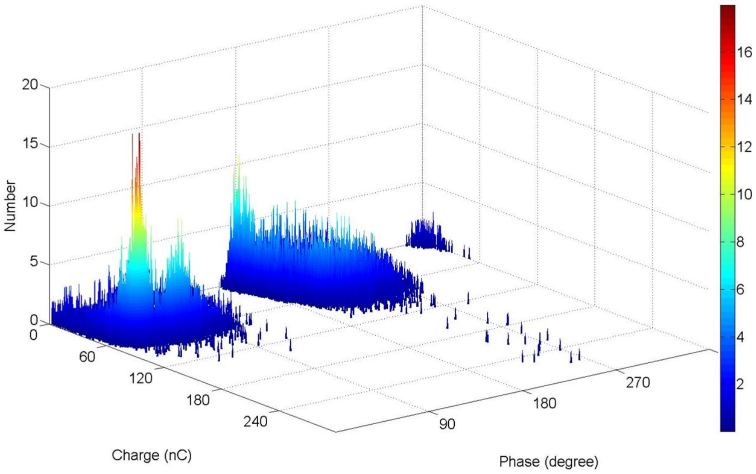

(b) Unipolar

FIGURE 6.13: Accumulated PD pulses during one minute, GRP sample, 35 kV, 4 mm gap distance, 77.8±0.3 K, atmospheric pressure: (a) Mtronix histogram, (b) ϕ-q-n plot produced from (a).

6.3.2.1 Degradation of GRP barrier

Typical erosion behaviour of fibreglass insulation barriers caused by PD streamers in LN_2 is shown in Figure 6.16. Erosion appears in form of a circular hole together with further cracking on the surface of the material. Different to laser ablation results, not only the epoxy layer but also the glass fibre was removed. Recorded shadow graphs reveal that the eroded hole was within the attachment area of streamer channels (Figure 6.14 and Figure 6.15). It can be hypothesised that the major damage area, the circular pit, is caused by initial streamer attachments while the cracking is the consequence of streamer propagation along the surface of the composite. Microscopic images of the eroded hole (Figure 6.16 (b)) show that the glass fibre was broken mechanically rather than melted thermally. In fact, free particles were observed only during the degradation of GRP samples as shown in Figure 6.17. The particles must be the products of discharges

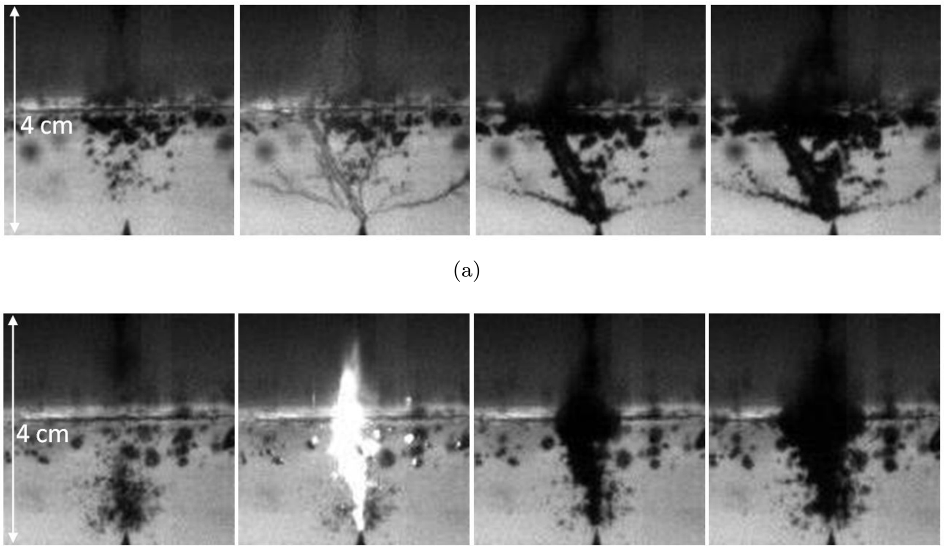

(a)

(b)

FIGURE 6.14: Examples of filamentary streamers with microscope lens at 35 kV, 4.5 mm gap distance, GRP sample, 77.8±0.3K, atmospheric pressure: (a) vaporising a large amount of LN_2 at the contact point, (b) development of streamer into an arc.

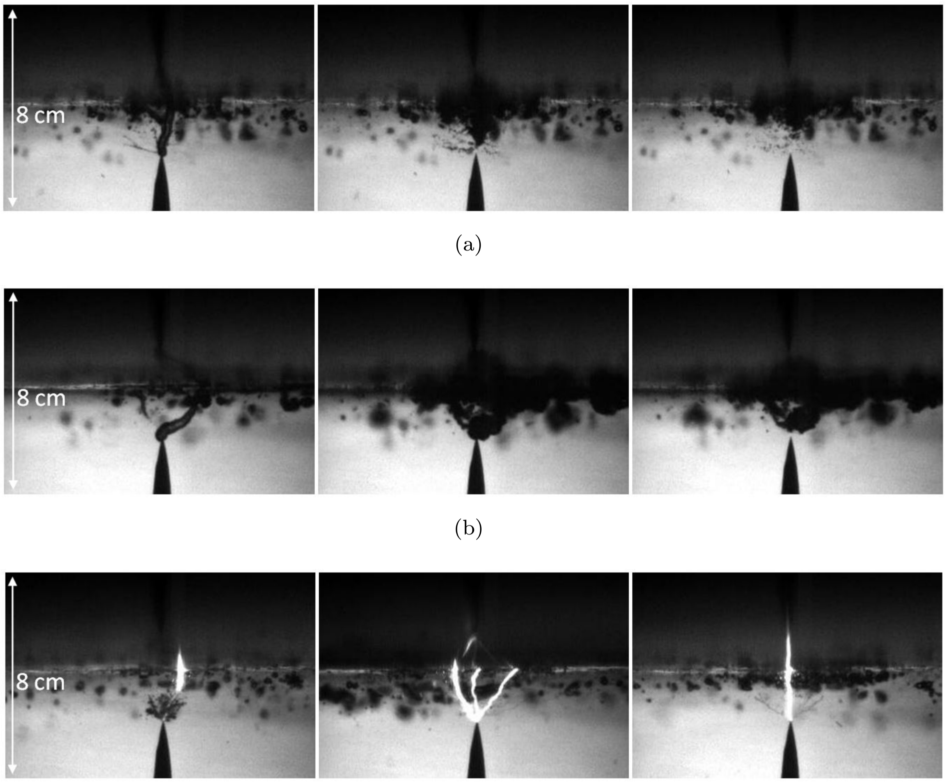

(a)

(b)

(c)

FIGURE 6.15: Examples of filamentary streamers with larger FOV lens at 35 kV, 4.5 mm gap distance, GRP sample, 77.8±0.3K, atmospheric pressure: (a) vaporising large amount of LN_2 at the contact point, (b) streamer propagating along the surface, (c) arc-type steamers.

into GRP sheets, e.g. glass fibre, due to several reasons. Firstly, the cryostat was vacuumed which means impurities must be produced during the experiments. Secondly, the particles were not observed during PTFE tests, and GRP samples at low-voltage conditions under which the composite sheets were not damaged. Lastly, parts of the glass fibre, approximately 0.1 mm in length, were observed on the surface of the insulation after the experiments.

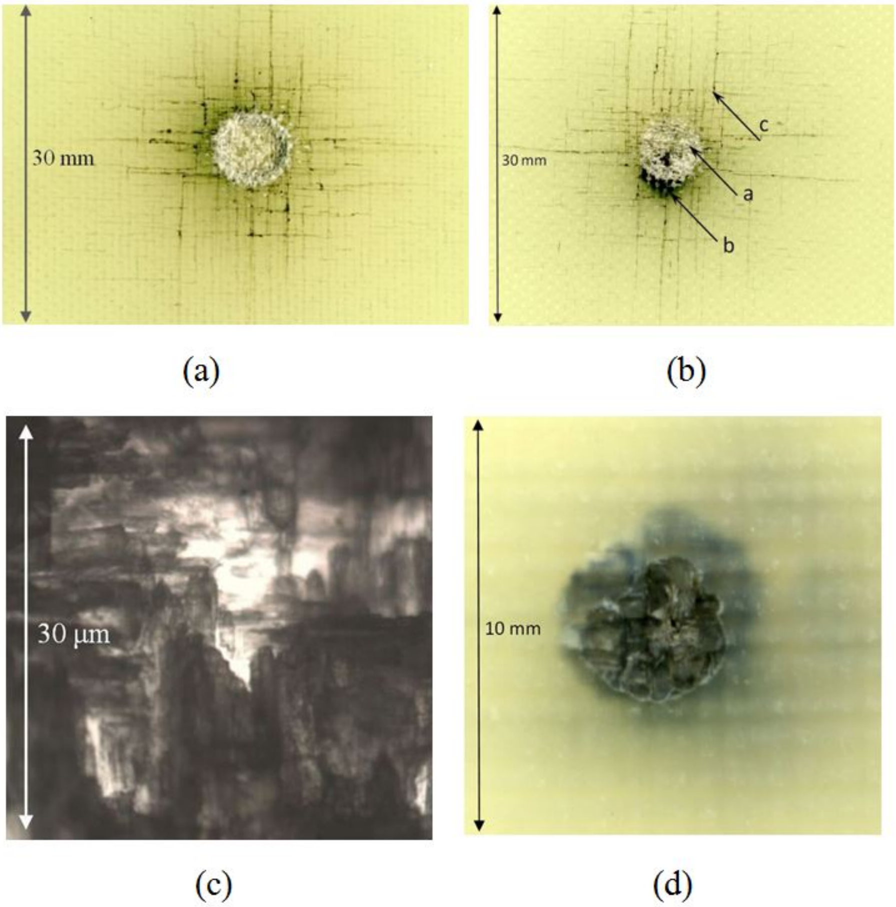

FIGURE 6.16: Surface degradation on GRP samples (a) 4.5 mm, (b) 4 mm a: eroded hole exposing glass fibre, b: breakdown hole, c: cracking area. (c) 1000x magnification of the eroded hole in (a), (d) the backside of the breakdown hole.

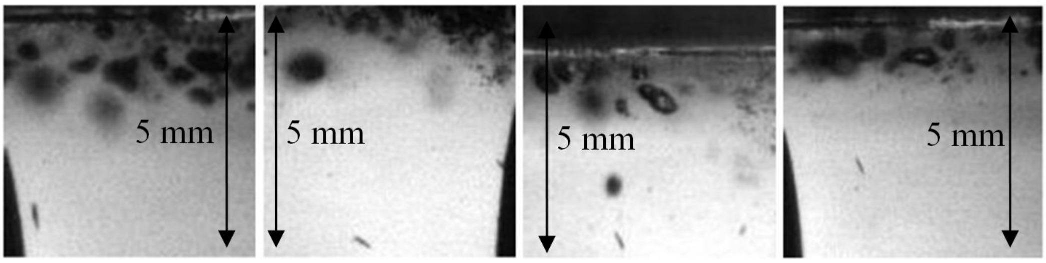

FIGURE 6.17: Particles generated during GRP experiments.

The mechanisms governing the degradation process of the GRP sample immersed in

LN_2 are discussed here. Under cryogenic conditions, insulating materials are operating below their glass transition temperature and therefore, are very brittle. Thus, although glass fibre is resistive to thermal degradation, it can easily be damaged mechanically and broken into smaller pieces. The two possible causes of the phenomenon could be thermal contraction at cryogenic temperature [133] and pressure shock waves produced by streamer propagation [8]. In addition, the composite structure of the GRP tends to introduce defects on the surface as well as inside the material due to the interface between the epoxy and glass fibre. It is possible that PD discharge occurs within these voids and produce micro explosions which leads to the breaking of the glass fibre as observed. A model for the development of discharge inside a void between glass fire and epoxy can be found in [132]. The process starts with the generation of initial electrons which in the case of LN_2/GRP system, can be available from streamer channels. Then PD occurs which leads to void surface current, chemical erosion [134] and eventually breakdown. Similar observation was reported by Park et al [135] in which discharges were found to originate at the fibre/epoxy interface.

For a closer gap distance, 4 mm, breakdown occurs after 20 minutes of applied voltage. Degradation characteristics are almost identical as experiments at 4.5-mm gap with a circular hole in the middle and further cracking on the GRP surface away from the attachment points. In this case, however, due to the higher electric field at the needle tip, the damage caused by PD is more severe and results in earlier failure of the insulation. The excessive current pulses from breakdown generate a large amount of heat dissipation and result in carbonization of the epoxy (Figure 6.16 (b) and (d)) as well as the generation of a single macroscopic bubble as shown in Figure 6.18.

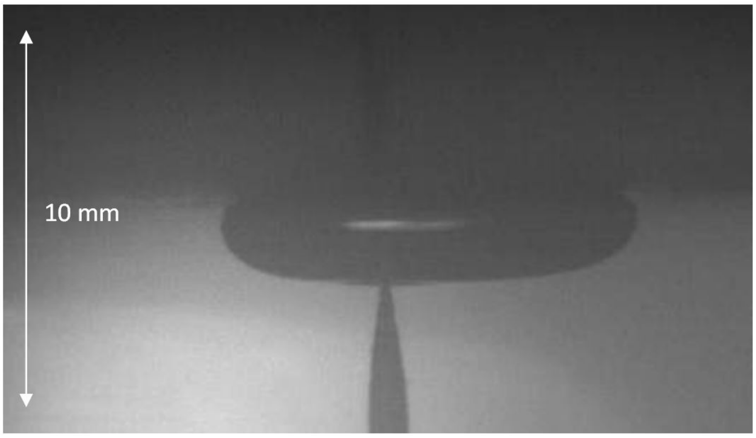

FIGURE 6.18: Bubble generation after breakdown.

Figure 6.19 shows the total charge transferred during a 20-ms cycle. The number was averaged from data captured from 3000 cycles at a certain time during the 30-minute of applied voltage. A closer gap distance would lead to higher magnitude PD pulses for both materials due to higher electric field at the needle tip. An increase in apparent charge of PD pulses over time was observed during fibreglass/LN_2 experiments due to the erosion phenomenon. The glass-fibre composite was damaged severely over time as the pit depth increased. Such degradation process would lead to a decrease of the sample thickness as well as an increase in the number of local trapping sites. Meanwhile, the degradation of PTFE barriers remain only on the material surfaces and is in the form of generation of new chemical compounds, e.g. high fluorescence and carbonaceous species. This might explain while the charge transferred remains fairly constant over the stressing period for experiments with PTFE samples.

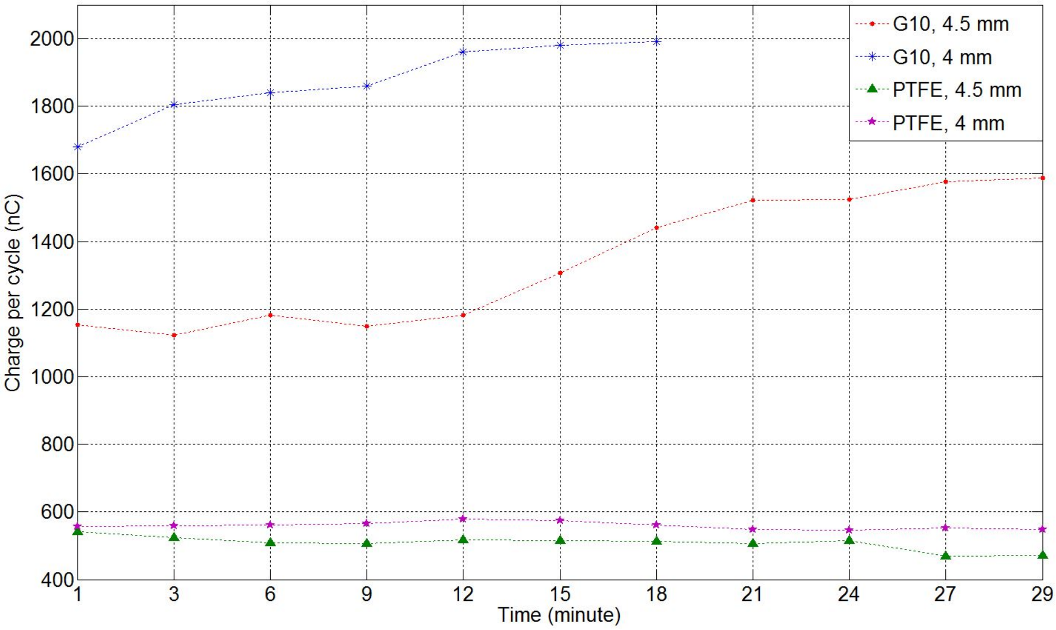

FIGURE 6.19: The change in measured charge over time per 50-Hz AC cycle.

6.3.2.2 Raman analysis of the damaged GRP surface

Figure 6.20 shows the Raman spectra of a damaged GRP barrier. Inside the pit, a broad peak around 1400 cm^{-1} is observed which has been reported as a result of the fluorescence of the glass [136]. On the cracking surface (Figure 6.20 B), along with the fluorescence from the glass fibre, other peaks can be assigned to the characteristics of the epoxy layer [137]. From the Raman result, it can be concluded that inside the eroded hole, the surface layer consists of mainly glass fibre with almost no epoxy resin. Therefore, it can be hypothesised that the degradation process begin with the removal of the epoxy layer similar to that observed during laser ablation of the GRP sheets. This is due to the fact that the reinforced polymer is less thermally and chemically stable than the glass fibre. Similar phenomenon was reported in [138] in which the degradation of glass-fibre composite happens in the polymer matrix first and resulting in the exposure of the glass fibre on the surface of the material. Once the polymer matrix has been removed, the mechanical properties of the GRP barrier are reduced significantly which leads to the breaking of the glass fibre as discussed in the previous section.

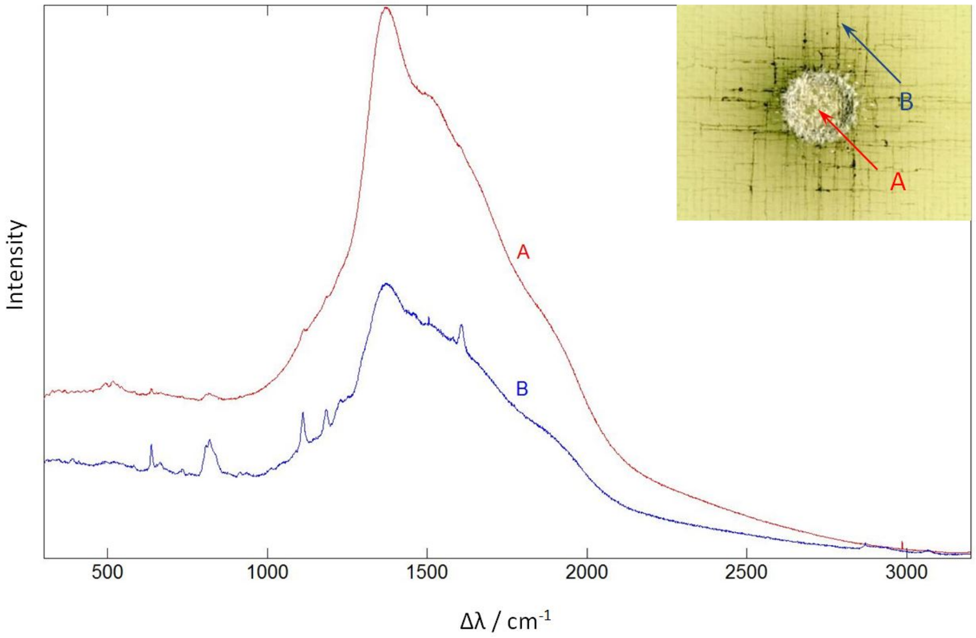

FIGURE 6.20: Raman spectroscopy of damaged GRP barrier.

6.3.3 Effects of sample thickness

In the previous sections, the degradation of solid dielectric barriers was found dependent on the properties of the materials especially the ability to trap charges on the surface. It is important to assess whether sample thickness affects erosion phenomenon. The use of an insulation barrier placing over an electrode is to prevent complete breakdown and should not influence streamer behaviour. This is because streamers are initiated from the needle tip where the electric field is the highest. Maximum external electric field is the function of applied voltage, needle radius and distance between the needle tip and planar electrode and is not affected by the insulation barrier.

The dominant factors contributing towards degradation phenomenon are believed to be bombardment of high energy charges and mechanical forces. The thickness of the solid barrier should not have any effect on both of those degradation mechanisms but rather the electric field across the insulation. Therefore, on the attachments of streamers, a thinner sample will experience a higher electric field and breakdown occurs once the electric field exceeds the dielectric strength of the material.

For this study, PTFE sheets with thickness of 2 mm were used instead of the 3-mm samples. Other experimental conditions remained unchanged. The samples then were tested under the same applied voltage 35 kV. Figure 6.21 shows the histogram and ϕ-q-n plot from an accumulated data over 3000 cycles. PD magnitude and pattern are similar to the results obtained during discharge to a 3-mm PTFE barrier (Figure 6.7). The only difference is an increase of the number of PD pulses observed during positive half cycles, e.g. the needle tip was negative. Nevertheless, the thickness of samples does not seem to have any significant effect on the PD signature. The insulation barrier material, on the other hand, can greatly influence the PD pattern and magnitude as illustrated in the case of GRP sample (Figure 6.12).

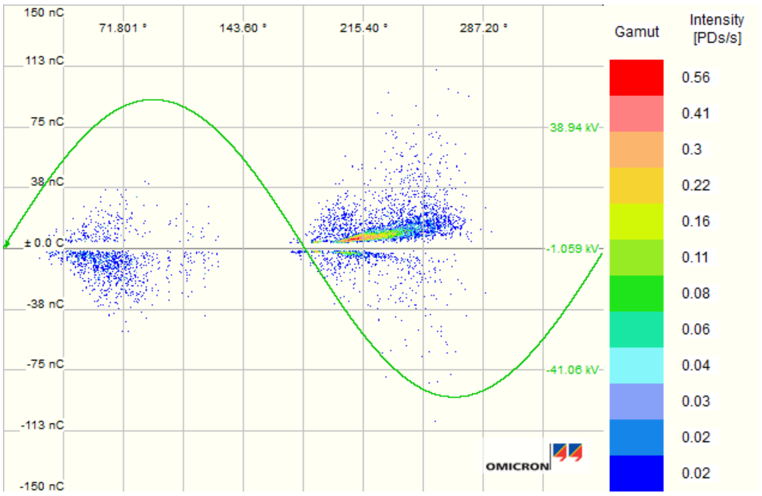

(a) Bipolar

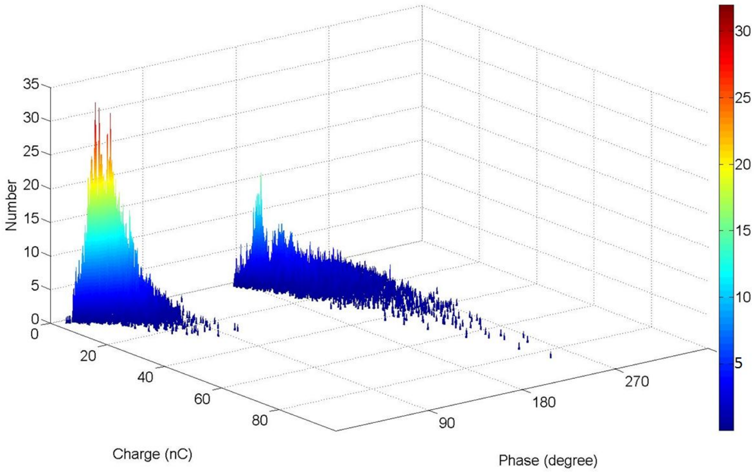

(b) Unipolar

FIGURE 6.21: Accumulated PD pulses during one minute, 2-mm PTFE sample, 35 kV, 4.5 mm gap distance, 77.8±0.3 K, atmospheric pressure: (a) Mtronix histogram, (b) ϕ-q-n plot produced from (a).

Erosion on the surface of a 2-mm sheet shows similar characteristics to the thicker PTFE samples (Figure 6.10). Damage appears on a large area but only on the surface of the insulation. However, eroded area is less clear than that in Figure 6.10 because of much shorter duration of applied voltage. Breakdown was found to be between 2-5 minutes. Two breakdown holes which completely puncture through the sample can be seen in Figure 6.22. The darkened paths leading to the breakdown holes suggest that the breakdown positions are not the initial attachment points of the streamer channels. Upon contact, streamer channels continue to propagate until weaker insulation

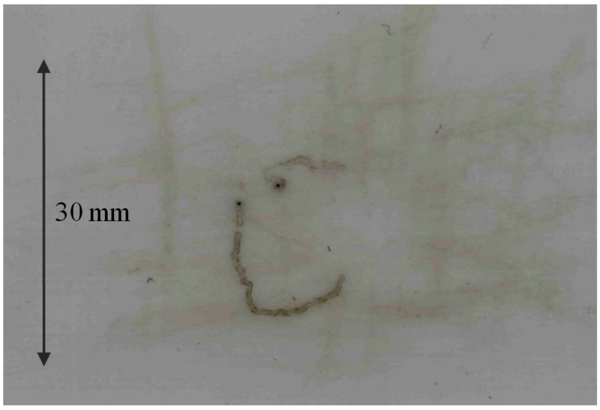

Figure 6.22: Surface erosion on 2mm-PTFE samples.

paths are found. Because the density change channels are considered to be conductive, together with the high amounts of charge at the streamer head, the electric field at the streamer tips can exceed the dielectric strength of PTFE. Breakdown did not happen for 3-mm samples since the thicker materials mean that a higher breakdown potential is required. In comparison with the breakdown observed for GRP barrier, dielectric failure in this scenario is suggested to be due to a particular single event rather than an accumulation of repetitive PD. The duration before breakdown (several minutes) is the time it takes for the streamer channels to find the weakest link of the polymer rather than to accumulatively degrade the material, such as the case for GRP barriers.

6.4 Summary

This Chapter has detailed the erosion phenomenon on solid dielectrics under cryogenic conditions. Previous research [107] [108] has shown correlated results between laser ablation and discharge tests at room temperature such as incline tracking tests. Materials radiated by a long-wavelength laser, e.g. visible or infra-red, only experience thermal decomposition since the energy of the laser photon is not sufficient to cause photochemical effects. Therefore, ranking of materials using laser ablation data relies on the fact that the important mechanism governing the erosion phenomenon is thermally related. Although this has been reported to be the case for incline tracking discharges [108], in a LN_2 environment, the obtained results suggest that laser ablation cannot be used to characterise degradation behaviour of solid dielectrics. From the two materials studied, PTFE and GRP, not only is the ranking opposite to the discharge results but also the erosion products were found to be very different. Ablated PTFE sheets were vaporised with almost no carbonisation whereas the damage caused by PD streamers appears in the form of chemical changes on the surface of the material such as carbonised and high-fluorescent species and vaporisation was not observed. Therefore, it is evident that thermal degradation is not important in the erosion of solid dielectrics at cryogenic temperatures. This is because for materials submerged in LN_2 at 77.8±0.3 K, any local heating due to the attachment of hot streamer filaments can be quickly dissipated into the large volume of LN_2. Thus, although the surface temperature can be increased, it is not sufficient to cause thermal degradation. In this sense, one would expect a better resistance to erosion for materials operating at cryogenic conditions compared with those at room temperature.

While thermal degradation is not an important process at LN_2 temperatures, cryogenic dielectrics are more susceptible to mechanical damage. At 77 K, insulation materials are operating below their glass transition and therefore tend to be very brittle. One example here is the glass fibre composite. Although the fibre itself is very stable thermally, during PD experiments, glass fibre was found broken into smaller pieces which were observed during the tests as well as on the surface of the material. Further examination of the damaged hole reveals that the erosion process initiated within the epoxy layer. Once the reinforced layer, epoxy resin, had been degraded, the glass fibre became very susceptible to mechanical forces from streamer propagation or cryogenic contraction. The result is the broken fibres and the formation of an eroded pit as observed.

Fibre/epoxy composites have been found to be less resistant to degradation caused by PD streamers than PTFE. In the case of GRP, erosion was in the form of a hole which reduced the thickness of the solid barrier. Thinner samples lead to higher electric fields across them and eventually breakdown occurs once the field exceeds the dielectric strength of the insulation. Whereas, in the case of PTFE, degradation remains only on the surface without penetrating into the bulk of the material. The difference in observed phenomenon between the two materials is suggested to be the consequence of the composite structure of the GRP barriers which tend to introduce voids as well as trapping sites for charges at the liquid/solid interface. Recombination between the trapped charges and streamer filaments leads to much larger PD events as well as glowing arcs. The results obtained here is in agreement with previous work in LN_2 [139] in which fibrous materials were found to degrade more rapidly than homogeneous polymers.

Chapter 7

Conclusions and further work

7.1 Findings

Over the past two decades, HTS technology has been moving from the research stage towards demonstrators for industrial applications. Prototypes for HTS power devices such as cables, transformers, fault current limiters, generators and motors have been developed. Many of those HTS apparatus have been operated in a live power grid and produced very promising results. In addition, the invention of second generation of HTS wires, based on YBCO, provide a larger critical current as well as a reduction in manufacturing cost. YBCO based conductors promise a cost-effective solution for HTS applications. With all the progress have been made in the HTS technology, widespread industrial applications of superconducting power apparatus can be expected in the near future.

The development of HTS applications urges research in the field of cryogenic dielectrics. Insulation system in a HTS power apparatus, in general, consists of solid dielectrics immersed in liquid nitrogen. Intrinsically, LN_2 is a good insulation of which breakdown strength is comparable to mineral oils. However, the narrow liquid range of LN_2 makes it very susceptible to vaporisation. Generation of bubbles in LN_2 can either be due to an electrical or thermal process. Breakdown strength of gaseous bubbles is much lower than that of the liquid which explains why the failure of LN_2 tends to occur below its intrinsic breakdown strength. Therefore, understanding pre-breakdown phenomena in LN_2 is of paramount importance in order to improve the reliability of future HTS power devices.

Besides dielectric properties, mechanical and thermal compatibility, degradation behaviour is also an important characteristic of a solid cryogenic dielectric. Partial discharges in LN_2 can cause irreversible damage to the solid parts of the insulation system. Accumulation of such damage will lead to premature failure of the dielectrics. In order to improve the reliability of HTS power apparatus, mechanisms governing the degradation process need to be better understood. This thesis has experimentally studied the performance of cryogenic dielectrics. Conclusions drawn from the obtained experimental results can be divided into three parts: PD detection methods, characterisation of PD streamers and degradation of solid dielectrics in cryogenic environment, which are discussed in the following sections. The results presented in this thesis will be useful in the design of future insulation systems and associated condition monitoring strategies for HTS power apparatus.

7.1.1 PD measurements in LN_2

Although partial discharge only causes a breakdown within part of a material, accumulation of PD events can lead to complete failure of the insulation. Therefore, the ability to detect PD pulses is essential for early identification of a developing fault as well as to prevent the device from suffering catastrophic failure. The thesis investigates two PD detection techniques namely conventional and non-conventional and their significance in a LN2-filled insulation system. In principle, both of the methods are similar since they both capture the electrical phenomenon during a PD event, current pulses in particular. The difference is in how the current is measured. The conventional method relies on a coupling capacitor which is in parallel with the discharge site. Signals measured at the capacitor can be related to the amount of charge transferred at the terminals. The conventional method has been developed over many years from which an international standard is defined and accepted. Non-conventional techniques, on the other hand, are not in direct contact with the discharge sites. They measure the effects of the discharge current pulses such as by detecting electromagnetic radiations. Two non-conventional PD detection methods were investigated in this study; namely the UHF sensor and RFCT sensor with the focus on the application of UHF sensors on measuring PD in LN2.

The obtained results show that PD pulses during pre-breakdown streamers in LN2 under AC voltages can be detected by a UHF sensor located on the outside walls of the cryostat. Fast current pulses during a streamer process radiate electromagnetic waves which propagate in the liquid medium towards the cryostat walls. The structure of the cryostat resembles a typical insulation system in a HTS applications, e.g. using a vacuum gap between two vessels. Therefore, in a design of future HTS power apparatus, two dielectric windows similar to the configuration in this work should be included so that the UHF detection method can be applied. This will provide a cost effective and easy-to-use solution for PD measurement system compared with the conventional method in which a blocking capacitor is required. In addition, since PD measurements can be taken without any interference with the operation of the device, UHF detection can be used in an on-line monitoring system. Applications of UHF sensor in a oil-filled transformer can be found in [140] [141]. Therefore, the results presented in this work lay the foundation for on-line monitoring systems using UHF sensors for a HTS power apparatus.

PD during pre-breakdown phenomena in LN2 during negative polarity is in the form of multiple pulses less than 1 μs apart from each other. While wideband detection systems can observe this pulse burst behaviour, conventional measurement via a coupling capacitor cannot distinguish these individual events. Instead, the total of charge transferred at the terminals during this process is recorded. When the duration of a pulse burst sequence exceeds 3 μs, superposition errors occur in measurements made using the conventional method. In these scenarios, the measured apparent charge which is based solely on the peak values of the captured PD waveform does not correctly represent the total amount of charge transferred at the terminals. Such errors can be overcome by the use of wideband measurement systems based around UHF sensors.

The main issue of wideband PD measurements is the lack of in-field experience. A standardised system is yet to be available. In the case of UHF sensors, calibration of UHF signal into a certain charge value is difficult because of the variations in the current waveforms. This issue can be solved if a method to relate the UHF captured waveform and the current pulse is available. However, the answer to this question is beyond the scope of this work. At this stage, the one conclusion that can be drawn is that the UHF sensor has proven to be the most effective method for detection of PD pulses in a LN2-filled system.

7.1.2 Characterisation of PD streamers in a LN$_2$/solid dielectric insulation system

From the experimental results, each PD event was observed to be accompanied by a single streamer growing from the needle tip. The recorded shadow graphs show that a pre-breakdown streamer is characterised by gaseous filaments which will eventually break into clouds of bubbles. Pre-breakdown phenomena in LN2 occur when the electric field across the liquid exceeds a certain value which was estimated from the data to be at $1.55{\cdot}10^9$ V/m. Close to the inception voltage, PD events show characteristics of corona discharge in air, e.g. PD pulses occur after almost the same interval as well as having similar magnitude. As the voltage increases, PD pulses appear in a more erratic manner mainly due to the existence of multiple propagation modes of streamers. Corona-like discharge in LN2 is due to the space charge built up in front of the needle which reduces the local electric field at the tip. The low mobility of electrons in LN2, which has been proposed as a result of electron trapping in local vacant sites, would enhance the development of the space charge layer.

During the positive half cycle when the needle is negative to the planar electrode, both bush-like and filamentary propagation modes were observed. Initiation and propagation of a negative streamer is accompanied by a sequence of PD pulses. This pulse sequence can only be observed by wideband detection using the UHF sensor. For a bush-like streamer, the sequence starts with a smaller magnitude pulse which is followed by larger events. The smaller PD pulse is believed to be correlated to the avalanche in the liquid phase which leads to the formation of initial bubbles. Above the inception voltage, the electric field at the needle tip is sufficient for electron injection from the cathode following Fowler-Nordheim theory. The Fowler-Nordheim current profile has been observed in LN2 but for a very sharp tip ($r_p < 0.1$ μm) and for a short period of time [14]. The current quickly becomes space-charge limited due to the low mobility of electron in LN2. Injected electrons from cathode can gain enough energy from the intensive electric field and start an avalanche. A reduction of liquid density due to the electric field [19] would certainly assist this avalanche process. Heat dissipation will quickly result in a vaporisation of the liquid and lead to the generation of initial cavities. Once gaseous bubbles have been formed, discharge takes place within the bubbles due to the lower breakdown strength of gas compared with liquid. Each discharge event leads to the growth of the streamer channels. Also, discharges inside a larger gaseous filament have higher magnitudes. This explains the step-wise growth of the PD sequences observed. Streamer propagation stops when the voltage across the filament is insufficient to create breakdown.

For negative filamentary streamers, the PD sequence appears in two parts with the first part showing characteristics of bush-like propagation mode. The second part of the sequence consists of several pulses of much higher magnitude. The corresponding images show that a filamentary streamer appears to grown out of the bush-like structure. Together with the PD sequence, it can be hypothesised that the bushy base was formed initially in a similar manner to bush-like streamer discussed above. The development of space charge at the end of the bush-like streamer enhances the local electric field such that molecular ionisation become feasible. The result is larger PD event as well as streamer propagation a following filamentary mode.

Pre-breakdown phenomena during the positive streamer process remains less well understood than the negative one. The step-wise pulse sequence was not observed when the needle is positive to the planar electrode. In most cases, a single event was recorded by both UHF and RFCT measurements. Both bush-like and filamentary modes were observed. However, different to negative streamers, the filamentary shape is dominant. For applied voltages well above the inception voltage, positive bush-like streamers were not observed. It is difficult to explain the initiation of positive streamer due to the lack of seed electrons as well as the generation of initial cavities. Further research on this topic is required to understand the characteristics of positive streamer generation in LN2.

ϕ-q-n plots were used in the phase resolved analysis of PD patterns in a LN2/solid dielectric insulation system. Two solid barriers have been studied: PTFE and glass fibre reinforced resin. For both solid dielectrics, PD occurs primarily in the first and third quadrant of the applied voltage. As the voltage increases, the active phase window broadens towards the zero crossing of the applied waveform. Eventually, back discharge occurs during both polarities. The observed PD patterns signify the importance of the charge storage within the insulation system. The excessive charges produced during the previous half cycle can be trapped either in the liquid or on the surface of the solid barriers. When the voltage polarity reverses, these charges will move towards the needle tip and enhance the electric field. Therefore, PD can occur at a earlier phase on the voltage waveform. This becomes more effective as the applied voltage increases since more charges can be deposited into the insulation system. The occurrence of back discharge shows the importance of the space charge field such that streamers can be initiated without the influence of the external field, e.g. at the zero crossing point of the applied voltage.

Streamers which completely bridge the liquid gap are accompanied by much larger PD events (in nC) compared with those localising at the needle tip. Fully developed streamers were only observed when the applied voltage exceeded a certain threshold. This value rises as the gap distance increases. Similarly, the apparent charge of PD streamers that reach the solid barrier also increases with the liquid gap. Larger PD events were observed during experiments with GRP barriers. Although it is difficult to explain this behaviour due to the lack of knowledge on charge storage in cryogenic environments, the inhomogeneous structure of GRP can introduce more surface defects than PTFE barriers. Thus, one would expect more charge can be trapped on the surface of GRP barriers. Recombination of these charges and those from the approaching streamers can result in the much larger PD events as observed.

7.1.3 Degradation of solid dielectrics caused by PD in LN_2

Since density change streamers in liquid dielectrics are conductive, direct contact between the gaseous filaments and the electrodes can lead to a complete breakdown. In order to protect a system from a complete failure, a liquid/solid insulation configuration is used such that in the event of liquid breakdown, streamer channels cannot reach the conductor but rather stop at the interface between the liquid and solid dielectric. The results from this study have shown that pre-breakdown streamers in LN2 can cause significant damage to solid dielectric barriers. The damage depends on the insulation material structure.

For PTFE barriers, damage is in the form of surface degradation. Raman spectroscopy reveals the formation of high-fluorescence and carbonised species. These products were found far away from the streamer attachment area. In fact, the initial attachment of streamers did not cause any damage to the PTFE barriers. Degradation is due to the propagation of streamers along the surface of the barriers. Interactions between high energy charges with the polymer chain can create bond breaking which result in the formation of chemical compounds as shown in the Raman spectra. The long term effects of these products are not clear at this point. However, during the 30-minute duration of the experiments, the total charge transferred per cycle remain fairly constant. The generation of carbonaceous products does not appear to have any significant affects on the PD behaviour of the LN_2/PTFE insulation system.

For similar experimental conditions, damage on GRP barriers is more severe than PTFE. Degradation penetrates into the bulk of the material and creates a hole at the streamer contact points. Cracks outside of the eroded pit are also observed due to the propagation of streamer along the surface. Fragments of glass fibre were seen during the experiments as well as on the surface of the barrier after the experiment. This would indicate that the glass fibre was broken rather than melted. At cryogenic temperature, the glass fibre is operating below its glass transition temperature and therefore is very susceptible to mechanical damage. Cryogenic shock and pressure waves from streamer channels are the likely causes for breaking of the glass fibre.

A laser ablation study was conducted to analyse the effects of thermal decomposition on the two materials. The obtained results suggest that thermal degradation is not important at cryogenic temperatures. Any heating created by PD pulses can be quickly dissipated into the surrounding liquid nitrogen. The mechanisms governing the degradation phenomenon of solid dielectrics in a LN2-filled environment are believed to be mechanical forces and bombardment of high energy charges on the surface of the solid insulation.

Towards the design of insulation system for HTS applications, besides dielectric, thermal, mechanical properties of a material, its degradation behaviour also needs to be considered. Under faulty conditions, large PD events in LN2 can degrade the solid dielectric and result in premature failure as shown in the case of GRP barriers. Composite materials, although possessing good mechanical properties, tend to introduce defects on the surface as well as in the bulk. Such imperfections can create trapping sites for electric charges which results in larger PD events. Whereas, homogeneous materials experience much lower PD magnitudes and therefore exhibit higher resistance to degradation. Design of future HTS apparatus must take in to account the degradation phenomenon of solid dielectrics under cryogenic conditions in order to improve the lifetime as well as reliability of the insulation system.

7.2 Further work

The potential of UHF sensor in measuring PD in LN2 has been realised in this research. However, the challenge of calibrating the recorded UHF waveforms to apparent charge still requires further study. The problem remains in the variations of the current waveform during pre-breakdown phenomena in LN2. A model relating the captured signals to the incident current pulses needs to be developed. Such a model needs to take into account the generation and propagation of electromagnetic radiations through the liquid as well as the cryogenic vessels. If the information of the current waveform can be extracted from the measured UHF signals, calibration would be relatively straight forward.

The information in the time domain from the UHF measurements has proved to be useful in the understanding the processes of streamer propagation in LN2. Further work should focus on the ability to classify different PD sources as well as locate PD sites. In an oil-filled transformer, by using multiple sensors to map the structure of the device, location of the PD can be found from time of flight analysis of signals from UHF sensors [142]. Discriminations of PD sources can be achieved by analysing the energy content in the frequency domain since different defects tends to have different current waveforms [143] [144]. Further laboratory as well as in-field research could provide the required experience for the development of a UHF sensor-based effective condition monitoring tool for HTS power apparatus.

Further work is also required to understand pre-breakdown phenomena during positive polarity especially the production of seed electrons and initial cavities. A computational model of initiation and propagation of streamers in LN2 under AC voltage has yet to be developed. Although there has been a few models of streamer behaviour in other dielectric liquids such as transformer oil, work only focuses on DC and impulse voltages. Obviously, the case for AC applied voltages will be more complicated due to the occurrence of multiple streamer events and their effects on the following half cycle of the applied voltage. In addition, these available models have yet to consider the phase transition which would affect many parameters such as density, mobility, mean free path. Certainly, pre-breakdown streamers in liquid dielectrics involve many different physical processes and some assumptions, therefore, need to be made for the sake of simplicity of a given model.

Charge storage on the surface of solid barriers requires further investigation. In addition, a study of surface discharge in a LN2/solid dielectric system is also required. Any obtained results will further confirm the hypotheses proposed in this thesis. Since the streamer damage is accumulative over time, the ability of detecting early erosion is of interest in order to protect the power apparatus from complete breakdown. In the case of GRP samples, an increase in the total charge over time was observed due the erosion of the material. Therefore, it might be possible to develop a methodology to assess the degradation stage of a material based on PD measurements alone.

Further degradation experiments need to be undertaken with other solid dielectrics and electrode arrangements. Effects of temperature and pressure on the erosion phenomenon are also of interest. Lowering the liquid temperature or increasing the hydrostatic pressure can increase the PDIV in LN2 [10] since it will require more energy to create initial bubbles. However, the influence of these two parameters on the degradation phenomenon is unclear at this point. Results from these experiments together with erosion data of other cryogenic dielectrics would aid understanding of the mechanisms governing the degradation process of solid dielectrics under cryogenic conditions.

References

[1] Shoji Tanaka. High temperature superconductivity history and outlook. *Journal of the Japan Society of Applied Physics*, 6:17–22, 2002.

[2] J.O. Willis. Superconducting transmission cables. *IEEE Power Engineering Review*, pages 10–14, August 2000.

[3] B.W. McConnell and M.S. Walker. HTS transformers. *Power Engineering Review IEEE*, 22:29–37, 2006.

[4] D.J. Swaffield, P.L. Lewin, G. Chen, and J. Sykulski. Cryogenic dielectrics and HTS power apparatus: Research at the University of Southampton. *DEIS*, 20:7–11, 2000.

[5] Ying Xin. Introduction of china's first live grid installed HTS power cable system. *IEEE Transactions on Applied Superconductivity*, 15(2):1814–1817, 2005.

[6] A. Hobl and J. Bock. Progress in the development of hts application at nexans. *The Development and Application of HTS conductors*, 2010.

[7] J. Gerhold. Cryogenic liquids - a prospective insulation basis for future power equipment. *IEEE Transactions on Dielectrics and Electrical Insulation*, 9(1):7, 2002.

[8] A. Denat. High field conduction and pre-breakdown phenomena in dielectric liquids. *IEEE Transactions on Dielectrics and Electrical Insulation*, 13:518–525, 2006.

[9] M. Pompili, C. Mazzetti, and R. Bartnikas. Phase relationship of PD pulses in dielectric liquids under AC conditions. *IEEE Transactions on Electrical Insulation*, 7:113–117, 2000.

[10] D.J Swaffield. Effect of liquid nitrogen bubble dynamics on insulation performance for high temperature superconducting power apparatus. *Phd Thesis, University of Southampton*, 2005.

[11] J. Gerhold. Properties of cryogenic insulants. *Cryogenics*, 38:1063–1081, 1998.

[12] Y. Suda, M. Itoh, Y. Sakai, K. Matsuura, N. Honma, and T. Kimura. Behaviour of liquid nitrogen between electrodes in a microgravity environment. *Cryogenics*, 36(8):567–571, 1996.

[13] T. Judendorfer, A. Pirker, and M. Muhr. Conductivity measurements of electrical insulating oils. *IEEE International Conference on Dielectric Liquids 2011*, pages 1–4, 2011.

[14] N. Bonifaci and A. Denat. Work function for a hv cathode in nonpolar liquids. *IEEE Transactions on Electrical Insulation*, 1(4):657–662, 1994.

[15] D. Peier. Breakdown of LN_2 by field induced micro bubbles. *Journal of Electrostatics*, 7:113–122, 1979.

[16] G.J FitzPatrick, E.O. Forster, R.E. Hebner, and E.F. Kelly. Prebreakdown cathod process in liquid hydrocarbons. *IEEE Transactions on Electrical Insulation*, EI-22(4):453–458, 1987.

[17] O. Lesaint and R. Tobazeon. Streamer generation and propagation in transformer oil under AC divergent field conditions. *IEEE Transactions on Electrical Insulation*, 23(6):941–954, 1988.

[18] J. Frenkel. *Kinetic Theory of Liquids.* Oxford University Press, 1946.

[19] T.J Lewis. A new model for the primary process of electrical breakdown in liquids. *IEEE Transactions on Dielectrics and Electrical Insulation*, 5:306–315, 1998.

[20] W.F. Schmidt. *Liquid State Electronics of Insulating Liquids.* CRC Press, 1997.

[21] R. Bartnikas. *Engineering Dielectrics Volume III Electrical Insulating Liquids.* ASTM International, 1994.

[22] S.G. Lias, R.D. Levin, and S.A. Kafafi. Gas phase ion energetics data. *NIST Standard Reference Database Number 69, (http://webbook.nist.gov/chemistry/). Number 69, June 2005 ed, ed. Linstrom, P.J. and Mallard, W.G. June 2005: NIST, National Institute of Standards and Technology*, 2005.

[23] W. Tauchert, H. Jungblut, and W.F. Schmidt. Photoelectric determination of V_0 values and electron ranges in some cryogenic liquids. *Canadian Journal of Chemistry*, 55:1860–1866, 1977.

[24] W.J. Nellis, D.C. Hamilton, R.J. Trainor, H.B. Radousky, A.C. Mitchell, and N.C. Holmes. Fluids at high dynamic pressures and temperatures. *Physica B+C*, 139-140:565–567, 1986.

[25] W.F. Schmidt. Electron mobility in nonpolar liquids: the effect of molecular structure, temperature, and electric field. *Canadian Journal of Chemistry*, 55(11):2197–2209, 1977.

[26] W.F. Jortner and A. Gaathon. Effects of phase density on ionization processes and electron localization in fluids. *Canadian Journal of Chemistry*, 55(11):1801–1819, 1977.

[27] A.G. Kharapak, Y. Sakai, Bottcher, E.H., and W. Schmidt. Stability of electron bubbles in liquid neon. *IEEE Transactions on Electrical Insulation*, 26:582–585, 1991.

[28] Y. Sakia, W.F. Schmidt, and A.G. Khrapak. Self-trapping of electrons in liquid nitrogen. *IEEE Transactions on Dielectrics and Electrical Insulation*, 1:724–727, 1994.

[29] N. Gee, M.A. Floriano, T. Wada, S.S. Huang, and G. Freeman. Ion and electron mobilities in cryogenic liquids: argon, nitrogen, methane, and ethane. *Journal of Applied Physics*, 57:1097–1101, 1985.

[30] T. Wada and G. Freeman. Electron localization in dense nitrogen vapour. *Journal of Chemical Physics*, 72(12):6726–6730, 1980.

[31] W.F. Schmidt. Electronic conduction processes in dielectric liquids. *IEEE Transactions on Electrical Insulation*, EI-19(5):389–418, 1984.

[32] Y. Murooka. Observations on the intermittent electron emission in liquefied nitrogen. *Journal of Physics*, 48(1):136–142, 1977.

[33] W.F. Schmidt, O. Hilt, E. Illemberger, and A.G. Khrapak. The mobility of positive and negative ions in liquid xenon. *Radiation Physics and Chemistry*, 74:152–159, 2005.

[34] M.P. deHaas, J.M. Warman, P.P. Infelta, and A. Hummel. The measurement of a positive charge mobility larger than that of the excess electron in irradiated liquid trans-decalin. *Journal of Chemical Physics*, 65:5019–5020, 1976.

[35] B.L. Henson. Mobility of positive ions in liquefied argon and nitrogen. *Physical Review*, 135(4A):A1002–A1008, 1964.

[36] L. Solymar and D. Walsh. *Electrical Properties of Materials.* Oxford University Press, 2004.

[37] R.H. Fowler and L. Nordheim. Electron emission in intense electric fields. *Proceedings of the Royal Society*, 119:73–181, 1928.

[38] F.M. O'Sullivan. A model for the initiation and propagation of electrical streamers in transformer oil and transformer oil base nanofluids. *Phd Thesis, Massachusetts Institute of Technology*, 2007.

[39] K. Dotoku, H. Yamada, and S. Sakamoto. Field emission into nonpolar organic liquids. *Journal of Chemical Physics*, 69:1121–1125, 1978.

[40] B. Halpern and R. Gomer. Field emission in liquids. *Journal of Chemical Physics*, 51(3):1031–1047, 1969.

[41] B. Halpern and R. Gomer. Field ionization in liquids. *Journal of Chemical Physics*, 51(3):1048–1056, 1969.

[42] A. Denat. Conduction and breakdown initiation in dielectric liquids. *International Conference on Dielectric Liquids 2011*, 2011.

[43] L. Onsager. Deviations from ohm's law in weak electrolytes. *Journal of Chemical Physics*, 2:559–615, 1934.

[44] S. Ingebrigtsen, L.E. Lundgaard, and P-O. Astrand. Effects of additives on prebreakdown phenomena in liquid cyclohexane: I. streamer initiation. *Journal of Applied Physics*, 40:5161–5169, 2007.

[45] S. Ingebrigtsen, L.E. Lundgaard, and P-O. Astrand. Effects of additives on prebreakdown phenomena in liquid cyclohexane: II. streamer propagation. *Journal of Applied Physics*, 40:5624–5634, 2007.

[46] A. Denat, F. Jomni, F. Aitken, and N. Bonifaci. Thermally and electrically induced bubbles in liquid argon and liquid nitrogen. *IEEE Transactions on Dielectrics and Electrical Insulation*, 9:17–22, 2002.

[47] T.S. Derenzo, T.S. Mast, H. Zaklad, and R.A. Muller. Electron avalanche in liquid xenon. *Physical Review A*, 9:2582–2591, 1974.

[48] N. Bonifaci, A. Denat, and V. Atrazhev. Ionization phenomenon in high density gaseous and liquid argon in corona discharge experiments. *Journal of Applied Physics*, 30:2717–2725, 1997.

[49] J.L Hernandez-Avila, N. Bonifaci, and A. Denat. Hot electron phenomena in liquid and gaseous Ar and N2 in divergent electric fields. *IEEE Transactions on Electrical Insulation*, 1:412–418, 1994.

[50] M. Haidara and A. Denat. Electron multiplication in liquid cyclohexane and propane. *IEEE Transactions on Electrical Insulation*, 26:592–597, 1991.

[51] K. Yhoshino, K. Ohseko, M. Shiraishi, M. Terauchi, and Y. Inuishi. Dielectric breakdown of cryogenic liquid in terms of pressure, polarity, pulse width and impurity. *Journal of Electrostatics*, 12:305–314, 1982.

[52] A.H. Sharbaugh, J.C. Devins, and S.J. Rzad. Progress in the field of electric breakdown in dielectric liquids. *IEEE Transactions on Electrical Insulation*, 13:249–276, 1978.

[53] M. Hara and Zen-Chao Wang. An analytical study of bubble motion in liquid nitrogen under DC nonuniform electric fields. *Proceedings of the 4th International Conference on Properties and Applications of Dielectric Materials*, 2:459–462, 1994.

[54] M. Hara. Effect of thermally induced bubbles on the electrical breakdown characteristics of liquid nitrogen. *IEE Proceedings A, Physical Science, Measurement and Instrumentation, Management and Education*, 137(4):209–216, 2002.

[55] J.K Nelson and I.F.M. Hashid. Evidence for cavitation in flourocarbon liquids subjected to alternating electric fields. *Journal of Physics D: Applied Physics*, 9:203–210, 1976.

[56] W.G. Chadband. From bubbles to breakdown or vice-versa. *Proceedings of the 11th IEEE International Conference on Conduction and Breakdown in Dielectric Liquids*, pages 184–193, 1993.

[57] K. Yamazawa, M. Okumura, M. Uemura, H. Yamashita, and E.O. Forster. Observation of cathode streamer initiation in dielectric liquids under high magnification. *IEEE Conference Electric Insulation Dielectric Phenomena*, pages 324–329, 1993.

[58] P.E Frayssines, N. Bonifaci, A. Denat, and O. Lesaint. Streamer in liquid nitrogen: characterization and spectroscopic determination of gaseous filament temperature and electron density. *Journal of Physics D: Applied Physics*, 35:369–377, 2002.

[59] T.J Lewis. Breakdown initiating mechanisms at electrode interfaces in liquids. *IEEE Transactions on Dielectrics and Electrical Insulation*, 10(6):948–955, 2003.

[60] R. Kattan, A. Denat, and N. Bonifaci. Formation of vapor bubbles in non-polar liquids initiated by current pulses. *IEEE Transactions on Electrical Insulation*, 26:656–662, 1991.

[61] A.A Belevtsev and V.V Markovets. Nanosecond breakdown in liquid nitrogen. *Journal of Physics*, 34:L52–L56, 2001.

[62] A. Denat, J-P. Gosse, and B. Goss. Electrical conduction of purified cyclohexane in a divergent electric field. *IEEE Transactions on Electrical Insulation*, 23:545–554, 1988.

[63] L. Dumitrescu, O. Lesaint, N. Bonifaci, A. Denat, and P. Notinger. Study of streamer inception in cyclohexane with a sensitive charge measurement technique under impulse voltage. *Journal of Electrostatics*, 53:135–146, 2001.

[64] Kazuaki Yamazawa and Hisanao Yamashita. Pre-breakdown density change streamer in liquid nitrogen. *Japanese Journal of Applied Physics*, 9:17–22, 1997.

[65] D.J. Swaffield, P.L Lewin, G. Chen, and S.G. Swingler. Partial discharge characterisation of streamers in liquid nitrogen under applied AC voltages. *IEEE Transactions on Dielectrics and Electrical Insulation*, 15(3):635–646, 2008.

[66] G. Chen and A.E. Davis. Electric stress computation - a needle-plane electrode system with space charge effects. *COMPEL - The International Journal for Computation and Mathematics in Electrical and Electronic Engineering*, 5(1):40–56, 1996.

[67] Yuzo Takahashi and Kaoru Ohtsuka. Corona dischrages and bubbling in liquid nitrogen. *Journal of Physics*, 8:165–169, 1975.

[68] R. Coelho and J. Debeau. Properties of the tip-plane configuration. *Journal of Physics D: Applied Physics*, 4:1266–1280, 1974.

[69] M.D. Judd and O. Farish. A pulsed GTEM system for UHF sensor calibration. *IEEE Transactions on Instrumentation and Measurement*, 47:875–880, 1998.

[70] G.P. Cleary and M.D. Judd. UHF and current pulse measurements of partial discharge activity in mineral oil. *IEE Proceedings - Science, Measurement and Technology*, 153:47–54, 2006.

[71] V.Torshin Yu. On the existence of leader discharges in mineral oil. *IEEE Transactions on Electrical Insulation*, 2(1):167–179, 1995.

[72] R. Tobazeon. Prebreakdown phenomena in dielectric liquids. *IEEE Transactions on Electrical Insulation*, 1(6):1132–1147, 1994.

[73] B. Faramund. Study of electric breakdown of liquid dielectrics using schlieren optical techniques. *British Journal of Applied Physics*, 12:251–254, 1961.

[74] W.G. Chadband and G.T. Wright. A pre-breakdown phenomenon in the liquid dielectric hexane. *British Journal of Applied Physics*, 18:305–313, 1965.

[75] E.O. Forster and P. Wong. High speed schlieren studies of electrical breakdown in liquid hydrocarbons. *IEEE Transactions on Electrical Insulation*, EI-12(4):435–442, 1977.

[76] E.O. Forster. Progress in the field of electrical breakdown in dielectric fluids. *IEEE Transactions on Electrical Insulation*, EI-20(6):905–912, 1985.

[77] M. Pompili and C. Mazzetti. Simultaneous ultrawide and narrowband detection of PD pulses in dielectric liquids. *IEEE Transactions on Electrical Insulation*, 5:402–406, 1998.

[78] M. Pompili, C. Mazzetti, and R. Bartnikas. PD burst characteristics of transformer oils. *IEEE Transactions on Power Delivery*, 21:689–98, 2006.

[79] M.D. Judd, O. Farish, J.S. Pearson, and B.F. Hampton. Dielectric windows for UHF partial discharge detection. *IEEE Transactions on Dielectrics and Electrical Insulation*, 8:953–958, 2001.

[80] M.D. Judd, O. Farish, and B.F. Hampton. The excitation of UHF signals by partial discharges in gis. *IEEE Transactions on Dielectrics and Electrical Insulation*, 3:213–228, 1996.

[81] R. Sarathi, A.V. Giridhar, and Abirami Mani. Investigation of partial discharge activity of conducting particles in liquid nitrogen under DC voltages using UHF technique. *IEEE Transactions on Dielectrics and Electrical Insulation*, 15(3):655–662, 2008.

[82] R. Sarathi, A.V. Giridhar, and K. Sethupathi. Analysis of partial discharge activity by a conducting particle in liquid nitrogen under AC voltages adopting UHF technique. *Cryogenics*, 50:43–49, 2010.

[83] R. Sarathi, A.V. Giridhar, and Abirami Mani. Understanding the incipient discharge activity in liquid nitrogen under AC voltage by adopting UHF technique. *IEEE Transactions on Dielectrics and Electrical Insulation*, 18(3):707–713, 2011.

[84] O. Lesaint and P. Gournay. Initiation and propagation thresholds of positive prebreakdown phenomena in hydrocarbon liquids. *IEEE Transactions on Electrical Insulation*, 1(4):702–708, 1994.

[85] M.D. Judd, O. Farish, and B.F. Hampton. Modelling partial discharge excitation of UHF signals in waveguide structures using green's functions. *IEE Proceeding of Science Measurement Technology*, 143:63–70, 1996.

[86] E.O. Forster. The metal/liquid interface: The charge injection process. *IEEE Transactions on Electrical Insulation*, EI-19(6):524–528, 1984.

[87] F.M.J. McCluskey, A. Denate, and O. Lesaint. Breakdown and prebreakdown phenomena in liquid under positive impulse voltages. *IEEE Transactions on Electrical Insulation*, 1(3):377–382, 1994.

[88] P. Rain, C. Boisdon, O. Lesaint, and R. Tobazeon. Behavior of streamers under divergent AC fields in transformer oils at large gaps. *IEEE Transactions on Electrical Insulation*, 26(4):715–725, 1991.

[89] Kazuaki Yamazawa and Hisanao Yamashita. Pre-breakdown light emission and current pulses in liquid nitrogen. *Japanese Journal of Applied Physics*, 9:17–22, 1998.

[90] M. Pompili, C. Mazzetti, and M. Libotte. The effect of the definition used in measuring partial discharge inception voltages. *IEEE Transactions on Electrical Insulation*, 28:1002–1006, 1993.

[91] E.O. Forster. Partial discharges and streamers in liquid dielectrics the significance of the inception voltage. *IEEE Transactions on Electrical Insulation*, 28(6):941–946, 1993.

[92] N. Bonifaci, A. Denat, and V.M. Atrazhev. Onset voltage for corona pulses in gaseous Ar under high pressure and in liquid Ar. *IEEE Transactions on Electrical Insulation*, 2(1):137–142, 1995.

[93] K. Arii and W.F. Schmidt. Current injection and light emission in liquid argon and xenon in a divergent electric field. *IEEE Transactions on Electrical Insulation*, 19:16–23, 1984.

[94] J.L Hernandez-Avila, N. Bonifaci, and A. Denat. Corona discharge inception as a function of pressure in gaseous and liquid nitrogen. *IEEE International Symposium on Electrical Insulation*, pages 493–496, 1994.

[95] T.J Lewis. Mechanism of electrical breakdown in saturated hydrocarbons. *IEEE Transactions on Dielectrics and Electrical Insulation*, 26:645–650, 1956.

[96] J.C. Devins, S.J Rzad, and R.J. Schwabe. Breakdown and pre-breakdown phenomena in liquids. *Journal of Applied Physics*, 52:4531–4545, 1981.

[97] O. Lesaint and P. Gournay. Investigation on transient currents associated with streamer propagation in dielectric liquids. *IEEE Transactions on Electrical Insulation*, 26(4):699–707, 1991.

[98] M. Pompili, C. Mazzetti, and R. Bartnikas. Partial discharge development and detection in dielectric liquids. *IEEE Transactions on Electrical Insulation*, 16(6):1648–1654, 2009.

[99] P. Wang, D.J. Swaffield, P.L. Lewin, and G. Chen. Thermal bubble behaviour in liquid nitrogen under electric fields. *IEEE Transactions on Dielectrics and Electrical Insulation*, 15(3):626–634, 2008.

[100] P. Rain and O. Lesaint. Prebreakdown phenomena in mineral oil under step and AC voltage in large-gap divergent fields. *IEEE Transactions on Electrical Insulation*, 1(4):702–708, 1994.

[101] Ignacy Adamczewski. *Ionization, Conductivity and Breakdown in Dielectric Liquids.* Taylor and Francis LTD, 1969.

[102] S. Sakamoto and H. Yamada. Optical study of conduction and breakdown in dielectric liquids. *IEEE Transactions on Electrical Insulation*, 15:171–181, 1980.

[103] G. Berg and L.E. Lundgaard. Discharges in combined transformer oil/paper insulation. *13th IEEE International Conference on Dielectric Liquids*, Japan:144–147, 1999.

[104] G. Massala and O. Lesaint. Positive streamer propagation in large oil gaps electrical properties of streamers. *IEEE Transactions on Electrical Insulation*, 5(3):371–381, 1998.

[105] B.Y. Seok, M. Komatsu, M. Kushinaga, J. Suehiro, and M. Hara. Pressurizing and sub-cooling effects on electrical breakdown of LN_2 in modeled hts coils. *IEEE Transactions on Power Delivery*, 8(6):1016–1024, 2001.

[106] P. Wang, D.J. Swaffield, P.L. Lewin, and G. Chen. Electric field effects on boiling heat transfer of liquid nitrogen. *Cryogenics*, 49:379–389, 2009.

[107] D. Srinivasan and G.G. Karady. Development of the dry-band arc on all dielectric self-supporting cables during laboratory tests. *IEEE Transactions on Power Delivery*, 19:1746–1750, 2004.

[108] L.H. Meyer, S.H. Jayaram, and E.A. Cherney. A novel technique to evaluate the erosion resistance of silicone rubber composites for high voltage outdoor insulation using infrared laser erosion. *IEEE Transactions on Electrical Insulation*, 12(6):1201–1208, 2006.

[109] B. Pinnangudi, R.S. Gorur, and C.D. Poweleit. Quantification of degradation in nonceramic insulator housing materials by laser ablation. *IEEE Transactions on Electrical Insulation*, 13(1):423–429, 2006.

[110] B.J. Garrison and R. Srinivansan. Laser ablation of organic polymers - microscopic models for photochemical and thermal processes. *Journal of Applied Physics*, 57:2909–2914, 1985.

[111] I.L. Hosier, M.S. Abd Rahman, E.W. Westenbrink, and A.S. Vaughan. Laser ablation of polymeric composites. *Proceedings of the 2010 IEEE International Conference on Solid Dielectrics, Germany*, 2010.

[112] I.L. Hosier, M.S. Abd Rahman, A.S. Vaughan, A. Krivda, X. Kommann, and L.E. Schmidt. Laser ablation of silicone composites. *Journal of Applied Physics: Conference Series 310 0012010*, 2011.

[113] K.C.A. Crane and J.R. Brown. Laser induced ablation of fibre epoxy composites. *Journal of Physics D: Applied Physics*, 14:2341–2349, 1981.

[114] P.T. Tsilingiris. Comparative evaluation of the infrared transmission of polymer films. *Energy Conversion and Management*, 44(18):2839 –2856, 2003.

[115] T. Wentink and W.G. Planet. Infrared transmission and emission of teflon. *Air force ballistic missile division air research and development*, pages 1–8, 1960.

[116] J.G Grasseli and B.J. Bulkin. *Analytical Raman Spectroscopy.* New York: Wiley, 1991.

[117] A.S. Vaughan, S.J. Dodd, and S.J. Sutton. A raman microprobe study of electrical treeing in polyethylene. *Journal of Material Science*, 39(1):181–191, 2004.

[118] A.S. Vaughan, I.L. Hosier, S.J. Dodd, and S.J. Sutton. On the structure and chemistry of electrical trees in polyethylene. *Journal of Physics D: Applied Physics*, 39(5):962–978, 2006.

[119] J.L. Koenig and F.J. Boerio. Raman scattering and band assignments in polytetrafluoroethylene. *Journal of Chemical Physics*, 50:2823–2829, 1969.

[120] P.W. Sayers, T.J. Lewis, J.P. Llewellyn, and C.L. Griffiths. Investigation of the structural changes in ldpe and xlpe induced by high electrical stress. *Proceedings of the 8th International Conference on Dielectric Materials Measurements and Applications, Edinburgh*, pages 403–407, 2000.

[121] A.C. Ferrari and J. Robertson. Interpretation of raman spectra of disordered and amorphous carbon. *PHYSICAL REVIEW B*, 61(20):14 096–14 106, 2000.

[122] F. Krahenbiihl, B. Bernstein, M. Danikas, J. Densley, K. Kadotani, M. Kahle, M. Kosaki, H. Mitsui, M. Nagao, J.Smit, and T. Tanaka. Properties of electrical insulating materials at cryogenic temperatures: A literature review. *IEEE Electrical Insulation Magazine*, 10(4):10–22, 1994.

[123] Weedy B.M., S.G. Swingler, and S. Shaikh. Life expectancy and failure mechanisms of lapped synthetic tape impregnated with supercritical He. *IEE Proceeding*, 129(Part A):328–331, 1982.

[124] M. Goldman and R.S. Sigmond. Corona and insulation. *IEEE Transactions on Electrical Insulation*, EI-17(2):90–104, 1982.

[125] Y. Zhu, K. Haji, M. Otsubo, and C. Honda. Surface degradation of silicon rubber exposed to corona discharge. *IEEE Transactions on Electrical Insulation*, 34(4):1094–1098, 2006.

[126] T. Toriyama, H. Okamoto, M. Kanazashi, and K. Horii. Degradation of polyethylene by partial discharge. *IEEE Transactions on Electrical Insulation*, EI-2(2):83–92, 1967.

[127] Weedy B.M. and S.G. Swingler. Life expectancy of taped cable insulation. *IEEE Transactions on Electrical Insulation*, EI-14:222–227, 1979.

[128] C. Mayoux. Corona discharge and ageing process of an insulation. *IEEE Transactions on Electrical Insulation*, EI-12(2):153–158, 1977.

[129] J. Brydson. *Plastic Materials.* Butterworth-Heinemann, 1999.

[130] N. Vandencasteele, H. Fairbrother, and F. Reniers. Selected effect of the ions and the neutrals in the plasma treatment of PTFE surfaces: An oes-afm-contact angle and xps study. *Plasma Processes and Polymers*, 2:493–500, 2005.

[131] A. Vesel, M. Mozetic, and A. Zalar. Xps characterization of PTFE after treatment with rf oxygen and nitrogen plasma. *Surface and Interface Analysis*, 40:661663, 2008.

[132] Alexander Kutil. Quantification of fibre-reinforced insulating materials based on PD analysis. *IEEE Transactions on Electrical Insulation*, 5(4):603–611, 1998.

[133] W. Weihan and H. Fengnian. Mechanical and dielectric assessment of ultrahigh molecular weight polyethylene insulation for cryogenic applications. *IEEE Transactions on Electrical Insulation*, 27(3):504–512, 1992.

[134] Peter.H.F. Morshuis. Degradation of solid dielectrics due to internal partial discharge: Some thoughts on progress made and where to go now. *IEEE Transactions on Electrical Insulation*, 12(5):905–913, 2005.

[135] C.H. Park, T. Kaneko, M. Hara, and M. Akazaki. Effects of mechanical stresses on the dielectric breakdown strengths of pet and FRP. *IEEE Transactions on Electrical Insulation*, EI-17(3):234–240, 1987.

[136] J.V. Miller and E.G. Bartick. Forensic analysis of single fibers by raman spectroscopy. *Applied Spectroscopy*, 55(12):1729–1732, 2001.

[137] H. Vaskova and V. Kresalek. Quasi real-time monitoring of epoxy resin crosslinking via raman microscopy. *International Journal of Mathematical Models and Methods in Applied Sciences*, 5(7):1197–1204, 2011.

[138] M. Kozako, N. Fuse, Y. Ohki, T. Okamoto, and T. Tanaka. Surface degradation of polyamide nanocomposites caused by partial discharges using iec (b) electrodes. *IEEE Transactions on Electrical Insulation*, 11(5):905–913, 2004.

[139] T. Tanaka. Characteristics of composite insulation: Liquid-impregnated insulation. *IEEE Transactions on Electrical Insulation*, EI-21(6):881–888, 1986.

[140] M.D. Judd, L. Yang, and I.B.B Hunter. Partial discharge monitoring of power transformers using UHF sensors. Part 1: sensors and signal interpretation. *IEEE Electrical Insulation Magazine*, 12:5–13, 2005.

[141] M.D. Judd, L. Yang, and I.B.B Hunter. Partial discharge monitoring for power transformer using UHF sensors. Part 2: field experience. *IEEE Electrical Insulation Magazine*, 21:5–13, 2005.

[142] H.H. Sinaga, B.T. Phung, and T.R. Blackburn. Partial discharge localization in transformers using UHF detection method. *IEEE Transactions on Dielectrics and Electrical Insulation*, 19(6):1891–1900, 2012.

[143] L. Yang and M.D. Judd. Recognising multiple partial discharge sources in power transformers by wavelet analysis of UHF signals. *IEE Proceedings - Science, Measurement and Technology*, 150(3):119–126, 2002.

[144] T. Pinpart and M.D. Judd. Differentiating between partial discharge sources using envelope comparison of ultra-high-frequency signals. *IET Journals Science, Measurement and Technology*, 4(5):156–267, 2010.

[145] R. Hobara, S. Yoshimoto, and S. Hasegawa. Dynamic electrochemical-etching technique for tungsten tips suitable for multi-tip scanning tunnelling microscopes. *e-Journal of Surface Science and Nanotechnology*, 5:94–98, 2007.

[146] Y. Nakamura, Y. Mera, and K. Maeda. A reproducible method to fabricate atomically sharp tips for scanning tunnelling microscopy. *Scientific Instruments*, 78:3373–3376, 1999.

Appendix A
Electrochemical Etching of Tungsten

The chosen method for preparing sharp needle tips is called "drop-off" electrochemical etching. This is one of the most widely used techniques since it is fast, cheap, convenient and reliable. The basic idea is to dip a small diameter wire in an electrolyte solution as an anode and counter electrode, cathode, are is also immersed in the solution. The etching process occurring at the air/electrolyte interface reduces the thickness of the material. When the tensile stress at liquid/gas interface exceeds the tensile strength of tungsten, the part of the wire in the solution will drop off and a tip is formed. This method can either be static, or dynamic, e.g. the etched wire is slowly pulled out of the solution. The difference in the shapes of the produced tips between the two techniques is illustrated in Figure 1. The tips fabricated by the static etching method always have sharp points at the boundary which can cause undesirable partial discharges when high voltages are applied. Therefore, the dynamic method is used instead.

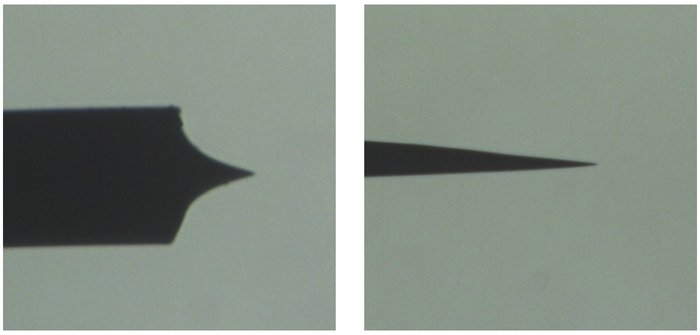

(a) A tip fabricated from static etching

(b) A tip fabricated from dynamic etching

Figure 1: Static and dynamic etching.

Tips are etched from polycrystalline tungsten wires with a diameter of 1 mm. A fine stepper motor is used to slowly pull the wire out of the solution. Every step of the motor corresponds to 2.5 μ m linear movement of the wire. Motor speed is normally kept from

2 to 5 $\mu m/s$. The electrolyte solution is sodium hydroxide (NaOH). The applied voltage is DC and can vary from 0 to 20V. Cathode is also made of tungsten wire with the same diameter. Cathode electrodes are shielded by plastic tubes in order to prevent hydrogen bubbles generated during etching from affecting the reproducibility of the tip profile. A simplified process of oxidation of tungsten at anode can be expressed as [145]:

$$W + 6OH^- \rightarrow WO_{3(s)} + 3H_20 + 6e^- \tag{1}$$

$$WO_{3(s)} + 2OH^- \rightarrow {WO_4}^{2-} + H_20 \tag{2}$$

The production rate of tungstate ($WO_{3(s)}$) in Equation (1) is proportional to the etching current. The tungstate then reacts with OH$^-$ and dissolves into the solution following Equation (2). This reaction happens spontaneously and does not depend on current or voltage. This process can be controlled by the concentration of the solution. The tip radius, on the other hand, is dependent on the cut-off time of the current after the bottom part of the wire drops. The faster the cut-off time, the sharper the resulting tips. This parameter can be controlled by a electronic circuit which has been suggested in [146].

From many trial tests, the optimum conditions for tungsten tip fabrication are: 3M/l NaOH, 10 V of applied voltage,150 mA of etching current and 3 μms^{-1} of motor speed. Sharp tips can be produced repeatably under these conditions. A close-up image of a tip fabricated by this method is shown in Figure 2. The tip radius, r_p, is measured by fitting a circle around the end of the tip. The radius of the circle is the value of r_p and is found to be 0.8 μm.

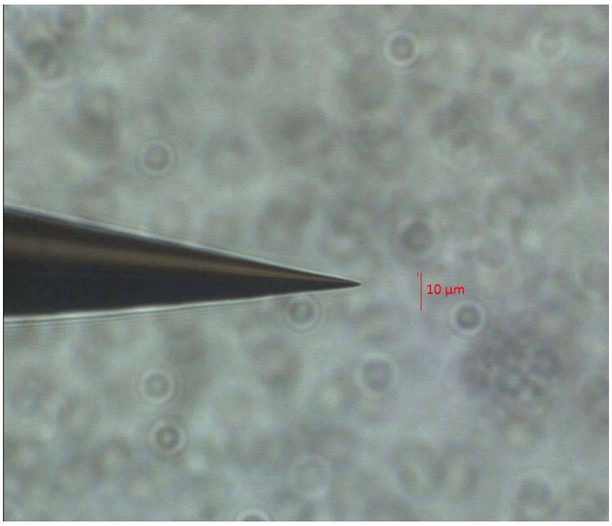

Figure 2: A close-up image of a tip fabricated by dynamic etching method

Appendix B
Cryostat modelling

Modelling Of UHF PD Signals From a Cryostat Using FDTD

Department of Electronic & Electrical Engineering
University of Strathclyde
Glasgow, United Kingdom

Prepared by: Mr. Asnor Mazuan Ishak
Supervisor: Dr. Martin Judd

Date: 26th June 2010

Cryostat Modelling

Two kinds of simulation have been done using XFdtd software, which are simulations of the geometrical arrangement of the cryostat, with and without the material structures. The position of PD source and sensors are the same, as shown in Figures 1 and 2, respectively. Without the structure configuration, the geometries of the windows (Sapphire and BK7 windows) and cryostat walls (inner and outer walls); and also liquid nitrogen are not present. Four point sensors are located 2 mm from the centre of the outer windows (BK7).

Four different PD pulse widths have been applied as a vertically-directed PD current source simulated as flowing from the coordinates {200 mm, 200 mm, 549 mm} to the point {200 mm, 200 mm, 551 mm}. The grid system has been defined on an FDTD cell size of 2 mm in all three axes. Table 1 details the simulation periods required for the different PD pulse widths. The simulation time without the material structure is shorter than with the structure because it needs shorter time to reach the convergence and stability of the signals. Table 2 shows the material properties used in the simulation.

Figures 3 to 8 indicate the three different PD signals of with and without material structures for 4 different positions of the sensors. Figure 11 shows that the ratio of signal peak with structure to peak without structure decreases dramatically with increasing pulse width, demonstrating the high-pass nature of the cryostat windows.

Figures 12 and 13 are basically from Figures 3 and 4, respectively after applying Fast Fourier Transform (FFT) with number of samples, N and sampling rate equal to 16 and 0.26THz.

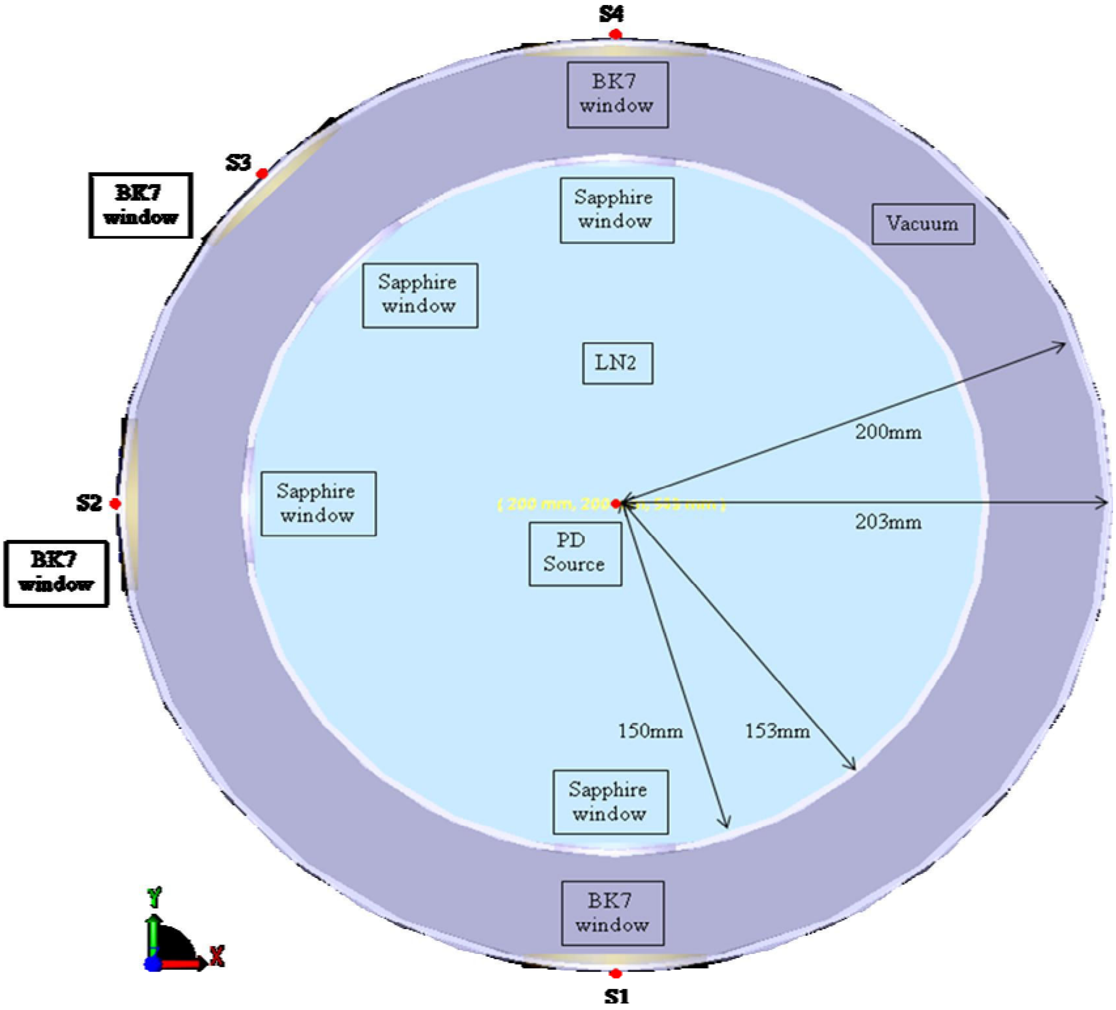

Figure 1 (a): Top view of the cryostat

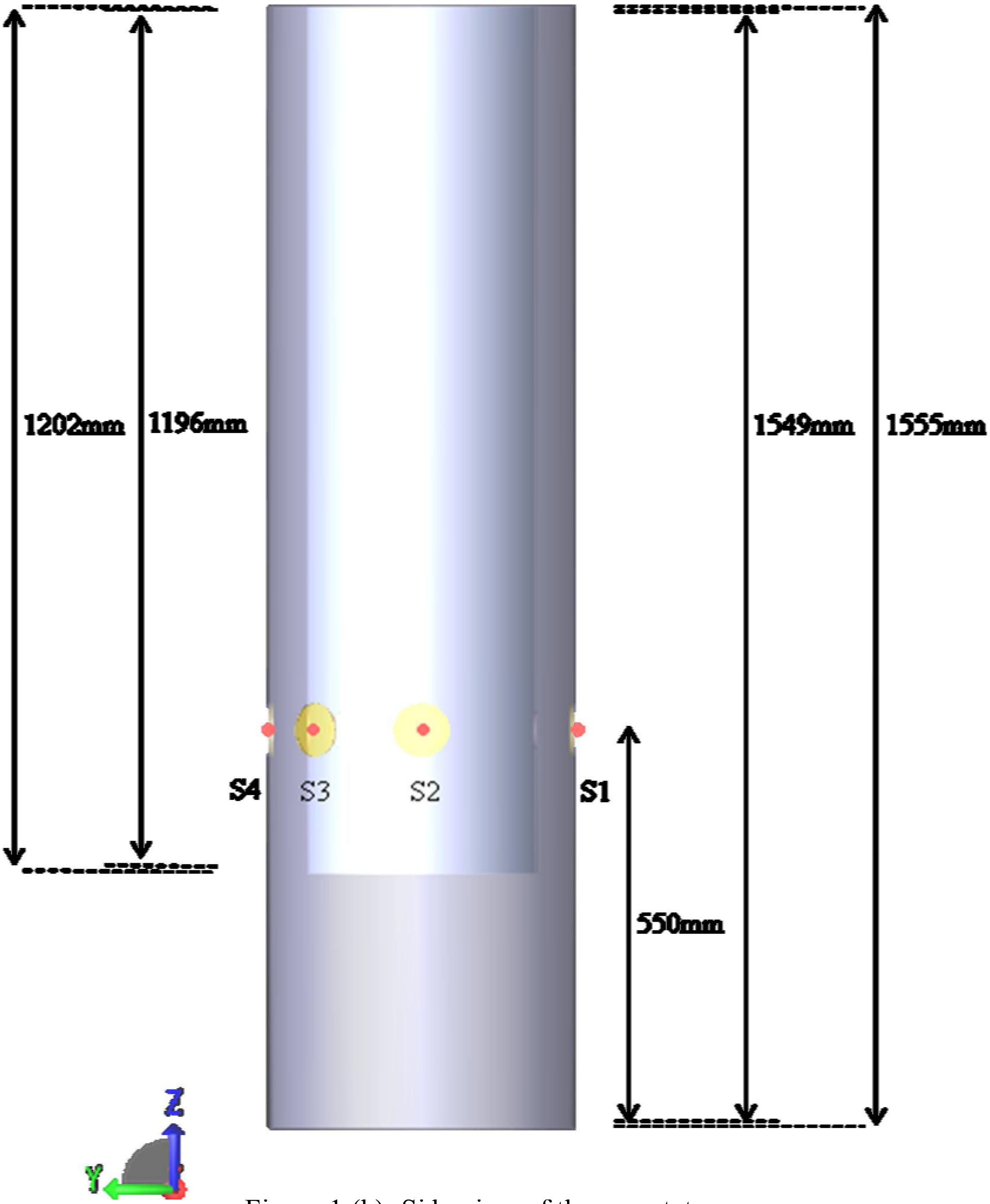

Figure 1 (b): Side view of the cryostat

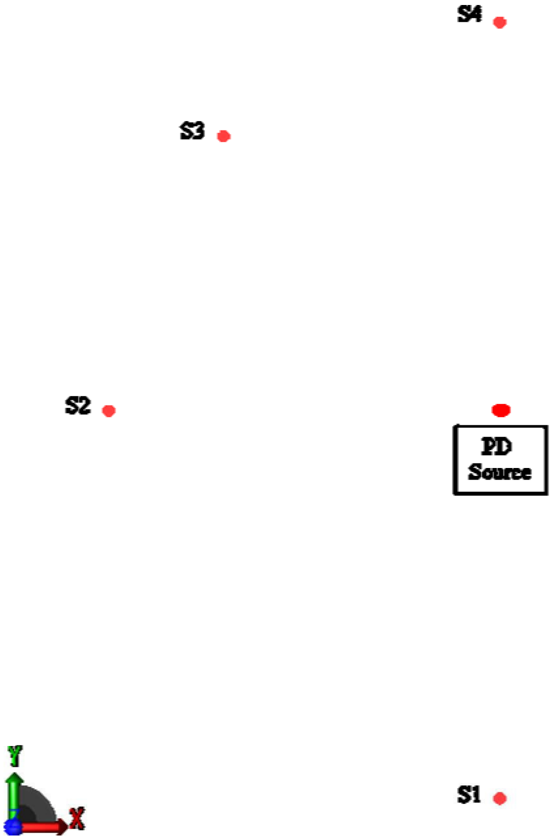

Figure 2 (a): Top view of the cryostat (without material structures)

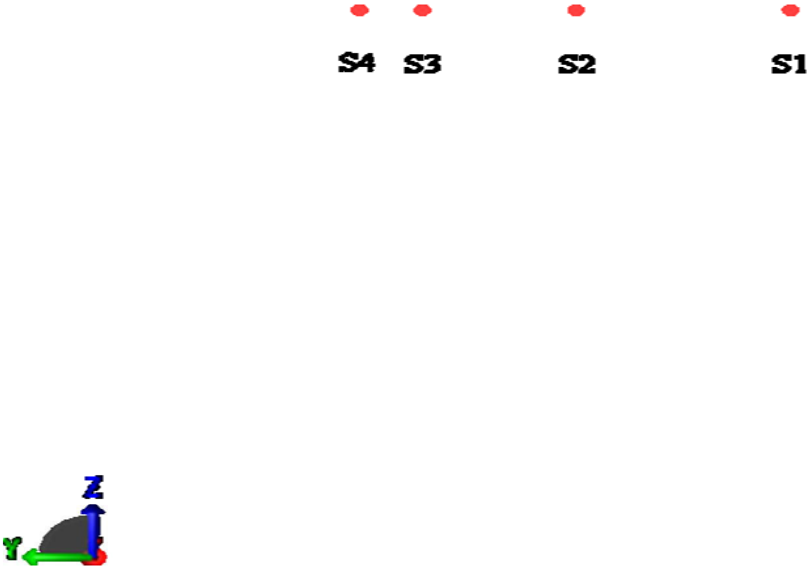

Figure 2 (b): Side view of the cryostat (without material structure)

Table 1: The simulation details for with and without material structures

PD Signal (pulse width)	Configuration	Simulation Time	Simulation Length
0.05 ns	With Structure	5 hrs, 18 m, 49 s	77.0 ns (20000 time steps)
	Without Structure	6 m, 45 s	3.85 ns (1000 time steps)
0.24 ns	With Structure	5 hrs, 18 m, 53 s	77.0 ns (20,000 time steps)
	Without Structure	8 m, 3 s	4.62 ns (1200 time steps)
0.81 ns	With Structure	5 hrs, 22 m, 40 s	77.0 ns (20,000 time steps)
	Without Structure	12 m, 1 s	8.46 ns (2200 time steps)
1.25 ns	With Structure	5 hrs, 19 m, 36 s	77.0 ns (20,000 time steps)
	Without Structure	16 m, 11 s	9.28 ns (2412 time steps)

Table 2: The materials of the cryostat

Parameter Geometry	Relative Permeability	Relative Permittivity	Conductivity (S/m)
Aluminium	1	1	3.53×10^7
Vacuum/Freespace	1	1	0
LN_2	1	1.454	0
Sapphire	1	9	0
BK7(Borosilicate)	1	4.6	0

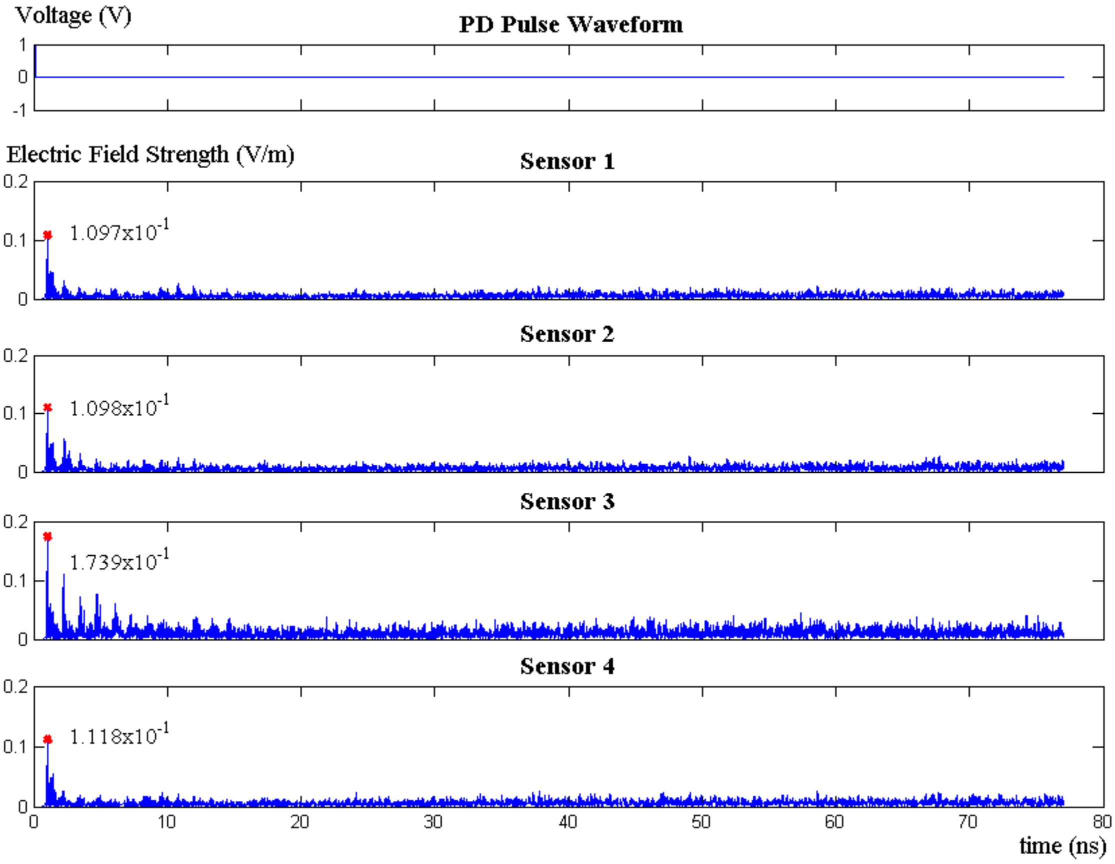

Figure 3: Absolute total of electric field strength for 4 different positions of sensors (with material structures, **0.05 ns** pulse width). Labels show the magnitude of the largest peak in the signal received at each sensor.

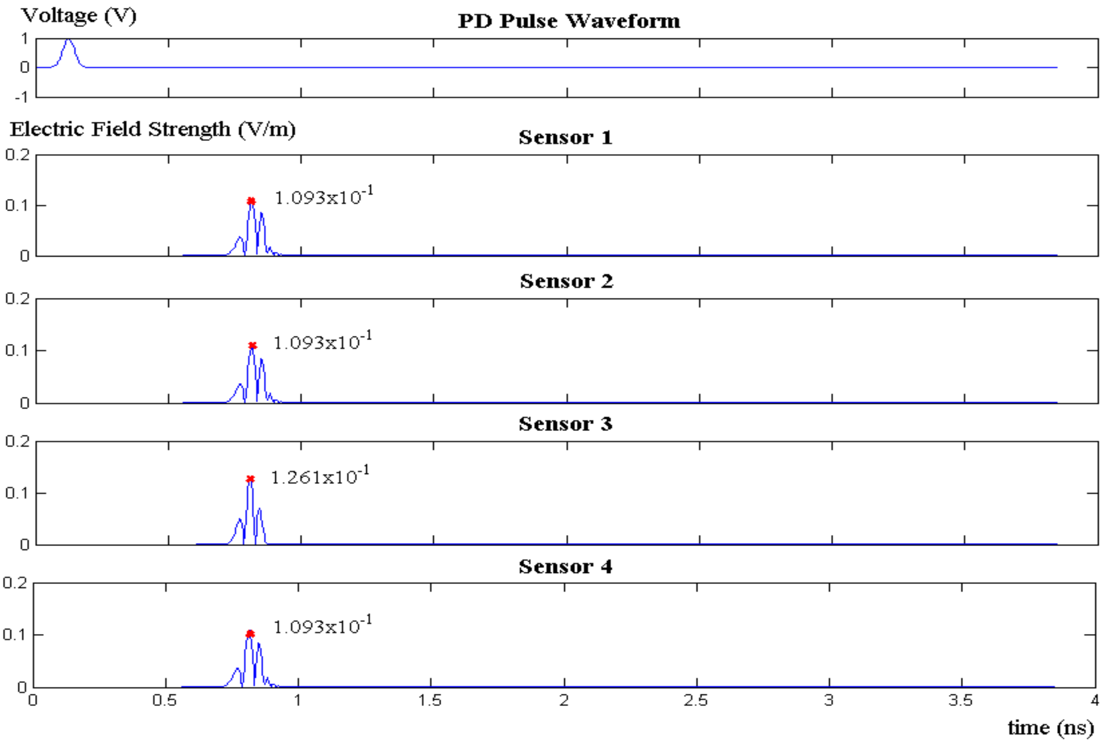

Figure 4: Absolute total of electric field strength (without material structure, **0.05 ns** pulse width). Labels show the magnitude of the largest peak in the signal received at each sensor.

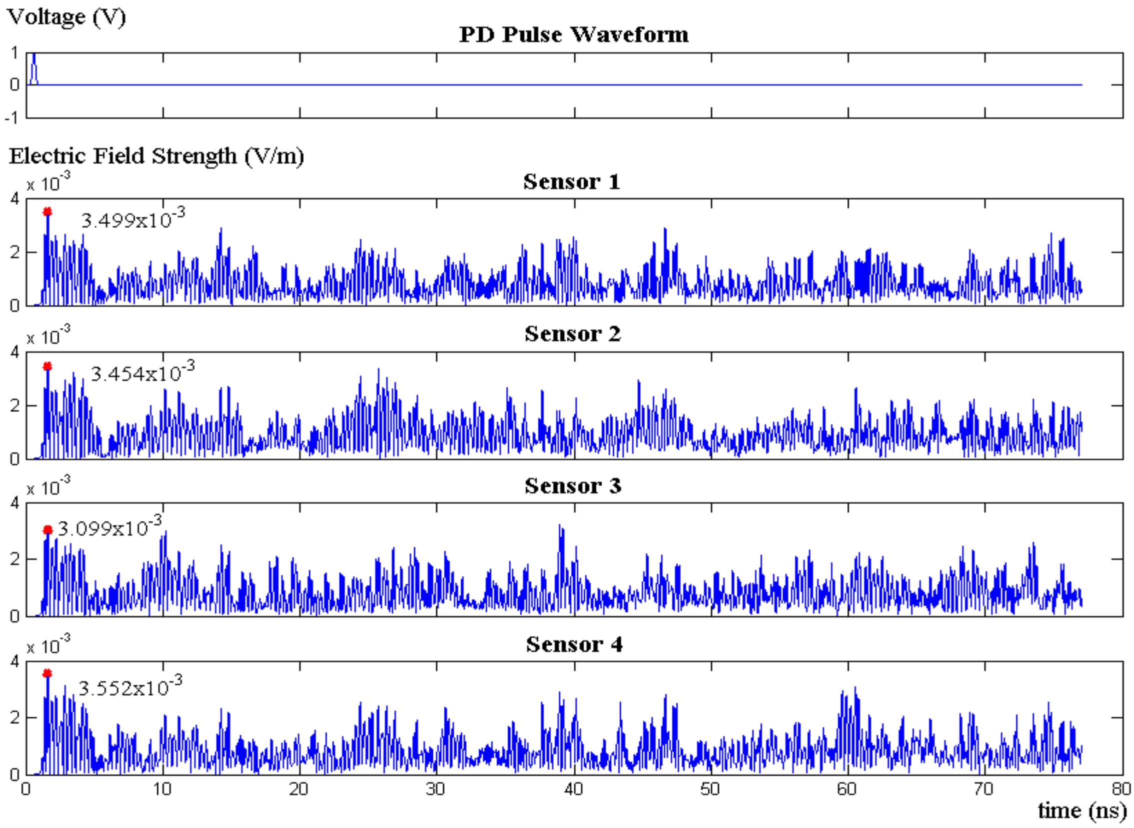

Figure 5: Absolute total of electric field strength for 4 different positions of sensors (with material structures, **0.24 ns** pulse width). Labels show the magnitude of the peak in the signal received at each sensor.

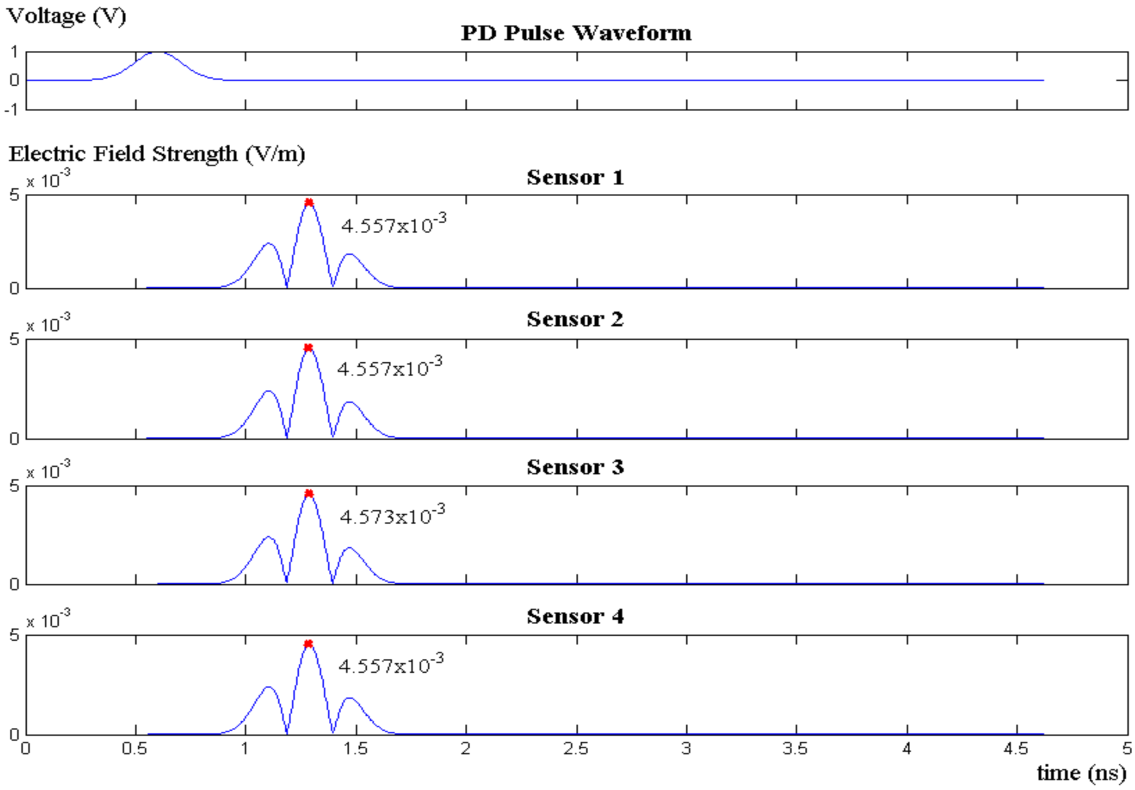

Figure 6: Absolute total of electric field strength (without material structure, **0.24 ns** pulse width). Labels show the magnitude of the peak in the signal received at each sensor.

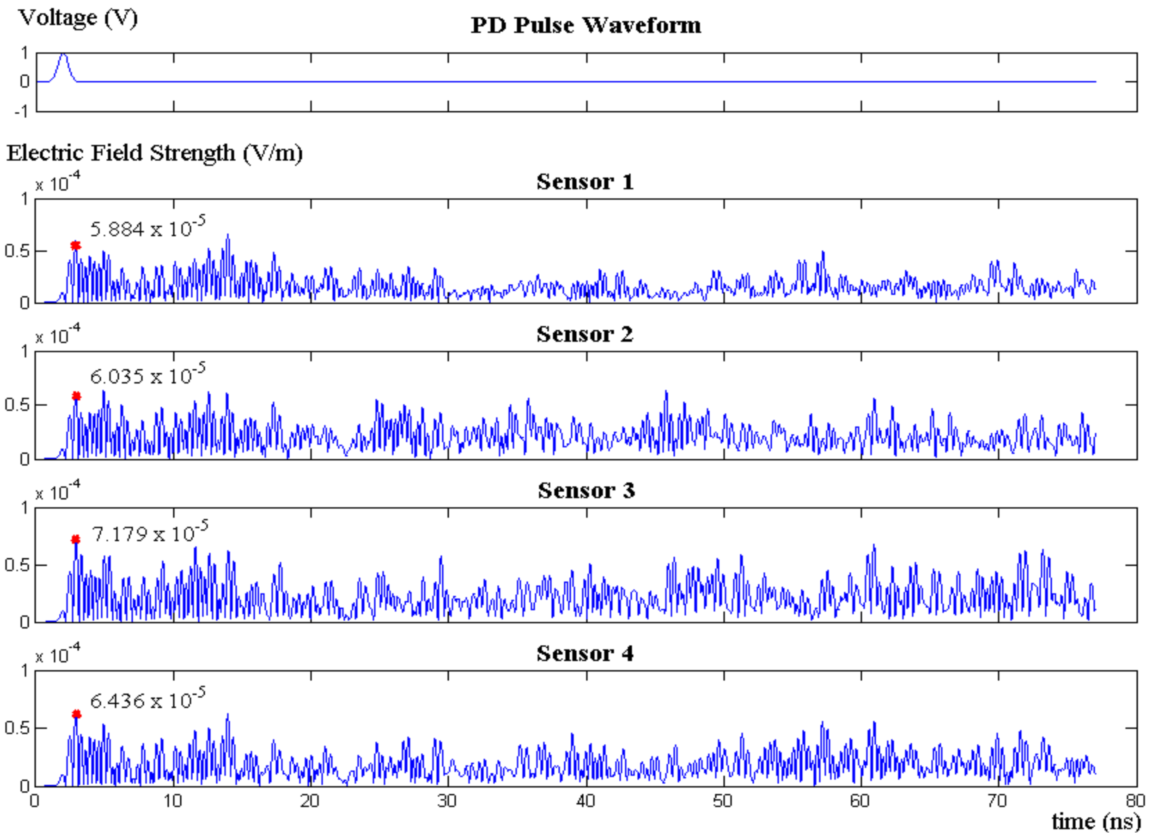

Figure 7: Absolute total of electric field strength for 4 different positions of sensors (with material structures, **0.81 ns** pulse width). Labels show the magnitude of the peak in the signal received at each sensor.

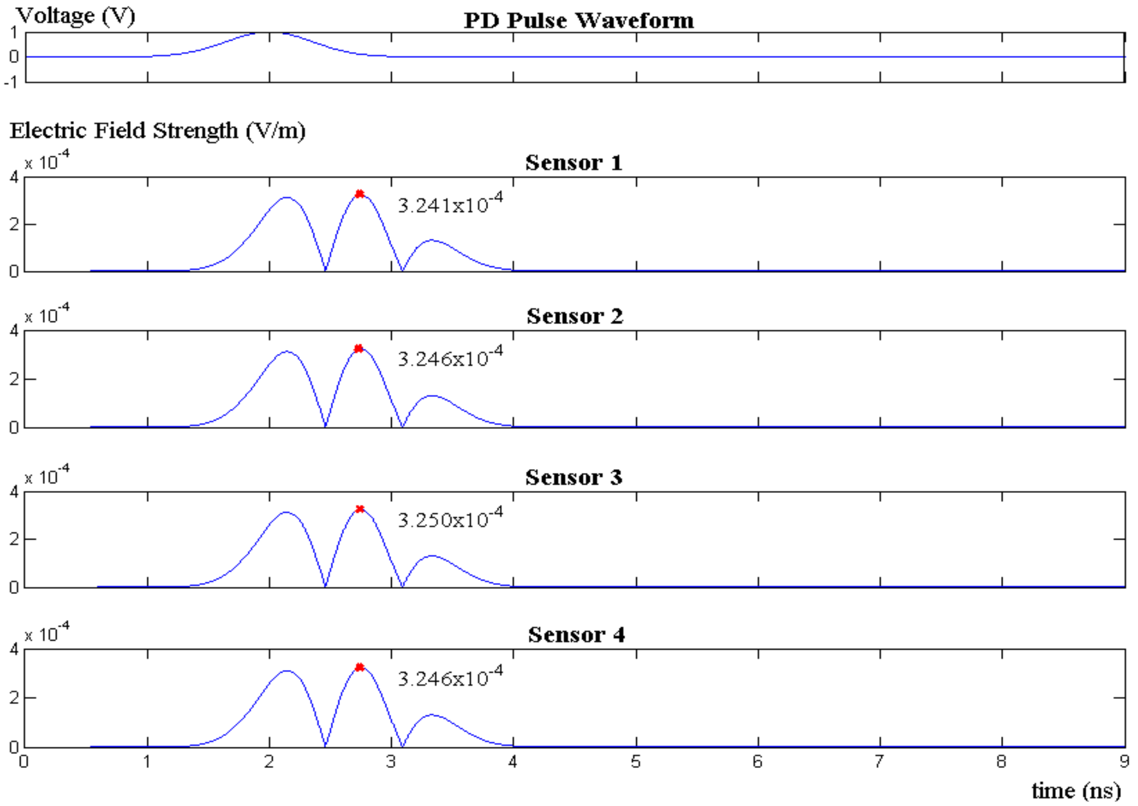

Figure 8: Absolute total of electric field strength (without material structure, **0.81 ns** pulse width). Labels show the magnitude of the peak in the signal received at each sensor.

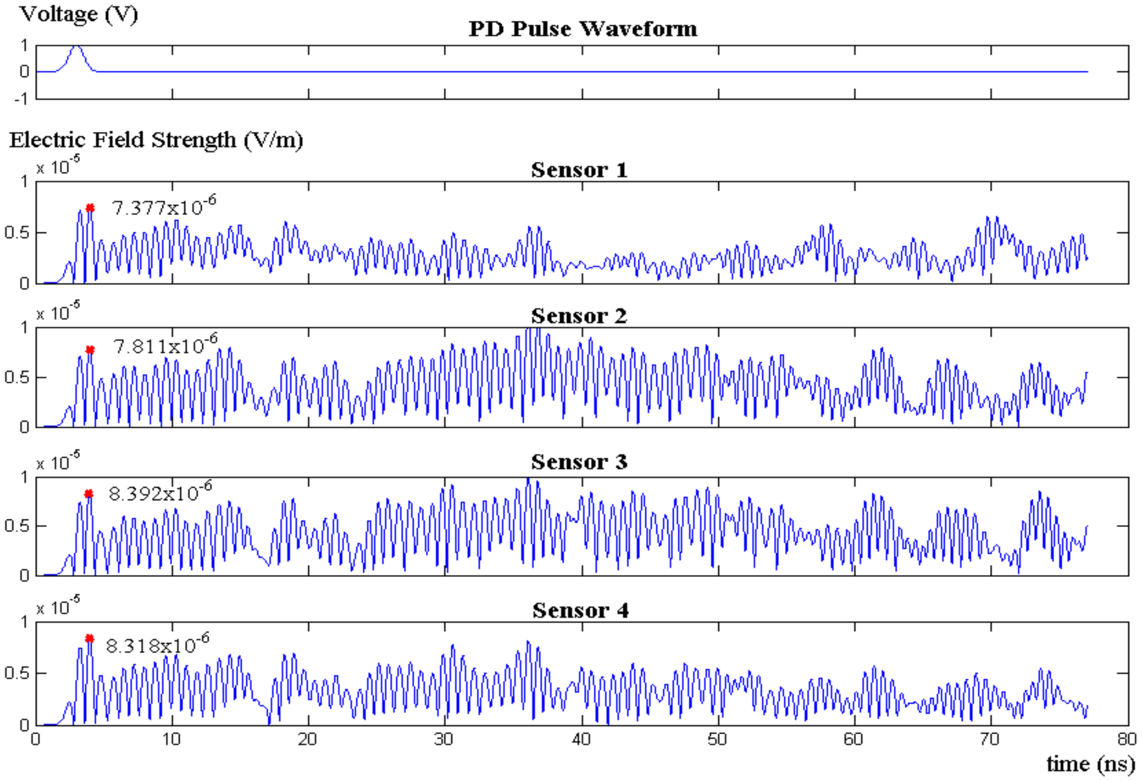

Figure 9: Absolute total of electric field strength for 4 different positions of sensors (with material structures, **1.25 ns** pulse width). Labels show the magnitude of the peak in the signal received at each sensor.

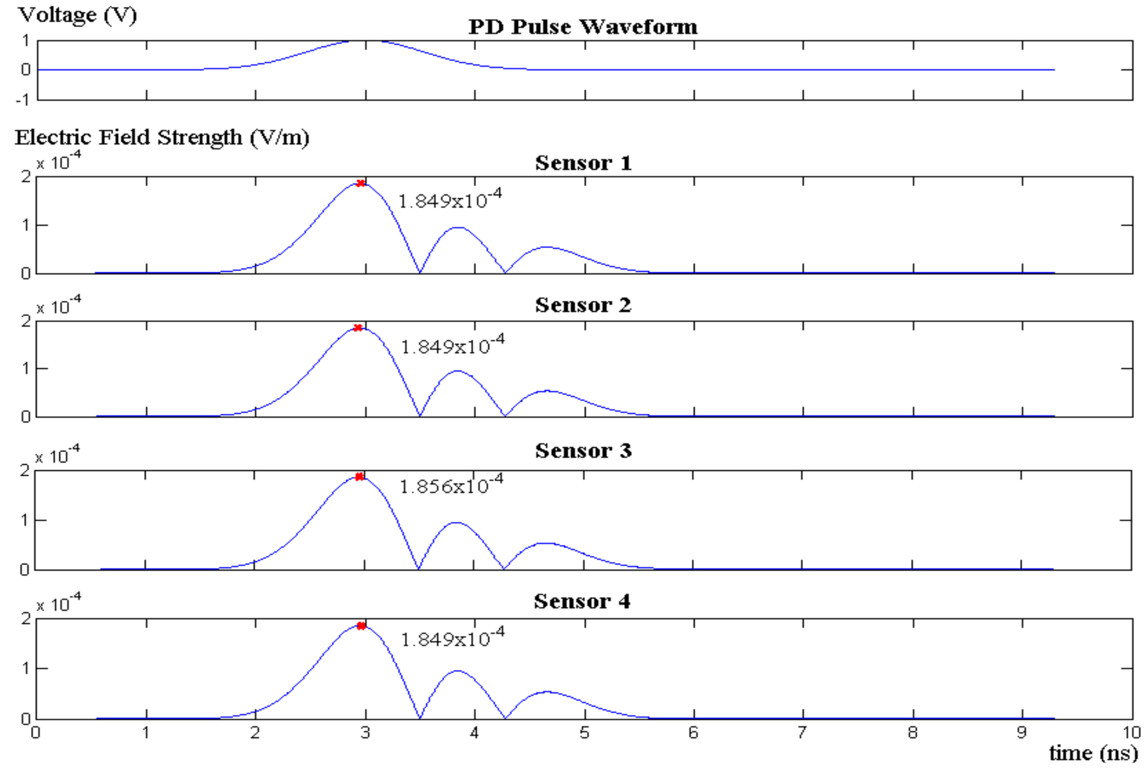

Figure 10: Absolute total of electric field strength (without material structure, **1.25 ns** pulse width). Labels show the magnitude of the peak in the signal received at each sensor.

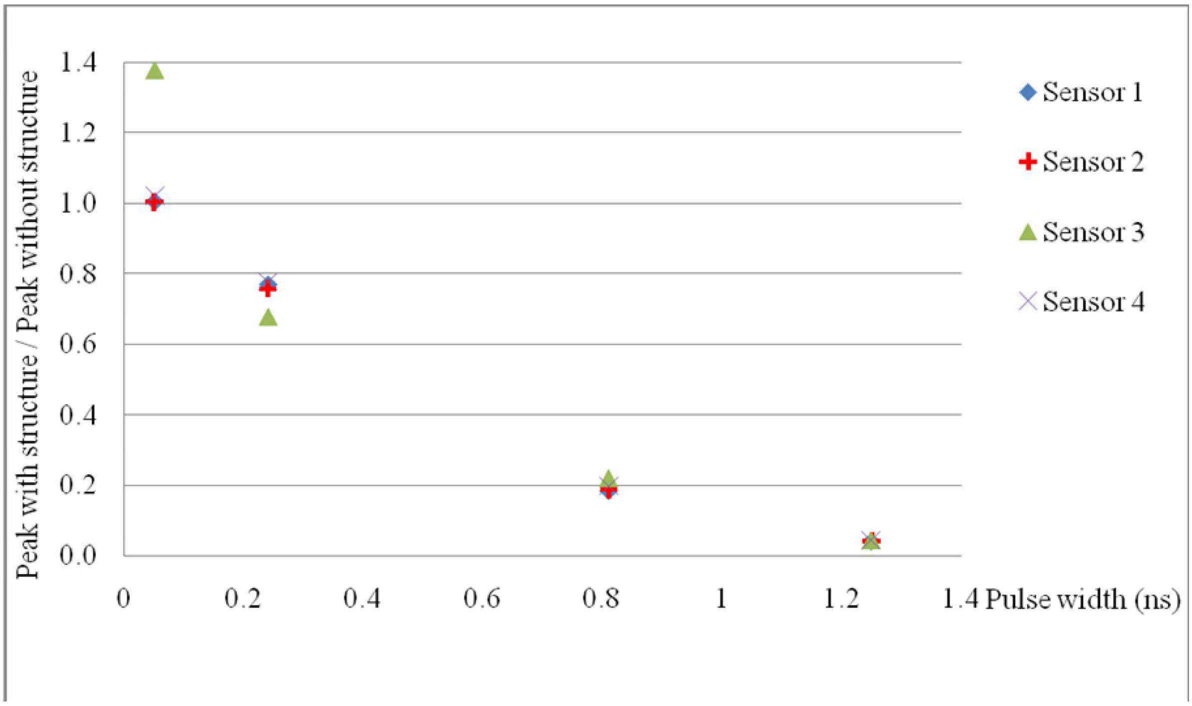

Figure 11: Ratio of (signal peak with material structures) / (peak without material structure) as a function of PD pulse width.

Fig. 11 indicates that, for very short pulses, the structure is almost transparent to radiated signals emerging from the windows. However, as the pulse width increases towards 1 ns and above, the attenuation caused by the cryostat structure becomes increasingly severe. The cause of this phenomenon is the internal reflection of signals whose wavelength is now too long to permit them to propagate efficiently through the windows.

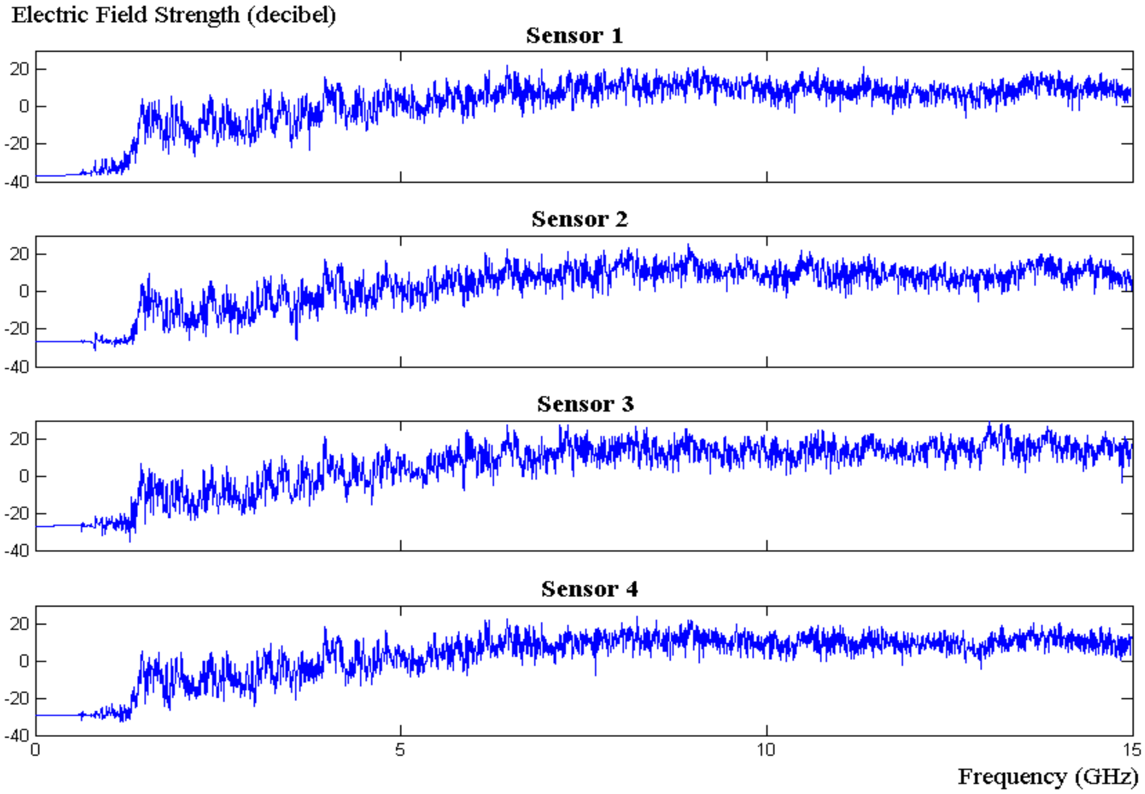

Figure 12: FFT of electric field strength for 4 different positions of sensors (with material structures, 0.05 ns pulse width).

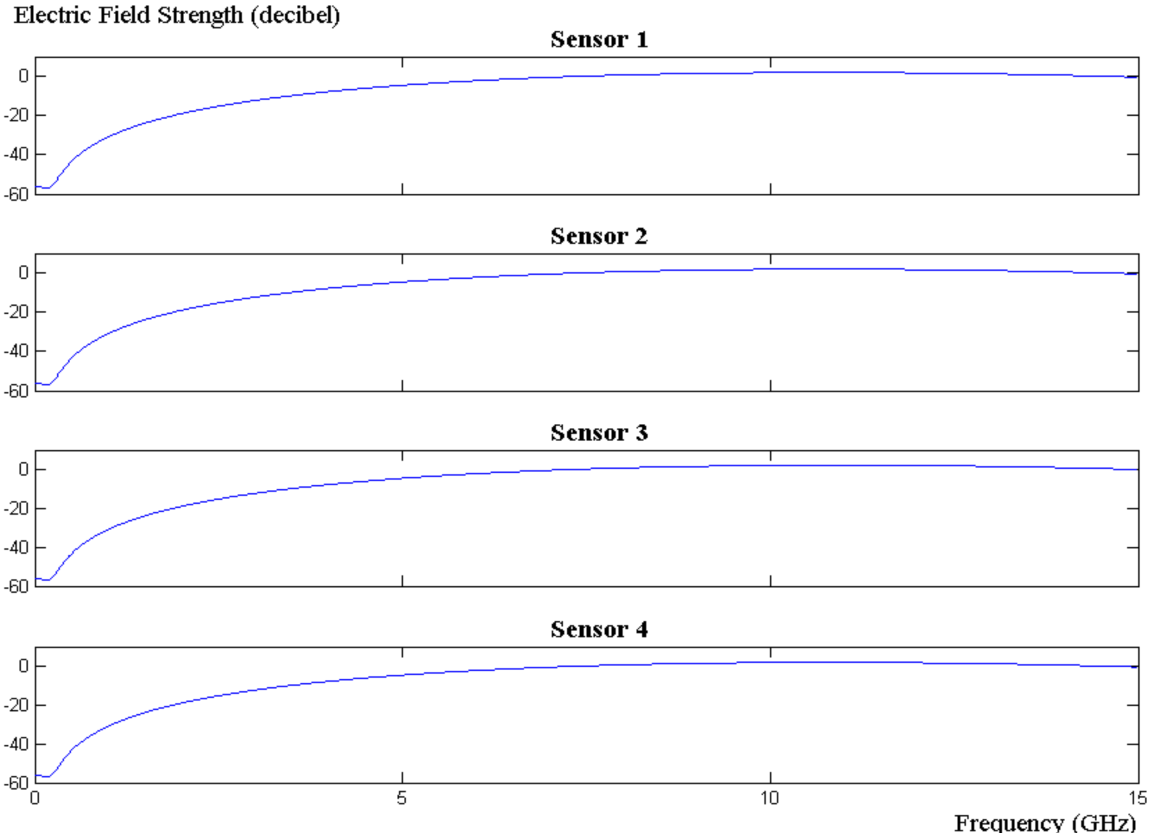

Figure 13: FFT of electric field strength (without material structure, 0.05 ns pulse width).

Conclusions

The structure and windows can attenuate the PD signals. As the pulse width of the PD waveform increases, the electric field strength of the PD signals with and without the material structures will decrease; and the ratio of signal peak with material structure to peak without structure will decrease.

The electric field strength of the PD signals received at sensor 3 is higher than the other three sensors. The exact reason for this is not known, but it may be an artefact of the FDTD modelling, in which the other sensors lie along the faces of the cubic mesh, while sensor 3 is at an angle of 45 degrees to them.

Appendix C
List of publications

Conferences

1. Truong, L H, Swaffield, D J, Lewin, P L and Judd, M D. "The feasibility of using UHF sensors to measure partial discharges in liquid nitrogen", *17th IEEE International Conference on Dielectric Liquids*, Trondheim, Norway, 26 - 30 Jun 2011. IEEE, CD-ROM.

2. Truong, L.H., Lewin, P.L. and Judd, M.D. "Partial discharge measurements of streamers in liquid nitrogen under AC voltages using UHF sensor", *2012 IEEE Conference on Electrical Insulation and Dielectric Phenomena*, Montreal, 14 - 17 Oct 2012. pp, 68-71.

3. Truong, L.H., Lewin, P.L. and Judd, M.D. "Laser ablation of cryogenic dielectrics", *Proceedings of the 2013 International Electrical Insulation Conference Birmingham*, May 2013, pp 52-57.

4. Truong, L.H., Lewin, P.L. and Judd, M.D. "Partial discharge measurements of streamers in liquid nitrogen under AC voltages using UHF sensor", *2013 IEEE International Conference on Solid Dielectrics*, Bologna, June 2013 (accepted).

Journals

1. Truong, L.H., Lewin, P.L. "Towards Condition Monitoring of High Temperature Superconducting Power Apparatus: Phase Resolved Analysis of Partial Discharges in Liquid Nitrogen Under AC Voltages", *IEEE Transactions on Electrical Insulation Special Issue* (accepted).

2. Truong, L.H., Lewin, P.L. and Judd, M.D. "Towards Condition Monitoring of High Temperature Superconducting Power Apparatus: Characterization of Streamers in Liquid Nitrogen Under AC Voltages Using UHF Techniques" *IEEE Transactions on Electrical Insulation Special Issue* (submitted).